A Detailed Spatial and Spectral Study of Synchrotron X-rays from Supernova Remnants with *Chandra*

Aya Bamba

Department of Physics, Graduate School of Science, Kyoto University
Kitashirakawa Oiwake-cho, Sakyo-ku, Kyoto, 606-8502, Japan
bamba@cr.scphys.kyoto-u.ac.jp

Reprinted from the thesis submitted to the Department of Physics,
Graduate School of Science, Kyoto University
on January 5, 2004
in partial fulfillment of the requirements
for the degree of Doctor of Philosophy in physics.

Abstract

We present the first results of a systematic spatial and spectral X-ray study of small scale structures on the shock of five supernova remnants (Cas A, Kepler's remnant, Tycho's remnant, SN 1006, and RCW 86) and a super bubble (30 Dor C), with excellent spatial resolution of the *Chandra* X-ray observatory. All targets have synchrotron X-ray emission which concentrate on a very narrow region of the outer edge of the shock. The scale length of the region emitting synchrotron X-rays is incredibly small, less than 1% of the radius of the system ($\sim$arcsec) both in the upstream and the downstream, in which smaller lengths are seen in the upstream than in the downstream. Together with the information of wide band spectra from radio to X-ray, both age-limited and loss-limited assumptions are checked for the acceleration history of all the SNRs. We found a possible magnetic field strength and configuration, and the maximum energy of accelerated electrons estimated for each target. The perpendicular magnetic field to the shock normal is accepted in all cases, with highly turbulent magnetic field downstream.

Comparing the samples, we found that the scale length of shocks grows as its age increases, in the same rate of Sedov similarity solution for upstream ($\propto t^{4/5}$) and in a faster rate for downstream ($\propto t^{1/2}$). The energy density of magnetic field and cosmic rays evolve keeping an equipartition with the thermal and kinetic energies of the shock ($\propto t^{-6/5}$) under the assumption that the system is in the age-limited case, implying that there are strong energy interaction between kinetic, thermal, magnetic field, and cosmic ray energy densities. The magnetic field is always near to perpendicular. These are the first results to estimate observationally the magnetic field and its direction, energy density of magnetic field and cosmic rays, and their evolutions.

Contents

List of Figures

List of Tables

Chapter 1

Introduction

Cosmic rays are particles with very high energy up to 10^{20} eV, which is higher than the maximum energy we can accelerate in accelerators human being made. Since the discovery of cosmic rays (Hess, 1911, 1912), the origin and mechanism of the acceleration have been one of the biggest long-standing problems.

Since cosmic rays with the energy of $\sim 10^{15}$ eV emit synchrotron X-rays in the interstellar magnetic field, hard X-rays are the good indicator of cosmic rays. A breakthrough came from the hard X-ray study of a young supernova remnant (SNR), SN 1006; Koyama et al. (1995) discovered synchrotron X-rays from the shells of this SNR, indicating the existence of extremely high energy electrons up to the knee energy produced by the first order Fermi acceleration, thanks to the imaging capability of hard X-ray observations. Further, Tanimori et al. (1998) confirmed the presence of high energy electrons with the detection of the TeV γ-rays, which are cosmic microwave photons up-scattered by high energy electrons (the inverse Compton process) in the north eastern shell (the NE shell) of SN 1006. Since these discoveries, detections of synchrotron X-rays and/or TeV γ-rays from other shell-like SNRs have been accumulating, G347.3$-$0.5 (Koyama et al., 1997; Slane et al., 1999; Muraishi et al., 2000; Enomoto et al., 2002), RCW 86 (Bamba et al., 2000; Borkowski et al., 2001b), and G266.6$-$1.2 (Slane et al., 2001). Recently, a significant number of SNRs with synchrotron X-rays have been discovered with the *ASCA* Galactic plane survey (Bamba et al., 2001; Ueno et al., 2003; Bamba et al., 2003a). These discoveries provide good evidence for the cosmic ray acceleration at the shocked shell of SNRs.

The mechanism of the cosmic ray acceleration has also been studied for a long time and the most plausible process is diffusive shock acceleration (DSA) (e.g., Bell, 1978; Blandford & Ostriker, 1978; Drury, 1983; Blandford & Eichler, 1987; Jones & Ellison, 1991; Malkov & Drury, 2001); this process can accelerate particles on the shock with the power-law spectra similar to the observed spectrum of cosmic rays. Apart from the globally successful picture of DSA, detailed but important processes, such as the injection, magnetic field configuration, and the reflection of accelerated particles, have not yet been well understood, partly because there is no information

about the spatial distribution of accelerated particles, which must provide key information on these unclear subjects. Previous observations, however, are limited in spatial resolution for a detailed study on the structure of shock acceleration process and injection efficiency. There is no theoretical study about the acceleration in the evolving shocks like the shocks of SNRs. Although many observations and theoretical models are made for SN 1006 case, these problems are still open issues (Reynolds, 1998; Aharonian & Atoyan, 1999; Vink et al., 2000; Ellison, Berezhko, & Baring, 2000; Dyer et al., 2001; Allen et al., 2001; Berezhko et al., 2002). There is still no systematic view widely believed for acceleration history in SNRs in order to understand the energy budget in a SNR from the shock energy to cosmic rays.

In this thesis, we draw a history of acceleration sites on the shock of SNRs for the first time using the excellent spatial resolution of the *Chandra* X-ray observatory. We review cosmic rays, their acceleration, and SNRs themselves in § 2, § 3, and § 4, respectively. § 5 is devoted to summarize the basic characteristics of the instruments onboard *Chandra* we used in this work. The first results on the spatial and spectral analyses of SN 1006 north eastern shell with *Chandra* are reported in § 6. We extend our method of analyses to four other SNRs and a super-bubble with synchrotron X-rays (Cas A, Kepler, Tycho, RCW 86, and 30 Dor C) in § 7. Combining all the works, we discuss and summarize the cosmic ray acceleration history in SNRs in § 8 and § 9, respectively.

Chapter 2

Review of Cosmic Rays

Cosmic rays are ionized atomic nuclei mainly composed of protons (90%) and α particles (9%). The energy density is $\sim$1 eV cm^{-3}, which is a main form of energy in our Galaxy in the condition of equipartition with cosmic microwave background, magnetic field, and stellar lights. Since the discovery with a balloon experiments (Hess, 1912), the origin and the acceleration mechanism have been one of the biggest problems. In this chapter, we summarize the observational facts and methods of cosmic rays.

2.1 Observational Facts

2.1.1 Chemical Composition and Energy Budget

Figure 2.1 shows the chemical composition of solar particles and cosmic rays. Cosmic rays consist of not only proton but also many kinds of heavy elements, suggesting that they are accelerated in the environment with rich metals. The abundances of the elements with even atomic numbers (Z) are significantly larger than those with odd Z for both solar and cosmic rays. On the other hand, the abundances of Li, Be, B, Sc, Ti, V, Cr, and Mn are significantly higher than those of solar abundance (Figure 2.1). Since these elements can not be created in the stellar evolution, they are considered to be produced by collisions of cosmic rays and interstellar medium (ISM). The column density that a cosmic ray particle passes since they it is produced is 5–10 g cm^{-2}, using the cross sections of the separation which are already known. The passed distance is about 1000 kpc when we assume the average ISM density to be 1 cm^{-3}, which is far longer than the diameter of our Galaxy. This fact shows that cosmic rays are shut by diffusion before escaping into intra-galactic space. The age of cosmic rays (t_{cr}) can be estimated with the ratio of radio isotopes; Garcia-Munoz et al. (1977) determined t_{cr}, using a radio isotope (^{10}Be), to be $\sim 6 \times 10^6$ yrs. It is mainly determined by the escape of cosmic rays from our Galaxy. When we assume the volume of our Galaxy (V_{gal}) and the energy density of cosmic rays (η_{cr}) to be 5×10^{66} cm^3 and 1.6×10^{-12} ergs cm^{-3} respectively,

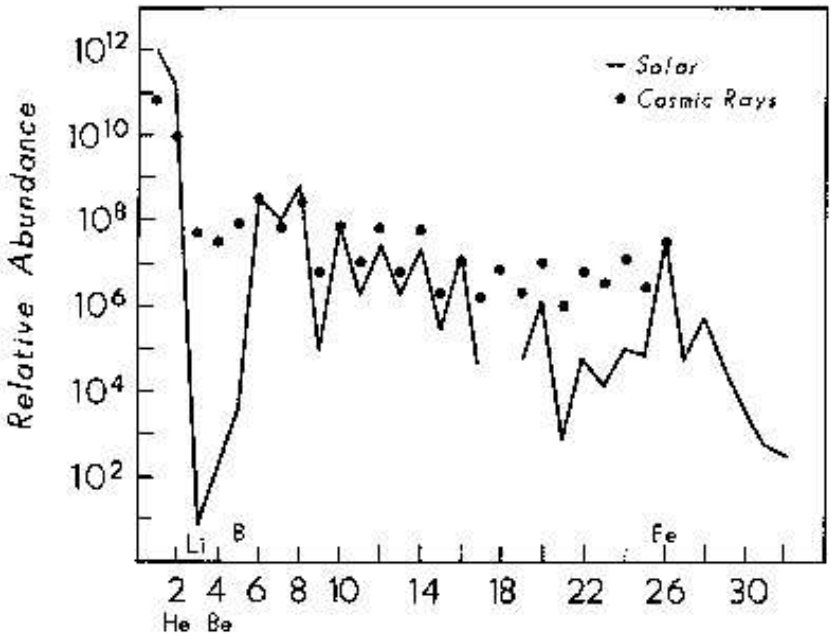

Fig. 2.1.— Chemical composition of cosmic rays (Sokolsky, 1989). The horizontal and vertical axes present atomic number and relative abundance. respectively.

the required energy supply to cosmic rays (P_{cr}) is estimated to be

$$\begin{aligned} P_{cr} &= \frac{V_{gal} \times \eta_{cr}}{t_{cr}} \\ &= 1 \times 10^{40} \text{ ergs s}^{-1} \quad . \end{aligned} \tag{2.1}$$

This injection rate can be explained with supernova explosions, when we assume that (1) their rate is ~ 1 per 30 years, (2) explosion energy is $\sim 10^{51}$ ergs (see §4), and (3) injection rate is about 1% of each supernova energy.

2.1.2 Energy Spectrum

Figure 2.2 shows the energy spectrum of cosmic protons. The spectrum is well represented by two power-law functions as

$$N(E) \propto E^{-2.7} \quad (\leq 10^{15.5} \text{ eV}) \tag{2.2}$$

$$N(E) \propto E^{-3.0} \quad (\geq 10^{15.5} \text{ eV}) \quad . \tag{2.3}$$

The most energetic cosmic rays have the energy up to 10^{20} eV; they are the most energetic particles which human beings know. The spectrum has a break energy at $10^{15.5}$ eV, which is called the "knee"

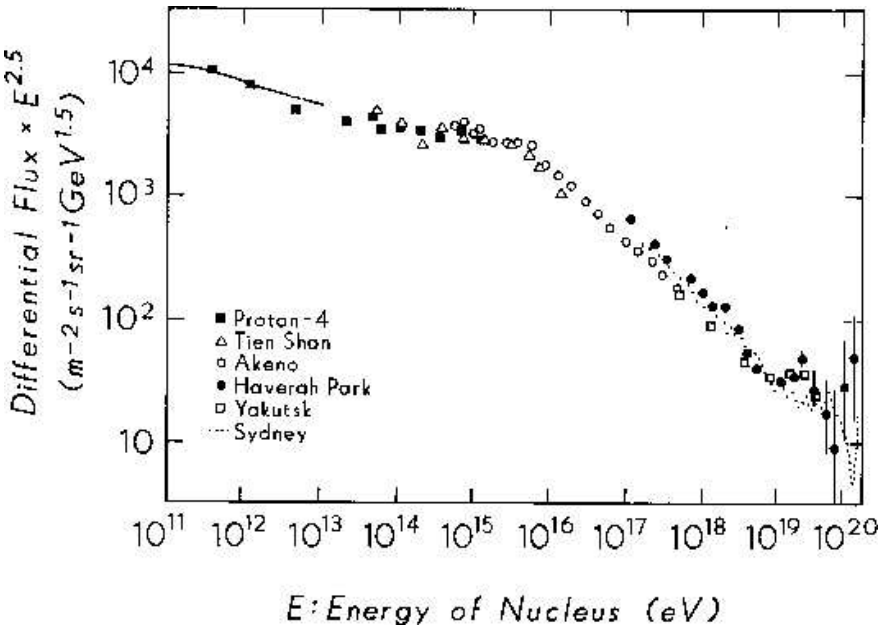

Fig. 2.2.— Energy spectrum of cosmic protons (Sokolsky, 1989). In order to make it clear the structure of the spectrum at the knee energy, the vertical axis is written in differential flux times $E^{2.5}$.

energy. The gyro radius of particles at the knee is about 3 pc in the average interstellar magnetic field ($\sim$1 μG), then the accelerators of cosmic rays which energy with lower energy than the knee must be in our Galaxy.

Most of elements have energy spectrum similar to that of protons. In the case of B, which is produced by the decays of O and C nuclei, the index of the spectrum is smaller. It indicates that nuclei with higher energy decays faster and produce more B than those with lower energy, and that the particles with higher energy escape from our Galaxy faster.

2.2 How to "See" Cosmic Rays?

Since the discovery of cosmic rays, many methods lead us to understanding cosmic rays. In this section, we summarize the methods to "see" cosmic rays, directly or indirectly.

2.2.1 Direct Observations of Cosmic Rays

Cosmic rays fill the universe. We can observe them directly with balloons, satellites, or instruments on the ground. These methods, however, cannot point out where cosmic rays with energies lower

than 10^{18} eV come from due to their gyro motion, the radius of which (gyro radius; r_g) can be written as;

$$r_g \sim \frac{E}{qB} \quad . \tag{2.4}$$

Cosmic rays with the knee energy ($10^{15.5}$ eV) have $r_g \sim 3$ pc in interstellar magnetic field of $\sim \mu$G, then their track bend again and again even they come from the nearest star. Only those who can pass our Galaxy without their track being bent have energy larger than $\sim 10^{19}$ eV, which may be made in extra-galactic sources (see § 3).

When cosmic rays rush into the air, they make an air shower, a particle cascade induced by interaction of a cosmic ray and atoms in the air. The shower mainly consists of photons, muons, and hadrons (Greisen, 1956). The energy of the primary cosmic ray (E_0) is estimated to be

$$E_0 \sim a \times \int_0^\infty dx n(x) \quad , \tag{2.5}$$

where $n(x)$ and a are the number density of charged particles in the shower of the depth x and the energy loss par the unit length of flight, respectively.

There are two type observations of cosmic rays on the ground, which should be selected properly depending on the energy of cosmic rays (Lamb & Weekes, 1987). When one wants to observe very high energy (VHE) cosmic rays of $\sim$ TeV energy, the observations of Cerenkov lights from shower particles with a reflection telescope (Weekes, 1988). Since shower particles made by more energetic (ultra high energy; UHE) cosmic rays can reach the ground, we can detect them directly with ground detector arrays. The biggest project for UHE cosmic ray observations currently planed is the Pierre Auger Observatory, which is composed of 1600 detector surface arrays covering 3000 km^2 overlooked by 24 fluorescence telescopes (e.g., Mantsch, 2003).

Cosmic ray observations with satellites are also performed in many projects. The cosmic rays from the Sun is observed by, for example, the *GEOTAIL* satellite (e.g. Terasawa et al., 2000). *Voyeger I* may have reached the edge of the Solar system (Krimigis et al., 2003; McDonald et al., 2003; Fisk, 2003). The number of detected cosmic rays increases rapidly, suggesting that the satellite might have gone go out of the terminal shock. The remaining life time of the satellite is more than 10 years, then *Voyeger I* will continue to measure cosmic rays far from the Earth.

2.2.2 Observations of Synchrotron Emission

Charged particles emit synchrotron radiation in magnetic field. The synchrotron radiation power per unit frequency from a single electron of energy E in a magnetic field B is (Rybicki & Lightman, 1979)

$$P(\omega, \alpha) = \frac{\sqrt{3}}{2\pi} \frac{\mathrm{e}^3 B \sin\alpha}{m_\mathrm{e} c^2} F\left(\frac{\omega}{\omega_c}\right) \quad , \tag{2.6}$$

where α and $F(x)$ are the pitch angle and the function given by Rybicki & Lightman (1979). The peak frequency ω_c is

$$\omega_c = \frac{3\gamma^2 \mathrm{e} B \sin\alpha}{2(m_e c)} \quad . \tag{2.7}$$

Note that protons radiate weaker synchrotron radiation since they are as 1000 times heavy as electrons; this method is valid only for electrons. Integrating over ω, we find that total emission power is written

$$P_{sync} = \frac{4}{3}\sigma_T c \beta^2 \gamma^2 U_B \quad . \tag{2.8}$$

Here $\sigma_T = 8\pi r_0^2/3$ is the Thomson cross section and U_B is the magnetic field energy density ($U_B = B^2/8\pi$).

Assume that the number density of electrons is represented by a power-law distribution expressed in the form of

$$N(E)dE = CE^{-p}dE \quad , \tag{2.9}$$

or

$$N(\gamma)d\gamma = C\gamma^{-p}d\gamma \quad . \tag{2.10}$$

The quantity C can vary with pitch angle and the like. The total power radiated per unit volume per unit frequency by such a distribution is given by the integral of $N(\gamma)d\gamma$ times the single particle radiation formula over all energies or γ. Thus, we have

$$P_{tot}(\omega) = C\int_0^{+\infty} P(\omega)\gamma^{-p}d\gamma \ \propto \int F\left(\frac{\omega}{\omega_c}\right)\gamma^{-p}d\gamma \quad . \tag{2.11}$$

Let us change variables of integration to $x \equiv \omega/\omega_c$, noting $\omega_c \propto \gamma^2$;

$$P_{tot}(\omega) \propto \omega^{-(p-1)/2}\int_0^{+\infty} F(x)x^{(p-3)/2}dx \quad . \tag{2.12}$$

The integral of this equation becomes constant, then we have

$$P_{tot}(\omega) \propto \omega^{-(p-1)/2} \quad , \tag{2.13}$$

so that the spectral index of synchrotron radiation (s) is related to the particle distribution index p by

$$s = \frac{p-1}{2} \quad . \tag{2.14}$$

Thanks to that the radiation travels straight, we can point out where cosmic rays (electrons in this case) are concentrated; this is a strong advantage over direct observations. In the case for electrons with energy of ~GeV in $\sim \mu$G magnetic field, ν_c is $\sim 10^{12}$ Hz in the radio band. When electrons have the energy of ~TeV, ν_c becomes $\sim 10^{18}$ Hz in the X-ray band. Since there is little thermal emission in these two bands, the observations of cosmic rays are usually made in these bands. The power-law emission is an indicator of synchrotron emission, in other words, accelerated electrons.

2.2.3 Observations of Inverse Compton Emission

When particles in the universe collide with photons (cosmic microwave background [CMB] or emission from particles' synchrotron radiation), they are scattered via Compton scattering. The total power of inverse Compton from a single electron can be written as,

$$P_{compt} = \frac{4}{3}\sigma_T c\gamma^2\beta^2 U_{ph} \quad , \tag{2.15}$$

$$U_{ph} \equiv \int \epsilon v d\epsilon \quad , \tag{2.16}$$

where U_{ph} is the energy density of the scattered photons (Rybicki & Lightman, 1979). In the case that the seed photons are the CMB, the energy density of the photons can be written as

$$\epsilon(\epsilon) = \frac{1}{\pi^2(\hbar c)^3}\frac{\epsilon^3}{\exp(\epsilon/kT)-1} \quad . \tag{2.17}$$

Comparing with the synchrotron power P_{sync} we have the general result:

$$\frac{P_{sync}}{P_{compt}} = \frac{U_B}{U_{ph}} \quad , \tag{2.18}$$

that is, the radiation losses due to synchrotron emission and to inverse Compton effect are in the same ratio with the magnetic field energy density and photon energy density. In the constant U_{ph} case, such as the upscattered photons being CMB, we can determine the strength of magnetic field directly comparing P_{sync} and P_{comp}. However, we must keep in mind that this relation also holds for arbitrary values of the electron's velocity, not just for ultra-relativistic values. It does, however, depend on the validity of the Thomson scattering in the rest frame so that $\gamma\epsilon \ll m_e c^2$. Jones (1968) calculated the spectrum of inverse Compton emission as

$$q(\epsilon) = \int d\epsilon' n(\epsilon') \int d\gamma N(\gamma) C(\epsilon,\ \gamma,\ \epsilon') \quad , \tag{2.19}$$

where $C(\epsilon,\ \gamma\ ,\epsilon')$ is the Compton kernel by Jones (1968) with the formulation of

$$C(\epsilon,\ \gamma,\ \epsilon') = \frac{2\pi r_0^2 c}{\gamma^2\epsilon'}\left[2\kappa lm\kappa + (1+2\kappa)(1-\kappa) + \frac{(4\epsilon'\gamma\kappa)^2}{2(1+4\epsilon\gamma\kappa)}(1-\kappa)\right] \quad , \tag{2.20}$$

$$\kappa = \frac{\epsilon}{4\epsilon'\gamma(\gamma-\epsilon)} \quad . \tag{2.21}$$

2.2.4 Observations of π_0 Decay

Protons with higher energy than $\sim$ 1 GeV sometimes collide with other protons in interstellar matter like molecular clouds. They produce a π_0 meson, which decays into two γ-rays with a life time of $8.3\times10^{-16}\gamma_\pi$ sec, where γ_π is the Lorentz factor of the π_0 meson. The decay is summarized as;

$$p + p \longrightarrow p + p + \pi_0 \longrightarrow p + p + \gamma + \gamma \quad . \tag{2.22}$$

Studies of γ-ray production from decay of π_0 produced in the p-p collisions have been developed to investigate the Galactic γ-ray background (Stecker, 1979; Stephens & Badhwar, 1981). Using the model for all pions by Lipkin & Peshkin (1972), Stephens & Badhwar (1981) calculated the invariant cross section of π_0 decays. The wide band radiation (0.01–10^7 GeV) $F(E)$ expected in SNRs was calculated as;

$$\frac{dF}{dE} = \frac{4\pi}{d^2} \int dr \cdot r^2 n_{\rm H} \int dT_p \cdot p^2 f \frac{d\sigma(T_\pi,\ T_p)}{dT_\pi} \quad , \tag{2.23}$$

where the term $\frac{d\sigma(T_\pi,\ T_p)}{dT_\pi}$ is the cross section calculated by Naito & Takahara (1994). Note that the radiation via π_0 decay becomes brighter in denser matter.

Chapter 3

The Acceleration of Cosmic Rays

The acceleration mechanism of cosmic rays has been studied for a long time. The most plausible site is large scale shock fronts, as shown in solar winds, stellar winds, SNRs, pulsar winds, jets of Active Galactic nuclei (AGNs), and so on. §3.2 and §3.3 are devoted to explain the structure of shock front and some acceleration mechanisms, respectively.

3.1 Size and Maximum Energy of Accelerated Particles

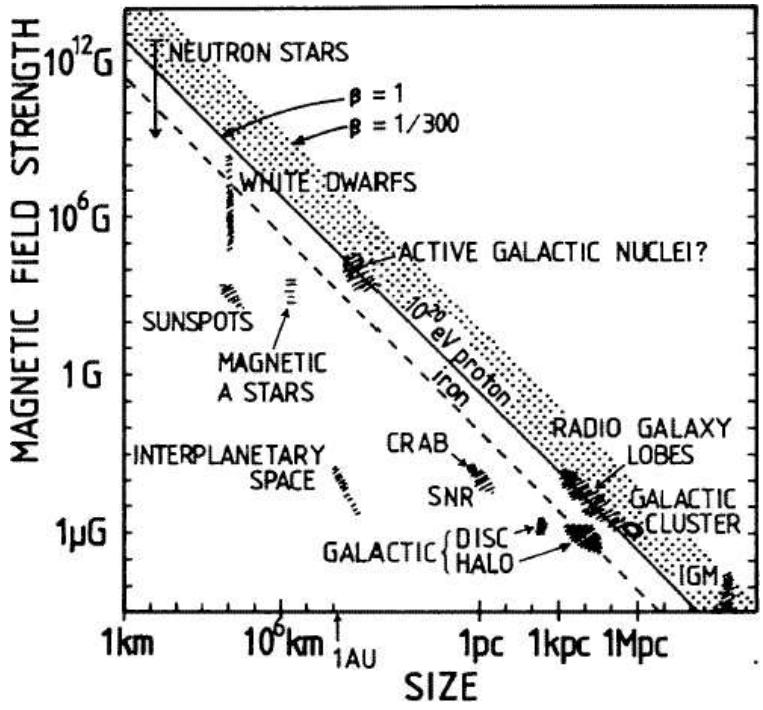

Fig. 3.1.— Size and magnetic field strength of possible sites of particle acceleration (Hillas, 1984). Objects below the diagonal line cannot accelerate protons to 10^{20} eV.

Cosmic rays in the interstellar magnetic field run following gyro motions. The gyro radius of a relativistic particle of a charge Ze in a magnetic field B is $r_g = 1.1 \times E_{15}/ZB_{\mu\mathrm{G}}$ pc, where E_{15} is the particle's energy in the unit of 10^{15} eV and $B_{\mu\mathrm{G}}$ is the magnetic field in μG. A typical length L of the essential part of the accelerating region containing the field must be much greater than $2r_g \sim 2E_{15}/B_{\mu\mathrm{G}}$, regardless the acceleration mechanism is statistical or one-shot. In fact, a characteristic velocity βc of scattering centers is of vital importance, then the energy that a system with a scale of L_{pc} pc can accelerate is

$$E_{15} < \frac{L_{\mathrm{pc}} B_{\mu\mathrm{G}} Z \beta}{2} \quad . \tag{3.1}$$

Figure 3.1 summarizes many sites where particle acceleration may occur, with sizes ranging from kilometers to mega-parsecs (Hillas, 1984). The sites lying below the diagonal line fail to satisfy eq.3.1 even for $\beta = 1$, for 10^{20} eV protons (the dashed line refers to 10^{20} eV iron nuclei). For more reasonable plasma velocities in the range of $c > v >$1000 km s^{-1}, the line will lie even higher, somewhere within the stippled band. In the case of SNRs, where $L_{\mathrm{pc}} \sim 10$ pc, $B_{\mu\mathrm{G}} \sim 10$, and $\beta \sim 3\times10^{-3}$, the estimated maximum energy of accelerated protons and electrons are $\sim 5\times10^{14}$ eV, which is lower than the knee energy. On the other hand, when we assume higher magnetic field considering the compression and amplification of magnetic field and so on, the maximum energy can be higher.

3.2 Shock Wave

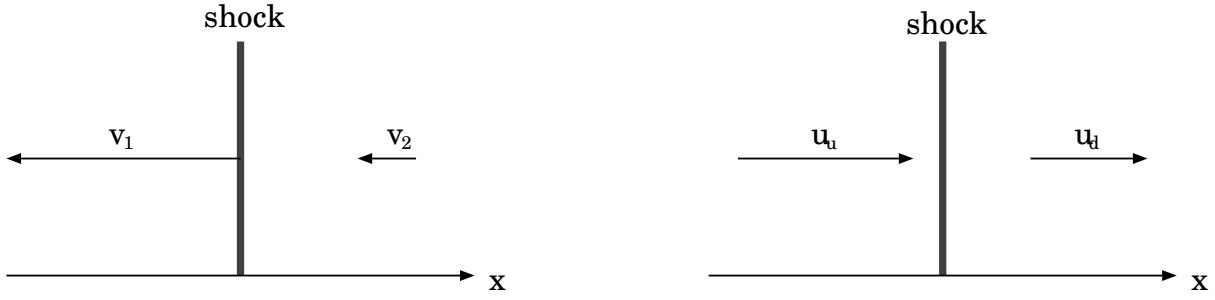

Fig. 3.2.— A schematic view of the shock front in lab. frame (left) and shock's frame (right).

Figure 3.2 shows the schematic view of the shock front. The boundary condition on the shock is assumed to be a step function and each condition in upstream and downstream is uniform. In a coordinate moving with the shock front, the conservation of mass, energy, and momentum are described as

$$\frac{\partial \rho}{\partial t} + \frac{\partial(\rho c)}{\partial x} = 0 \quad , \tag{3.2}$$

$$\frac{\partial(\rho u)}{\partial t} + \frac{\partial(\rho u^2 + P)}{\partial x} = 0 \quad , \tag{3.3}$$

$$\frac{\partial}{\partial t}\left[\rho\left(\frac{1}{2}u^2 + E\right)\right] + \frac{\partial}{\partial x}\left[Pu + \rho\left(\frac{1}{2}u^2 + E\right)u\right] = 0 \quad , \tag{3.4}$$

where ρ, u, P, and E are the density, the velocity, the pressure, and the energy per unit mass, respectively. With the condition of Figure 3.2, we obtain

$$\rho_u u_u = \rho_d u_d \quad , \tag{3.5}$$

$$\rho_u u_u^2 + P_u = \rho_d u_d^2 + P_d \quad , \tag{3.6}$$

$$u_u\left[P_u + \rho_u\left(\frac{1}{2}u_u^2 + E_u\right)\right] = u_d\left[P_d + \rho_d\left(\frac{1}{2}u_d^2 + E_d\right)\right] \quad , \tag{3.7}$$

where the subscripts u and d represent upstream and downstream, respectively. If we assume that the fluid is a perfect gas, we can derive the equations of

$$\frac{\rho_d}{\rho_u} = \frac{u_u}{u_d} = \frac{(\gamma-1)P_u + (\gamma+1)P_d}{(\gamma+1)P_u + (\gamma-1)P_d} \equiv r \quad , \tag{3.8}$$

$$\frac{T_u}{T_d} = \frac{P_u}{P_d}\cdot\frac{(\gamma-1)P_u + (\gamma+1)P_d}{(\gamma+1)P_u + (\gamma-1)P_d} \quad , \tag{3.9}$$

where γ and r are the ratio of specific heats and the compression ratio. Note that $u_u = ru_d = v_s$, where v_s is the shock velocity in the lab. frame. These equations are known as the Rankine-Hugoniot relation (Rankine, 1870).

For very strong shocks ($P_u \ll P_d$), the compression ratio r becomes as follows;

$$r \to \frac{(\gamma+1)}{(\gamma-1)} \quad . \tag{3.10}$$

For a non-relativistic mono-atomic gas, $\gamma = \frac{5}{3}$, the limiting r in a strong shock is 4. When the fluid is relativistic, such as the cases that accelerated particles govern the fluid, γ, and as a result, r become larger up to $\gamma = \frac{4}{3}$, or $r = 7$ in the steady state.

In the magnetic field, compression occurs only for the perpendicular component, $B\sin\theta$, where θ is the angle between the shock normal and the magnetic field. Therefore, the compression ratio of the magnetic field ($\equiv R(\theta)$) can be written as

$$R(\theta) \equiv \frac{B_d}{B_u} = \left(\cos^2\theta + r^2\sin^2\theta\right)^{\frac{1}{2}} \quad , \tag{3.11}$$

under the condition that the Mach number $M \to \infty$. It needs the magnetohydro-dynamic method to have a precise consideration about $R(\theta)$ when $M < +\infty$ (Landau & Lifshits, 1959).

3.3 The Acceleration Mechanism

3.3.1 The Diffusive Shock Acceleration

The most plausible and well studied process of cosmic ray acceleration is a diffusive shock acceleration (DSA) mechanism (Bell, 1978; Blandford & Ostriker, 1978; Drury, 1983; Blandford & Eichler, 1987). Here, we introduce the essence of DSA concisely under the test particle assumption, which means that the pressure of accelerated particle is negligible and makes no effect for the shock. The particles (electrons or protons) we discuss have energies high enough for their gyro radii to be much larger than the thickness of the shock front, which is of the order of the gyro radius of a thermal proton (Boyd & Sanderson, 1969). On the upstream of the shock, there is a turbulence in the form of Alfvén waves excited by energetic particles which passes through the shock and attempts to escape upstream. Particles are scattered by the waves and caught by the shock again, and as a result, they can cross the shock many times. Note that all particles in the upstream region return to the downstream but it is not the case for those traveling downstream.

Spectrum and Spatial Distribution

We derive the spectrum and spatial distribution of particles following the works by Bell (1978) and Blandford & Ostriker (1978). Let us consider a strong one-dimensional shock across which the density increases by a compression ratio r (see also Figure 3.2). The angle between the magnetic field and the shock normal is θ and θ_d in upstream and downstream region, respectively. The diffusion convection equation (DCE) can be written as;

$$\frac{\partial f}{\partial t} + u\frac{\partial f}{\partial x} - \frac{\partial}{\partial x}\left(K\frac{\partial f}{\partial x}\right) = \frac{1}{3}\frac{\partial u}{\partial x}p\frac{\partial f}{\partial p} \quad , \tag{3.12}$$

where u, p, f, and K are the velocity of fluid, pressure, distribution function, and diffusion coefficient of accelerated particles (see later), respectively. On the steady condition; $\frac{\partial u}{\partial x} = -(u_u - u_d)\delta(x)$, and eq.(3.12) becomes

$$u\frac{\partial f}{\partial x} - \frac{\partial}{\partial x}\left(K\frac{\partial f}{\partial x}\right) = -\frac{1}{3}(u_u - u_d)\delta(x)p\frac{\partial f}{\partial p} \quad . \tag{3.13}$$

When we ignore the point of $x = 0$, the equation becomes

$$\frac{\partial}{\partial x}\left(uf - K\frac{\partial f}{\partial x}\right) = 0 \quad . \tag{3.14}$$

Since the boundary conditions on $x = \pm\infty$ are

$$\frac{\partial f}{\partial x} = 0 \text{ on } x = \pm\infty \quad , \tag{3.15}$$

$$f = f_u(p) \text{ on } x = -\infty \quad , \tag{3.16}$$

$$f = f_d(p) \text{ on } x = +\infty \quad , \tag{3.17}$$

we can rewrite the DCE as

$$K\frac{\partial f}{\partial x} = \begin{cases} u_u f - u_u f_u & \text{upstream} \\ u_d f - u_d f_d & \text{downstream} \end{cases} . \tag{3.18}$$

Transforming them into the equation about f, we get

$$f(x) = \begin{cases} f_u + C_u \exp(\frac{u_u}{K_u} x) & \text{upstream} \\ f_d + C_d \exp(\frac{u_d}{K_d} x) & \text{downstream} \end{cases} . \tag{3.19}$$

In order to be $f < +\infty$ at $x = +\infty$ $(u/K > 0)$, C_d must be zero. Therefore, the particle distribution is exponential upstream and constant downstream in the time independent condition. Considered the continuity at $x = 0$, the upstream normalization C_u becomes $f_d - f_u$. As a result, the distribution of the accelerated particle is

$$f(x) = \begin{cases} f_u + (f_d - f_u) \exp(\frac{u_u}{K_u} x) & \text{upstream} \\ f_d & \text{downstream} \end{cases} . \tag{3.20}$$

Next, we derive the spectrum of accelerated particles using eqs.(3.13) and (3.20). Differentiating eq.(3.20) with x, one can get $\partial f/\partial x$ as;

$$\frac{\partial f}{\partial x} = \begin{cases} \frac{u_u}{K_u}(f_d - f_u) \exp(\frac{u_u}{K_u} x) & \text{upstream} \\ 0 & \text{downstream} \end{cases} . \tag{3.21}$$

The integration of eq.(3.13) in the range of $x = [-\epsilon, \epsilon]$ $(\epsilon \to 0)$ is calculated with eq.(3.21) as

$$p\frac{\partial f_d}{\partial p} = -\frac{3u_u}{u_u - u_d}(f_d - f_u) \equiv -\mu(f_d - f_u) , \tag{3.22}$$

$$\mu = \frac{3r}{r-1} , \tag{3.23}$$

where $f_u(p)$ and r are the distribution function of injected particles and the compression ratio, which becomes 0 in the range of p we consider. It is curious that the distribution function is independent from the diffusion coefficient, K. The integration can be carried out and we get

$$f_d(p) = \mu p^{-q} \int_0^p dp' \cdot p'^{\mu-1} f_u(p') \tag{3.24}$$

$$\propto p^{-\mu} . \tag{3.25}$$

The precise description of this equation has been calculated by Jones & Ellison (1991). As a result, the spectrum of accelerated particles $N \propto p^2 f$ can be written with μ as

$$N(p) \propto p^2 f \propto p^{2-\mu} \propto p^{-\frac{r+2}{r-1}} . \tag{3.26}$$

Note that the index of the accelerated particles is -2 in the strong shock of non-radiative ideal gas ($r = 4$; see eq.(3.8)), and becomes flatter when the gas energy is transfered into the accelerated

particles as discussed in Malkov & Drury (2001), for example. Considered the spectrum in the supra-thermal (non-relativistic) energy band and maximum energy of the particle (E_{max}), the spectrum of non-thermal electrons accelerated by the diffusive shock is (Bell, 1978);

$$\frac{\mathrm{d}N}{\mathrm{d}E} = \kappa(E+mc^2)(E^2+2mc^2E)^{-\mu} \times \exp\left(-\frac{E}{E_{\max}}\right) \quad . \tag{3.27}$$

Bell (1978) has derived the spectrum of accelerated particles independently from the distribution functions as follows using eq.(3.14). The flow of particles away from the shock to $x > 0$ is $u_d - K\frac{\partial f}{\partial x}$ and must be equal to $u_d f(0,t)$, which means the rate at which particles escape from the shock at a large distance downstream. The rate at which the particles with v are cross and recross the shock is

$$\frac{1}{4}f(0,t)v \quad , \tag{3.28}$$

then the probability of the escape η is

$$\eta = 4\frac{u_d}{v} \tag{3.29}$$

For very energetic particles ($v \sim c$), η is independent of energy. Particle energies remain unchanged in the fluid frame while a particle is in the upstream or downstream regions, When it crosses from one region to the other, a Lorentz transformation gives its energy in the frame of the new region. A particle with an energy E_k that has experienced k cycles, passing from the upstream to the downstream and back to the upstream, performs another cycle and has its energy increased by

$$E_{k+1} = E_k\left(\frac{1+v_{ku}(u_u-u_d)\cos\theta_{ku}/c^2}{1+v_{kd}(u_u-u_d)\cos\theta_{kd}/c^2}\right) \quad , \tag{3.30}$$

where v_{ku} is the velocity at which the particle crosses from the upstream to the downstream, its motion making an angle θ_{ku} with the shock normal, and v_{kd} and θ_{kd} are the corresponding quantities for the return crossing; all measured in the rest frame of the upstream scattering center. If the particle is injected into the system with the energy E_0, which is much greater than its rest mass energy, then $v_{ku} \sim v_{kd} \sim c$ and

$$\begin{aligned}\ln\left(\frac{E_l}{E_0}\right) &= l\left[\left\langle\ln\left(1+\frac{u_u-u_d}{c}\cos\theta_{ku}\right)\right\rangle - \left\langle\ln\left(1+\frac{u_u-u_d}{c}\cos\theta_{kd}\right)\right\rangle\right] \\ &\simeq \frac{4}{3}l\frac{u_u-u_d}{c}\left(1+O\left(\frac{u_u-u_d}{c}\right)\right) \quad ,\end{aligned} \tag{3.31}$$

with the reasonable assumption that $(u_u - u_d) \ll c$ and the distribution of the particles is isotropic. The probability P_l of a particle completing at least l cycles, and therefore of reaching an energy E_l is given by

$$\ln P_l = l\ln\left(1-4\frac{u_d}{c}\right) = -\left(\frac{3u_d}{u_u-u_d}+O\left(\frac{u_u-u_d}{c}\right)\right)\ln\left(\frac{E_l}{E_0}\right) \quad , \tag{3.32}$$

so the differential energy spectrum is

$$N(E)dE = \frac{\mu-1}{E_0}\left(\frac{E}{E_0}\right)^{-\mu}dE \quad , \tag{3.33}$$

where

$$\mu = \frac{2u_d + u_u}{u_u - u_d} + O\left(\frac{u_u - u_d}{c}\right) \sim \frac{2+r}{1-r} \quad , \tag{3.34}$$

which is the same result by Blandford & Eichler (1987).

The diffusion Coefficient

The diffusion coefficient K in the parallel magnetic field to the shock normal is estimated as follows (Skilling, 1975);

$$K = \frac{1}{3}\xi r_g c \quad , \tag{3.35}$$

$$\xi \sim \left(\frac{B}{\delta B}\right)^2 \quad , \tag{3.36}$$

where r_g is the gyro radius of a particle and ξ is a non-dimensional parameter (> 1) in the order of the fluctuation of the magnetic field. Jokipii (1987) extended this formula into the oblique magnetic field cases;

$$K_u = \frac{1}{3}\xi_u \left(\cos^2\theta + \frac{\sin^2\theta}{1+\xi_u^2}\right)\frac{E_{max}}{eB_u}c \equiv \frac{E_{max}c}{eB_d} f(\xi_u, \theta) \quad , \tag{3.37}$$

$$K_d = \frac{1}{3}\xi_d \left(\cos^2\theta + r^2\sin^2\theta\right)^{-1}\left(\cos^2\theta + \frac{r^2\sin^2\theta}{1+\xi_d^2}\right)\frac{E_{max}}{eB_d}c \equiv \frac{E_{max}c}{eB_d} g(\xi_d, \theta) \quad , \tag{3.38}$$

where the functions f and g are

$$f(\xi_u, \theta) = \xi_u \left(\cos^2\theta + r^2\sin^2\theta\right)^{1/2}\left(\cos^2\theta + \frac{r^2\sin^2\theta}{1+\xi_u^2}\right) \quad , \tag{3.39}$$

$$g(\xi_d, \theta) = \xi_d \left(\cos^2\theta + r^2\sin^2\theta\right)^{-1}\left(\cos^2\theta + \frac{r^2\sin^2\theta}{1+\xi_d^2}\right) \quad . \tag{3.40}$$

Note that K can be smaller when θ becomes close to $90°$, since the diffusion occur along the magnetic field.

Time Scales

The acceleration time scale t_{acc} can be roughly estimated as follows. The energy gain of the particle $\triangle E$ with the energy E in one cycle is calculated from eq.(3.31) as

$$\triangle E = \frac{4}{3}\frac{u_u - u_d}{c}E \tag{3.41}$$

The time of a cycle $\triangle t$ is estimated separately for the upstream ($\triangle t_u$) and the downstream ($\triangle t_d$) regions. Comparing the cosmic ray flux density in the upstream, we get the following relation with

eq.(3.19) and (3.28)

$$\begin{aligned} \int_{-\infty}^{0} dx \cdot n\mathrm{e}^{\frac{u_u}{K_u}x} &= \triangle t_u \cdot \frac{nc}{4} \\ \triangle t_u &= \frac{4K_u}{u_u c} \quad . \end{aligned} \tag{3.42}$$

The downstream particles have uniform distribution (see eq.(3.19)). However, in order to be accelerated, they must be scattered into upstream region again with the probability $P_{ret}(x)$, which can be estimated as

$$P_{ret}(x) = 1 - \frac{u_d x}{K_d} \sim \exp\left(-\frac{u_d}{K_d}x\right) \quad . \tag{3.43}$$

Therefore, in a similar way to the estimation of $\triangle t_u$, $\triangle t_d$ can be estimated as follows;

$$\begin{aligned} \int_{0}^{+\infty} dx \cdot nP_{ret}(x) &= \frac{K_d n}{u_d} = \triangle t_d \cdot \frac{nc}{4} \\ \triangle t_d &= \frac{4K_d}{u_d c} \quad . \end{aligned} \tag{3.44}$$

Now we can estimate $\triangle t$ as

$$\triangle t = \triangle t_u + \triangle t_d = \frac{4}{c}\left(\frac{K_u}{u_u} + \frac{K_d}{u_d}\right) \quad . \tag{3.45}$$

As a result, we can estimate t_{acc} as

$$t_{acc} = E\Big/\frac{\triangle E}{\triangle t} = \frac{3}{u_u - u_d}\left(\frac{K_u}{u_u} + \frac{K_d}{u_d}\right) \quad . \tag{3.46}$$

Intuitively, particles are accelerated faster in larger magnetic field with larger turbulence (in other words, smaller K; see eqs.(3.37) and (3.38)) and in faster shocks. The time scale becomes larger when particles are accelerated up to very high energy and K becomes larger.

The energy loss time scale t_{loss} for electrons is mainly determined by the synchrotron loss time scale in the case of SNR shocks (the loss via inverse Compton scattering can be ignored because the photon density is low enough in SNRs). The radiation energy (P) by synchrotron of a relativistic electron of energy E can be written as (see eq.(2.8));

$$\begin{aligned} P &= \frac{4}{3}\sigma_T c\beta^2\gamma^2\frac{B^2}{8\pi} \\ &\simeq \frac{4}{3}\sigma_T c\frac{E^2}{m_e^2 c^4}\frac{B^2}{8\pi} \\ &= 1.6 \times 10^{-3} E^2 B^2 \quad [\mathrm{ergs\ s^{-1}}], \end{aligned} \tag{3.47}$$

where σ_T, β, γ, m_e, are the Thomson cross section, the electron velocity relative to the light speed ($\frac{v}{c}$), the Lorentz factor, and the electron mass, respectively. Thus the time scale t_{loss} that the electron lose its energy by $\frac{1}{e}$ via synchrotron radiation is;

$$\begin{aligned} t_{loss} &= \frac{E}{P} \\ &= 6.3 \times 10^2 E^{-1} B^{-2} \quad [\mathrm{s}] \end{aligned} \tag{3.48}$$

Note that electrons with higher energy in higher magnetic field lose their energy faster. The electrons with the knee energy lose their energy with $t_{loss} \sim 40$ years in the average interstellar magnetic field (~ 10 μG).

The Non-Linear Effect

When the acceleration efficiency is very high and the pressure of cosmic rays can not be neglected, the "back reaction" of accelerated particles must be considered. This effect is summarized by Malkov & Drury (2001) as "non-linear effect", which makes the flow in upstream region decelerate. The feed-back of the effect is positive, then non-linear effect distorts the spectrum of accelerated particles. Furthermore, Lucek & Bell (2000) suggested that the cosmic ray streaming energy is very efficiently transferred to the magnetic field turbulence, and finally reaches $(\delta B/B)^2 > 10$. Non-linear effect makes the compression ratio r larger, since the accelerated particles get energy from background plasma, which cools down and gets denser. Berezhko, Ksenofontov, & Völk (2002) insists that non-linear effects in SN 1006 makes r to be ~ 6, based on a fully time-dependent solution of the cosmic ray transport equation together with the gas dynamic equations in a spherical symmetry.

3.3.2 The Shock Surfing Acceleration Mechanism

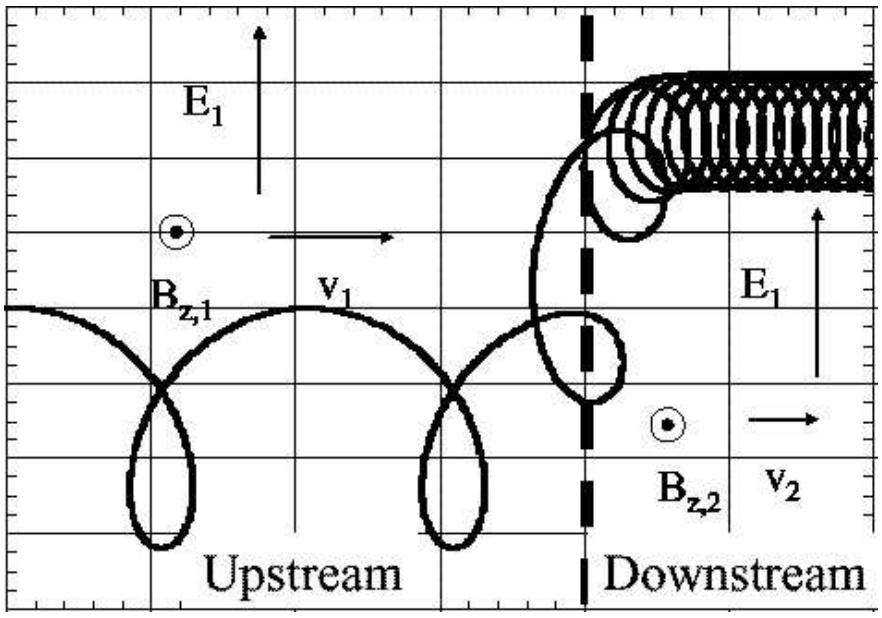

Fig. 3.3.— Schematic view of shock and magnetic field perpendicular to the shock normal. (courtesy; Hoshino, M. in Univ. of Tokyo.).

In addition to the statistical acceleration such as DSA, charged particles can be accelerated directly when the magnetic field is quasi-perpendicular to the shock normal. This mechanism is called shock drift acceleration. Consider charged ions with a charge q in the magnetic field (Figure 3.3). The upstream particles gyrate with a large gyro radius. When it enters into downstream, where the magnetic field is compressed, their gyro radii becomes smaller. The particle comes upstream again, they drifts to the direction of the electric field, and as a result, get energy qE_1 via the motional electric field. This mechanism, however, keeps the relation,

$$\frac{v_\perp^2}{B} = const. \quad . \tag{3.49}$$

Therefore many traps are needed for an efficient acceleration.

In the shock with a high Mach number, there emerges a strong magnetic field region called "overshoot" just behind the shock, which can "trap" ions. As a result, ions continue to get energy via shock drift acceleration. There are many works on this fast acceleration for ions (e.g., Zank et al., 1996; Sagdeev & Shapiro, 1973).

Papadopoulos (1988) and Cargill & Papadopoulos (1988) proposed the electron heating process up to 10 keV at high Mach number shocks, in which electron heating is produced through two-step instabilities in the shock transition region where the reflected ions coexist with the incident ions and electrons (Leroy et al., 1982; Wu et al., 1984). Shimada & Hoshino (2000) extended their study to the shock structure including the electron dynamics by using a particle-in-cell simulation where both ions and electrons are treated as particles. They found the formation of a phase space "electron hole" in association with a localized, large-amplitude, electrostatic solitary wave (ESW) in the shock front region. Hoshino & Shimada (2002) studied in detail the supra-thermal electron acceleration through the interaction of electrons with ESWs in a transverse, magnetosonic, high Mach number shock, and pointed out that the electrons can be accelerated up to $v \sim c$, relativistic range in other words in "shock surfing acceleration", which is named by Hoshino & Shimada (2002) since electrons trapped electron holes seem to be enjoying surfing on the shock. There are still many unresolved problems for electron surfing acceleration, the spectra for accelerated particles and so on. This mechanism must be very important for cosmic ray acceleration in supernova remnants, at least in the injection phase.

Chapter 4

Review of Supernovae and Supernova Remnants

Supernova (SN) is one of the most spectacular phenomena in the universe with the energy release of $\geq 10^{51}$ ergs, which is caused by the explosions of stars. It is believed that a SN occurs per about 30 years in our Galaxy. SNe leave stellar and diffuse remnants; compact stars (neutron stars or black holes) and/or shocks and hot plasmas called supernova remnants (SNRs). Now, about 230 SNRs are identified in our Galaxy (Green, 2001), although Case & Bhattacharya (1998) suggests that only half of Galactic SNRs have been identified. This chapter is devoted to explain the basic characteristics of SNe and SNRs.

4.1 Classes of SNe

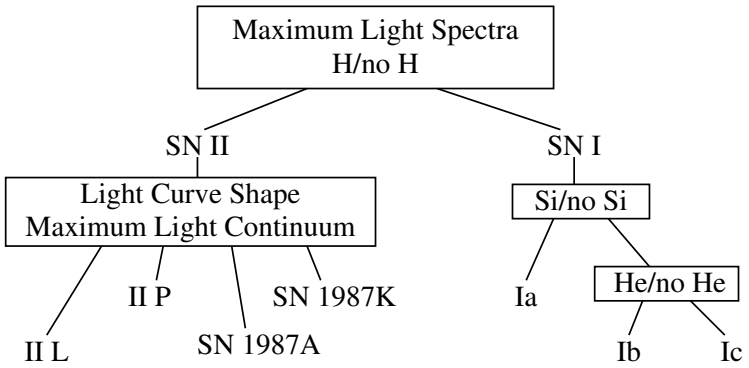

Fig. 4.1.— The basic classification scheme for supernovae based on spectral features at early times (Harkness & Wheeler, 1990).

The definition of the classification of SNe is traditionally based on their optical spectra near the maximum light as shown in Figure 4.1, without considering their origins; the spectra of Type II SNe have H lines, whereas those of Type I show no H line (Minkowski, 1941). Type I SNe are classed into two subclasses depending on whether the Si absorption feature exists (Type Ia) or not (Type Ib). Wheeler & Harkness (1986) proposed another class, Type Ic, which does not have neither H, Si, nor He line. Type II SNe have further subclasses based on the shape of light curves; those with a pronounced plateau (SN II-P) and those with a linear decline (SN II-L Barbon, Ciatti, & Rosino, 1973). SN 1987A, a Type II SN which occurred in the Large Magellanic Cloud (LMC) on 1987, can not be classified into neither subclasses.

Type II SNe are now identified as explosions of massive stars ($\geq 8M_{\odot}$). Fe cores in red giants can not release the bounding energy and are compressed by gravity up to $\sim 10^{10}$ g cm^{-3}. In such a high density matter, electrons are captured into nuclei and endothermic decompositions of Fe occur, and as a result, the pressure is rapidly reduced and a gravitational collapse starts. The falling matter bounces back on the core surface and forms a shock wave, which blows back the collapsing matter with kinetic energy of about 10^{51} ergs.

Although all progenitors of Type I SNe may have no outer hydrogen layer, the reason of what is different for each type. The progenitors of Type Ia SNe are mass accreting white dwarfs (WDs). The accretion from the companion star fattens the WD to the Chandrasekhar limit (1.4 $M_{\odot}$). When the gravity in the WD exceeds the electron degenerate pressure, explosive ignition of a collapse induces mass ejection and creates a radio-active nuclei whose decay (^{56}Ni$\rightarrow^{56}$Co$\rightarrow^{56}$Fe) powers the emission, leaving no stellar remnant. The total energy is estimated to be 1.3×10^{51} ergs. They often appear in the outskirts of elliptical galaxies (Maza & can den Bergh, 1976), which implies that the progenitors are old halo stars of $\sim 10^{10}$ years old with a mass of $\sim 1M_{\odot}$. On the other hand, Type Ibs occur in the arms of spiral galaxies and are often associated with H II regions, thus are believed as explosions of massive stars. The absence of H line is caused by their shedding their outer layer via stellar winds. Progenitors of Type Ic SNe may be also massive stars. The detailed standard model of Type I explosions is described by Nomoto et al. (1984).

4.2 Nucleosynthesis in SN

The universe was made of hydrogen, helium, and tiny other light elements such as lithium and so on, at the time of its birth. Other elements lighter than iron were synthesized in the core of stars via nuclear fusion called "nucleosynthesis".

The atomic mass a star can create depends on the star's mass. Sun produces elements as heavy as carbon and oxygen, but their densities and temperatures are too low to fuse themselves into heavier elements. More massive stars can synthesize heavier elements such as magnesium, silicon, iron, and so on. The produced elements are sprinkled to the space when the progenitor star explodes. Therefore, we can estimate the mass of progenitors by examining the chemical

abundances in supernova remnants. Tsujimoto et al. (1995) calculated the nucleosynthesis products of stars with various masses. Figure 4.2 shows the predicted relative abundances of heavy elements by Tsujimoto et al. (1995), which are normalized to the corresponding cosmic abundance (Allen, 1973). The abundance of Mg is normalized to 1. Light elements like Ne is produced mainly in type II SNe, thus can be indicators of massive progenitors. On the other hand, iron produced in massive stars falls into the compact remnants (neutron stars or black hole) and is not sprinkled, then it is an indicator of type Ia SN.

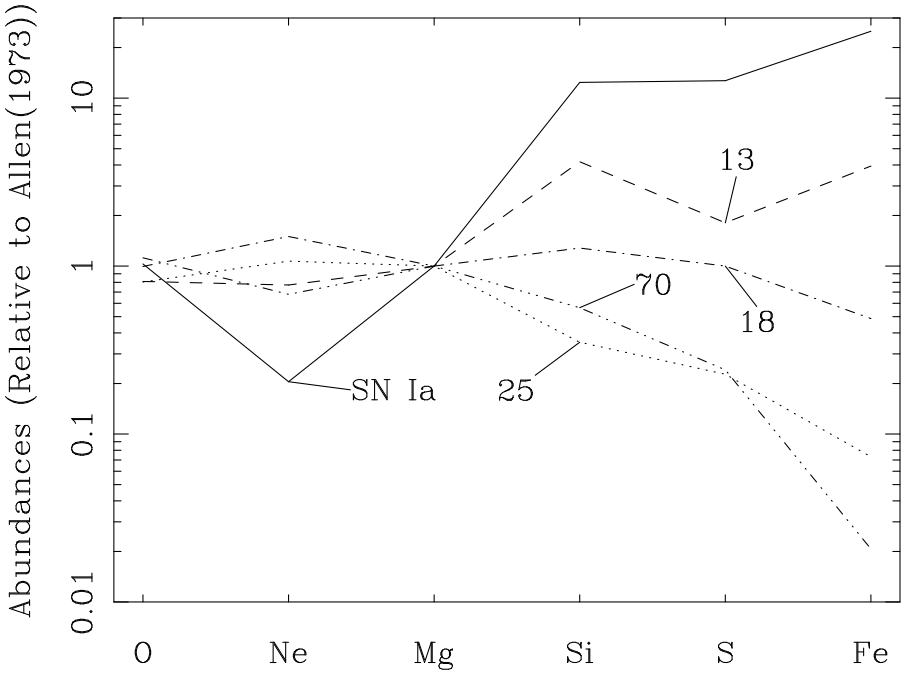

Fig. 4.2.— Predicted relative abundances of synthesized heavy elements (Tsujimoto et al., 1995). The ratios to the cosmic abundances of Allen (1973) are plotted for type Ia SN, type II SN of 13, 18, 25, and 70 $M_\odot$ stars.

4.3 Historical SNRs

Supernova explosions were believed to be portents in the ancient Orient, then Chinese astrologers described them as "guest stars". Since 15th century, when the modern physics began, some astronomers have observed SNe and recorded a lot of information; date, direction, luminosity, light

Table 4.1: Historical supernova explosions in our Galaxy.

Year	Constellation	Name	Type	Recorder
185?	Centaurus	RCW 86?	II?	Chinese
386	Sagittarius	G11.2−0.3	II	Chinese
1006	Lupus	SN 1006	Ia	Japanese, Chinese, Korean
1054	Taurus	Crab	II	Japanese, Chinese, Korean
1181	Cassiopeia	3C 58	II	Japanese, Chinese, Korean
1572	Cassiopeia	Tycho	Ia	Tycho
1604	Ophiuchus	Kepler	?	Kepler
1680s	Cassiopeia	Cas A	Ib	Flamstead

curve, and so on. Table 4.1 lists the supernova explosions which have been witnessed and recorded in our Galaxy. Thanks to these recorders, we can know their age and type. Strom (1994) also summarizes the historical SNRs.

4.4 Evolution of SNRs

An exploded supernova ejects some amount of gas (M_e) with high velocity into the interstellar medium (ISM). The condition of evolution is determined by the ratio of M_e and the swept up mass ($M_b = 4\pi/3 \cdot \rho_0 R^3$, where ρ_0 is the ambient density and R is the radius of the SNR). In this section, we briefly introduce the evolution of SNRs. The detailed descriptions are shown in Trulove & McKee (1999) for young stages and Cioffi, McKee, & Bertschinger (1988) for aged stages.

4.4.1 Free Expansion Phase

The ejected gas mainly determines the evolution of the SNR in the initial phase ($M_e > M_b$). Most of the explosion energy is released kinetically, while 2–3% of the energy converted into the thermal energy. The ejected matter expands at a velocity of about $5\text{–}10\times10^3$ km s^{-1}, which is much larger than the sound speed in the ambient gas and is preceded by a shock wave (the blast-wave shock). The shock expands without deceleration with the time dependence of the radius $R(t)$ as

$$R(t) \propto t \quad . \tag{4.1}$$

Then, this phase is called as free expansion phase or ejecta-dominated phase.

Heated ISM and outer ejecta expand and convect heat to inner ejecta. The front of discontinuity also makes a density shock, which runs toward the center of the SNR and is called as "reverse shock". The similarity solution for this shock is discovered by Hamilton & Sarazin (1984a) and analyzed by Hamilton & Sarazin (1984b).

At the end of this phase, the expansion begins deceleration by ISM and $\mathrm{d}R/\mathrm{d}t$ becomes smaller. In this phase, the radius can be written as

$$R(t) \propto t^m \quad , \tag{4.2}$$

where m is expansion parameter defined by Hughes (1999). It grows from 1 (the early phase of free expansion) to 0.4 (next phase, adiabatic phase), as the SNR expands.

4.4.2 Adiabatic Phase (Sedov Phase)

The mass ratio M_b/M_e increases as the SNR ages. When M_b becomes as large as M_e, the deceleration of the blast wave can not be neglected. The critical radius R_s is derived from

$$\frac{4}{3}\pi R_s^3 \rho_0 = M_e \tag{4.3}$$

$$\text{as} \quad R_s^0 = 5.8 \left(\frac{M_e}{10 M_\odot}\right)^{\frac{1}{3}} \left(\frac{n_0}{0.5\ [\mathrm{cm}^{-3}]}\right)^{-\frac{1}{3}} \quad [\mathrm{pc}]. \tag{4.4}$$

Assuming typical values of the supernova explosion and ISM, it takes about 600 yrs for the radius of the SNR becomes R_s. In the tenuous interstellar matter, such as cavities made by stellar winds, the critical R_s (R_s^0) becomes larger.

In this condition, the expansion is adiabatic since the radiative cooling is still negligible. Therefore, the condition can be written as the results of the similarity solution of a point explosion (Sedov, 1959). Assuming that a large amount of energy E is instantaneously released in a small volume, the gas flow can be characterized only by two parameters, ρ_0 and E. We can define a non-dimensional parameter ζ as

$$\zeta = R \left(\frac{E t^2}{\rho_0}\right)^{-\frac{1}{5}} \quad , \tag{4.5}$$

where t is the age of the SNR. ζ enables to draw the flow as similar solutions. The radius of the expanding shell R_s is written as

$$R_s = \zeta_o \left(\frac{E t^2}{\rho_0}\right)^{1/5} \quad , \tag{4.6}$$

where ζ_0 can be determined from the energy conservation equation. Using $\zeta_0 = 1.17$ for ideal gas ($\gamma = 5/3$) (Landau & Lifshits, 1959), the radius (R_s), temperature (T_s), and the velocity of the shock (v_s) are written as

$$R_s = 5.0 \times \left(\frac{E_{51}}{n_0}\right)^{1/5} t_3^{2/5} \ [\mathrm{pc}] \ , \tag{4.7}$$

$$T_s = 1.5 \times 10^{10} \times \left(\frac{E_{51}}{n_0}\right) R_s^{-3} \ [\mathrm{K}]$$

$$= 1.2 \times 10^8 \times \left(\frac{E_{51}}{n_0}\right)^{2/5} t_3^{-6/5} \ [\mathrm{K}] \ , \tag{4.8}$$

$$v_s = \frac{dR_s}{dt} = 2.1 \times 10^8 \times \left(\frac{E_{51}}{n_0}\right)^{1/5} t_3^{-3/5} \ [\mathrm{cm\ s^{-1}}] \ , \quad (4.9)$$
$$\left(= \frac{2}{5}\frac{R_s}{t_3} \times 10^8 \ [\mathrm{cm\ s^{-1}}] \right) \ ,$$

where E_{51}, n_0, and t_3 are the explosion energy in the unit of 10^{51} ergs, the number density of proton in the unit of cm^{-3}, and the age in the unit of 10^3 yrs, respectively. Until the end of this stage, about 70% of the initial explosion energy is converted into thermal energy of swept-up matter (Chevalier, 1974).

We ignored radiative cooling in this subsection. When the emission cools down the system, the shock evolves in a different way from the Sedov solution. Berezhko et al. (2002) calculated the influence of cosmic rays to the evolution of shock structures.

4.4.3 Radiative Cooling Phase

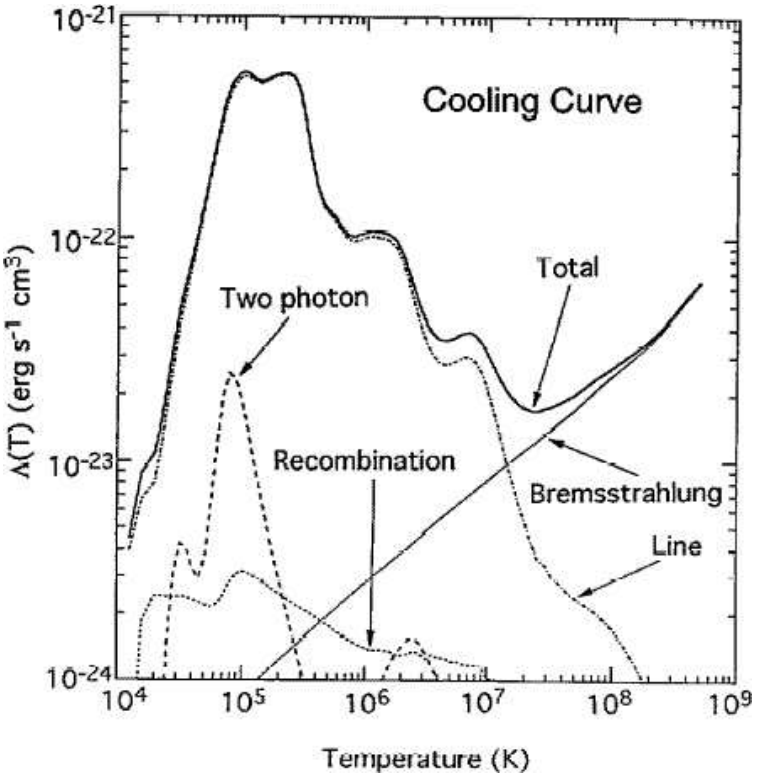

Fig. 4.3.— Temperature dependence of the cooling coefficient and its components for an optically thin plasma of the cosmic abundance (Allen, 1973; Gehrels & Williams, 1993).

The shock temperature T_s decreases with time. and the cooling effect becomes indispensable and the Sedov approximation is broken. Although it is difficult to solve analytically, we can discuss it concisely with a handful emission model. The radiative cooling coefficient is a temperature-dependent function defined as

$$\Lambda = n_e n_i \Lambda_0(T) \ , \quad (4.10)$$

where $\Lambda_0(T)$ is the radiative cooling function calculated by Gaetz & Salpeter (1983), and so on. Figure 4.3 shows the temperature dependence of $\Lambda(T)$. The function can be represented approximately as

$$\Lambda_0(T) = 6.3 \times 10^{-40} T_s^{-0.7} + 2.3 \times 10^{-34} T_s^{0.5} \quad [\mathrm{J\ m^3\ s^{-1}}] \quad , \tag{4.11}$$

where the first and second term of the right hand side is the cooling due to line and bremsstrahlung emission (see also the next section).

Assuming the emission occurs in the dense shell with $\triangle r = 1/12 R_s$, the time evolution of the emission $L(t)$ is written as

$$L(t) = 4\pi R_s^2 \triangle r (4n_0)^2 \Lambda_0(T) = \frac{16}{3} R_s^3 n_0^2 \Lambda_0(T) \quad . \tag{4.12}$$

In the case of $T_s > 10^7$ K, the cooling is mainly due to bremsstrahlung. and the time dependence of $L(t) \propto t^{0.6}$, since $T_s \propto t^{-1.2}$ and $R_s \propto t^{0.4}$. It becomes $T_s < 10^7$ K when the radiation cooling becomes significant, because the first term of eq.(4.11) becomes significant and $L(t)$ grows up with $\propto t^{2.04}$. As a result, the cooling is accelerated.

4.4.4 Snowplow Phase

When the shock velocity is decelerated down to ~ 200 km s^{-1}, the radiative cooling begins to affect the dynamics of the shock evolution. The density of shock front becomes highest where the timescale of radiative cooling becomes shortest, with the temperature of $T_s \sim 10^5$ K (see Figure 4.3). As a result, a cool and dense shell is formed just behind the shock front, whereas the inner gas still has high temperature and high pressure due to the low density. The cool shell continues the expansion further collecting the ISM gas as the snowplow, then this phase is called as "snowplow phase". At the first stage of this phase, the gas expands adiabatically then $pV^{5/3}$ becomes a constant. The shock expands with the time dependency of $R_s \propto t^{2/7}$. As the temperature cools down further, the pressure can be ignored and the cool shell expands at a constant radial momentum with the time dependency of roughly $R_s \propto t^{1/4}$.

4.4.5 Disappearance Phase

As the SNR becomes older yet, the expansion velocity becomes smaller. When the shock slows down to the velocity comparable to the proper motion of surrounding ISM (10–20 km s^{-1}), the SNR loses its boundary between the outside and disappears into the ISM. This phase is called "disappearance phase". The age of SNRs in this phase is larger than $\sim 10^6$ yrs.

4.4.6 Influence of Magnetic Field to the Evolution

SNe explode in the interstellar magnetic field, then their evolution may be influenced by it. The condition in which we must consider the influence of the magnetic field is determined by the balance of pressure as

$$\rho_0 v_s^2 < \frac{B_0^2}{8\pi} \quad . \tag{4.13}$$

In the early phase of the evolution, the shock evolves without feeling the pressure from the magnetic field and expands spherically. The shock evolution can be represented by a self-similar solution derived by Ratkiewicz, Axford, & McKenzie (1994). The SNR ages and the shock velocity decreases, and as a result the pressure of the magnetic field distorts the shock structure. In this phase, the shock evolution can not be represented analytically but needs some simulations.

4.5 Thermal X-ray Emission from SNRs

SNRs emits both thermal and non-thermal X-rays; the former from hot plasma of $kT \leq 1$ keV via thermal bremsstrahlung plus emission lines, which can be seen almost all X-ray emitting SNRs. The latter is from ≥ 1 TeV electrons in $\sim \mu$G magnetic field via synchrotron radiation process (see §2.2.2), which have been detected in several SNRs. Here, we summarize thermal X-ray emission mechanism of SNRs which tells us a plenty of information about the SNR itself.

4.5.1 Bremsstrahlung (Free-Free Emission)

Charged particles in the Coulomb field of other charged particles emit radiation called bremsstrahlung or free-free emission. The most intense emission in neutral plasma is the bremsstrahlung from electrons by the Coulomb field of ions. The power of the emission per unit time, volume, and frequency is given by

$$\frac{dW}{dV dt d\nu} = \frac{2^5 \pi^2 e^6}{3\sqrt{3} c^3 m_e^2 v_e} n_e n_i Z^2 g_{ff}(v,\ \nu) \quad , \tag{4.14}$$

where n_e, n_i, e, m_e, v_e, c, Z, and g_{ff} are electron and ion density, charge unit, electron mass and velocity, light speed, and Gaunt factor, respectively. Gaunt factor is a function of the energy of electrons and of the frequency of emission, which is reviewed in Bressaard & van de Hulst (1962) and Karzas & Latter (1961).

The shocked ejecta and ISM are heated up to $\sim$ keV and become a hot and thin ($\sim$1 cm^{-3}) plasma. When the plasma temperature is kT, the probability dP that a particle has a velocity in the range of $v_e \sim v_e + dv_e$ is estimated under the assumption of an isotropic distribution of velocities to be

$$dP \propto v^2 \exp\left(-\frac{m_e v_e^2}{2kT}\right) dv \quad . \tag{4.15}$$

Combining these equations, one can know the emission power of plasma in an isotropic thermal distribution (thermal bremsstrahlung) as

$$\frac{dW}{dV\,dt d\nu} = \frac{2^5\pi e^6}{3mc^3}\left(\frac{2\pi}{3km_e}\right)^{1/2} T^{-1/2} Z^2 n_e n_i \mathrm{e}^{-h\nu/kT}\overline{g_{ff}} \quad , \tag{4.16}$$

where $\overline{g_{ff}}(T,\ \nu)$ is a velocity averaged Gaunt factor. Evaluating eq.(4.16) in the CGS units, we obtain

$$\frac{dW}{dV\,dt d\nu} = 6.8\times10^{-38} Z^2 n_e n_i T^{-1/2}\mathrm{e}^{-h\nu/kT}\overline{g_{ff}} \ \ [\mathrm{ergs\ s^{-1}cm^{-3}}]. \tag{4.17}$$

Plasmas with high densities emits bremsstrahlung emission higher.

4.5.2 Line Emission (Bound-Bound Emission)

The transitions between two discrete quantum levels often accompany photon emission called line emission or bound-bound emission. In the pure Coulomb cases for hydrogen and for other hydrogen-like ions, such as He II and Li III (they have only one trapped electron), a fairly complete discussion of transition rate can be given purely theoretically. The energy of a photon absorbed or emitted in a transition between two discrete levels with principal quantum numbers n and n' is given by

$$E_{bb} = R_y\left(\frac{1}{n^2} - \frac{1}{n'^2}\right) \quad , \tag{4.18}$$

where Ry is Rydberg constant (=13.6 eV). For heavy elements, E_{bb} roughly becomes

$$E_{bb} \sim Z^2 R_y\left(\frac{1}{n^2} - \frac{1}{n'^2}\right) \quad . \tag{4.19}$$

In order to calculate the dipole oscillator strength, we must evaluate the dipole operator matrix element. This will involve integrals over the radial wave functions $R_{nl}(r)$ of the form

$$\int R_{nl} R_{n'(l-1)} r dr \quad . \tag{4.20}$$

Since the radial functions are analytically known as Laguerre polynomials, the integrals can be performed but are complicated (Gordon, 1929). When the integral is performed, it can then be summed over all l appropriate to a given n and n'. For members of the Lyman series ($n' = 1$), the oscillator strengths f times statistical weight g becomes

$$g_1 f_{1n} = \frac{2^9 n^5 (n-1)^{2n-4}}{3(n+1)^{2n-4}} \quad . \tag{4.21}$$

Note that for high values of n the oscillator strength decrease rapidly

$$\begin{aligned} g_1 f_{1n} &= \frac{2^9}{3n^3}\frac{\left(1-\frac{1}{n}\right)^{2n-4}}{\left(1-\frac{1}{n}\right)^{2n-4}} \\ &\sim \frac{2^9}{3n^3}\frac{\mathrm{e}^{-2}}{\mathrm{e}^2} \sim 3.2\frac{1}{n^3} \quad . \end{aligned} \tag{4.22}$$

In reality, the line energy and oscillator strength depend on the ionization states, azimuthal quantum number, and so on. For example, hydrogen-like atoms (only one electrons is captured by an ion) emit photons with higher energy than that of helium-like ones (ions with two electrons). Mewe, Gronenschild, & van den Oord (1985) calculated the line energy and temperature dependence of oscillator strength for H- and He-like lines plus their satellites produced by innershell transitions. The number of investigated lines is up to >2000 The L-shell transitions of highly ionized Fe was revised by Liedahl, Osterheld, & Goldstein (1995). We use the thermal plasma models in this paper based on their calculations, together with those for continuum emission by Mewe, Lemen, & van den Oord (1986).

4.6 Non-Equilibrium State

The density of plasma in SNRs are very low, then interactions between ions and electrons are very rare. As a result, it takes a long time for plasma to reach equilibrium. The state in such a condition is called non-equilibrium state. We review this state concisely in this section.

4.6.1 Non-equilibrium of Thermal Energy

Since the temperatures of heated ions and electrons are proportional to the particle mass, protons should be much hotter than electrons. Electrons are gradually heated up by the energy transfer from ions. The time scale of the energy transfer (t_{ie}) is given by Spitzer (1962) as

$$t_{ie} = 9.9 \times 10^{12} \left\langle \frac{A_i}{Z_i^2} \right\rangle^2 \frac{(kT_e)^{3/2}}{n_e \lg \Lambda} \quad , \tag{4.23}$$

where A_i, Z_i, kT_e, n_e, and Λ are ion mass in atomic units, ion charge, electron temperature in keV, electron number density in cm^{-3}, and the Coulomb logarithm, respectively. The brackets mean the average value over various ions. With typical SNR values of $A_i = 1$, $Z_i = 1$, kT_e =1 keV, n_e =1 cm^{-3}, and $\Lambda = 30$, t_{ie} is about 3×10^{11} sec $= 10^4$ yrs, which is comparable or longer than the SNR age. Therefore, electrons may not have the same energy as protons in young and/or low density SNRs.

4.6.2 Non-Equilibrium Ionization

After heated up by shock wave, the matter is ionized to some ionization degree depending on the electron temperature. Since the density and/or elapsed time after the shock-heating is small, the number of Coulomb collisions is also small. In this case, the ionization of matter does not reach the level expected from the electron temperature. This is called non-equilibrium ionization (NEI). After a long time, the NEI plasma may evolve to collisional ionized equilibrium (CIE) plasma,

in which the ionization degree coincides with the value expected from electron temperature. The characteristic time scale for plasma to reach CIE is given by Masai (1989) as

$$t_{ionize} \sim \frac{10^{12}}{n_e} \quad [\mathrm{sec}] \tag{4.24}$$

where n_e is a electron density in cm^{-3}. Ions in an NEI state capture more electrons compared with those in CIE, then the temperature estimated from ionization degree is lower than electron temperature. Therefore, we must be careful about the fact that line emission in NEI state is different from that in CIE, which is discussed in the previous subsection.

For NEI plasma and their emission in SNRs, many calculations have been done. Hamilton, Chevalier, & Sarazin (1983) carried on the extensive computations of NEI plasma spectra for SNR blast waves in Sedov phase (Sedov, 1959), which can be characterized two parameters, the post-shock temperature and a quantity $n_o^2 E$ which characterizes the rate at which the plasma relaxes toward CIE. Borkowski et al. (1994) developed a method to do NEI ionization calculations on the results of two-dimensional hydrodynamical simulations, based on the algorithm of Hughes & Helfand (1985).

Chapter 5

Instruments on-board *Chandra*

Chandra is a space observatory by NASA characterized by the finest spatial resolution (about $0''.5$) among the other X-ray satellite. In this chapter, we will briefly show the basic properties of the *Chandra*. The details are seen in *Chandra* X-ray Observatory Guide 2003[1].

5.1 Overview of the *Chandra* X-ray Observatory

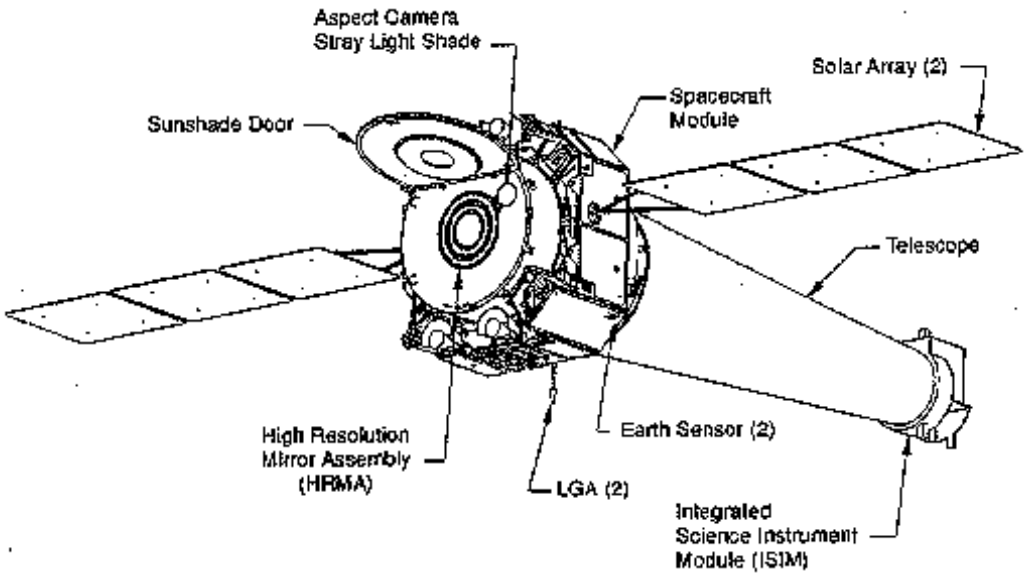

Fig. 5.1.— *Chandra* X-ray Observatory with some subsystems labeled (by CXO guide HP).

[1] http://asc.harvard.edu/cdo/about_chandra/

Chandra (Weisskopf et al., 2002) was successfully launched by NASA's space shuttle Columbia on July 23, 1999. It has a highly elliptical orbit that varies with time. As of September 2002, the apogee is $\sim 132,000$ km and the perigee is $\sim 16,800$ km. The orbit allows for a reasonably high observing efficiency as the satellite spends most of the time well above the radiation belt ($\sim 75\%$) and long continuous observations (~ 160 ksec) are made possible by the orbital period of 63.5 hours. There is a particle detector mounted near the telescope, which is used to monitor the local charged particle environment as a part of the scheme to protect the focal-plane instruments from particle radiation damages.

Chandra has a X-ray telescope (HRMA) and focal-plane science instruments (SIs), CCD arrays (ACIS-I and ACIS-S) and microchannel plate arrays (HRC-I and HRC-S). For observations of point-like sources with high energy resolution, we can use transmission grating systems (HETG and LETG), which are located between HRMA and SIs. The following sections show basic characteristics for each instrument.

5.2 PCAD — Pointing Control and Aspect Determination System

The pointing control and aspect determination (PCAD) system controls the pointing of the observatory and provides the data from which both the relative and absolute aspect are determined. Since the point spread function (PSF) radius of *Chandra* is comparable to the pixel size of SIs, sometimes it happens that X-ray photons from some directions fall into a certain bad pixel or gaps of SI chips. To avoid them, the PCAD makes the spacecraft to dither in a Lissajous shape, and as a result, the photons are spread over many different pixels of the focal plane detector and the variations between pixels are smoothed out. The PCAD system is the set of redundant gyroscopes, momentum wheels, and an aspect system consisting of a four inch optical telescope with CCD detector. The aspect camera can be also used as a real-time optical monitor for bright optical counterparts of the X-ray targets.

5.3 HRMA — High Resolution Mirror Assembly

The *Chandra* telescope consists of four pairs of concentric thin-walled, grazing-incidence Wolter Type-I mirrors. X-ray optics are reviewed by Aschenbach (1985). The front mirror of each pair is a paraboloid and the back a hyperboloid. The eight mirrors were fabricated from Zerodur glass, polished, and coated with iridium on a binding layer of chromium. The High Resolution Mirror Assembly (HRMA) is shown schematically in Figure 5.2.

The unobscured geometric clear aperture of the HRMA is 1145 cm^2. The obstruction of the HRMA clear aperture by supporting struts is less than 10%. Since reflectivity depends on energy as well as grazing angle, the HRMA throughput varies with X-ray energy. The left panel

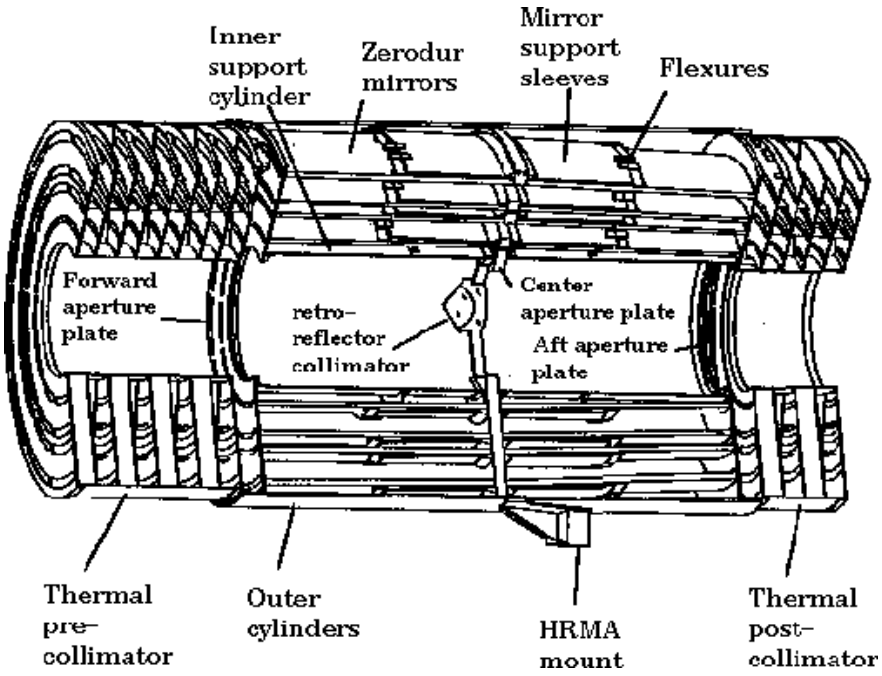

Fig. 5.2.— Schematic view of HRMA. Source photons come from the left side and are detected on the right side (by CXO guide HP).

of Figure 5.3 shows the on-axis HRMA effective area as a function of X-ray energy, as well as the HRMA/ACIS and HRMA/HRC effective areas, in linear scale, and the right panel shows effects of off-axis vignetting on the effective area for various energies; the plotted results are averages over the azimuthal angle.

The PSF of *Chandra* HRMA has been simulated with numerical ray-trace calculations. One of the most useful parameters is the encircled energy fraction (the two-dimensional integral of the PSF) as a function of radius from the PSF center. The PSF and the encircled energy fraction for a given radius depend upon off-axis angle and energy. Figure 5.4 (left) shows the encircled energy fraction as a function of radius for on-axis rays with different energies. The increase in image size with higher energy is apparent. The PSF also broadens for off-axis sources, and there is a considerable distortion in the image even for a perfect mirror set. This distortion is due to the aberrations of Wolter type I optics and to the different focal surfaces for the four mirror pairs. The increase in image size with off-axis angle is the greatest for the inner shell, and hence is larger for higher X-ray energies. The ACIS-I surface is not axially symmetric with respect to the HRMA optical axis, because the HRMA aimpoint is located at the inner corner of one of the four ACIS-I chips - I3. Thus the off-axis encircled energy radii are not azimuthally symmetric. Figure 5.4 shows the dependence of encircled energy radii on off-axis angle on the four ACIS-I chips.

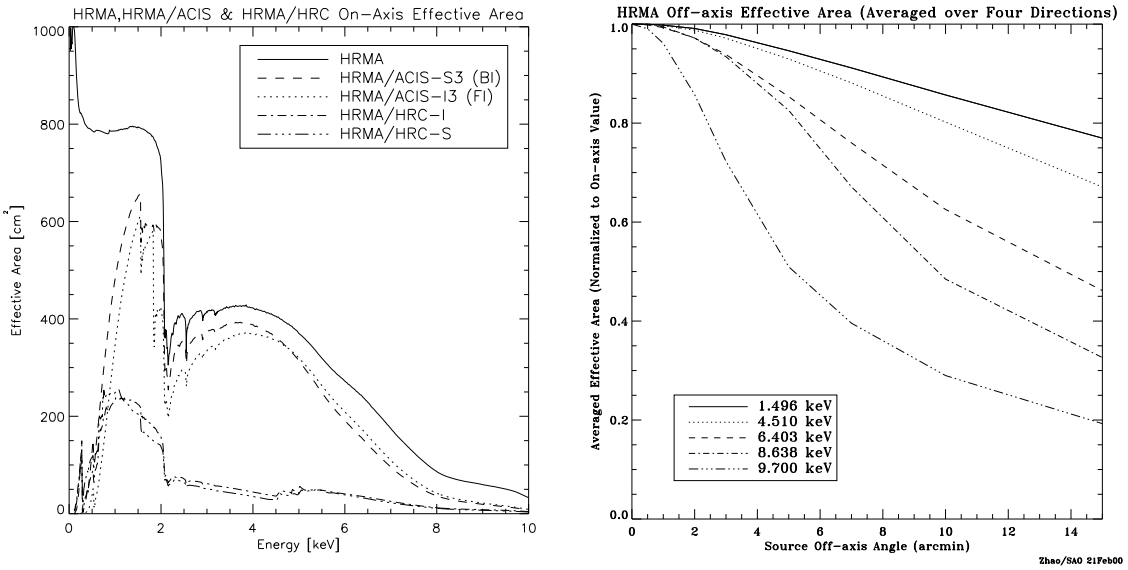

Fig. 5.3.— Left: The HRMA, HRMA/ACIS, and HRMA/HRC effective areas versus X-ray energy in linear scale. Right: The HRMA effective area versus off-axis angle, averaged over azimuth, for selected energies, normalized to the on-axis area for that energy (by CXO guide HP).

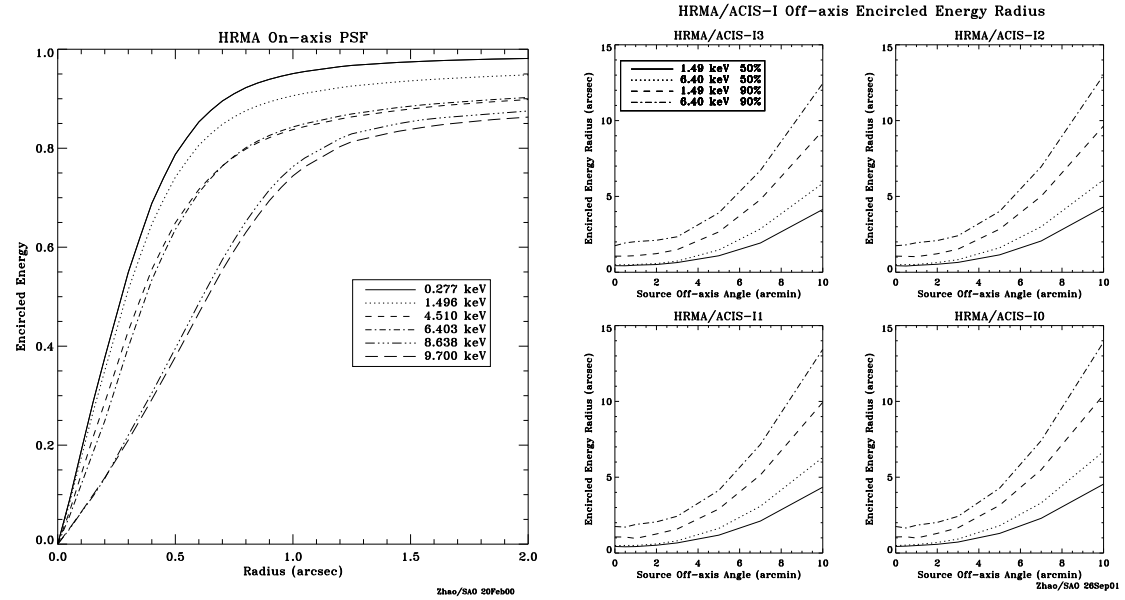

Fig. 5.4.— Left: Fractional encircled energy as a function of angular radius calculated for an on-axis point-source, at selected X-ray energies. The curves are the combined response of the four nested mirror pairs. Right: HRMA/ACIS-I encircled energy radii for circles enclosing 50% and 90% of the total energy at 1.49 and 6.40 keV as a function of off-axis angle (by CXO guide HP).

5.4 ACIS — Advanced CCD Imaging Spectrometer

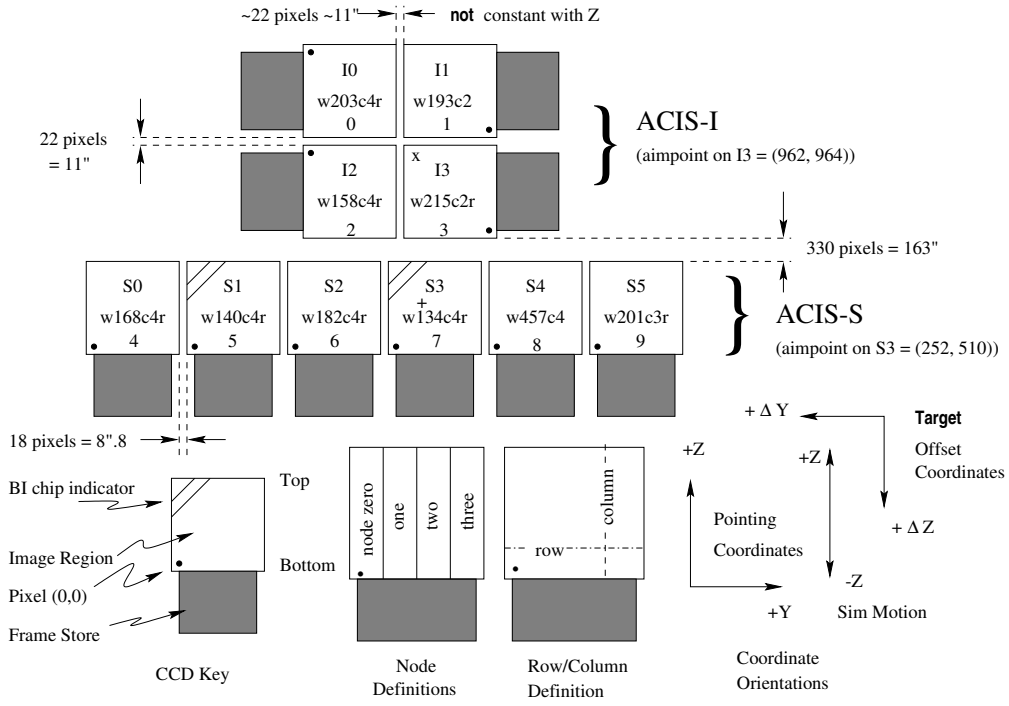

Fig. 5.5.— Schematic drawing of the ACIS focal plane (by CXO guide HP).

The Advanced CCD Imaging Spectrometer (ACIS) offers the capability to simultaneously acquire high-resolution images and moderate resolution spectra. The instrument can also be used in conjunction with the High Energy Transmission Grating (HETG) or Low Energy Transmission Grating (LETG) to obtain higher resolution spectra. ACIS contains 10 planar, 1024 × 1024 pixel CCDs (Figure 5.5); four arranged in a 2 × 2 array (ACIS-I) used for imaging, and six arranged in a 1 × 6 array (ACIS-S) used either for an imaging or grating readout. Two CCDs are back-illuminated (BI) and eight are front-illuminated (FI). The sensitivity of the BI devices extends to energies below that accessible by the FI chips. The chip-average energy resolution of the BI devices is, currently, better than that of the FI devices. Any combination of up to 6 CCDs may be operated simultaneously. Operating six chips increases the chances of serendipitous science but at the price of increased total background counting rate and therefore enhanced probability of saturating telemetry.

CCD is a solid-state electronic device composed primarily of silicon. A “gate” structure on one surface defines the pixel boundaries by alternating voltages on three electrodes spanning a

pixel. The silicon in the active (depletion) region (the region below the gates wherein most of the absorption takes place) has electric field so that charges move quickly to the gate surface. The gates allow confined charges to be passed in a "bucket brigade" (the buried channel) of pixels in parallel to a serial readout at one edge by appropriately varying ("clocking") the voltages in the gates. The ACIS front-illuminated CCDs have the gate structures facing the incident X-ray beam. Two of the chips on the ACIS-S array (S1 and S3) have had treatments applied to the back sides of the chips, removing insensitive, undepleted, bulk silicon material and leaving the photo-sensitive depletion region exposed. These are the BI chips and are deployed with the back side.

As the first step in the algorithm for detecting X-ray events, the on-board processing examines every pixel in the full CCD image and selects as events regions with bias-subtracted pixel values that both exceed the event threshold and are greater than all of the touching or neighboring pixels. The surrounding 3×3 neighboring pixels are then compared to the bias-subtracted split-event threshold; The pixel pattern is defined by above the threshold. On the basis of this pattern, the pixels are assigned a grade. Depending on the grade, the data are then included in or discard from the telemetry. On-board suppression of certain grades is used to limit the telemetry bandwidth devoted to background events.

The grade of an event is thus a code that defines which pixels, of the three-by-three pixel island centered on the local charge maximum, are above certain amplitude thresholds. A help to understand the ACIS grade assignments is shown in Figure 5.6, and the relationship to the *ASCA*/SIS grading scheme is given in Table 5.1. Ordinary, *ASCA* grade 0, 2, 3, 4, and 6 events are treated as X-ray events.

32	64	128
8	0	16
1	2	4

Fig. 5.6.— Schematic view to determine the grade of an event. The grade is determined by summing the numbers for those pixels that are above the thresholds.

The spatial resolution for on-axis imaging with ACIS is limited by the physical size of the CCD pixels (24.0 μm $\sim 0.492''$) and not by the HRMA. This limitation applies regardless of whether the aimpoint is selected to be the nominal aimpoint on I3 or S3. Approximately 90% of the encircled energy lands within 4 pixels ($2''$) of the center pixel at 1.49 keV and within 5 pixels ($2.5''$) at 6.4 keV. As the offset from the aimpoint becomes larger, the PSF radius becomes larger as shown in Figure 5.7.

The ACIS FI CCDs originally approached the theoretical limit of the energy resolution at almost all energies, while the BI CCDs exhibited a poorer resolution. The pre-launch energy resolution as a function of energy is shown in Figure 5.8 (left). Following the launch and orbital

Table 5.1: *ASCA*/SIS and *Chandra*/ACIS grades

ASCA	ACIS	Description
0	0	Single pixel events
1	1, 4, 5, 32, 33, 36, 37, 128, 129, 132, 133, 160, 161, 164, 165	Diagonal Split
2	2, 34, 64, 65, 68, 69, 130, 162	Vertical Split
3	8, 12, 136, 140	Horizontal Split Left
4	16, 17, 48, 49	Horizontal Split Right
5	3, 6, 9, 13, 20, 21, 35, 38, 40, 44, 52, 53, 96, 97, 100, 101, 131, 134, 137, 141, 144, 145, 163, 166, 168, 172, 176, 177, 192, 193, 196, 197	"L"-Shaped
6	10, 11, 18, 22, 50, 54, 72, 76, 80, 81, 104, 108, 138, 139, 208, 209	"L" & Quad
7	All other grades	

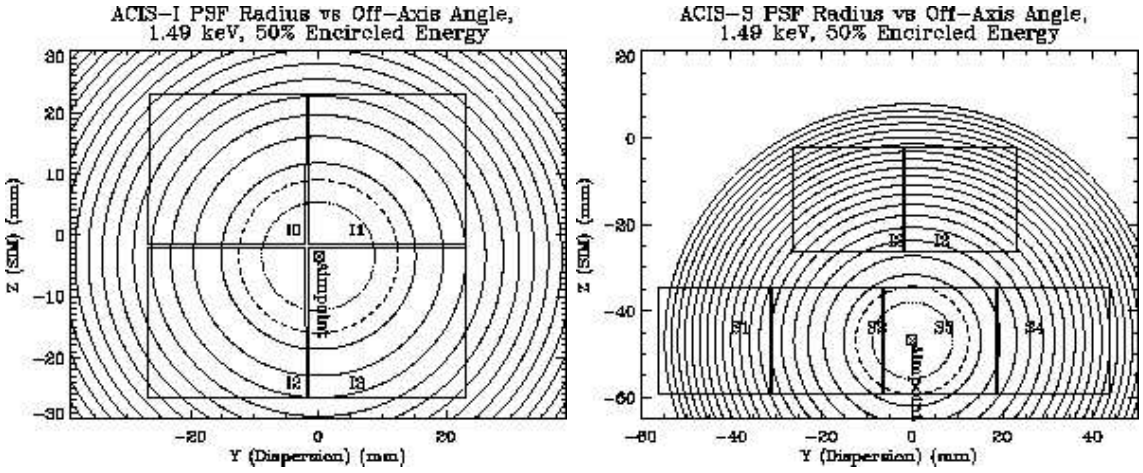

Fig. 5.7.— Contours of constant 50% encircled energy at 1.49 keV for ACIS-I (left) and ACIS-S (right).

activation, the energy resolution of the FI CCDs has become a function of the row number, being near pre-launch values at the position close to the frame store region and substantially degraded in the farthest row. An illustration of the dependence on the row is shown in Figure 5.8 (right).

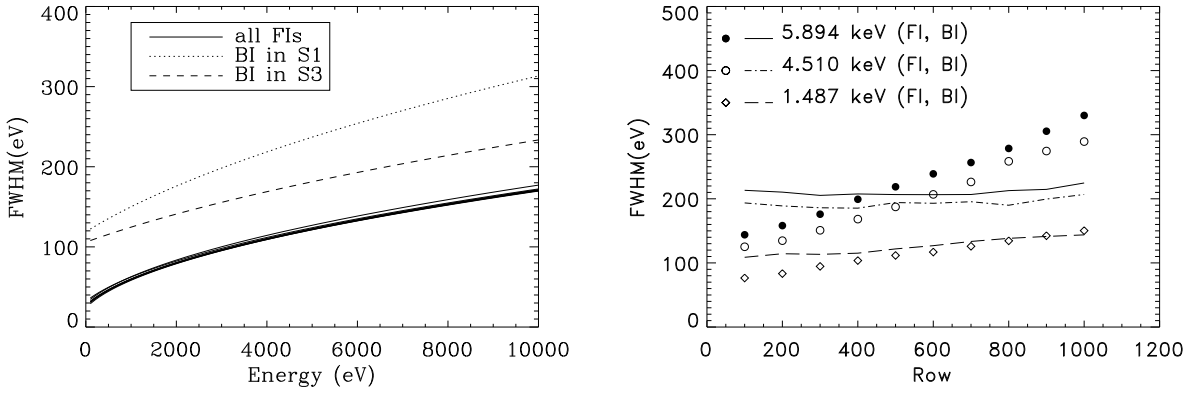

Fig. 5.8.— Left: ACIS pre-launch energy resolution as a function of energy. Right: The energy resolution of S3 and I3 as a function of row number. These data were taken at $-120C^{\circ}$ (by CXO guide HP).

5.5 HRC, HETG, and LETG

Since we do not use these instruments, only their basic characteristics are shown in the following subsections.

5.5.1 HRC — High Resolution Camera

The High Resolution Camera (HRC) is a microchannel plate (MCP) instrument comprised of two detectors, one optimized for imaging (HRC-I), and one (HRC-S) serves as a readout for the Low Energy Transmission Grating (LETG). The HRC-I provides the largest field-of-view ($30'' \times 30''$) of any detector aboard *Chandra*, and its response extends to energies below the sensitivity of the ACIS, albeit without comparable spectral resolution. The time resolution of the detectors (16 μsec) is the best on the observatory, but can only be exploited under certain conditions.

5.5.2 HETG — High Energy Transmission Grating

HETG is the High Energy Transmission Grating. In operation with the HRMA and a focal plane imager, the complete instrument is referred to as the HETGS — the High-Energy Transmission

Grating Spectrometer. The HETGS provides high resolution spectra (with $E/\triangle E$ up to 1000) between 0.4 keV and 10.0 keV for point and slightly extended (few arc seconds) sources. The HETG itself consists of two sets of gratings, each with different period. One set, the Medium Energy Grating (MEG), intercepts rays from the outer HRMA shells and is optimized for medium energies. The second set, the High Energy Gratings (HEG), intercepts rays from the two inner shells and is optimized for high energies.

5.5.3 LETG — Low Energy Transmission Grating

The Low Energy Transmission Grating Spectrometer (LETGS) is comprised of the LETG, a focal plane imaging detector and the HRMA. The *Chandra* HRC spectroscopic array (HRC-S) is the primary detector designed for use with the LETG. The spectroscopic array of the ACIS-S can also be used, though with decreased quantum efficiency below 0.6 keV and a smaller detectable wavelength range. The HETG used in combination with ACIS-S offers superior energy resolution and quantum efficiency above 0.78 keV. The LETGS provides high-resolution spectroscopy ($E/\triangle E > 1000$) between 0.07–0.15 keV and moderate resolving power at shorter wavelengths. The nominal LETGS wavelength range accessible with the HRC-S 0.07–10 keV); ACIS-S coverage is 0.20–10 keV.

Chapter 6

Analyses of SN 1006

SN 1006 is a milestone in the history of study of cosmic ray acceleration in SNRs. In this chapter, we revisit this remnant with excellent spatial resolution of *Chandra* and consider the condition of acceleration.

6.1 Previous Observations

SN 1006 (G327.6+14.6) is the remnant of one of the brightest historical SN explosions on May 1, A.D. 1006 (Fujiwara, 1242), which was observed and recorded in all over the world; Europe, Egypt, Middle East, China, and Japan (Goldstein & Peng Yoke, 1965). More than 20 documents show us that the explosion was visible for more than a year, suggesting that the SN is type Ia (Minkowski, 1966).

A thousand years later, SN 1006 was catalogued by Bolton, Gardner, & Mackey (1964) as a radio source and identified as the remnant of SN 1006 by Gardner & Milne (1965). The spectral index is measured by Allen, Petre, & Gotthelf (2001) to be $\alpha = 0.57$. Reynolds & Gilmore (1993) measured the radio polarization in the north-eastern shell of SN 1006 and found that the magnetic field in downstream is turbulent with the scale less than 0.2 pc. Winkler et al. (2003) observed the proper motion of the outer shock in the optical band and found that the SNR is expanding with the ratio of 280±8 mas yr^{-1}. With the shock velocity measurement with Hα lines (v_s = 2890±100 km s^{-1}; Ghavamian et al. 2002), the distance to SN 1006 is estimated to be 2.18±0.08 kpc and we refer this value throughout this thesis.

X-ray observations make SN 1006 one of the most famous SNRs; *Einstein* SSS spectra of SN 1006 were featureless, unlike other young pulsar-less SNRs (Becker et al., 1980), leading to an early controversy about the origin of the X-ray emission. Reynolds & Chevalier (1981) proposed that the emission was synchrotron from the steepened tail of the shock-accelerated electron distribution responsible for the radio emission, but Hamilton, Sarazin, & Szymkowiak (1986) produced an

elaborate thermal model capable of suppressing line emission. The controversy was resolved with *ASCA*, which has imaging capability in the hard band (Ohashi et al., 1996). Koyama et al. (1995) observed the SNR with *ASCA* and found that the spectra of the rims are very different from other SNRs, it shows sparse line structures and hard emission. The hard X-rays are well described as synchrotron X-rays from ∼TeV electrons. Together with the discovery of inverse Compton photons from the north-eastern shell of the SNR in the TeV γ-ray band (Tanimori et al., 1998, 2001), the shock front of SN 1006 became the first confirmed sample of cosmic ray acceleration site. On the other hand, Berezhko et al. (2002) insists that there is some debate that the TeV γ-ray emission is inverse Compton or π^0 decay. Recently, HEGRA also detected TeV γ-rays from the north-eastern shell of the remnant (Tonello et al., 2003).

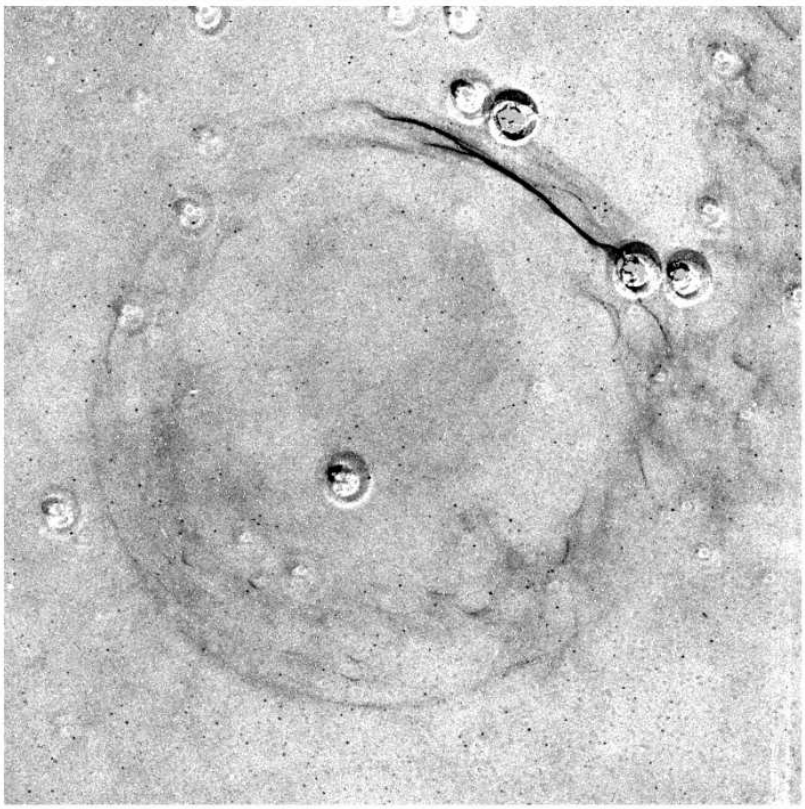

Fig. 6.1.— Hα image of SN 1006 (Winkler, Gupta, & Long, 2003).

There are many recent works on SN 1006 in the X-ray band. Vink et al. (2000) analysed the integrated spectrum from *BeppoSAX* of SN 1006 and found an adequate two temperature fit to the thermal emission and super-solar abundances. Allen et al. (2001) and Dyer et al. (2001) made wide band spectrum with *ROSAT*, *ASCA*, and *RXTE*, and made detailed model for SN 1006. Dyer, Reynolds, & Borkowski (2004) suggested that there are two thermal components to explain the spectra of north-eastern and south-western shells. New *Chandra* observations of the north-eastern

and north-western shells provide the best spatial resolution images to date and several groups have been exploring the fine details. Long et al. (2003) found no evidence for the halo predicted by Reynolds (1996) and that the radio and X-ray features were perfectly correlated in the north-eastern shell although above 0.8 keV X-ray limb brightening is more pronounced. Clumps of thermal X-ray material were found in the interior of the shock in the north-eastern and north-western shells. Bamba et al. (2003b) carried out spatial and spectral fits of profiles of the *Chandra* observation of sharp fine filaments in the north-eastern shell. This chapter mainly follows this paper.

6.2 *Chandra* Observation

We used the *Chandra* archival data of the ACIS on the north-eastern (NE) shell of SN 1006 (Observation ID = 00732) observed on July 10–11, 2000 with the targeted position at (R.A., Decl.) = ($15^{\rm h}03^{\rm m}51\overset{\rm s}{.}6$, $-41^{\rm d}51^{\rm m}18\overset{\rm s}{.}8$). CCD chips I2, I3, S1, S2, S3, and S4 were used with the pointing center on S3. Data acquisition from the ACIS was made in the Timed-Exposure Faint mode. The data reductions and analyses were made using the *Chandra* Interactive Analysis of Observations (CIAO) software version 2.2.1. Using the level 2 processed events provided by the pipeline processing at the *Chandra* X-ray Center, we selected *ASCA* grades 0, 2, 3, 4, and 6 as X-ray events. The effective exposure was ~ 68 ks for the observation. In this chapter, we concentrated on the data of S3 (BI chip) because this chip has the best efficiency in soft X-rays required for the spectral analyses and its on-axis position provides the smallest point-spread function required for the spatial analysis.

6.3 Overall Images

Figure 6.2 (see also Figure C.4) shows the true-color image from I2, I3, and S1–S4 for the NE shell of SN 1006. The image is contrasted in the 0.5–2.0 keV band (hereinafter, the soft1 band; left) and in the 2.0–10.0 keV band (hereinafter, the hard band; right). The fine spatial resolution of *Chandra* unveils extremely narrow filaments in the hard band. They run from north to south along the outer edge of the NE shell, parallel to the shock fronts observed by Hα emission line (Winkler et al., 2003). These filaments resemble the sheet-like structure of the shock simulated by Hester (1987). The soft1 band image, on the other hand, has a larger scale width similar to the *ROSAT* HRI image (Winkler & Long, 1997). Many clumpy sub-structures are also seen in this energy band.

6.4 Inner Shell Region

To resolve the thermal and non-thermal components, we made a spectrum from a bright clump found in the soft1 band image, which is located in the inner part of the NE shell ("Inner region" with the dashed ellipse in Figure 6.3). The background region was selected from a region outside

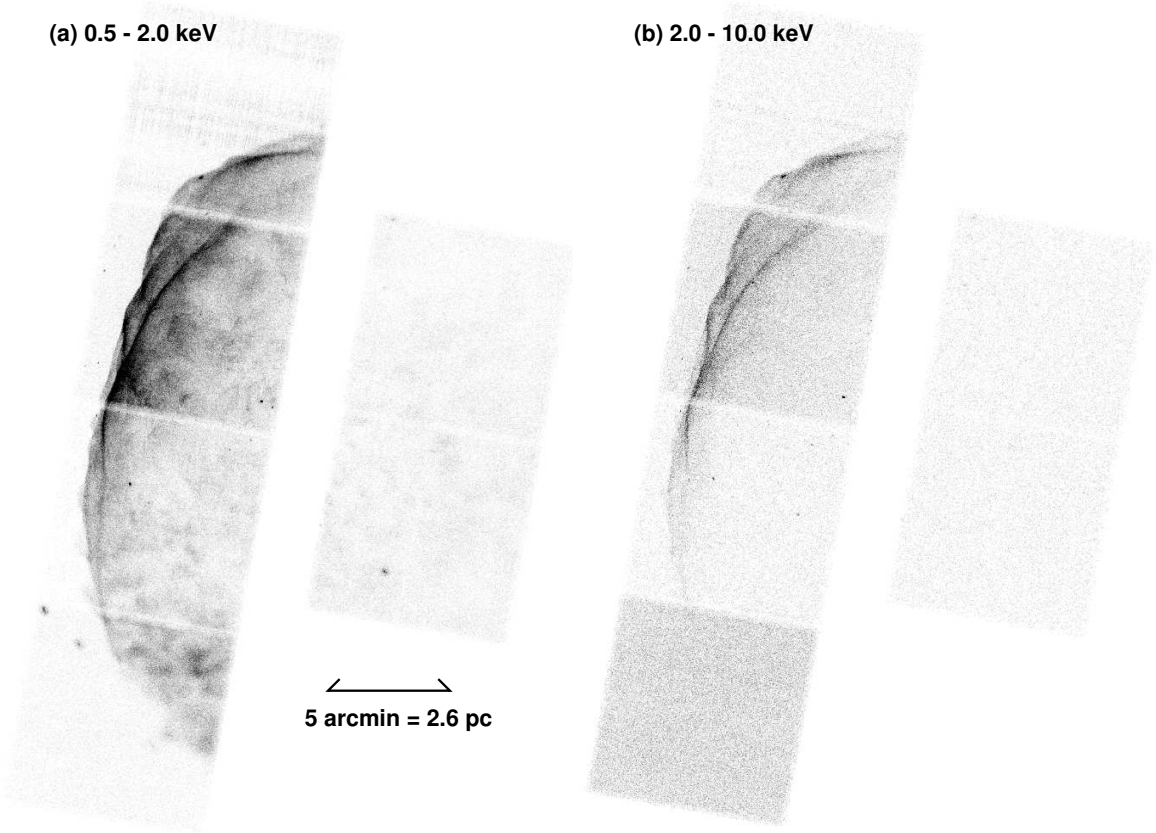

Fig. 6.2.— Images of SN 1006 NE shell in 0.5-2.0 keV (left) and 2.0–10.0 keV (right), respectively, both in logarithmic scale.

of the SNR, as is shown in Figure 6.3 with the dashed lines.

The background-subtracted spectrum shown in Figure 6.4 has many emission lines. We hence determined the peak energies of the five brightest lines with a phenomenological model, a power-law continuum plus Gaussian lines. The strongest line structures are the peak at 0.55 keV and the hump at 0.67 keV. These energies are nearly equal to the Kα lines of He- and H-like oxygen, hence are attributable to highly ionized oxygen. Likewise, the other clear peaks at 0.87, 1.31, and 1.76 keV are most likely He-like Kα of Ne, Mg and Si, respectively. However, all the observed line energies are systematically smaller than those of the relevant atomic data. These apparent energy shifts have been usually observed in a young SNR plasma in non-equilibrium ionization (NEI). The "energy shift" in this case is due to the different line ratio of many sub-levels and/or different ionization states. The oxygen Lyman α is isolated from the other lines of different ionization states, hence the NEI effect gives no energy shift. Still we see apparent down-shift of the observed line energy from that of the laboratory data. He-like Kα lines are complex of many fine structures with the split-energy of at most $\sim$ 25 eV (for He-like silicon). Although the energy shift of He-like Kα lines

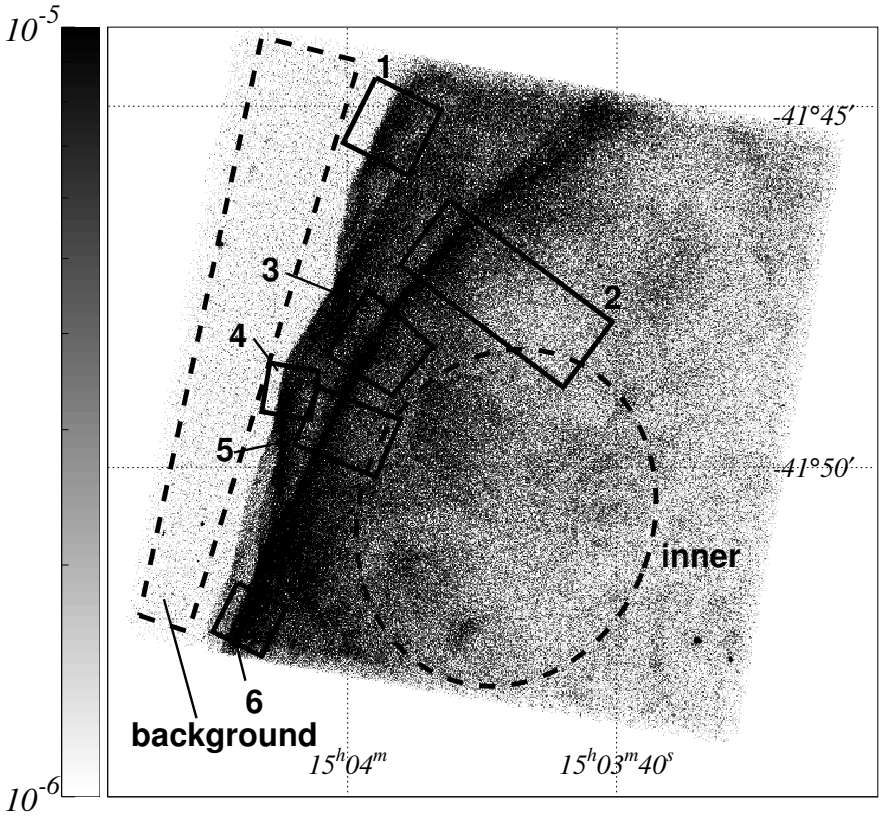

Fig. 6.3.— Close-up view of the 0.5–10.0 keV band image of S3 chip with J2000 coordinates, binned with 1 arcsec scale. The gray scale (the left bar) is given logarithmically ranging from 1×10^{-6} to 1×10^{-5} cnts s^{-1} arcsec^{-2} . The inner and background regions for the spectral analyses and the filament regions for the spatial analyses (No.1–6) are shown with dashed and solid lines, respectively. The picture is credited by Bamba et al. (2003b).

due to NEI should be smaller than this split-energy, the observed energy shifts are systematically larger than the split-energy. We therefore regard that the apparent energy shifts are due mainly to energy calibration uncertainty, hence fine-tuned the energy gain to reduce it by 3.8%, the average shift of the 5 brightest lines. We then fitted the spectrum with a thin thermal plasma model in NEI calculated by Borkowski et al. (2001a). The abundances of C, N, O, Ne, Mg, Si, S, and Fe in the plasma were treated to be free parameters, whereas those of the other elements were fixed to the solar values (Anders & Grevesse, 1989). The absorption column was calculated using the cross sections by Morrison & McCammon (1983) with the solar abundances. Since this NEI model exhibited a systematic data excess at high energy above 2 keV, we added a power-law component and the fit improved dramatically. Figure 6.4 and Table 6.1 show the best-fit models (dashed and solid lines for thermal and power-law components) and parameters, respectively.

Instead of the phenomenological power-law model, we applied *srcut* in the XSPEC package as

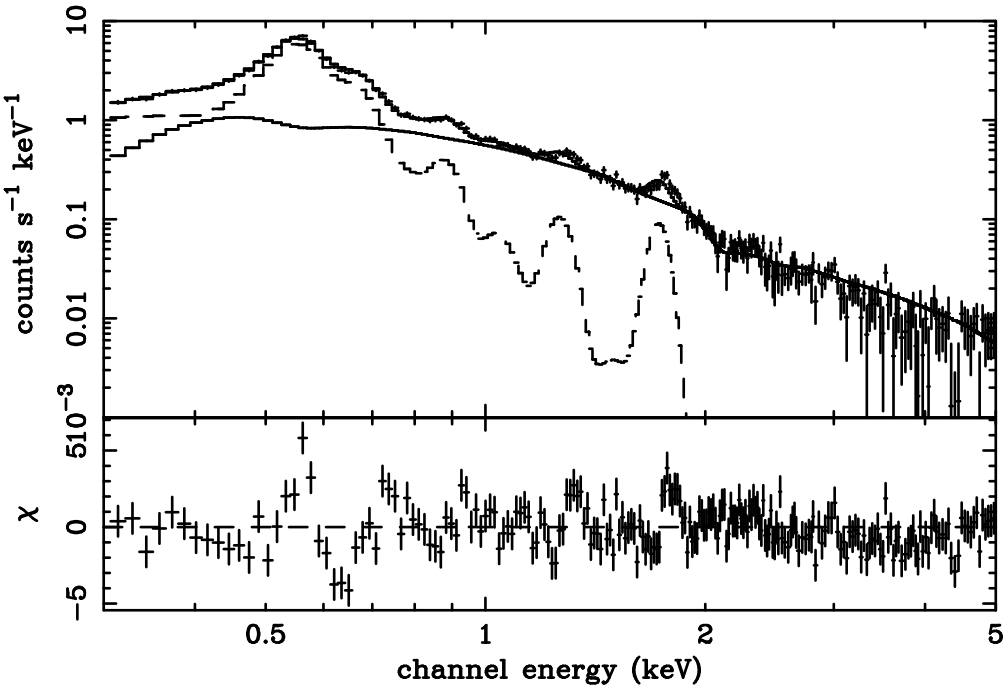

Fig. 6.4.— Upper: The background-subtracted spectrum of the inner region (crosses). Dashed line and solid liens are the best-fit thin thermal and power-law models, respectively. Lower: The data residuals from the best-fit two-components model. The picture is credited by Bamba et al. (2003b).

a more physical model. This model are made by Reynolds (1998) and represents the synchrotron spectrum from an exponentially cut off power-law distribution of electrons in a homogeneous magnetic field. This spectrum is itself a power-law, rolling off more slowly than exponential in photon energies. Though more realistic than a power-law, it is highly oversimplified, but does give the maximally curved physically plausible spectrum and can be used to set limits on maximum accelerated-electron energies even in remnants whose X-rays are thermal. The parameters in *srcut* model is normalization, the radio spectral index p, and the roll-off frequency $\nu_{rolloff}$, which can be written (Reynolds & Keohane, 1999) as

$$\nu_{rolloff} = 5 \times 10^{17}\ \mathrm{Hz} \left(\frac{B}{10\ \mu\mathrm{G}}\right) \left(\frac{E_{max}}{100\ \mathrm{TeV}}\right)^2 \quad . \tag{6.1}$$

We fixed $p = 0.57$, the observed value by Allen et al. (2001). The best-fit ν_{rolloff} is 9.2 (8.6–10.3) $\times 10^{16}$ Hz, with a better reduced χ^2 of 389.0/215 than that of the power-law model of 447.9/215 (see Table 6.1).

As for the thermal components, we also tried the fitting with a plane shock model (XSPEC model *vpshock*) plus either a power-law or *srcut* and found no essential difference from the case of an NEI model.

Table 6.1: The best-fit parameters of the spectrum of the inner region[a].

Parameters	Best-fit value
Power-law Model	
Photon Index.....	2.51 (2.48–2.53)
Flux[b] [ergs cm^{-2} s^{-1}].....	3.8×10^{-12}
NEI model	
Temperature [keV].....	0.24 (0.21–0.26)
Abundances[c]	
C	(<0.1)
N	(<0.03)
O	3.3 (3.0–3.5)
Ne	4.8 (4.4–5.2)
Mg	51 (42–61)
Si	131 (121–140)
S	10 (6.8-13)
Fe	37 (28–46)
$n\tau$ [$\times 10^9$ s cm^{-3}].....	10.8 (9.9–11.1)
$E.M.$[d] [$\times 10^{55}$cm^{-3}].....	2.1 (1.9–2.2)
Flux[b] [ergs cm^{-2} s^{-1}].....	3.3×10^{-12}
$N_{\rm H}$ [10^{20} H cm^{-2}]	9.0 (8.5–9.4)
Reduced χ^2 [χ^2/d.o.f].....	447.9/215

[a]: Parentheses indicate single-parameter 90% confidence regions.

[b]: In the 0.3–10.0 keV band.

[c]: Abundance ratio relative to the solar value (Anders & Grevesse, 1989).

[d]: $E.M. = n_{\rm e}^2 V$, where $n_{\rm e}$ and V are the electron density and the volume, respectively.

Although these simple models globally follow the data very well, all are rejected in the statistical point of view, leaving wavy residuals near the line structures as shown in Figure 6.4 (lower panel). This may be caused by improper response function in energy scale and/or in energy resolution. We assumed that the photons are uniformly distributed in flux and in temperature in the whole source region. This simple assumption may also be partly responsible for the above systematic error, because in reality the source region is apparently clumpy (see Figure 6.2) and may have different temperatures, abundances, and/or ionization time scales. Since our principal aim of this chapter is to examine the spatial structures and the spectra of non-thermal component, we do not examine in further detail for the thermal model. In the following analyses and discussion, we use the physical parameters cited in Table 6.1 as a good approximation.

The spectrum of the inner region clump is softer than any other regions in the NE shell, which indicates that the contribution of the thermal component is the largest. Nevertheless the

thermal photons are only 0.02% of the non-thermal ones if we limit the energy band to 2.0–10.0 keV (the hard band); the non-thermal photons in the hard band are 8.9×10^{-2} cnts s^{-1}, while thermal photons are 2.0×10^{-5} cnts s^{-1}. Therefore, in the following spatial analyses, we regard that all the photons in the hard band are of non-thermal origin.

As for the spatial analysis of the thermal emission, we use the limited band of 0.4–0.8 keV (hereafter; the soft2 band) to optimize the signal-to-noise ratio, in which K-shell lines from He-like oxygen (0.57 keV) contribute the largest fraction of the X-ray emission (see Figure 6.4). Even in this optimized band for the thermal emission, however, the count rates of the thermal and non-thermal emissions are comparable: thermal photons are 8.1×10^{-1} cnts s^{-1}, while those of non-thermal are 5.4×10^{-1} cnts s^{-1}.

6.5 The Filaments

The outer edge of the NE shell is outlined by several thin X-ray filaments. For the study of these filaments, we selected 6 rectangle regions in Figure 6.3, in which the filaments are straight and free from other structures like another filament and/or clumps. These regions (solid boxes) are shown in Figure 6.3 with the designations of Nos.1–6 from north to south. Since the SNR shell is moving (expanding) from the right to the left, we call the right and left side as downstream and upstream following the terminology of the shock phenomena.

Figure 6.5 shows the intensity profile in the hard (2.0–10.0 keV: upper panel) and soft2 (0.4–0.8 keV: lower panel) bands for each filament with the spatial resolution of 0.5 arcsec, where the horizontal axis (x-coordinate) runs from the east to west (upstream to downstream) along the line normal to the filaments. We see very fast decay in the downstream side and even faster rise in the upstream side.

To estimate the typical scale width, we define a simple empirical model for the count rate as a function of position (x);

$$f(x) = \begin{cases} A\exp\left(-\left|\frac{x_0-x}{w_u}\right|\right) & \text{in upstream} \\ A\exp\left(-\left|\frac{x_0-x}{w_d}\right|\right) & \text{in downstream} \end{cases}, \tag{6.2}$$

where A and x_0 are the flux and position at the filament peak, respectively. The scale widths are given by w_u and w_d for upstream and downstream, respectively (hereafter, "u" and "d" represent upstream and downstream, respectively). Since the scale width of the filaments is larger than the spatial resolution of *Chandra* ($\sim$ 0.5 arcsec = 1 bin in Figure 6.5), we ignore the effect of the point-spread function.

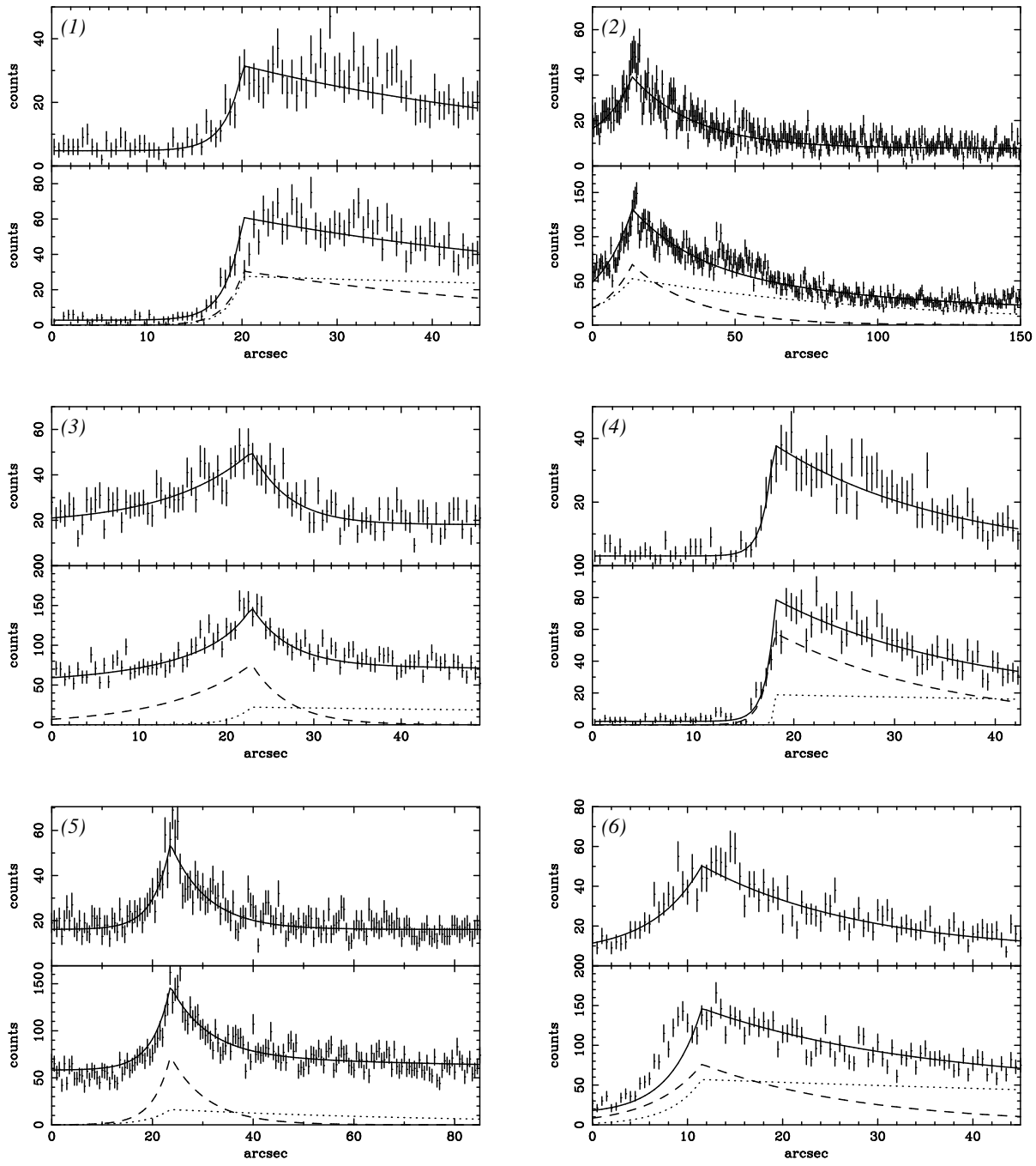

Fig. 6.5.— The profiles of the filaments in SN 1006 NE shell. Upper panels show the profiles in the hard (2.0–10.0 keV) band, whereas the lower panels in the soft2 (0.4–0.8 keV) band with the best-fit models (solid lines). The dashed lines in the lower panels represent non-thermal photons extrapolated from the hard band flux of the power-law (see the upper panels). The dotted lines are the thermal component after subtracting the non-thermal contamination (dashed lines). Upstream is to the left and downstream is to the right. These pictures are credited by Bamba et al. (2003b).

Table 6.2: The best-fit parameters of the profiles of the filaments.[a]

	hard band				soft2 band			
No.	A^h [cnts arcsec^{-1}][b]	w_u^h [arcsec]	w_d^h [arcsec]	Reduced χ^2 [χ^2/d.o.f.]	A^s [cnts arcsec^{-1}][c]	w_u^s [arcsec]	w_d^s [arcsec]	Reduced χ^2 [χ^2/d.o.f.]
1 . .	53	1.9	36	119.1/105	55	1.7	160	104.0/94
	(49–58)	(1.3–3.0)	(30–44)	···	(49–61)	(1.3–2.2)	(>92)	···
2 . .	63	11	22	347.3/296	100	14	93	481.8/298
	(58–68)	(8.7–14)	(19–25)	···	(95–120)	(9.8–21)	(73–130)	···
3 . .	66	10	5.5	141.3/114	44	2.3	150	119.8/95
	(58–74)	(8.2–13)	(4.1–7.2)	···	(37–52)	(0.78–4.3)	(>56)	···
4 . .	68	0.98	18	103.2/99	38	0.12	150	106.1/81
	(62–74)	(0.73–1.3)	(16–21)	···	(34–42)	ND[d]	(>78)	···
5 . .	75	3.8	8.0	218.3/166	33	4.5	62	236.5/167
	(66–85)	(2.8–4.9)	(6.5–9.9)	···	(24–41)	(2.2–8.7)	(43–100)	···
6 . .	87	3.5	19	99.9/86	110	3.4	1.3×10^2	118.4/87
	(79–96)	(2.1–5.4)	(15–26)	···	(100–130)	(2.4–5.0)	(86–250)	···

[a]: Parentheses indicate single-parameter 90% confidence regions.
[b]: In the 2.0–10.0 keV band.
[c]: In the 0.4–0.8 keV band.
[d]: Not determined.

Non-Thermal Structure

As is already noted in § 6.4, the hard band (2.0–10.0 keV) flux is nearly of pure non-thermal origin (see also the next paragraph). We therefore used the hard band profiles for the study of the non-thermal X-ray structures. The hard band profiles were fitted with a function $f^{\rm h}(x) + C^{\rm h}$ (hereafter, "h" represents the hard X-ray band), where C^h is the background constant, which includes the cosmic and Galactic X-ray background and non X-ray events. The fittings were statistically accepted for all the filament profiles. The best-fit models and parameters are shown in Figure 6.5 with the solid lines and in Table 6.2, respectively.

We then made the spectra of the filaments within the scale widths: ($x_0^h - w_u^h \leq x \leq x_0^h + w_d^h$) in Figure 6.5. The background spectra were made from the off-filament downstream regions. All the background-subtracted spectra are featureless (no line structure) and extend to high energy side as shown in Figure 6.6, which were fitted with an absorbed power-law model with the best-fit parameters given in Table 6.3. We thus confirm that the hard X-ray profiles represent those of non-thermal X-rays.

Since the spectra have similar parameters for each other, in order to increase statistics, we summed all the data of six filaments (the combined-filament). The best-fit power-law model and parameters for the combined spectrum of the filaments are shown in Figure 6.7 and listed in Table 6.3. The spectrum was also fitted with a *srcut* model (Reynolds & Keohane, 1999). The best-fit $\nu_{\rm rolloff}$ and the other parameters are also listed in Table 6.3. We note that the *srcut* model

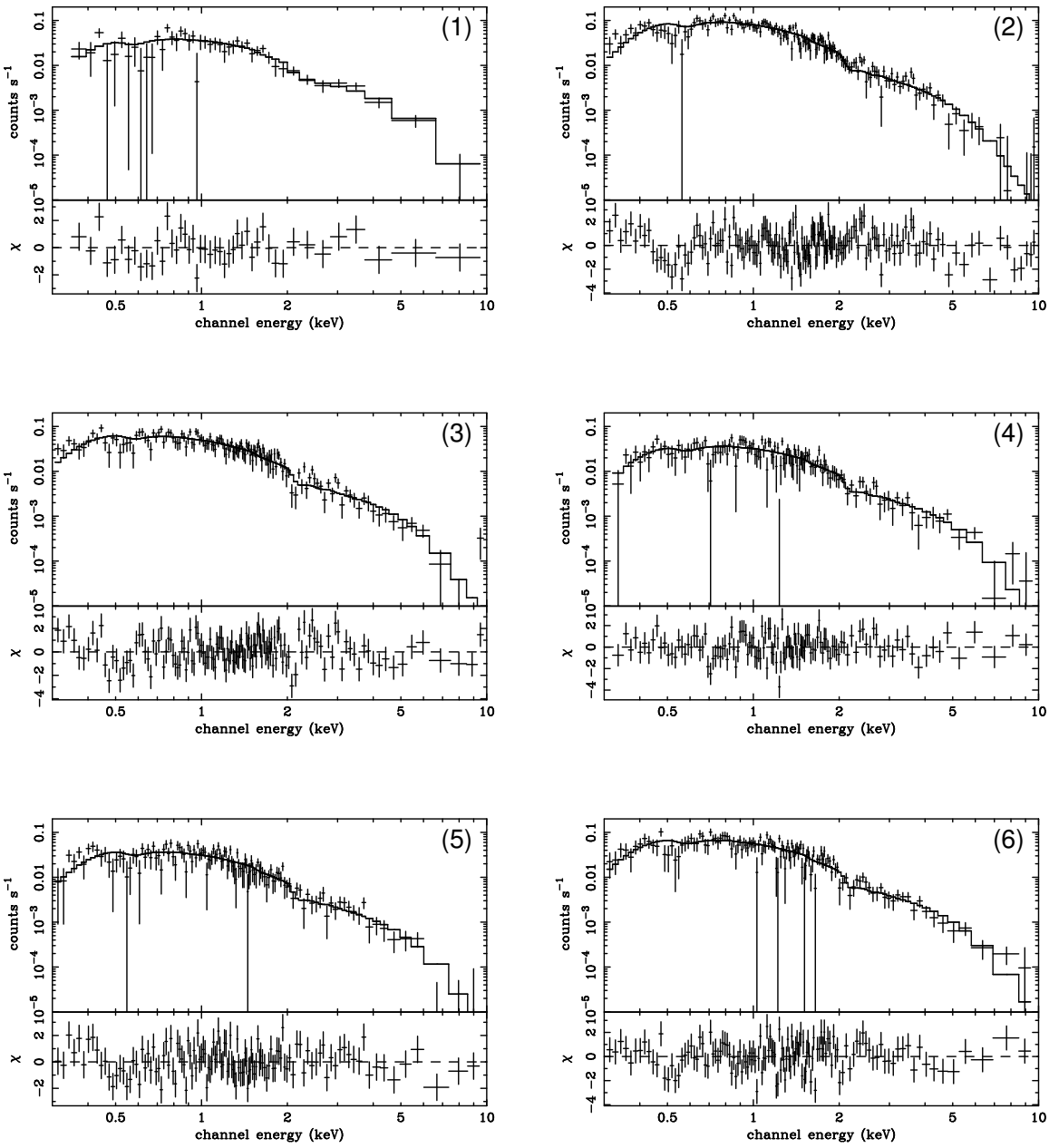

Fig. 6.6.— Upper: The spectrum of each filament (the crosses). The best-fit power-low model is also shown in the solid line. Lower: The residuals from the best-fit model.

give slightly better χ^2/d.o.f. than that of a phenomenological power-law model (see Table 6.3).

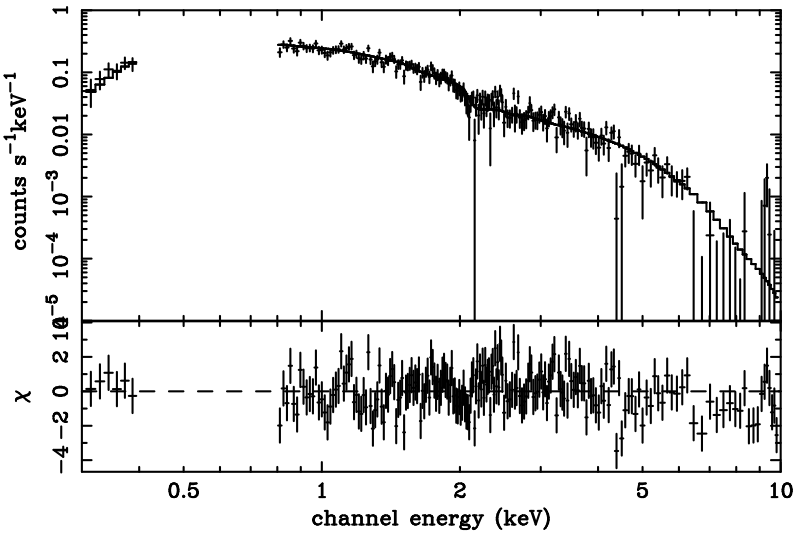

Fig. 6.7.— Spectrum of combined-filament (the crosses). The best-fit power-low model is also shown in the solid line. The photons in 0.4–0.8 keV are ignored because of a heavy contamination of oxygen lines.

We further made combined spectra of upstream and downstream regions separately. The downstream regions were also divided into near and far side of the shock and compared. However, there was no significant difference between the downstream and upstream, nor within the downstream; the photon index was nearly constant along the x-axis in the combined-filament.

Thermal Structure

To examine the structure of the thermal component, we used the soft2 band profiles (the lower panels of Figure 6.5). Contamination by non-thermal photons would be very large even in this optimized band (see § 6.4). Therefore we calculated the flux ratio between the non-thermal photons in the hard and soft2 bands using the spectral parameters given in Table 6.3. From the flux ratio and the best-fit hard band profiles, we estimated the non-thermal contaminations as are given with the dashed lines in Figure 6.5.

After subtracting these non-thermal contaminations, we fitted the soft2 band profiles with a model of $f^s(x) + C^s$, where $C^{\rm s}$ is the background constant in the same sense as C^h. Note that although we use "s" as the abbreviation of the soft2 band, it actually represents thermal X-rays.

Table 6.3: The best-fit parameters of the spectral fittings for the filaments.[a]

Parameters	1	2	3	4	5	6	Combined
Power-low model							
Γ	2.0 (1.8–2.2)	2.4 (2.3–2.6)	2.3 (2.1–2.4)	2.3 (2.1–2.4)	2.3 (2.1–2.5)	2.3 (2.1–2.4)	2.31 (2.29–2.33)
$N_{\rm H}$ [b]	1.5 (0.9–2.1)	1.8 (1.5–2.0)	1.2 (1.0–1.5)	1.6 (1.3–2.0)	1.4 (1.1–1.8)	1.4 (1.1–1.7)	1.6 (1.6–1.7)
Flux[c]	3.7×10^{-13}	5.4×10^{-13}	3.7×10^{-13}	2.5×10^{-13}	2.3×10^{-13}	4.2×10^{-13}	1.8×10^{-12}
χ^2/d.o.f....	44.1/43	232.5/164	196.3/140	139.8/125	143.8/125	173.4/130	273.3/211
srcut							
$\nu_{\rm rolloff}$ [d] ...	13 (3.6–94)	1.7 (1.1–2.3)	2.8 (1.8–4.7)	2.9 (1.5–6.2)	2.4 (1.3–5.0)	2.8 (1.7–5.0)	2.6 (1.9–3.3)
$N_{\rm H}$ [b]	1.3 (1.0–1.7)	1.4 (1.2–1.5)	1.0 (0.8–1.1)	1.3 (1.1–1.5)	1.1 (0.9–1.4)	1.1 (0.9–1.3)	1.3 (1.2–1.5)
Flux[c]	3.6×10^{-13}	5.3×10^{-13}	3.6×10^{-13}	2.4×10^{-13}	2.2×10^{-13}	4.1×10^{-13}	1.8×10^{-12}
χ^2/d.o.f....	43.7/43	225.1/164	190.9/140	139.1/125	141.1/125	170.7/130	265.2/211

[a]: Parentheses indicate single-parameter 90% confidence regions.
[b]: Absorption column in the unit of 10^{21} H cm^{-2}.
[c]: In the 0.3–10.0 keV band flux in the unit of ergs cm^{-2} s^{-1} .
[d]: Roll-off frequency in the unit of 10^{17}Hz.

From Figure 6.5, we see that most of the photons at the filament peak is non-thermal origin, hence the statistics becomes poor to determine the position of the thermal peak (x_0^s) independently. We thus fixed x_0^s to the best fit peak in the hard hand x_0^h. Also we set the upper bound of the fitting parameter w_d^s to be 900 arcsec, the same as the radius of SN 1006 (Green, 2001). The best-fit models and parameters for the thermal components ($f^s(x)$) are shown with dotted lines in the lower panels of Figure 6.5 and in Table 6.2, respectively.

6.5.1 Non-Thermal versus Thermal

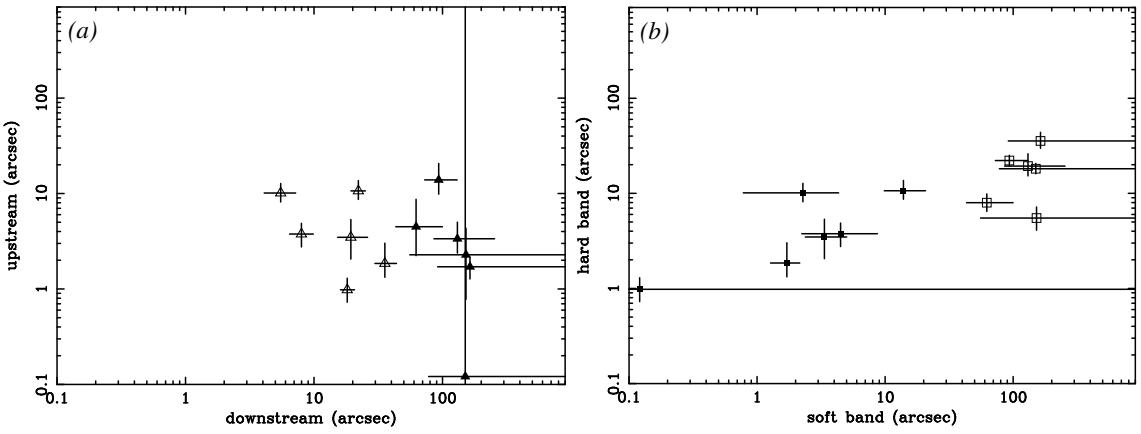

Fig. 6.8.— (a) The relation between $w_{\rm u}$ and $w_{\rm d}$. The close and open triangles are for the thermal and non-thermal emissions, respectively. (b) The relation between w^s and w^h. The close and open boxes are in the upstream and downstream, respectively.

Figure 6.8 (a) shows the relation of the scale widths between the downstream and upstream sides for each filament. Although there is a large scatter, w_u is systematically smaller than w_d in both the non-thermal and thermal emissions.

Figure 6.8 (b) shows the relation between w^s and w^h. We find that w_d^s is significantly larger than w_d^h, whereas w_u^s and w_u^d are comparable with each other. The mean values are $\overline{w_u^s} = 4.3$ arcsec $= 0.05$ pc, $\overline{w_d^s} = 1.3 \times 10^2$ arcsec $= 1.4$ pc, $\overline{w_u^h} = 5.1$ arcsec $= 0.05$ pc, and $\overline{w_d^h} = 18$ arcsec $= 0.2$ pc. Note that the minimum value of w_u^h is only 0.98 arcsec $= 0.01$ pc (filament 4). Maybe since their wide scatter is due to that these are the projected values of the possible sheet-like with wavy and/or curved shape.

6.6 Discussion for SN 1006

6.6.1 Thermal Emission

Although the best-fit NEI model in Table 6.1 is rejected statistically, it globally fits the thermal emission of SN 1006 as shown in Figure 6.4. The temperature ($kT = 0.24$ keV) is similar to the results obtained by Vink et al. (2000), Dyer et al. (2001), and Allen et al. (2001), but lower than that by *ASCA* in Koyama et al. (1995). Since the spatial resolution of *Chandra* enables us to remove the non-thermal photons from the thermal emission more accurately than the *ASCA* case, the present results should give a more precise description on the thermal plasma. Like the previous observations (Koyama et al., 1995; Allen et al., 2001), heavy elements, in particular iron, are overabundant, which implies that the X-ray emitting thermal plasma is dominated by the ejecta from type Ia SN. The fact that the thermal emission is enhanced in the inner shell region also suggests the ejecta origin.

From the emission measure ($E.M.$) and assumptions of a uniform density plasma of a prorate shape with the 3-axis radii of 140, 120, and 120 arcsec, $n_e = n_p$, and filling factor $= 1$, we estimate the density n_e in the inner region to be 0.36 cm^{-3}. Then from the best-fit ionization parameter, τ is 2.6×10^{10} s $= 8.3 \times 10^2$ yr, roughly consistent with the age of SN 1006.

Even in the soft2 band profiles, the thermal component is not prominent (see Figure 6.5), which prevents us from conducting high quality study for the morphology of the thermal plasma. Nevertheless, we found that the profiles of thermal filaments are largely anti-symmetric. The scale width w_u^s is very sharp and comparable to w_u^h, whereas w_d^s shows a relatively large scale width. Although w_u^s couples with x_0, which is frozen to the best-fit value in the hard band (see Figure 6.8 (b)), we can say that the thermal shock has a very sharp rise in the upstream.

The downstream scale width w_d^s is comparable to the shock width derived from the Sedov solution of about 75 arcsec $= 0.8$ pc for SN 1006 having a 15 arcmin $= 9.5$ pc radius (Green, 2001). Therefore, the thermal filaments may trace the density profiles of the Sedov solution.

6.6.2 Non-Thermal Emission

We assume that the spatial distribution of non-thermal X-ray intensity coincides with that of the accelerated electrons to the maximum energy, while thermal X-rays trace the spatial profile of background plasma and hence magnetic field. For a steady state, there is no spatial structure of accelerated particles in the downstream (Blandford & Ostriker, 1978). However, one should consider the finite-time or energy-loss effect, which makes the spatial profile in the downstream region. For simplicity, we assume magnetic fields are spatially uniform both in the upstream and downstream at least in the nonthermal X-ray emitting region. Since the fraction of magnetic pressure to ram pressure is estimated as

$$\left(\frac{B^2}{8\pi}\right)/(m_H n u_s^2) \sim 2\times 10^{-5}\left(\frac{B}{10\ \mu\mathrm{G}}\right)^2 \quad , \tag{6.3}$$

where we assume the number density of thermal plasma $n \sim 1$ cm^{-3} and the shock velocity $u_s \sim 3\times 10^3$ km s^{-1}. The magnetic pressure does not affect the dynamics of SNR. We therefore can adopt the self-similar solution derived by Ratkiewicz et al. (1994). Our assumption of a spatially uniform magnetic field is a good approximation in the narrow range around the shock front.

First of all, we must compare three time scales; the age of the SNR (t_{age}), acceleration time scale (t_{acc}; see eq.(3.46)), and loss time scale (t_{loss}; see eq.(3.48)). The latter two scales depend on the magnetic field which accelerated electrons suffer. We estimated it ($< B >$) as

$$< B^2 >= \alpha B_u^2 + (1-\alpha)B_d^2 \equiv \chi B_d^2 \quad , \tag{6.4}$$

where $\alpha = \triangle t_u/(\triangle t_u + \triangle t_d)$ is the fraction of time in which accelerating electrons are in upstream. For the particles in the acceleration process, we can estimate that $\triangle t_u/\triangle t_d \sim f/(rg)$ from eqs.(3.42), (3.44). and (3.11). Then, we obtain χ as

$$\chi = \frac{f/R^2 + rg}{f + rg} \quad , \tag{6.5}$$

which ranges between 0 and 1.

Age-Limited Case

First, we investigate the case in which the acceleration time is nearly equal to the age of SN 1006, $t_{acc} \sim t_{age} \sim 10^3$ yrs. This condition implies that the observed non-thermal X-rays are emitted by electrons which are being accelerated now.

The particles in the diffusive shock acceleration process are transported to the upstream by diffusion, and are advected to the downstream at a the speed of u. The diffusion and advection time scales to move a scale length w are

$$t_{adv} \quad = \quad \frac{w}{u} \quad , \tag{6.6}$$

$$t_{dif} = \frac{w^2}{K} \quad . \tag{6.7}$$

In the upstream, the accelerated particles can reach up to the place at which the advection is balanced with the diffusion, i.e. $t_{adv} = t_{dif}$. Therefore, the observed width in upstream of non-thermal X-rays can be written as

$$w_u = \frac{K}{u_u} = \frac{E_{max}c}{3eB_d u_s} f(\xi_u, \theta) \quad . \tag{6.8}$$

In the downstream on the other hand, if the particles are advected too far from the shock front, they cannot return back to the upstream to get further energy. Therefore, the particles being accelerating should stay in the region where t_{dif} is smaller than t_{adv}. As a result, we obtain the same equation as the upstream case,

$$w_d = \frac{K}{u_d} = \frac{E_{max}c}{3eB_d u_s} r g(\xi_d, \theta) \quad . \tag{6.9}$$

Then, eq.(3.46) becomes

$$t_{acc} = \frac{3r}{r-1}\frac{w_u + w_d}{u_s} \sim 3.4 \times 10^2 \text{ yrs} \left(\frac{w_u + w_d}{0.25 \text{ pc}}\right). \tag{6.10}$$

Since t_{acc} is comparable to the age of the SN 1006, our assumption $t_{acc} \sim t_{age}$ is justified. Substituting E_{max} with eq.(6.1), we cam rewrite w_u and w_d as

$$w_u = 0.27 \text{ pc} \left(\frac{\nu_{rolloff}}{2.6 \times 10^{17} \text{ Hz}}\right)^{\frac{1}{2}} \left(\frac{B_d}{10\ \mu\text{G}}\right)^{-\frac{3}{2}} f(\xi_u, \theta) \quad , \tag{6.11}$$

$$w_u = 1.1 \text{ pc} \left(\frac{\nu_{rolloff}}{2.6 \times 10^{17} \text{ Hz}}\right)^{\frac{1}{2}} \left(\frac{B_d}{10\ \mu\text{G}}\right)^{-\frac{3}{2}} g(\xi_d, \theta) \quad , \tag{6.12}$$

respectively.

Let us vary observed quantities, w_u, w_d, and $\nu_{rolloff}$ in the range of observed uncertainty of 90% confidence level). We have six unknown parameters, E_{max}, B_u, B_d, ξ_u, ξ_d, and θ. Conditions (3.11), (6.1), (6.8), (6.9), and the equation $t_{acc} \leq t_{loss}$ are used to relate these quantities. One can derive from eqs.(6.8) and (6.9)

$$\frac{g}{f} = r^{-1}\frac{w_d}{w_u} \quad . \tag{6.13}$$

The condition $t_{acc} \leq t_{loss}$ gives an additional inequality. Substituting eqs.(3.37) and (3.38) into eq.(3.46), we derive

$$t_{acc} = 4\phi(f + rg)\frac{E_{max}c}{3eB_d u_s^2} \quad , \tag{6.14}$$

$$\phi \equiv \phi(r) = \frac{3}{4}\frac{r}{r-1} \quad . \tag{6.15}$$

Energy loss time scale, which should be compared with t_{acc}, is given by

$$t_{loss} = \frac{6\pi m_e^2 c^3}{\sigma_T E_{max} B_d^2} \frac{f + rg}{R^{-2} f + rg} \quad . \tag{6.16}$$

Using eq.(6.1), we can eliminate E_{max} and B_d, and obtain

$$R^{-2} f + rg \leq 4.8 \phi^{-1} \left(\frac{\nu_{rolloff}}{2.6 \times 10^{17} \text{ Hz}} \right)^{-1} \left(\frac{u_s}{2.89 \times 10^8 \text{ cm s}^{-1}} \right)^2 \quad . \tag{6.17}$$

The quantities f and g must satisfy eqs.(6.13) and (6.17).

The condition $t_{acc} \leq t_{loss}$ also gives the upper limit of B_d. In the age limited case, we can derive χ as

$$\chi = \frac{R^{-2} w_u + w_d}{w_u + w_d} \quad . \tag{6.18}$$

Then, using eqs.(3.48) and (6.12), B_d is estimated as

$$B_d \leq 30 \ \mu\text{G} \ \phi^{-\frac{2}{3}} \left(\frac{\nu_{rolloff}}{2.6 \times 10^{17} \text{ Hz}} \right)^{-\frac{1}{3}} \left(\frac{w_u R^{-2} + w_d}{0.25 \text{ pc}} \right)^{-\frac{2}{3}} \left(\frac{u_s}{2.89 \times 10^8 \text{ cm s}^{-1}} \right)^{\frac{2}{3}} \quad , \tag{6.19}$$

where we eliminate E_{max} with eq.(6.1).

Figure 6.9 shows allowed regions for fixed θ. When we fix $\theta = 0$, the case of $\xi_u = \xi_d = 1$ (Bohm limit in both upstream and downstream) is marginally acceptable, since ξ should satisfy $1 \leq c/u_s \sim 10^2$ (Jokipii, 1987). Then the magnetic field has a value of $B_u = B_d$ =20–78 μG. The eq.(6.19) shows that the maximum value of the magnetic field is achieved when observed quantities $\nu_{rolloff}$, w_u, and w_d have minimum values. On the other hand, small magnetic fields are possible when $\theta > 85°$. If we choose $w_u = 0.1$ pc, $w_d = 0.3$ pc, and $\nu_{rolloff} = 2 \times 10^{17}$ Hz, the $\xi_u \sim 10$ and $\xi_d \sim 1$, the magnetic fields are $B_d \sim 4 B_u$ ~14–20 μG.

The allowed region for E_{max} and B_d can be determined with eqs.(6.1) and (6.9) as

$$E_{max} = 41 \text{ TeV} \left(\frac{r}{4} \right)^{-\frac{1}{3}} \left(\frac{\nu_{rolloff}}{2.6 \times 10^{17} \text{ Hz}} \right)^{\frac{1}{3}} \left(\frac{g^{-1} w_d}{0.2 \ pc} \right)^{\frac{1}{3}} \left(\frac{u_s}{2.89 \times 10^8 \text{ cm s}^{-1}} \right)^{\frac{1}{3}} \quad , \tag{6.20}$$

$$B_d = 31 \ \mu\text{G} \left(\frac{r}{4} \right)^{\frac{2}{3}} \left(\frac{\nu_{rolloff}}{2.6 \times 10^{17} \text{ Hz}} \right)^{\frac{1}{3}} \left(\frac{g^{-1} w_d}{0.2 \ pc} \right)^{-\frac{2}{3}} \left(\frac{u_s}{2.89 \times 10^8 \text{ cm s}^{-1}} \right)^{-\frac{2}{3}} \quad , \tag{6.21}$$

respectively. Figure 6.10 represents the allowed region of E_{max} and B_d from eqs.(6.20) and (6.21). The allowed E_{max} is 22–69 TeV.

Energy Loss Limited Case

If the maximum energy of accelerated electrons E_{max} is determined by

$$t_{acc} = t_{loss} \quad , \tag{6.22}$$

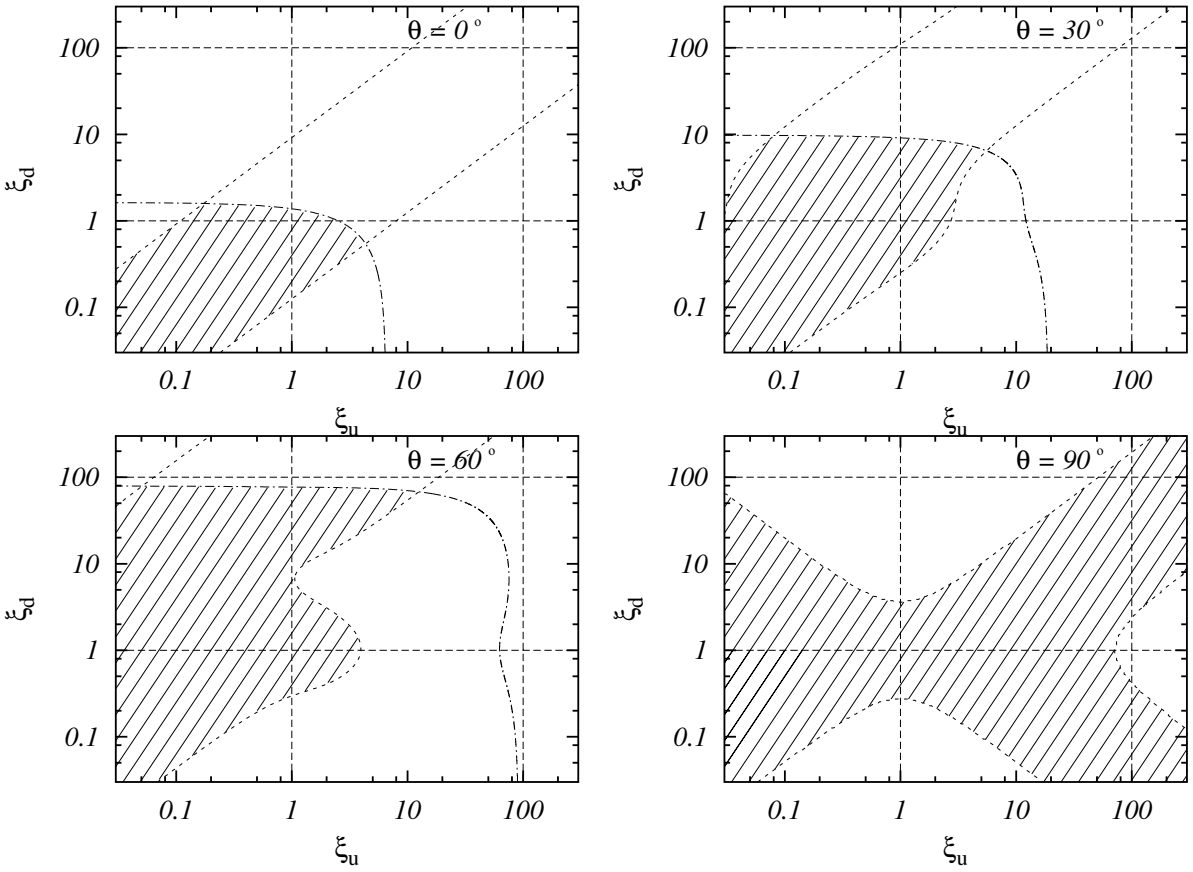

Fig. 6.9.— The allowed region for ξ_u and ξ_d for fixed θ in the age limited case (shaded regions). The region between dotted lines satisfy eq.(6.13) with $0.6 \leq w_d/w_u \leq 40$, whereas those under the dot-dashed one eq.(6.17) with $\nu_{rolloff} \geq 1.9 \times 10^{17}$ Hz. This figure is credited by Yamazaki et al. (2003).

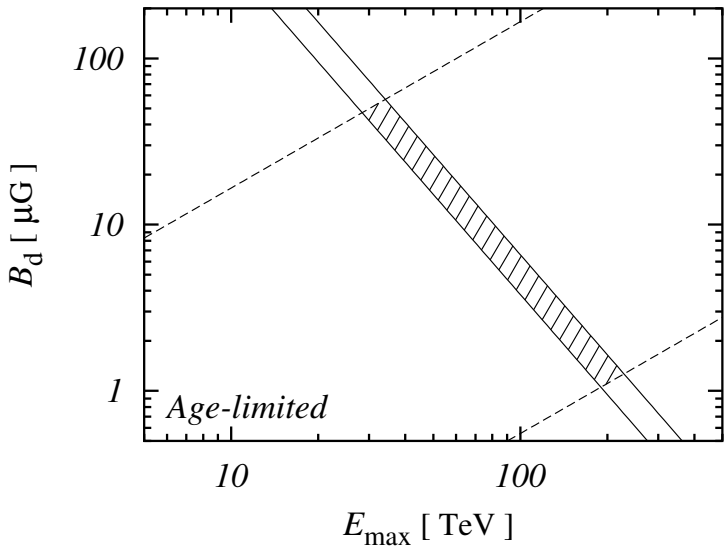

Fig. 6.10.— The allowed region for E_{max} and B_d in the age limited case (shaded area). The restriction from $\nu_{rolloff}$ (see eq.(6.1)) is between the two solid lines, whereas that from w_d and ξ_d (related with r_g) is between the two dashed lines. This figure is credited by Yamazaki et al. (2003).

the motion of accelerated particles toward the upstream might be obstructed by the energy loss effect as well as the advection. Let us consider the energy loss time scale t_{cool}, which is compared with t_{adv} or t_{dif}. When $t_{dif} = t_{adv} < t_{cool}$, the observed width of non-thermal X-rays in the upstream is given by $w_u = K_u/u_u$ as well as the age limited case, whereas in the case of $t_{dif} = t_{cool} < t_{adv}$, w_u is given by $w_u = (K_u t_{cool})^{\frac{1}{2}}$. Therefore, we can write w_u as

$$w_u = \min\left\{\frac{K_u}{u_u},\ (K_u t_{cool})^{\frac{1}{2}}\right\} \quad . \tag{6.23}$$

On the other hand, the observed scale length in downstream is determined the relation between the advection and diffusion as

$$w_d = \max\left\{u_d t_{cool},\ (K_d t_{cool})^{\frac{1}{2}}\right\} \quad . \tag{6.24}$$

We have five equations, (3.11), (6.1), (6.22), (6.23), and (6.24), for six unknown parameters E_{max}, B_u, B_d, ξ_u, ξ_d, and θ, and can solve these equations with fixed θ under the condition $t_{loss} < t_{age}$. Note that for our parameters, w_u and w_d are given by

$$w_u = \frac{K_u}{u_s} \quad , \tag{6.25}$$

$$w_d = u_d t_{cool} \quad , \tag{6.26}$$

as shown the detailed estimation in §A.2. E_{max} and B_d can be calculated from eq.(6.1) and (6.26)

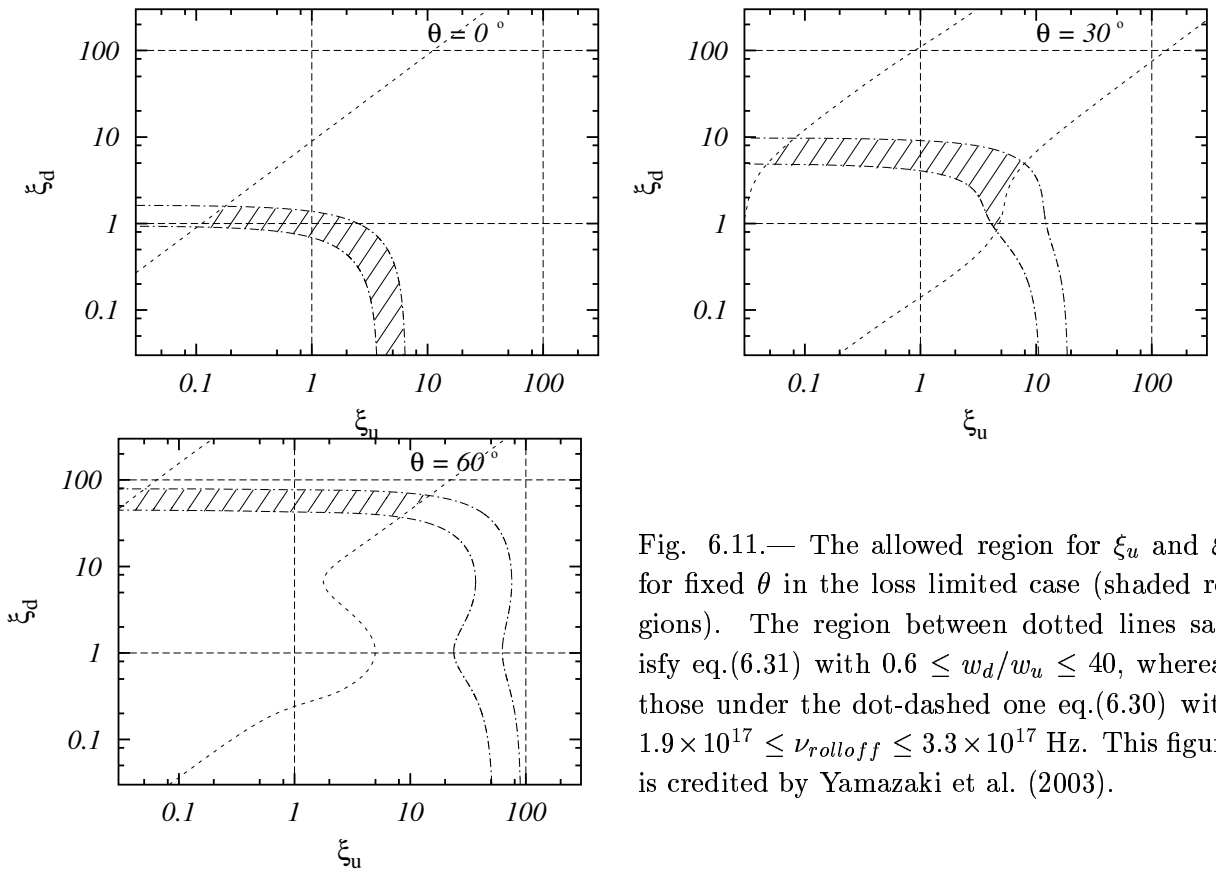

Fig. 6.11.— The allowed region for ξ_u and ξ_d for fixed θ in the loss limited case (shaded regions). The region between dotted lines satisfy eq.(6.31) with $0.6 \leq w_d/w_u \leq 40$, whereas those under the dot-dashed one eq.(6.30) with $1.9 \times 10^{17} \leq \nu_{rolloff} \leq 3.3 \times 10^{17}$ Hz. This figure is credited by Yamazaki et al. (2003).

as

$$E_{max} = 39 \text{ TeV} \left(\frac{r}{4}\right)^{\frac{1}{3}} \left(\frac{\nu_{rolloff}}{2.6 \times 10^{17} \text{ Hz}}\right)^{\frac{2}{3}} \left(\frac{w_d}{0.2\ pc}\right)^{\frac{1}{3}} \left(\frac{u_s}{2.89 \times 10^8 \text{ cm s}^{-1}}\right)^{-\frac{1}{3}} , \quad (6.27)$$

$$B_d = 35\ \mu\text{G} \left(\frac{r}{4}\right)^{\frac{1}{3}} \left(\frac{\nu_{rolloff}}{2.6 \times 10^{17} \text{ Hz}}\right)^{-\frac{1}{3}} q \left(\frac{w_d}{0.2\ pc}\right)^{-\frac{2}{3}} \left(\frac{u_s}{2.89 \times 10^8 \text{ cm s}^{-1}}\right)^{\frac{2}{3}} . \quad (6.28)$$

Then, from eq.(3.37) and (6.25), we derive

$$f = 4.8 \frac{w_u}{w_d} \left(\frac{r}{4}\right)^{-1} \left(\frac{\nu_{rolloff}}{2.6 \times 10^{17} \text{ Hz}}\right)^{-1} \left(\frac{u_s}{2.89 \times 10^8 \text{ cm s}^{-1}}\right)^{2} . \quad (6.29)$$

The condition $t_{acc} = t_{loss}$ gives

$$R^{-2} f + rg = 4.8 \phi^{-1} \left(\frac{\nu_{rolloff}}{2.6 \times 10^{17} \text{ Hz}}\right)^{-1} \left(\frac{u_s}{2.89 \times 10^8 \text{ cm s}^{-1}}\right)^{2} . \quad (6.30)$$

Eliminating $\nu_{rolloff}$ from eqs.(6.29) and (6.29), we derive

$$\frac{g}{f} = \frac{1}{4} \left[\phi^{-} 1 \frac{w_d}{w_u} - \left(\frac{r}{4}\right)^{-1} R^{-2} \right] . \quad (6.31)$$

Equation (6.30) and (6.29) determine the (f, g).

Figure 6.11 shows the results for individual θ. When $\theta = 0°$, the case of $\xi_u = \xi_d = 1$ is acceptable again. Then, the magnetic field is in the range of $B_u = B_d = 23 - 85\ \mu$G. However, when θ becomes larger than $\sim 35°$, then $\xi_d \geq 10$ and $\xi_u \leq 10$. This implies that the magnetic field in upstream is more turbulent than that in downstream, which seems to be quite unrealistic. Therefore, we concluded that the allowed θ in loss limited case is $\leq 35°$. The allowed region for E_{max} is 26–54 TeV.

Since E_{max} and B_d are given by eqs.(6.27) and (6.28), the allowed region for them in the loss limited case is the shaded region in Figure 6.12.

6.6.3 Injection Efficiency

In this subsection, we estimate the injection efficiency defined as $\eta \equiv \frac{n_e^{NT}}{n_e^T}$, where n_e^{NT} and n_e^T are the number densities of non-thermal and thermal electrons in the filaments, under the assumption of the age limited case with parallel magnetic field. The depth of the filament (sheet-like) is assumed to be 1 pc, with uniform electron density.

The non-thermal electron flux (energy) are estimated using eq.(3.27), where the non-thermal X-ray flux and spectra of each filament are taken from Table 6.2 and Table 6.3. We adopt the minimum energy of non-thermal electrons (injection energy) E_{min} to be 0.24 keV (the temperature of the thermal plasma; see Table 6.1). The magnetic field and the maximum energy are unknown

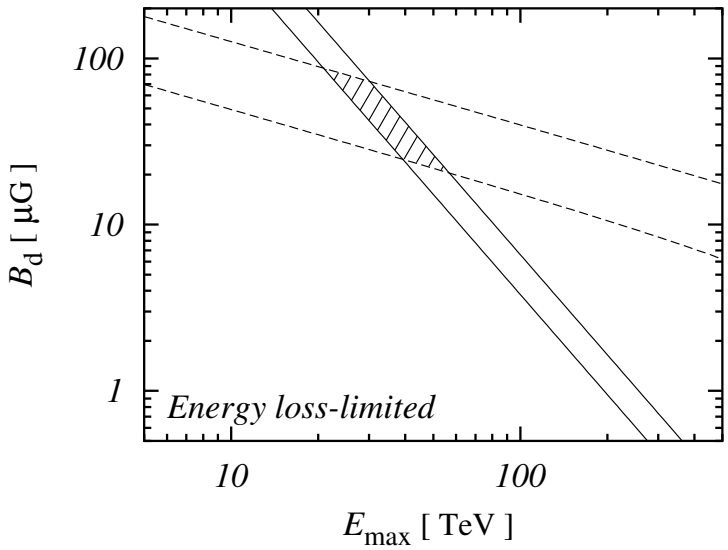

Fig. 6.12.— The allowed region for E_{max} and B_d in the loss limited case (shaded area). The restriction from $\nu_{rolloff}$ (see eq.(6.1)) is between the two solid lines, whereas that from w_d and ξ_d (related with r_g and advection) is between the two dashed lines. This figure is credited by Yamazaki et al. (2003).

parameters, nevertheless we can suggest that the magnetic field in downstream is significantly larger than that in upstream. In this subsection, we adopt the magnetic field B to be perpendicular to the shock normal, $B_d = 4B_u = 40$ μG arbitrary and the maximum energy E_{max} to be 37 TeV. The derived number density (n_e^{NT}), the total number (N_e^{NT}), and the total energy (E_e^{NT}) of non-thermal electrons in each filament are summarized in Table 6.4.

For the estimation of thermal electron flux (energy), we adopted the projected profile of the thermal X-rays (the soft2 band) given in Table 6.2 and the spectral parameters of thermal plasma given in Table 6.3. The resultant number density (n_e^T), total number (N_e^T), and total energy (E_e^T) of thermal electrons in each filament are given in Table 6.4. The injection efficiency η ($\equiv \frac{n_e^{NT}}{n_e^T}$) is then obtained as is shown in Table 6.4. All the values η are nearly identical in each filament of $\sim 1 \times 10^{-3}$ but are about 2 times larger than 5×10^{-4} derived from the *ASCA* data by Allen et al. (2001), although they also assumed as $B_{\rm d} = 40$ μG arbitrary.

For comparison, we estimate η with larger magnetic field of $B_{\rm d} = 40$ μG, and find a larger η than Allen et al. (2001). They estimated the number density of non-thermal electrons from larger regions than the filaments, because *ASCA* could not resolve the filaments. On the other hand, we found that the non-thermal electrons are confined in the thin filaments, which are the sites of ongoing acceleration of the non-thermal electrons. We thus regard that the present *Chandra* result suggests that the injection occurs more locally and more efficiently and as a result, it must be more realistic estimation of η than that by Allen et al. (2001). Under the assumption of larger magnetic

field, as suggested by (Lucek & Bell, 2000) and so on, the injection efficiency becomes lower since accelerated electrons can emit synchrotron X-rays more efficiently.

The energy densities of the magnetic field, the thermal plasma, and the non-thermal electrons in the filaments are 6.4×10^{-11} ergs cm^{-3}, 2.6×10^{-10} ergs cm^{-3}, and 6.9×10^{-11} ergs cm^{-3}, respectively. Thus, at the shocked region, the magnetic field and non-thermal electrons are in energy equi-partition and are slightly smaller than the thermal energy (about 30%).

Table 6.4: Number densities and energies of thermal and non-thermal electrons, and injection efficiencies.

Filament No.	1	2	3	4	5	6	Total
Thermal electrons							
$E.M.$ [cm^{-3}]	7.0×10^{53}	1.0×10^{54}	1.3×10^{53}	2.5×10^{53}	1.3×10^{53}	8.4×10^{53}	3.1×10^{54}
Density (n_e^T)^a [cm^{-3}] .	0.43	0.51	0.26	0.41	0.30	0.60	0.45
Total number (N_e^T) ...	1.6×10^{54}	2.1×10^{54}	5.0×10^{53}	6.1×10^{53}	4.3×10^{53}	1.4×10^{54}	6.8×10^{54}
Energy (E_e^T)^b [ergs] ...	9.2×10^{44}	1.2×10^{45}	2.8×10^{44}	3.5×10^{44}	2.4×10^{44}	7.9×10^{44}	3.9×10^{45}
Non-thermal electrons^c							
Density (n_e^{NT})^a [cm^{-3}]	4.7×10^{-4}	5.5×10^{-4}	7.9×10^{-4}	7.1×10^{-4}	6.5×10^{-4}	7.6×10^{-4}	6.2×10^{-4}
Total number (N_e^{NT})..	1.8×10^{51}	2.2×10^{51}	1.5×10^{51}	1.1×10^{51}	9.4×10^{50}	1.8×10^{51}	9.3×10^{51}
Energy (E_e^{NT}) [ergs] ..	2.0×10^{44}	2.4×10^{44}	1.7×10^{44}	1.2×10^{44}	1.1×10^{44}	2.0×10^{44}	1.0×10^{45}
Injection efficiency (η^d)..	1.1×10^{-3}	1.1×10^{-3}	3.0×10^{-3}	1.7×10^{-3}	2.2×10^{-3}	1.3×10^{-3}	1.4×10^{-3}

^{a}: We assumed that the depth of the emitting volume is 1 pc and that the filling factor = 1.
^{b}: $E_e^T = \frac{3}{2} n_e V^{NT} kT$.
^{c}: Integration from $E_{\rm min} = 0.24$ keV to $E_{\rm max} = 37$ TeV (see text).
^{d}; $\eta \equiv \frac{n_e^{NT}}{n_e^T}$ (see text).

6.6.4 Summary for SN 1006

We estimated E_{max} and B_d both in age limited case and loss limited case. When a magnetic field is nearly parallel to the shock normal, ξ_u and ξ_d should be nearly unity, which imply that the magnetic field is highly turbulent (near the Bohm limit), and $B_u \sim B_d$ is in the range of 20–85 μG, which seems to be higher than usual interstellar magnetic field of a few μG. However, Lucek & Bell (2000) pointed out a mechanism which may able to amplify the parallel magnetic field. Relatively strong parallel magnetic fields are considered by several authors (Berezhko et al., 2002; Ellison, Berezhko, & Baring, 2000). These situations can be realized both in the age limited and loss limited cases.

Consider the case which the magnetic field is nearly perpendicular to the shock normal. The allowed magnetic field range is $B_d = 4B_u$ =14–20 μG, which is relatively smaller than those in the case of parallel magnetic field. This is consistent value with the interstellar magnetic field and assumed valued in many papers (Reynolds, 1998; Allen et al., 2001; Bamba et al., 2003b) but slightly larger than that derived by CANGAROO observations (Tanimori et al., 1998, 2001), which assumed that TeV γ-rays are emitted by the inverse Compton process. This discrepancy may be solved if the filaments 1–6 are not the main sites of TeV γ-rays generated by the leptonic process,

The observed flux of TeV γ-rays which are up-scattered CMB photons by synchrotron emitting electrons is written as

$$\mathcal{F}_{IC} = 2.5 \times 10^{-2} \left(\frac{B_d}{20\ \mu\mathrm{G}} \right)^{-2} \mathcal{F}_{synch} \quad , \tag{6.32}$$

where $\mathcal{F}_{synch}$ is the observed flux of synchrotron X-rays and estimated as 1.8×10^{-12} ergs s^{-1}cm^{-2} in the 0.5–10.0 keV band (see Table 6.3). Then, the contribution of the IC γ-rays generated in these six filaments is only $\sim 0.5\%$ of the whole flux coming from SN 1006 north-eastern shell. This shows that the IC γ-ray emitting sites have smaller magnetic field, hence radiate less synchrotron X-rays than in the filaments. Or, instead, the TeV γ-rays might be emitted by the hadronic process. In fact the most plausible position of the γ-ray emission determined by CANGAROO is located north of the filament 1 (Tanimori et al., 1998, 2001). However, the region where the significance is higher than half the maximum value extends over $\sim 0.2^\circ$, which is almost the same as the standard deviation of the point spread function of the CANGAROO telescope. We need stereoscopic observations of TeV γ-ray emissions by atmospheric Cherenkov telescopes (for example, CANGAROO-III, HEGRA, and H.E.S.S.) to establish the position and extent of the emission region.

6.7 Remaining Problems and Future Works for SN 1006

6.7.1 Considering the Projection Effect

Berezhko et al. (2003) suggests that we must consider the projection effect, which makes the real scale lengths smaller. With very small scale lengths of $w_u = 0.08$ pc and $w_d = 0.03$ pc as shown in the left panel of Figure 6.13, they calculated the projection effect under the assumption that the shock is exactly circular. Their result is well fitted with the observational data of filament No.4 as shown in the right panel of Figure 6.13. They also claim that the photons in w_u we measured do not come from "real" upstream, but from downstream. We checked the projection effect for the filament with real $w_u = 0.07$ pc and $w_d = 0.15$ pc, and found that it can produce the filament No.4 as shown in Figure 6.14. Although this is an important effect we must consider, there is large uncertainties, for example, the uncertainty which direction the shocks run and whether it is true or not the curvature of the filaments is determined by the SNR radius. In fact, the filament No.4 Berezhko et al. (2003) argued is apparently straight and the direction of the shock is not same as that of the radius as shown in Figure 6.3. Moreover, Long et al. (2003) reported that the peak position of the filaments located on the north-eastern region in the radio and X-ray bands are perfectly same, which has some discrepancy that these feature are made by projection effect. Therefore, we concluded that it is too difficult to solve and gave up considering it in this paper.

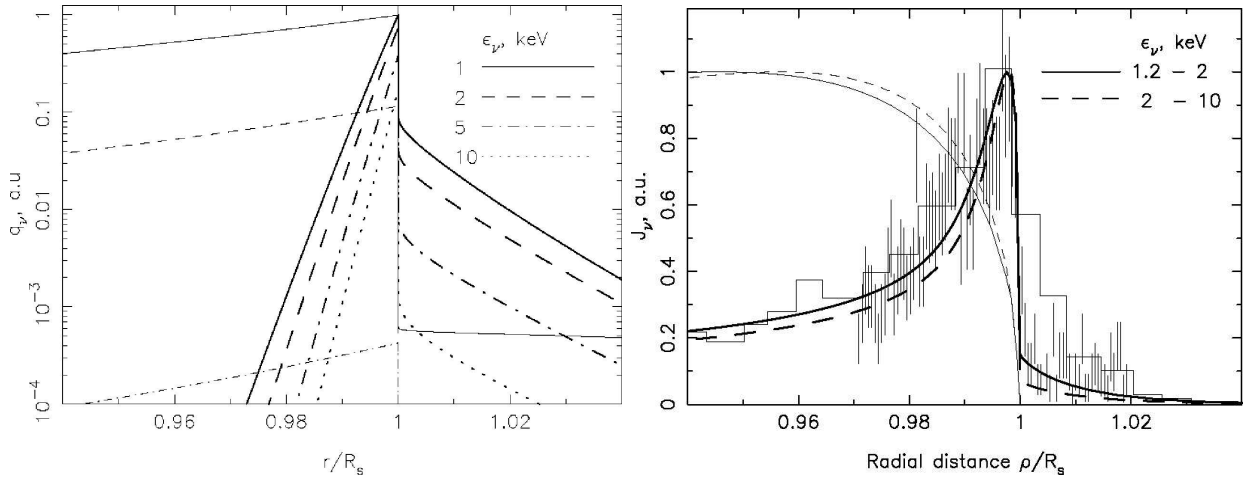

Fig. 6.13.— Left: Radial dependence of the X-ray emissivity at different X-ray energies. Thick and thin lines correspond to the efficient and the so-called inefficient model respectively. Right: Projected radial dependence of the X-ray brightness in the 1.2 to 2 keV (solid) and 2 to 10 keV (dashed) X-ray energy interval. Thick and thin lines correspond to the efficient and the so-called inefficient model respectively. The *Chandra data*, corresponding to the sharpest profile, are shown by the histogram (Long et al., 2003) and the vertical dashes (Bamba et al., 2003b). These figures are credited by (Berezhko et al., 2003).

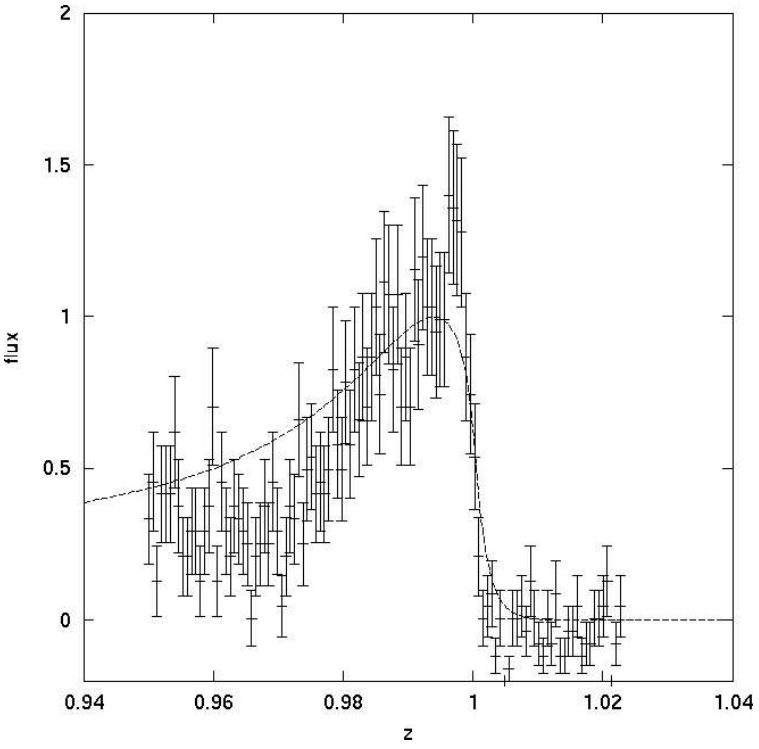

Fig. 6.14.— Profiles with the calculated model (solid line) considered the projection effect. The horizontal axis z represents r/R.

6.7.2 Considering the Profile Shapes in Downstream

We used the exponential model of eq.(6.2) empirically for the fittings of the filaments. It is exactly correct for upstream, but there is some doubt for downstream. For example, the downstream profile must be constant when the system is time independent (e.g.. Blandford & Eichler, 1987). In the case that the profile is determined by the diffusion, it must follow a Gaussian function. The former is not in the present case clearly, then we checked only the latter case with the function;

$$f(x) = \begin{cases} A_u \exp\left(-\left|\frac{x_0-x}{w_u}\right|\right) & \text{in upstream} \\ A_d \exp\left(-\left(\frac{x_0-x}{w_d}\right)^2\right) & \text{in downstream} \quad . \end{cases} \tag{6.33}$$

We could fit the profile of filament No.4 with eq.(6.33) with the best fit values of

$$w_u = 0.78\ (0.52 - 1.24)\ \text{[arcsec]}\ , \tag{6.34}$$

$$w_d = 13.5\ (12.4 - -15.1)\ \text{[arcsec]}\ , \tag{6.35}$$

$$\text{reduced } \chi^2 = 66.6/74\ . \tag{6.36}$$

Figure 6.15 shows the best-fit model of eq.(6.33) with the best-fit parameters. We can not distinguish statically which is the better fitting with eq.(6.2) or eq.(6.33). Since the best-fit values of w_d does not change dramatically, our discussion with simple model eq.(6.2) only is not so bad.

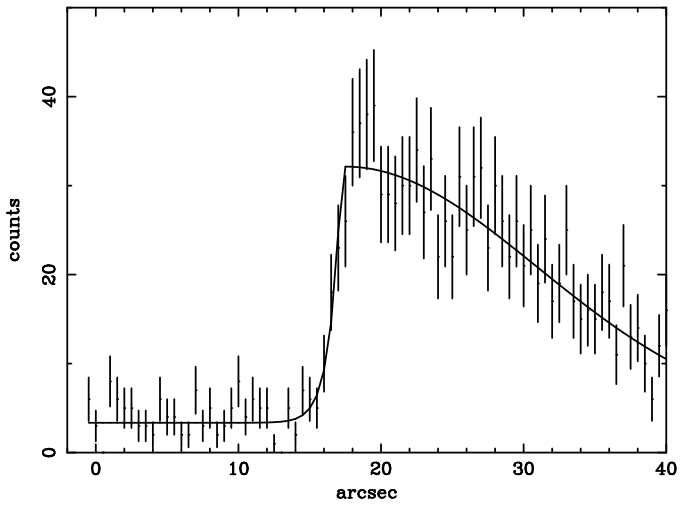

Fig. 6.15.— Same as (4) of Figure 6.5, but the best fit model in solid line is from eq.(6.33), instead of eq.(6.2).

6.7.3 Considering the Injection Efficiency

Bamba et al. (2003b) calculated the injection efficiency in the age-limited case and suggested that there is much more efficient injection than those calculated by previous observation (Allen et al.,

2001; Dyer et al., 2001). In this thesis, we did not consider the injection efficiency because the calculation in the loss-limited case is rather difficult.

The next breakthrough for the injection efficiency must be bring by *ASTRO-E II*, which must bring us much information about properties of thermal X-rays and maybe injection efficiency. The efficient injection translate the kinetic and thermal energy of the SNR into cosmic rays, and as a result, the shock speed and temperature of the plasma down, and the ionization timescale grows larger. Decourchelle, Ellison, & Ballet (2000) calculated these influences in the situation of efficient (non-linear) cosmic acceleration, and reported their calculation in the Kepler case, that non-linear effects from efficient particle acceleration strongly influence the X-ray emission in SNRs and may serve as a tracer of cosmic-ray acceleration. To determine the ion and electron temperature in north eastern shell and north western shell (for comparing), we will be able to measure the injection efficiency directly for the first time.

Another measurement method is proposed by Tatischeff, Ramaty, & Kozlovsky (1998), who attend to the accelerated ions. The K emission lines from accelerated ions up to $\sim MeV$ such as oxygen broaden, maybe in the order of ~ 60 eV (Tatischeff et al., 1998). *ASTRO-E II* may be able to detect the line broadening, which is the first detections of high energy ions.

Chapter 7

Analyses of Other SNRs

In the previous chapter, we developed a new estimation method of the maximum energy of accelerated electrons and magnetic field configurations, using the spatial distribution and spectral information of non-thermal X-rays, in the case of a prototype SNR with non-thermal X-rays, SN 1006. In this chapter, we apply the method discussed the previous chapter to other SNRs.

7.1 Cas A

7.1.1 Previous Observations

Cas A is one of the brightest sources in the radio band (especially in 100–1000 MHz), then has been studied both theoretically and observationally by many astrophysical scientists; the number of papers about Cas A is more than 400.

The remnant's precise age is still uncertain. From proper motion studies for ~ 100 of Cas A's optical knots (Kamper & van den Bergh, 1976; van den Bergh & Kamper, 1983), the year of the explosion was estimated to be AD 1658 ± 3. There are no unambiguous historical observations of a bright nova or variable star in Cassiopeia that might be associated with a late 17th century supernova. However, on 1680 August 16, Flemsteed (1725) reported an appearance of a 5–6th magnitude star which he designated "supra τ" and later renamed 3 Cassiopeia in his catalog (Ashworth, 1980). Its proximity to Cas A, together with the fact that he never observed this star again, raises the possibility that he sighted the Cas A supernova in the summer of 1680. In this paper, we adopt AD 1680 as the birth date of Cas A as many papers have adopted. The distance to the remnant is determined as $3.4^{+0.3}_{-0.1}$ kpc using optical expansion plus proper motions (Reed et al., 1995). The equipartition argument to explain the radio luminosity implies magnetic fields of $B \sim$0.4–2.0 mG (Longair, 1994; Wright et al., 1999). The average radio index of the remnant is 0.78 (Green, 2001).

Thermal X-ray emission from Cas A is very well studied by many people. With fine spectroscopy by *ASCA* in the hard X-ray band, Holt et al. (1994) detected more than 10 emission lines from highly ionized ions. The emission line intensity is different from place to place, indicating that the ejecta from the progenitor still remain as unmixed knots. The high abundances from light elements (Mg, Si, S, and so on) corresponds to the fact that the progenitor of Cas A is type Ib. It also support the Ib origin that the discovery of a point source located at the center of the remnant (Hughes et al., 2000), although it is still uncertain that the source is the stellar remnant of Cas A or not, because pulsating signal have been not yet discovered (e.g., McLaughlin et al., 2001; Chakrabarty et al., 2001; Murray et al., 2002). The fine spatial resolution of *Chandra* unveils the small scale structures in Cas A. The bulk Doppler velocity is measured to be 2000–3000 km s^{-1} (Hwang et al., 2001) with the complex X-ray patterns similar to the optical images. Later, Willingale et al. (2002) calculated the shock velocity 4000 ± 500 km s^{-1} using *XMM-Newton* data. Hwang et al. (2001) also suggested that the heavier elements, Fe and so on, are more concentrated in the inner region than lighter ones, Si and so on. This fact implies that the elements in SNRs are not mixed for a long time. There is a reverse shock, which is bright in thermal X-rays (Gotthelf et al., 2001).

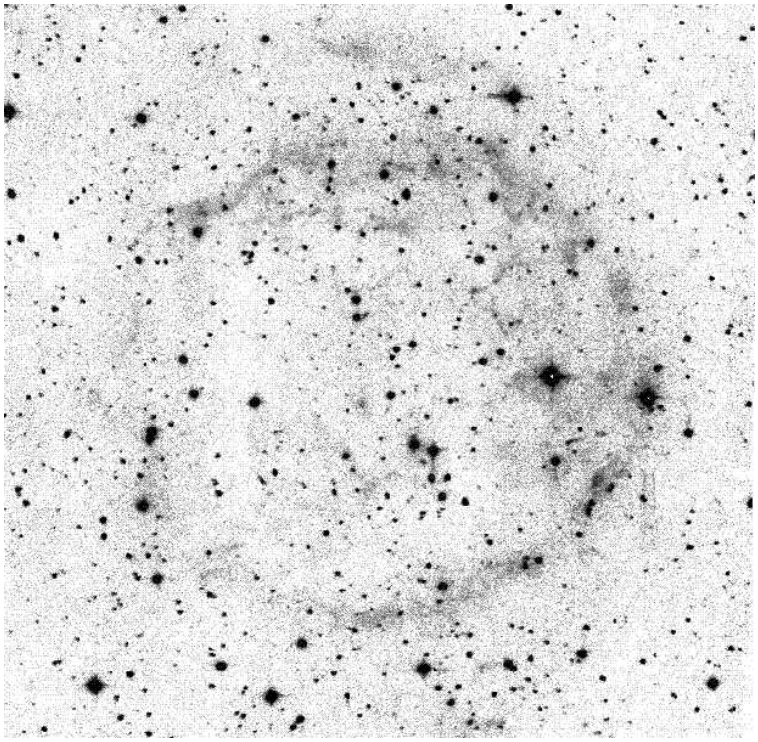

Fig. 7.1.— K_s-band image of Cas A (Rho et al., 2003).

The evidence of high energy electrons are discovered as the wide band non-thermal emissions. Rho et al. (2003) discovered synchrotron radiation in the near-infrared using Two Micron All-Sky

Survey (2MASS) and Palomar 200 inch (5.1 m) PFIRCAM observations. The hard X-ray emission was detected up to greater than 10 keV with *RXTE* (Allen et al., 1997) and *Beppo*SAX (Favata et al., 1997), and up to 100 keV with OSSE on the *GRO* (The et al., 1996). Recently, a 5σ detection of Cas A has been reported at gamma-ray energies above 1 TeV with the HEGRA Stereoscopic Cerenkov Telescope System (Aharonian et al., 2001a). The emission could be due to leptonic processes (non-thermal bremsstrahlung or inverse-Compton up-scattering of CMB) or hadronic (π^0 decay). The EGRET limits on emission above 100 MeV (Esposito et al., 1996) can be used to put a lower limit on the magnetic field strength of at least 0.4 mG (Atoyan et al., 2000); if the field were weaker, the required relativistic electron density would have to be higher to explain the radio emission, and those electrons would emit non-thermal bremsstrahlung at levels higher than the upper limit in the EGRET band. Thus, Cas A seems to have a much larger magnetic field than those inferred for other remnants. Vink & Laming (2003) calculated the magnetic field and the maximum energy of electrons to be 0.08–0.16 mG and 57–40 TeV, using non-thermal filaments with analyses similar to ours in SN 1006.

7.1.2 *Chandra* Observation

We used the *Chandra* archival data of the ACIS-S on Cas A (Observation ID = 00114) observed on January 30 – 31, 2000 with the targeted position at (R.A., Decl.) = ($23^{\rm h}23^{\rm m}40\overset{\rm s}{.}2$, $58^{\rm d}47^{\rm m}34\overset{\rm s}{.}1$). The south-eastern side of Cas A is located at the aimpoint in CCD chip S3. Data acquisition from the ACIS was made in the Timed-Exposure Graded mode. The data reductions and analyses were made using the *Chandra* Interactive Analysis of Observations (CIAO) software version 2.3. The effective exposure was ~ 50 ks for the observation.

7.1.3 Entire Images in the X-Ray Band

Figure 7.2 shows the *Chandra* images in the soft and hard X-ray bands (see also Figure C.1). There are many structures in both bands; a central point source, a blow-out on the north-eastern side, dim forward shocks and bright reverse shocks, and many knotty and/or filamentary structures, which have been already reported by previous papers (e.g., Hughes et al., 2000; Gotthelf et al., 2001; Hwang et al., 2001). Vink & Laming (2003) reported that a filament located on the north-eastern side has a non-thermal spectrum. In this paper. we omit the spectral and spatial analyses for many knots and concentrate on the analyses of non-thermal filaments in the same way with the previous chapter.

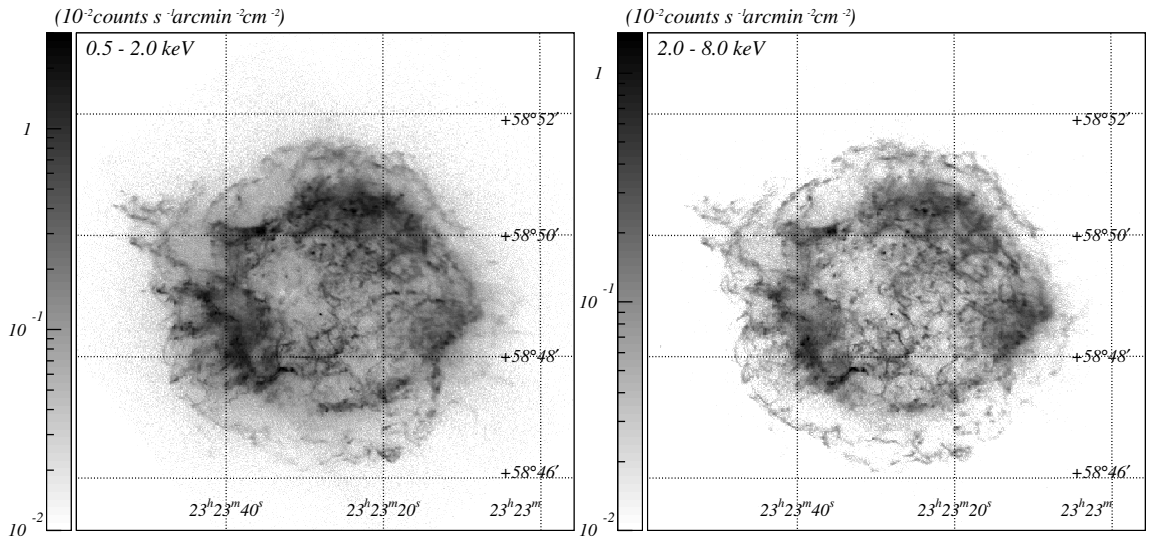

Fig. 7.2.— *Chandra* images of Cas A in 0.5–2.0 keV band (left) and 2.0–8.0 keV band (right) with J2000 coordinates. The scales in both images are in logarithmic.

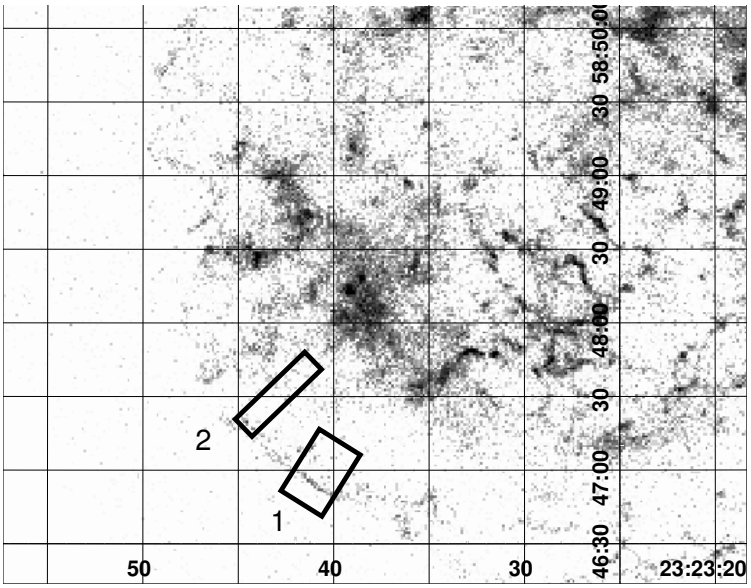

Fig. 7.3.— Close-up view of south-eastern region of Cas A in the 5.0–10.0 keV band. Grayscale is in logarithmic. The filament regions for spatial analyses (No.1 and 2) are also shown in solid lines.

7.1.4 Analyses of the Filaments

Analyses of Profiles

We made the hard X-ray image (5.0–10.0 keV), and selected filaments, which are bright in the image and relatively straight without contaminations of other structures, in order to make profiles. Since the aimpoint is on the south-eastern part of the SNR, we avoided selecting filaments located on north western region (see the previous subsection). In order to make profiles with pure non-thermal X-rays, we compared the Si line intensities in the filaments and just downstream of them. As a result, the X-ray photons in the 5.0–10.0 keV band include only less than 25% of thermal X-rays, even we assumed that the all of photons just downstream of the filament is thermal, which were used for the spatial analyses of the filaments. Figure 7.3 shows the 5.0–10.0 keV band images with the regions we used for analyses of filament (filament 1 and 2). Figure 7.4 shows the profiles of the filaments. In both figures, very sharp profiles can be seen both in the upstream and in the downstream. We fitted the profiles with eq.(6.2) in the similar way to the SN 1006 case. Best-fit models and parameters are shown in Figure 7.4 and Table 7.1, respectively.

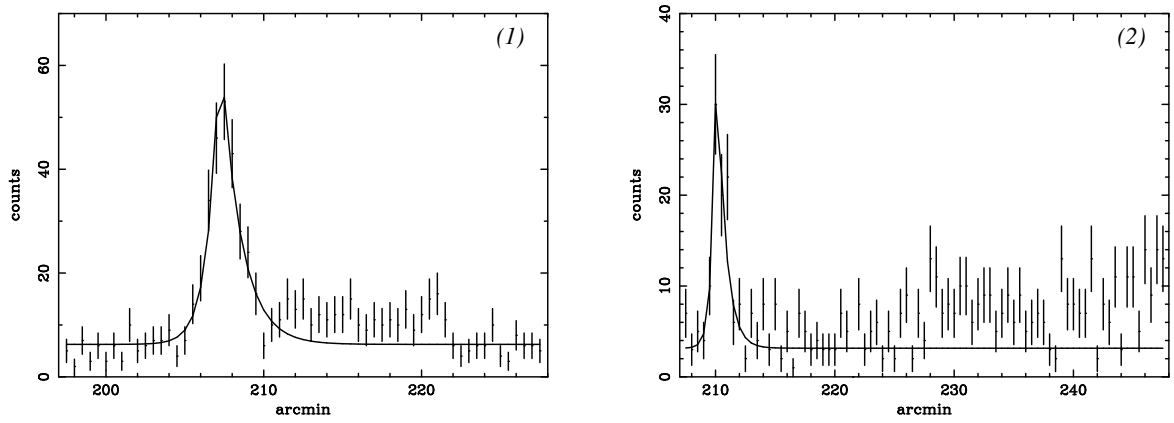

Fig. 7.4.— The profiles in the filaments in Cas A in the 5.0–10.0 keV band, binned with 0.5 arcsec. The best-fit models (see Table 7.4 are also shown with solid lines. Note that fittings were carried out in a part around the shock front. Upstream is to the left and downstream is to the right in both images. Typical PSF width is same as a data point.

Spectral Analyses

We made spectra of these filaments. The background regions were selected from source free regions in downstream. The both spectra were very hard as shown in Figure 7.5, and well fitted with both a power-law model and *nei* model with an absorption. The best-fit models and parameters are

Table 7.1: Best-fit parameters of the profiles of the filaments.[a]

No.	A [counts arcsec^{-1}]	w_u [arcsec]	w_d [arcsec]	Reduced χ^2 [χ^2/d.o.f.]
1	59 (46–72)	0.72 (0.55–0.93)	1.27 (0.96–1.81)	99.7/61
2	34 (24–49)	0.35 (0.18–0.57)	0.71 (0.45–1.59)	27.3/26

[a]: Parentheses indicate single-parameter 90% confidence regions.

shown in Figure 7.5 and Table 7.2, respectively.

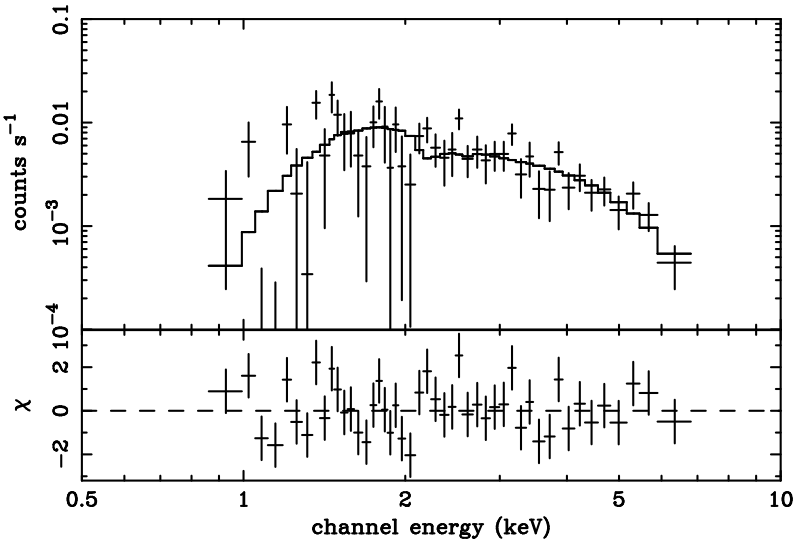

Fig. 7.5.— Upper: Integrated spectrum of the filaments. Best-fit power-law model is shown with solid line (see Table 7.2). Lower: Residuals from the best-fit model.

7.1.5 Discussion for Cas A

The spectra of the filaments is very hard as shown in Table 7.2. It is hard to think that the origin of the emission is thermal, because the best-fit temperature is too high. Sub-solar abundance of the best-fit model is also unnatural for thermal emission in SNRs. Therefore, we treat the emission as non-thermal in this paper. To make broad-band spectra from radio to X-rays, we fitted the spectra with *srcut* model with the fixed radio index at 1 GHz of 0.78 (Green, 2001). The fittings were also statically accepted with best-fit values in Table 7.2.

Table 7.2: Best-fit parameters of the spectra for the filaments.[a]

Parameters	1	2	Total[b]
Power-law			
Γ	2.3 (2.0–3.5)	2.2 (1.9–2.8)	2.1 (1.6–2.7)
$N_{\rm H}$[c]	2.7 (2.0–4.7)	2.0 (1.3–3.1)	2.3 (1.5–3.4)
Flux[d]	1.9×10^{-13}	1.1×10^{-13}	3.1×10^{-13}
χ^2/d.o.f.	29.2/33	22.1/29	57.6/44
srcut[e]			
$\nu_{rolloff}$[f]	0.93 (>0.44)	2.8 (>0.13)	2.4 (>0.18)
$N_{\rm H}$[c]	2.6 (2.0–3.3)	2.0 (1.6–2.4)	2.2 (1.9–2.7)
$\Sigma_{\rm 1GHz}$[g]	6.3 (5.1–7.6)	2.1 (1.7–2.5)	6.3 (5.4–7.2)
χ^2/d.o.f.	29.2/33	22.1/29	57.6/44
NEI			
kT (keV)	5.4 (>2.1)	5.7 (2.7–34)	5.4 (3.0–12.6)
abundance[h] ...	0.28 (<1.4)	(>0.19)	0.26 (0.02–0.73)
$n_e t$[i]	(not determined)	3.0×10^{-2} (1.1×10^{-2}–9.6×10^{-2})	3.8 (1.6–7.7)
EM[j]	3.6 (2.0–8.1)	0.15 (0.07–3.5)	5.6 (3.7–8.8)
$N_{\rm H}$[c]	2.7 (1.5–4.1)	1.7 (1.1–2.5)	2.5 (1.7–3.5)
χ^2/d.o.f.	28.0/31	19.1/27	56.4/42

[a]: Parentheses indicate single-parameter 90% confidence regions.
[b]: Combined results of filament No.1 and 2.
[c]: Absorption column in the unit of $10^{22}{\rm cm}^{-2}$.
[d]: Absorbed flux in the 0.5–10.0 keV band in the unit of ergs ${\rm cm}^{-2}{\rm s}^{-1}$.
[e]: The radio spectral index is frozen to be 0.78 (Green, 2001).
[f]: Roll-off frequency in the unit of 10^{18} Hz.
[g]: Flux density at 1 GHz in the unit of 0.1 Jy.
[h]: Abundance ratio relative to the solar value (Anders & Grevesse, 1989).
[i]: Ionization time-scale in the unit of 10^{10} s ${\rm cm}^{-3}$, where $n_{\rm e}$ and $t_{\rm p}$ are the electron density and age of the plasma.
[j]: Emission measure $EM = \int n_{\rm e} n_{\rm p} dV \simeq n_{\rm e}^2 V$ in the unit of $10^{55}{\rm cm}^{-3}$, where $n_{\rm p}$ and V are the proton density and the plasma volume, respectively. The distance to Cas A is assumed to be 3.4 kpc.

The spectra of all filaments are a little harder than the result in the north eastern rim by ($\Gamma = 2.4$; Vink & Laming 2003). The rim has a relatively large scale length and is located in the inner region of the shell (Vink & Laming, 2003). Both regions are acceleration sites of cosmic rays, but the filaments we selected may accelerate them up to higher energy. In fact, the hardness in the X-ray band is highest in the region we analysed (Bleeker et al., 2001). The rolloff frequency is very high, about 10 keV or more, which is consistent with the fact that Allen et al. (1997) fitted the spectrum from whole the remnant taken by *RXTE* with a broken power-law model and found that the break energy of ~ 16 keV.

Here, we estimated the magnetic fields and the maximum energy of electrons, in the similar way to the SN 1006 case. Because the magnetic field in Cas A is so strong, far in excess of the canonical value for ISM (Longair, 1994; Wright et al., 1999; Atoyan et al., 2000), the loss time scale t_{loss} must be very small. In fact, t_{loss} is only 2 yrs for 8 TeV electrons in $B = 1$ mG (see eq.(3.48)), which is very small compared with the age of Cas A, $t_{age} = 320$ yrs at the observation date. Similarly, a high magnetic field decreases the number density of relativistic electrons for a given radio brightness, which in turn implies a low inverse Compton contribution to the observed TeV emission. This is consistent with our result; the acceleration time scale derived from eq.(3.46) under the assumption of age limited case is

$$t_{acc} = \frac{4}{u_s}(w_u + w_d) = 8.5 \times 10^8 \text{ [sec]} = 28 \text{ [years]} \ll t_{age} \quad , \tag{7.1}$$

then the age limited case is rejected. Therefore, we consider only loss limited case. Note that the far infrared photon energy density from Cas A itself (u_{IR}) is higher than that of CMB. Vink & Laming (2003) estimated from IRAS data (Braun, 1987) to be $u_{IR} = 4.7 \times 10^{-12}$ ergs cm^{-3},c corresponding to an equivalent magnetic field of $B = 1.1 \times 10^{-5}$ G. Since many observational facts claim higher magnetic field than this equivalent value, we ignore inverse Compton emission from both CMB and IR photons.

We used the values of

$$w_u = 0.58\ (0.41 - 0.80) \text{ [arcsec]} = 9.6\ (6.8 - 13.2) \times 10^{-3} \text{ [pc]} \quad , \tag{7.2}$$

$$w_d = 1.07(0.77 - 1.73) \text{ [arcsec]} = 0.018\ (0.013 - 0.029) \text{ [pc]} \quad , \tag{7.3}$$

$$\nu_{rolloff} = 2.4\ (> 0.18)\ \times 10^{18} \text{ [Hz]} \quad , \tag{7.4}$$

$$t_{age} = 320 \text{ [yrs] at the observation time} \quad , \tag{7.5}$$

$$u_s = 4000 \text{ [km s}^{-1}\text{]} \quad . \tag{7.6}$$

The allowed regions for ξ_u–ξ_d maps for some values of θ have been derived in the similar way of SN 1006 case as shown in Figure 7.6. Under the natural constraint $\xi_u > \xi_d$, we can find the constraint of $\theta < 60°$. The allowed magnetic field and the maximum energy of electrons were searched for, and found that these values are

$$B_d = 139 - 305 \text{ [}\mu\text{G]} \quad , \tag{7.7}$$

$$E_{max} = 10 - 36 \text{ [TeV]} \quad . \tag{7.8}$$

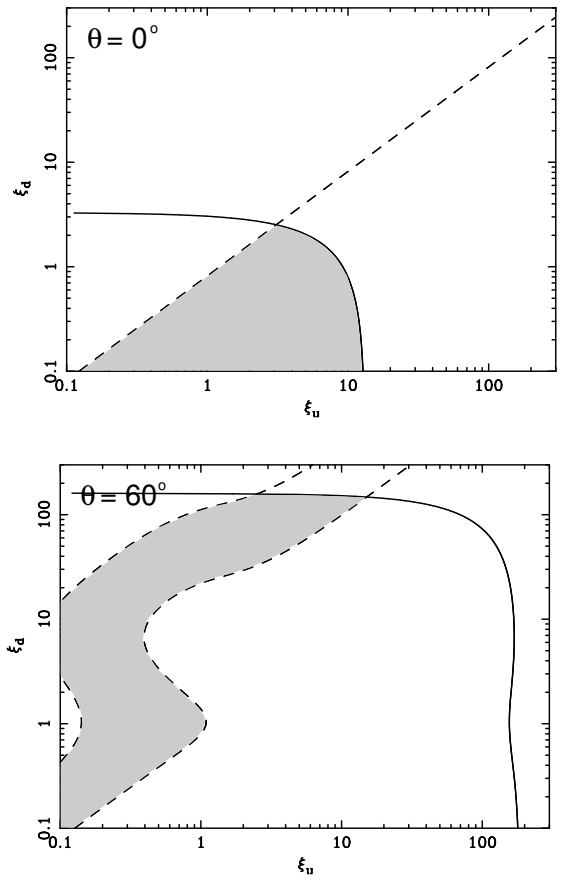

Fig. 7.6.— The allowed region for ξ_u and ξ_d for fixed θ in the loss limited case (shaded regions). Solid and dashed lines represents the condition written in eqs.(6.30) and (6.31) respectively, with parameters of Cas A.

The estimated B_d is rather high, which guarantees our assumption that the inverse Compton emission is negligible. Our result is roughly consistent with the previous result by Vink & Laming (2003), who analysed the different region of Cas A. The estimated magnetic field is roughly consistent with previous estimations (Atoyan et al., 2000; Longair, 1994; Wright et al., 1999).

7.2 Kepler

7.2.1 Previous Observations

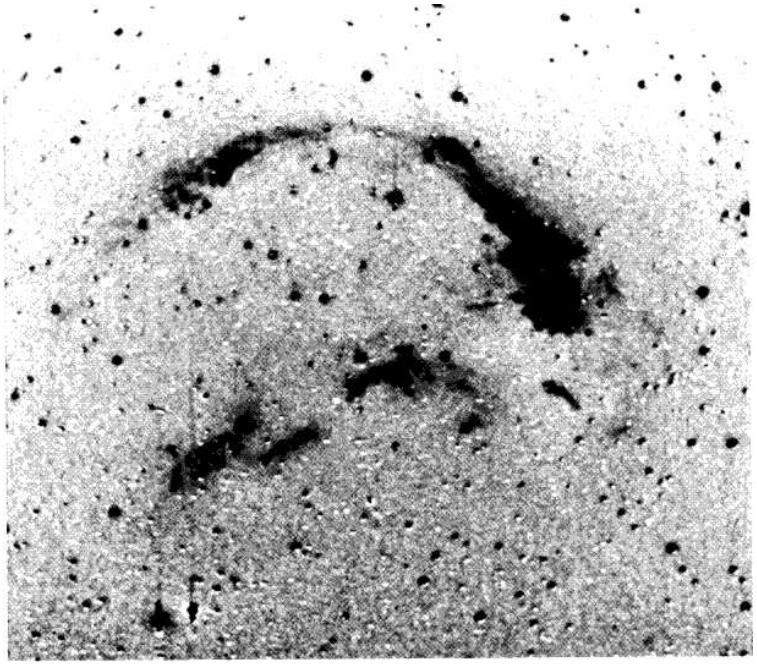

Fig. 7.7.— Hα image of Kepler remnant (Blair, Long, & Vancura, 1991).

Kepler remnant is the second youngest SNR in our Galaxy recorded by human beings, which appeared in the beginning of October 1604 (Kepler, 1606) and re-discovered as a supernova remnant in the optical band by Baade (1943). The Hα emission observed by Blair et al. (1991) concentrates on the northern shell and central region of the remnant (see Figure 7.7). Cold dust around the SNR is found (Morgan et al., 2003), in which flux density is the highest on the north and lower on east and west. Fesen et al. (1989) estimated the shock velocity of the Kepler to be 1670–2800 km s^{-1} with the H_α and H_β emission lines, and Blair et al. (1991) revised it to be 1550–2000 km s^{-1}; we adopt the value $v_s = 1800$ km s^{-1} in this thesis, which is the most widely used value in many articles (e.g., Sollerman et al., 2003). The first report in the radio band is by Baldwin & Edge (1957) using the Cambridge radio telescope. The most recent work in the radio band has been done by DeLaney

et al. (2002), who analysed the VLA data and found the spatial variation of the spectral index from -0.85 to -0.6 with the mean value of -0.71. The SNR has very a curious structure also in the radio band; the brightened northern shell, bar-like structure running from north-west to south-east on the center of the remnant, and ear-like structure on eastern and western edge. Reynoso & Goss (1999a) estimated the distance to the SNR to be 4.8 ± 1.4 kpc, using H I observations with VLA, which corresponds to an angular radius of 2.3 ± 0.7 pc.

The first X-ray imaging was made by *Einstein* (White & Long, 1983). The morphology is very similar to that in radio bands; bright northern shell and some structure on the center. Matsui et al. (1984) estimated the mean magnetic field to be 14–70 μG from mean energy density inferred from X-ray flux. The X-ray spectrum taken with *ASCA* shows incredibly strong emission lines, especially from iron in highly non-equilibrium plasma (Kinugasa & Tsunemi, 1999). Petre, Allen, & Hwang (1999) searched for hard tail emission above 10 keV with *RXTE* but could not find any significant excess, while Decourchelle & Petre (1999) insists the existence of hard X-rays. Cassam-Chenaï et al. (2004) observed the remnant with *XMM-Newton* and analysed spatially resolved spectra, and found iron is more concentrated at the center of the remnant than silicon. They also reported a non-thermal feature in the south-eastern rim.

Kepler's progenitor is somewhat of an enigma. Baade (1943) identified the remnant as the remainder of a Type I SN from the historical light curve, and its distance above the Galactic plane ($\sim$600 pc) is consistent with a Population II progenitor, suggesting a Type Ia event. The *ASCA* analyses by Kinugasa & Tsunemi (1999) also supports the Type Ia origin, since the spectrum of Kepler can not be reproduced the thermal SNR model by Chevalier (1982) due to very strong iron emission line. The fact that this remnant is categorized into "Balmer-dominated SNRs", which have non-radiative shocks caused by low density ISM (Chevalier & Raymond, 1978), is common to other Type Ia SNRs such as SN 1006 and Tycho (Kirshner, Winkler, & Chevalier, 1987; Smith et al., 1991). On the other hand, Doggett & Branch (1985) examined its historical light curve again and claimed that Kepler SN was one of Type II-L event. From detailed spectral analyses with *Einstein*, Borkowski, Sarazin, & Blondin (1994) suggested that Fe is not so abundant compared with Si and S and that the progenitor may be Type II using *Einstein* data. Bandiera (1987) solved the discrepancy for the scale height and type of the progenitor by considering a runaway system. It is still unclear which type the explosion was.

7.2.2 *Chandra* Observation

We used the *Chandra* archival data of the ACIS-S on Kepler (Observation ID = 00116) observed on June 30 – July 1, 2000 with the targeted position at (R.A., Decl.) = ($17^{\rm h}30^{\rm m}39\overset{\rm s}{.}6$, $-21^{\rm d}30^{\rm m}32\overset{\rm s}{.}5$). Kepler remnant is centered at the aimpoint in CCD chip S3. Data acquisition from the ACIS was made in the Timed-Exposure Faint mode. The data reductions and analyses were made using the *Chandra* Interactive Analysis of Observations (CIAO) software version 2.3. The effective exposure was $\sim$ 49 ks for the observation.

7.2.3 Overall X-ray Images

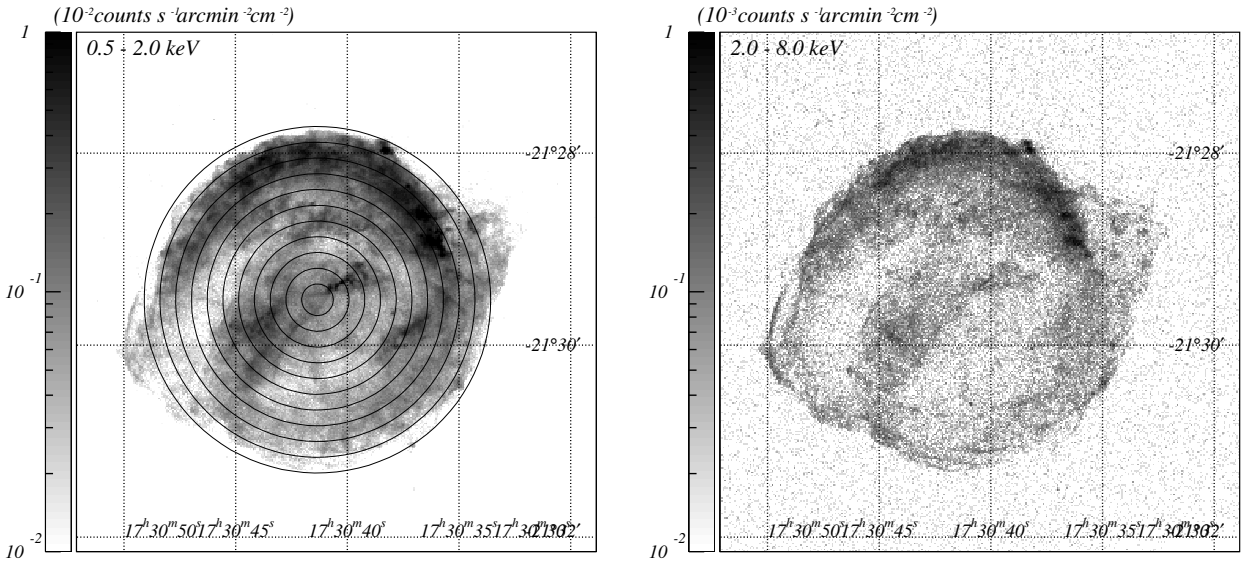

Fig. 7.8.— *Chandra* images of Kepler in 0.5–2.0 keV band (left) and 2.0–8.0 keV band (right) with J2000 coordinates. The scales in both images are in logarithmic. The regions for the spectral analyses are also shown in the left image.

Figure 7.8 is *Chandra* X-ray images in 0.5–2.0 keV (left) and 2.0–8.0 keV (right) bands (see also Figure C.2). The rough structure is very similar to that in the radio band (DeLaney et al., 2002). The shape in each band is nearly circular with ear-like structure on the western and eastern sides and bar-like emission on the central region running from north-west to south-east. Since both curious structure also can be seen in the radio band images and were named "ear" and "bar" by DeLaney et al. (2002), we call them following the radio name. We can see bright emission enhanced at the center and northern part in both images. Particularly in the hard band image, clear filamental structure can be seen on the outer edge of SNR, especially on western and eastern sides. Filaments also exist around the bar region.

In order to reveal the spatial distribution of elements, we first made a spectra of the entire SNR as shown in Figure 7.9. The background region was selected from the outside of the SNR in the same CCD chip. In addition to rather hard continuum, many emission lines from highly ionized elements can be seen; He-like Si Kα (1.81 keV) and Kβ (2.16 keV), S Kα (2.36 keV) and Kβ (2.81 keV), Ar Kα (3.03 keV), Ca Kα (3.77 keV), and Fe Kα (6.41 keV). There is some bump structures below 1 keV, which may be the unresolved line complex of Ne Kα, O K series, and Fe L series. Based on Figure 7.9, we selected the energy bands for each elements; 0.75–0.9 keV for Fe L, 1.6–2.0 keV for Si, 2.2–2.6 keV for S, 4.0–6.0 keV for continuum, and 6.2–6.7 keV for Fe K, and made the maps of elements and continuum emission. Figure 7.10 shows the band-sliced images.

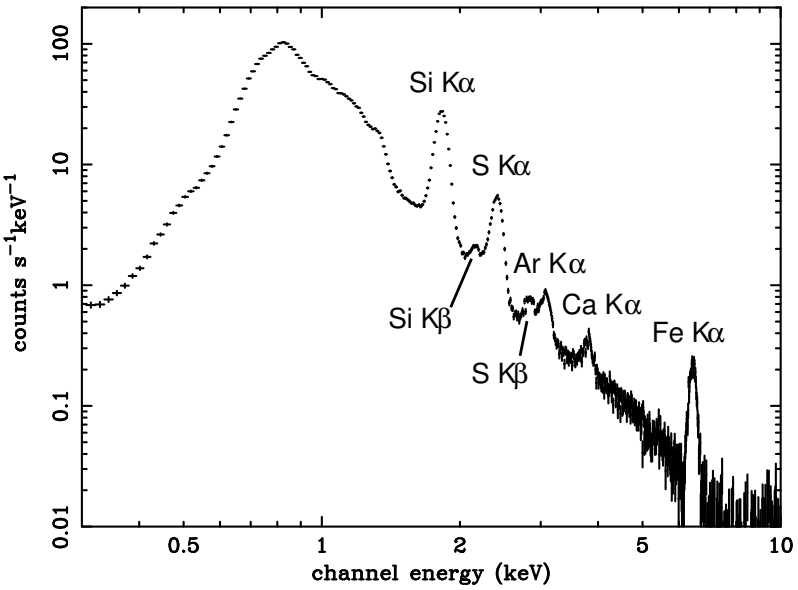

Fig. 7.9.— Background-subtracted spectrum of entire Kepler. The line identification is also shown.

The Si and S band images show similar structures with brightened northern, bar and ear parts with some some small blobs. Fe image is also bright in bar and northern regions, although it is dim in ear region. On the other hand, the continuum image show no bright blob-like structure; there is no enhancement in northern shell and central region. Instead, very thin and clear filaments surrounding the entire SNR, including the ear regions. The bar region is also sandwiched between two filaments.

To enhance the difference between the Si and Fe maps, we made equivalent width maps in the following way; (1) fitted the spectrum (Figure 7.9) with a power-law component (continuum) plus line components in narrow bands around each line, (2) estimated the count rate of continuum component in the Si and Fe band, (3) from the line band images, subtracted the continuum band image weighted with estimated count rates (the images are named as line images), (4) divided the line images by continuum band image, and (5) normalized in order to be equivalent width maps. Although we tried to make the equivalent width map of S, we failed it due to the lack of statistics.

Figure 7.11 show the equivalent width maps of K-emission lines from Si and Fe. Si distributes the whole area of the SNR with enhancements on eastern and southern edges of the SNR and both ear-like regions. On the other hand, the radius where Fe distributes is rather smaller than that for Si. There is no significant enhancement on the outer edge of the SNR and the ear regions. Instead, the inner of the bar region emits very intense iron line. The upper panels of Figure 7.12 also show the center concentration of Fe and uniform distribution of Si.

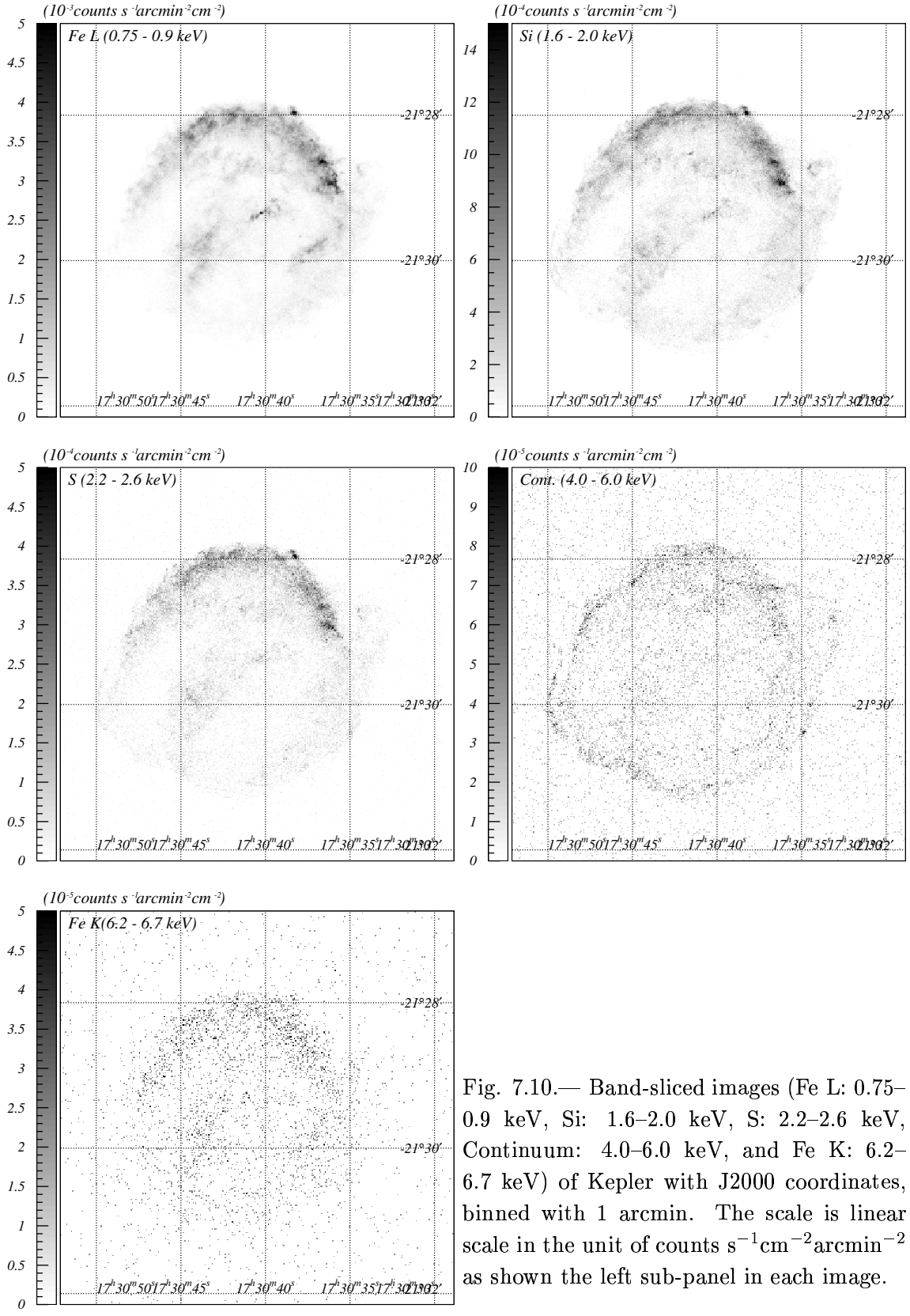

Fig. 7.10.— Band-sliced images (Fe L: 0.75–0.9 keV, Si: 1.6–2.0 keV, S: 2.2–2.6 keV, Continuum: 4.0–6.0 keV, and Fe K: 6.2–6.7 keV) of Kepler with J2000 coordinates, binned with 1 arcmin. The scale is linear scale in the unit of counts $s^{-1}cm^{-2}arcmin^{-2}$ as shown the left sub-panel in each image.

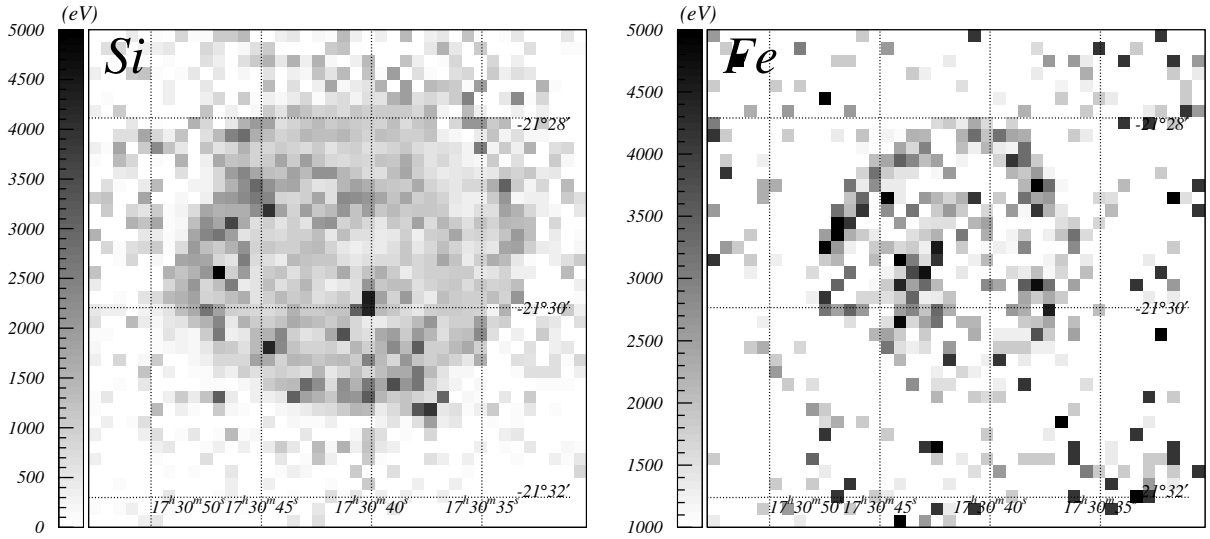

Fig. 7.11.— Equivalent width maps of Si (left) and Fe (right) with J2000 coordinates, binned with 8 arcsec scale to increase signal to noise ratio. The scale is linear scale in the unit of eV as shown the left sub-panel in each image.

To investigate the change of the line center energy, which is the indicator of the plasma age, we made spectra from annulus regions with the width of 10″ as shown in Figure 7.8, with a background region selected from the out of the SNR. The K-emission lines from highly ionized Si and Fe were extracted from the continuum component, fitted with Gaussian function, and derived flux, equivalent width, and the center energy of each line. The lower panels of Figure 7.12 show the radial dependences of the center energy of K-emission lines for Si and Fe.

7.2.4 Analyses of the Filaments

There are very thin filamental structure surrounding the SNR in the continuum band image (Figure 7.10), similar to the SN 1006 and Cas A cases. The low equivalent widths of Si and Fe K-emission line (see Figure 7.11) also support the similar emission mechanism to the former two cases, non-thermal emission. We selected three rectangle regions for analyses of filaments as shown in Figure 7.13, which include rather bright and straight filaments and are free from other structures. Comparing the line intensity of iron on the filaments and just downstream of them, we concluded that the contamination of thermal emission is less than 10% in the 4.0–10.0 keV, even on the assumption that the all of emission just downstream of the filament is thermal. As a result, we adopted this band as non-thermal band and made profiles of these filaments in this band as shown in Figure 7.14.

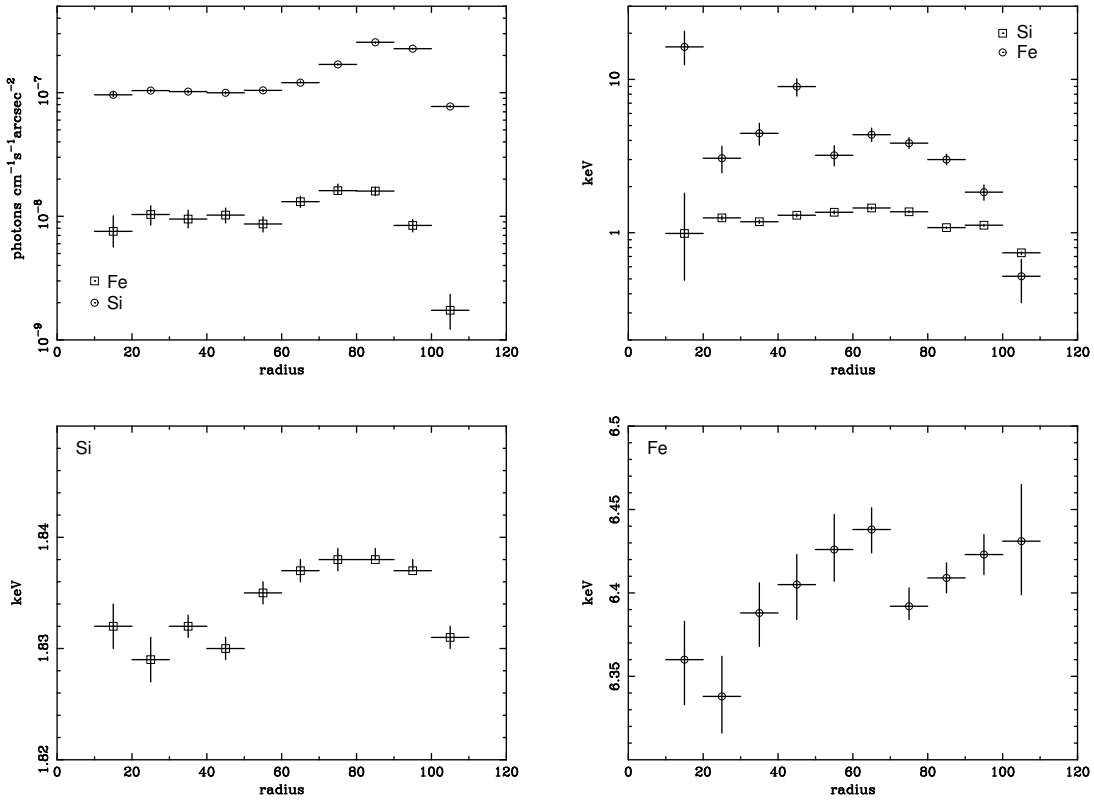

Fig. 7.12.— Radial dependences of the flux (upper left), equivalent width (upper right), center energy (lower panels), of K-emission lines of Si (box) and Fe (circle).

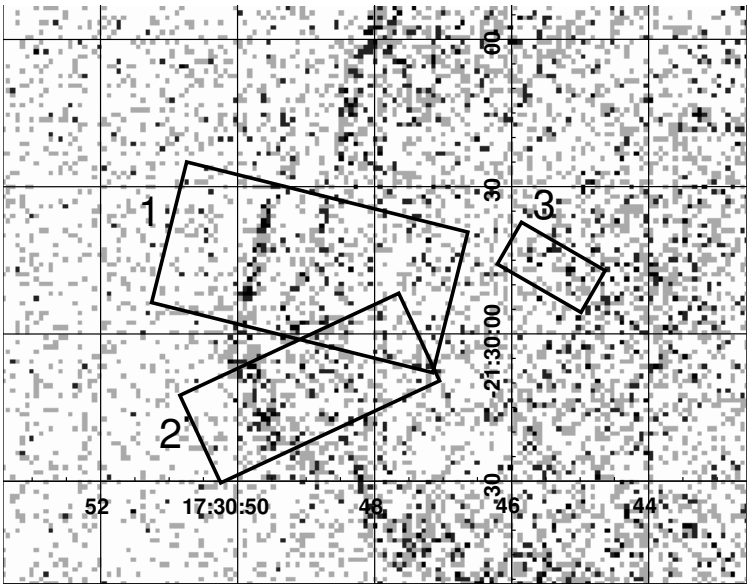

Fig. 7.13.— Closed-up image around the east ear region in the 4.0–10.0 keV band, binned with 1 arcsec. The gray scale is given logarithmically. The filament regions for spatial analyses (No.1–3) are also shown in solid lines.

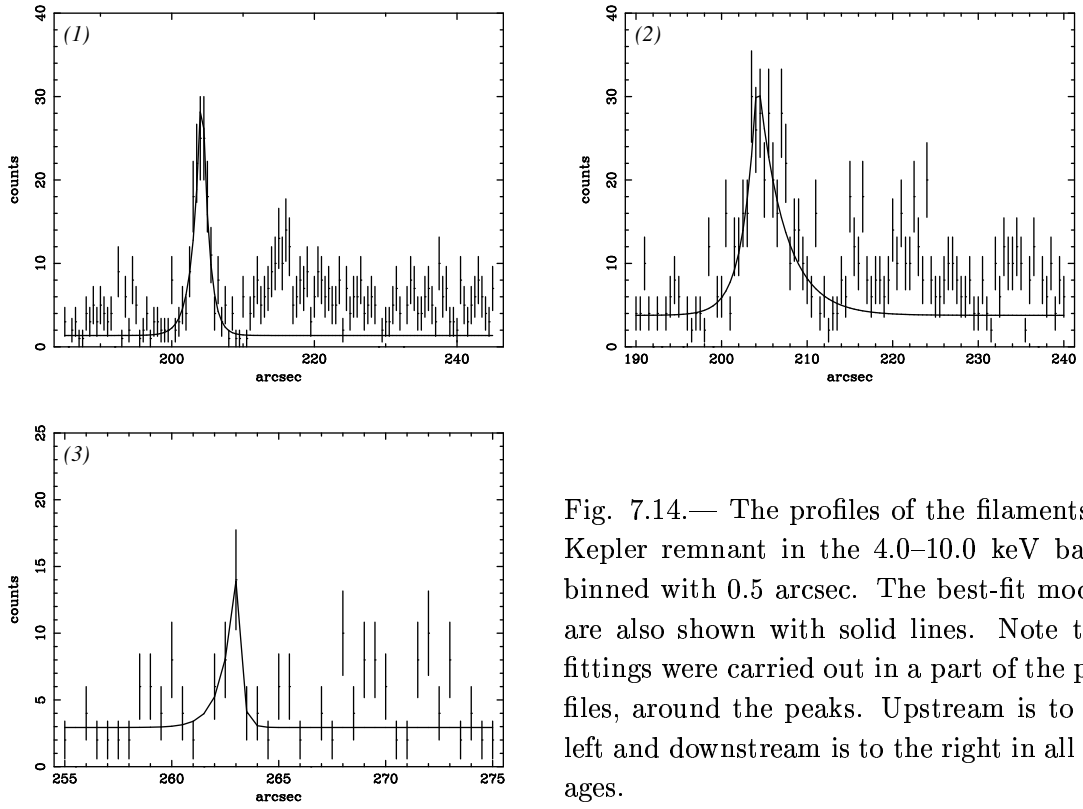

Fig. 7.14.— The profiles of the filaments in Kepler remnant in the 4.0–10.0 keV band, binned with 0.5 arcsec. The best-fit models are also shown with solid lines. Note that fittings were carried out in a part of the profiles, around the peaks. Upstream is to the left and downstream is to the right in all images.

All of the filaments have very small scale length both in upstream and downstream, near to the spatial resolution of *Chandra* (0.5 arcsec). The profiles were fitted with an empirical model (eq.(6.2)) in the same way of SN 1006. The best-fit models and parameters of the filaments are shown in Figure 7.14 and Table 7.3, respectively.

Table 7.3: Best-fit parameters of the profiles of the filaments.[a]

No.	A [cnts arcsec^{-1}]	w_u [arcsec]	w_d [arcsec]	Reduced χ^2 [χ^2/d.o.f.]
1	32.8 (25.8–40.7)	1.17 (0.87–1.59)	0.93 (0.65–1.41)	19.3/21
2	29.2 (24.6–34.1)	1.59 (1.17–2.19)	3.09 (2.46–3.87)	70.1/47
3	11.3 (6.30–18.1)	0.62 (not determined)	0.23 (not determined)	14.7/22

[a]: Parentheses indicate single-parameter 90% confidence regions.

Next, we made the spectra of the filaments within the scale lengths. The background spectra are made from the downstream regions of the filaments without other structures and subtracted. All the background-subtracted spectra are featureless (no line structure) and extend to high energy side, which were well fitted with an absorbed power-law model with the best-fit parameters given in Table 7.4. We also fitted them with a thin thermal plasma model in NEI. Although the fittings were accepted statistically, the temperature is too high and abundance is too low for the thermal emission from the ejecta of young SNRs (see Table 7.4). We thus confirm that the hard X-ray profiles represent those of non-thermal X-rays. This is the first confirmation of the existence of non-thermal filaments in Kepler remnant. Here, we summed up the data of filaments 1 and 2 (the filament 3 was eliminated because it is located on the central region of the SNR) to increase the statistics, and fitted with the same model. The combined-spectrum and the best-fit model, and best-fit parameters are shown in Figure 7.15 and Table 7.4, respectively. The parameters in this table is roughly consistent with the results by Cassam-Chenaï et al. (2004), Matsui et al. (1984), and DeLaney et al. (2002).

7.2.5 Discussion for Kepler

Entire Images of Thermal Emission

The entire image of X-ray emission is very similar to radio images (DeLaney et al., 2002) both in soft and X-ray band. The enhancement on the north region coincides with cold matter distribution (Morgan et al., 2003), therefore the shock is colliding with the stellar wind which is ejected by the progenitor of Kepler. On the other hand, there is no enhancement in the cold matter map on the ear region, which is bright in X-ray and radio band. Together with the fact that the radius on the ear region is larger than those on other regions as shown in Figure 7.8, we inferred that the ear-like structures are made of spouted out plasmas into the space with sparse cold matter.

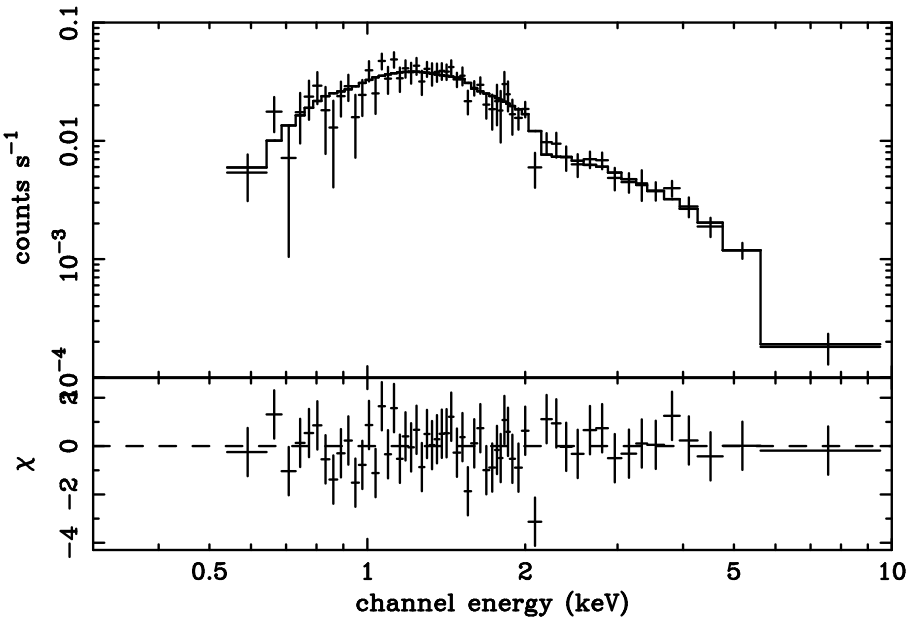

Fig. 7.15.— Upper: The spectrum of combined-filament (crosses). The best-fit power-law model is also shown in the solid line. Lower: Residuals from the model.

Table 7.4: Best-fit parameters of the spectral fittings for the filaments.[a]

Parameters	1	2	3	Total[b]
Power-law				
Γ	2.3 (2.1–2.5)	2.4 (2.2–2.6)	2.7 (2.4–3.3)	2.4 (2.2–2.6)
$N_{\rm H}$[c]	5.8 (4.8–7.0)	5.5 (4.5–6.7)	2.2 (1.1–3.3)	5.7 (4.9–6.6)
Flux[d]	1.7×10^{-13}	2.2×10^{-13}	3.1×10^{-14}	4.1×10^{-13}
χ^2/d.o.f.	42.2/54	24.9/32	20.2/16	44.9/55
srcut[e]				
$\nu_{rolloff}$[f]	5.5 (2.1–17)	4.0 (1.8–9.8)	1.1 (0.3–6.9)	3.6 (2.0–7.9)
$N_{\rm H}$[c]	5.3 (4.7–6.0)	4.9 (4.3–5.5)	1.7 (1.1–2.5)	5.2 (4.8–5.7)
$\Sigma_{\rm 1GHz}$[g]	0.9 (0.8–1.0)	1.4 (1.3–1.5)	0.4 (0.2–2.2)	2.8 (2.6–3.0)
χ^2/d.o.f.	42.9/54	25.0/32	21.3/16	45.5/55
nei				
kT (keV)	3.5 (2.7–4.9)	3.0 (2.5–3.8)	3.2 (1.7–8.5)	3.2 (2.6–3.9)
abundance[h]	($< 6.7 \times 10^{-2}$)	0.13 (<0.40)	0.28 (0.11–0.89)	(<0.34)
$n_e t$[i]	8.2 (3.4–28)	(not determined)	1.2 (0.79–1.7)	11 (>6.9)
EM[j]	5.5 (4.5–6.8)	7.9 (6.5–9.7)	0.81 (0.47–1.5)	14 (12–17)
$N_{\rm H}$[c]	4.3 (3.3–5.6)	3.7 (3.0–4.5)	5.6 (4.3–8.1)	4.0 (3.4–4.7)
χ^2/d.o.f.	43.2/52	25.7/30	7.41/14	47.6/53

[a]: Parentheses indicate single-parameter 90% confidence regions.

[b]: Combined results of filament No.1 and 2.

[c]: Absorption column in the unit of 10^{21}cm^{-2}.

[d]: Absorbed flux in the 0.5–10.0 keV band in the unit of ergs cm^{-2}s^{-1}.

[e]: The radio spectral index is frozen to be 0.7 (DeLaney et al., 2002).

[f]: Roll-off frequency in the unit of 10^{17} Hz.

[g]: Flux density at 1 GHz in the unit of 0.1 Jy.

[h]: Abundance ratio relative to the solar value (Anders & Grevesse, 1989).

[i]: Ionization time-scale in the unit of 10^{10} s cm^{-3}, where $n_{\rm e}$ and $t_{\rm p}$ are the electron density and age of the plasma.

[j]: Emission measure $EM = \int n_{\rm e} n_{\rm p} dV \simeq n_{\rm e}^2 V$ in the unit of 10^{55}cm^{-3}, where $n_{\rm p}$ and V are the proton density and the plasma volume, respectively. The distance to Kepler is assumed to be 4.8 kpc.

The ear regions have rich Si and poor Fe (Figure 7.11). The similar characteristics can be seen in other SNRs, north-east part of Cas A (Hwang, Holt, & Petre, 2000) and southern of Cygnus Loop (Miyata & Tsunemi, 1999). Iron emission is concentrates on the central region of the SNR, whereas Si distributes all of the SNR with enhancements on the southern outer shell and ear regions. This is a consistent result with that with *XMM-Newton* (Cassam-Chenaï et al., 2004). These facts are common in young SNRs, already suggested in the case of Cas A (Hwang et al., 2000) and Tycho (Decourchelle et al., 2001). There is no inversion of the Si and Fe layers as detected in Cas A (Hughes et al., 2000; Hwang et al., 2000; Willingale et al., 2002).

The line center energies becomes lower as the radius becomes smaller in both K-emission lines of Si and Fe (Figure 7.12), although the line shift of Si ($\sim$10 eV at 1.84 keV) is smaller than the energy resolution of *Chandra* (see Figure 5.8). The condition of Fe on the central region is almost neutral, whereas that of Si is slightly ionized. On the other hand, Fe located around the outer region is significantly ionized. It suggests that the plasma in central region has not been yet heated by reverse shock.

The morphology in the soft X-ray band is not uniform like type Ia SNRs such as SN 1006 and Tycho (see Figure 6.2 and Figure 7.21) but rather filamental like type Ib or II such as Cas A and RCW 86.

Non-Thermal Filaments

We made spectral fittings with *srcut* model (Reynolds, 1998; Reynolds & Keohane, 1999) for the spectra of the three filaments, in the same way to SN 1006. From the radio index map in DeLaney et al. (2002), we applied the spectral index of -0.7 at 1 GHz. The normalization at 1 GHz was treated as a free parameter since the flux density of each filament could not know due to the lack of spatial resolution of previous radio observations. The fittings were well accepted for all and combined filaments. Best-fit parameters are also listed in Table 7.4.

Here, we discuss the acceleration parameters such as B_u, B_d, E_{max}, and so on for Kepler, in the same way of SN 1006. We consider both age limited case and loss limited case with the parameters as

$$w_u = 1.37\ (1.01 - 1.87)\ [\mathrm{arcsec}] = 0.03\ (0.02 - 0.04)\ [\mathrm{pc}]\ , \tag{7.9}$$

$$w_d = 1.95\ (1.50 - 2.57))\ [\mathrm{arcsec}] = 0.05\ (0.04 - 0.06)\ [\mathrm{pc}]\ , \tag{7.10}$$

$$\nu_{rolloff} = 3.6\ (2.0 - 7.9)\ \times 10^{17}\ [\mathrm{Hz}]\ , \tag{7.11}$$

$$t_{age} = 396\ [\mathrm{yrs}]\ \text{on the observation time}\ , \tag{7.12}$$

$$u_s = 1800\ [\mathrm{km\ s^{-1}}]\ . \tag{7.13}$$

First, we consider the age limited case. The acceleration time scale t_{acc} for Kepler is estimated

with eq.(3.46) to be

$$t_{acc} = \frac{3}{u_u - u_d}(w_u + w_d) = 5.3 \times 10^9 \text{ [src]} = 168 \text{ [yrs]} \tag{7.14}$$

This is in the same order of $t_{age} = 396$ yrs, then the age limited case is allowed for this remnant. In this case, The allowed regions in (ξ_u, ξ_d) planes with a certain θ are shown in Figure 7.16. For $\xi_u > \xi_d > 1$ regions, the allowed region for the angle between the shock normal and magnetic field in upstream is only near to 90°. This result is mainly because the filaments have same order scale lengths in upstream and in downstream, on the contrary to the case of SN 1006. The magnetic field and the maximum energy of electrons all constraint satisfy are

$$B_u = \frac{B_d}{4} = 10 - 150 \text{ [}\mu\text{G]} \ , \tag{7.15}$$

$$E_{max} = 16 - 31 \text{ [TeV]} \ , \tag{7.16}$$

under the assumption that $\xi_u = \xi_d = 1$. The estimated magnetic field is roughly consistent with that derived by Matsui et al. (1984) (14–70 μG).

The loss limited case is also considered. The eqs.(6.25) and (6.26) is also true in the Kepler case. The allowed region for a certain θ is shown in Figure 7.2.5. There is no allowed region when the angle θ becomes larger than 60°, together with the condition $\xi_u > \xi_d$. We also found that θ must take value of $> 40°$ in order to satisfy the condition $\xi_d > 1$. Anyway, the allowed ξ_u and ξ_d are near to the Bohm limit. Assuming the conditions that $\xi_u = \xi_d = 1$ and $\theta = 60°$, we can get the B_d and E_{max} as

$$B_d = 72 - 85 \text{ [}\mu\text{G]} \ , \tag{7.17}$$

$$E_{max} = 50 - 54 \text{ [TeV]} \ , \tag{7.18}$$

respectively. The downstream magnetic field is slightly larger than the mean value estimated by Matsui et al. (1984). The allowed region is very small, then one must do fine parameter tunings when one want to assume the loss limited case for Kepler.

Acceleration on the Reverse Shock?

Filaments 1 and 2 is located on the forward shock region, which is similar cases to SN 1006 and Cas A. On the other hand, the position of filament 3 is not the apparent outer edge of the SNR but the inner region; it seems to be located on the edge of bar region. Gotthelf et al. (2001) found reverse shock in Cas A, which is slightly younger than Kepler, using the *Chandra* data. As shown in Tycho images by *Chandra* (Hwang et al., 2002), which is a little older than Kepler, there is no shock-like feature inner the shell. Therefore, it is possible that there still remain a reverse shock in the Kepler remnant. Indeed, DeLaney et al. (2002) suggests the existence of reverse shock indirectly in the radio band, the flat spectrum on the outer region of the SNR. Then, we consider the possibility that filament 3 is an acceleration site on the reverse shock.

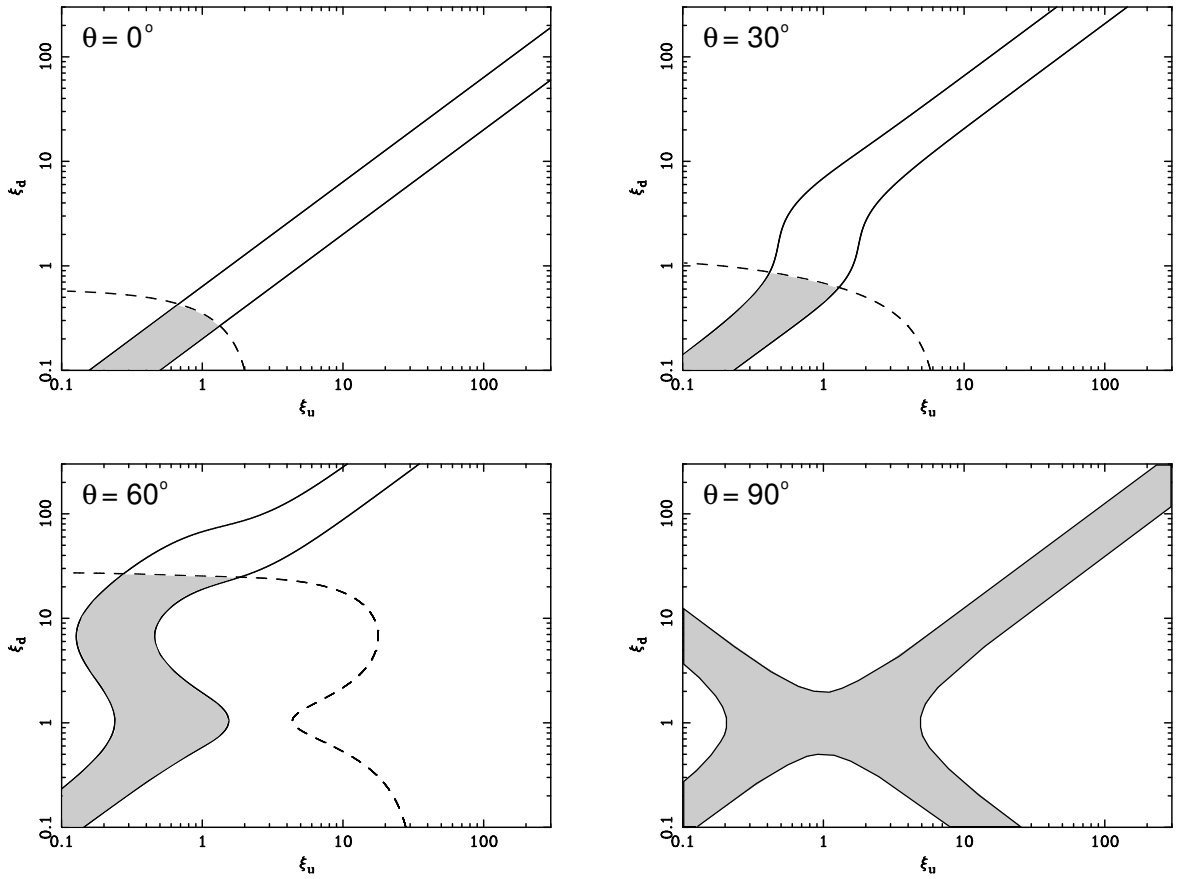

Fig. 7.16.— The allowed region for ξ_u and ξ_d for fixed θ in the age limited case (shaded regions). Solid and dashed lines represents the condition written in eqs.(6.13) and (6.17) respectively, with parameters of Kepler.

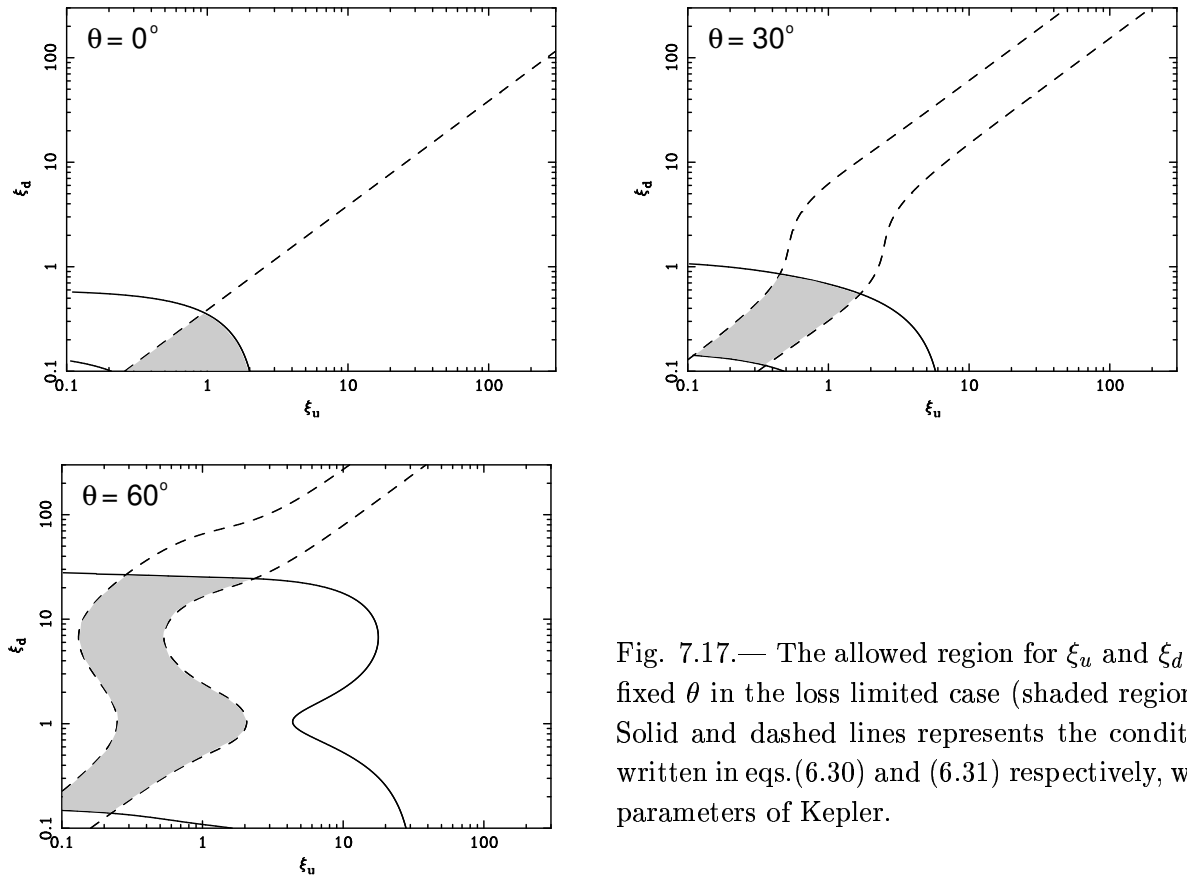

Fig. 7.17.— The allowed region for ξ_u and ξ_d for fixed θ in the loss limited case (shaded regions). Solid and dashed lines represents the condition written in eqs.(6.30) and (6.31) respectively, with parameters of Kepler.

Since the temperature and density of thermal plasma have discontinuity on the reverse shock, we examined the changes of line emission across the filament 3. Figure 7.18 shows the count rate ratio of Fe L to Si K line bands (see also Figure 7.10), representing the rough temperature variation (note that the continuum component is not subtracted). We can see an enhancement of Fe L/Si K around the filament 3 whereas no peak can be seen on the position of the other filaments, which implies that the filament 3 may be made by different mechanism from filament 1 and 2. The blob-like feature in the south-western side of the ratio map may be something like bullet reported in Cygnus Loop (Miyata & Tsunemi, 1999)

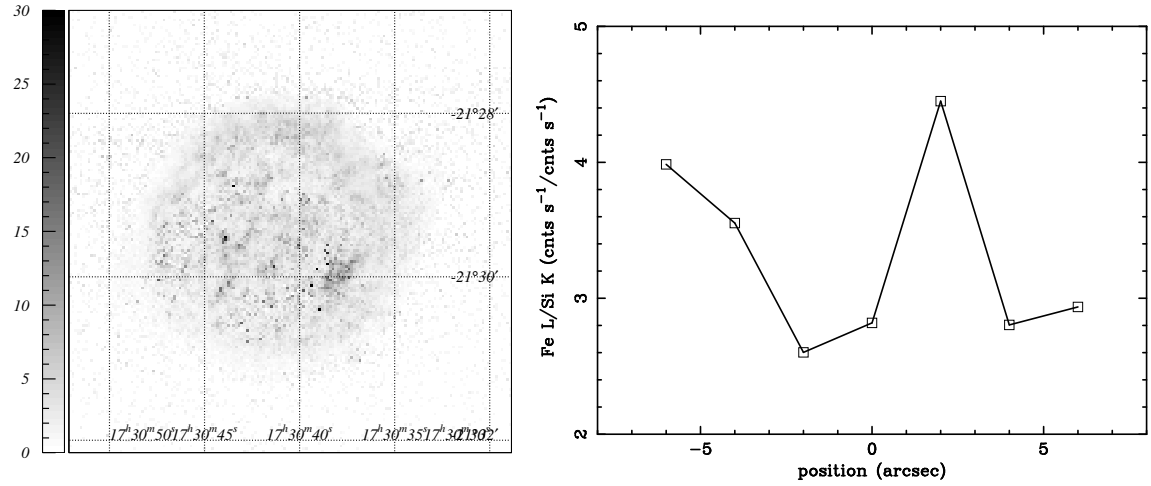

Fig. 7.18.— Left: Count-rate ratio map of Fe L to Si K line bands (0.75–0.9 keV and 1.6–2.0 keV, respectively), binned with 2 arcsec. Right: Position dependence of the count-rate ratio of these two bands. The position 0 means the peak of filament 3 and the center of the SNR is located on the right hand side. Note that the continuum component is not subtracted.

As shown in the right panel of Figure 7.18, we estimated the flux of Fe L and K and Si K line bands. There is a local peak of Fe L/Si K jest inner the filament 3, although the lack of statistics and uncertainty of contamination from continuum component prevent us from concluding that. The Fe L/Si K ratio becomes higher when the temperature of the plasma is low, then the just downstream region of filament 3 is cold component before being heated by reverse shock. We also made the Fe K/Fe L map, but lack of the statistics prevented us from reaching the significant result.

Next, we examined the ionization time scale of thermal components around the filament 3, using the intensity, equivalent width, and center energy of Si K line. Figure 7.19 shows the summary of our analyses. The Si line emission is strong in the outer region of the filament, whereas equivalent width is larger in the inner side. This fact also can be construed that the plasma in downstream is more abundant of Si and/or colder than in upstream. On the other hand, the center energy of Si is

always in NEI and does not change significantly. As a result, we can not conclude that the plasma in downstream of filament 3 is younger than that in upstream. In order to confirm the filament 3 as the acceleration site on the reverse shock, it is needed more information such as the proper motion.

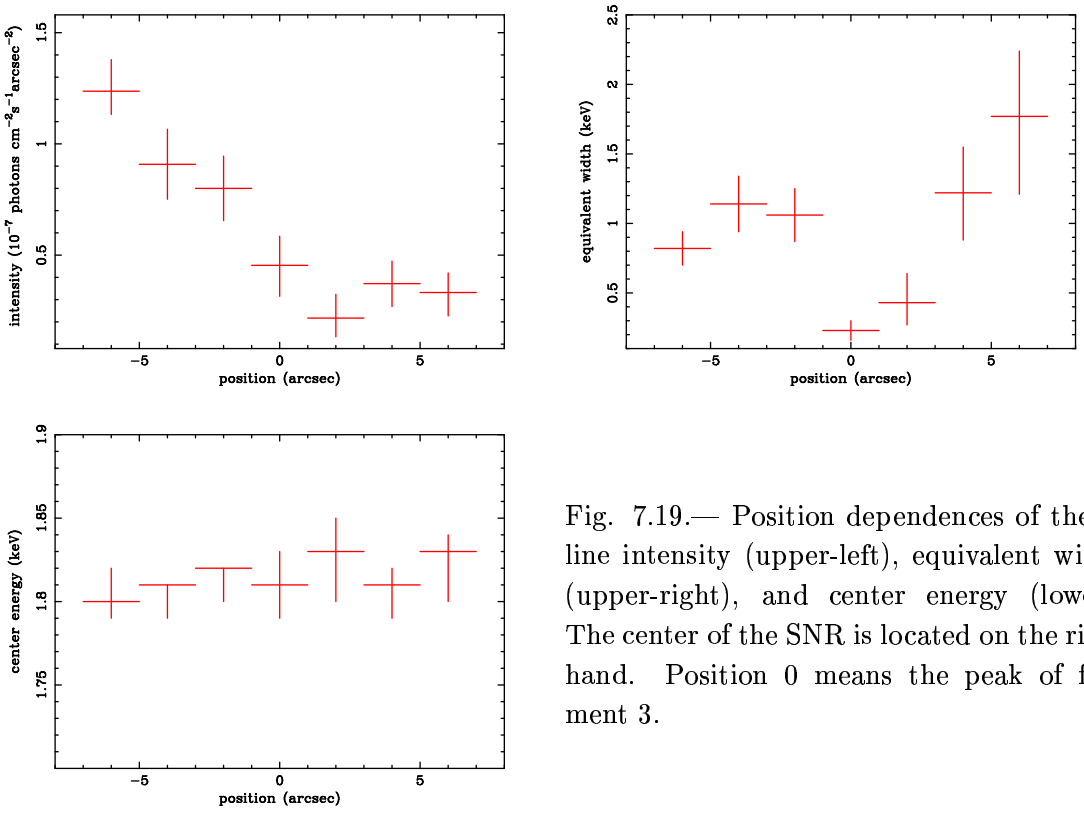

Fig. 7.19.— Position dependences of the Si line intensity (upper-left), equivalent width (upper-right), and center energy (lower). The center of the SNR is located on the right hand. Position 0 means the peak of filament 3.

7.3 Tycho

7.3.1 Previous Observations

Tycho supernova was recorded in 1572 by Tycho Brahe (Tycho, 1573). Minkowski (1966) identified a radio source 3C 10 (Hanbury & Hazard, 1952) as the remnant of Tycho's supernova in the radio band, hence, this is a relatively young supernova remnant. The Tycho remnant is considered as the prototype for type Ia remnants (Baade, 1945) from the light curve when it exploded, which is observed and recorded by Tycho (1573). Now, the remnant seems to be moving from the free expansion phase into the Sedov adiabatic phase of evolution with an average expansion rate of approximately 0.1% yrs^{-1} in the radio band (Strom et al., 1982).

The optical emission from this young remnant is virtually all H Balmer emission due to the

excitation of partially neutral ambient material by the outer shock wave (Smith et al., 1991). Ghavamian et al. (2001) estimated the equilibrium of electron-proton temperature to be less than <20% and calculated the shock velocity $v_s \sim 2000$ km s^{-1}; we adopted this value in this paper. The proper motion of optical filaments is 0.″18–0.″28 yrs^{-1} (Kamper & van den Bergh, 1978), indicating the distance to the remnant is about 1.5–3.1 kpc. In this thesis, we adopt the value 2.3 kpc as the distance, which is the most popular in previous papers. Katz-Stone et al. (2000) investigated the variations of radio spectral indices and found that the emission in the outer rim show a trend such that brighter clump have a flatter spectral index than the average index of $\alpha = -0.52 \pm 0.02$, maybe due to either SNR blast wave and ambient medium interactions or internal inhomogeneities of the magnetic field within the remnant.

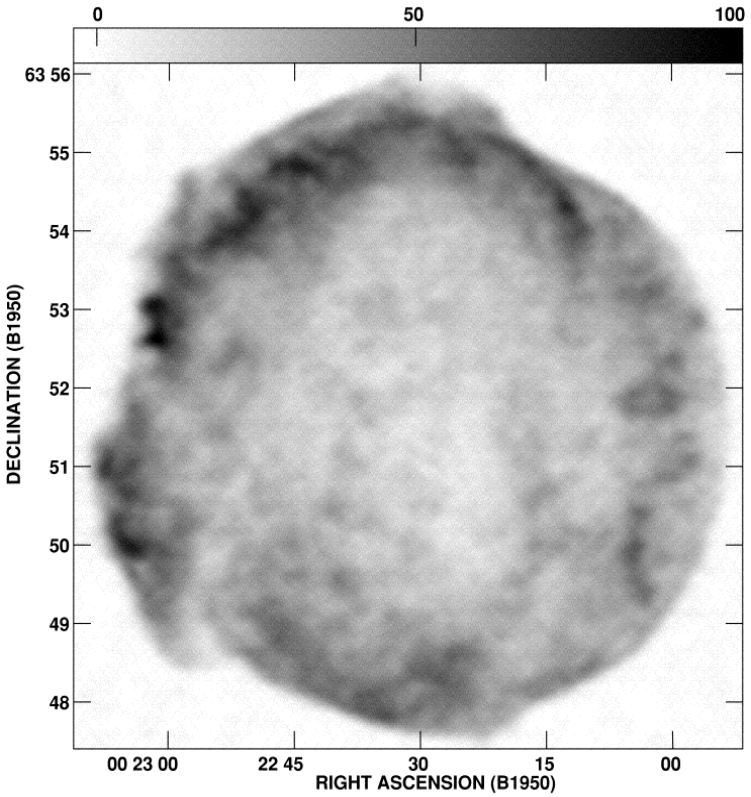

Fig. 7.20.— Tycho image at 90 cm (Katz-Stone et al., 2000)

.

The X-ray remnant was discovered by Friedman, Byram, & Chubb (1967). Hwang & Gotthelf (1997) found many emission line from highly ionized Mg, Si, S, Ar, Ca, and Fe, using data obtained by *ASCA*. *Chandra* and *XMM-Newton* also observed Tycho remnant. The good spatial resolutions of instruments onboard these satellites show us the spatial variety of X-ray emission (Hwang et al., 2002; Decourchelle et al., 2001). The cosmic ray acceleration in Tycho has been studied for

a long time. Völk, et al. (2002) calculated the magnetic field from the wide band spectrum from radio to X-ray to be ~ 240 μG, under the assumption of very efficient acceleration. In fact, hard X-ray emission was detected from Tycho's SNR, at energies up to 25 keV with *HEAO 1* (Pravdo & Smith, 1979); 20 keV with *Ginga* (Fink et al., 1994); and 30 keV with *RXTE* (Petre et al., 1999). However, it is still unknown which part of the remnant emits hard X-rays because of the lack of spatial resolution of previous instruments. Hwang et al. (2002) estimated the upper limit of non-thermal X-ray luminosity in the 0.5–10.0 keV band to be 1×10^{35} ergs s^{-1}, roughly in the same order of SN 1006. Non-thermal X-rays should be accompanied by TeV γ-ray emission. HEGRA observed this remnant but obtained only the 3σ upper limit in >1 TeV (Aharonian et al., 2001b), at a level that is a few to several times lower than the detection of SN 1006 (Tanimori et al., 1998). Thus upper-limits might be understandable from a consideration of the higher densities and/or magnetic fields in this remnant.

7.3.2 *Chandra* Observation

We used the *Chandra* archival data of the ACIS-S on Tycho (Observation ID = 00115) observed on September 20 – 21, 2000 with the targeted position at (R.A., Decl.) = ($10^{\rm h}25^{\rm m}07\overset{\rm s}{.}0$, $64^{\rm d}09^{\rm m}44\overset{\rm s}{.}7$). Kepler remnant is located at the aimpoint in the CCD chip S3. Data acquisition from the ACIS was made in the Timed-Exposure Faint mode. The data reductions and analyses were made using the *Chandra* Interactive Analysis of Observations (CIAO) software version 2.3. The effective exposure was ~ 49 ks for the observation.

7.3.3 Entire Images in the X-Ray Band

Figure 7.21 show the Tycho images in the soft band (left) and hard band (right) (see also Figure C.3). Bright X-ray emission fills the inner region of the remnant in both images. Hwang et al. (2002) reported that the filled emission has many strong emission lines from highly ionized S and Si, suggesting the ejecta origin of the emission. The pattern of the emission is relatively uniform and has no compact knot-like structures, which are similar to those in SN 1006 (Type Ia) and are different from those in Cas A (Type Ib). This fact is consistent with the fact that the progenitor of Tycho remnant is a typical Type Ia event.

In addition to the relatively uniform filled component, we can see a strikingly thin and smooth structure surrounding the remnant especially in the hard band (see the right panel of Figure 7.21). Hwang et al. (2001) have already suggested that the emission from these rims may have non-thermal origin, since the spectra of these structures have emission lines with very low equivalent width. The shock structure is not clear in the eastern side of the remnant, because the shock in the eastern side collides with dense H gas (Reynoso et al., 1999b).

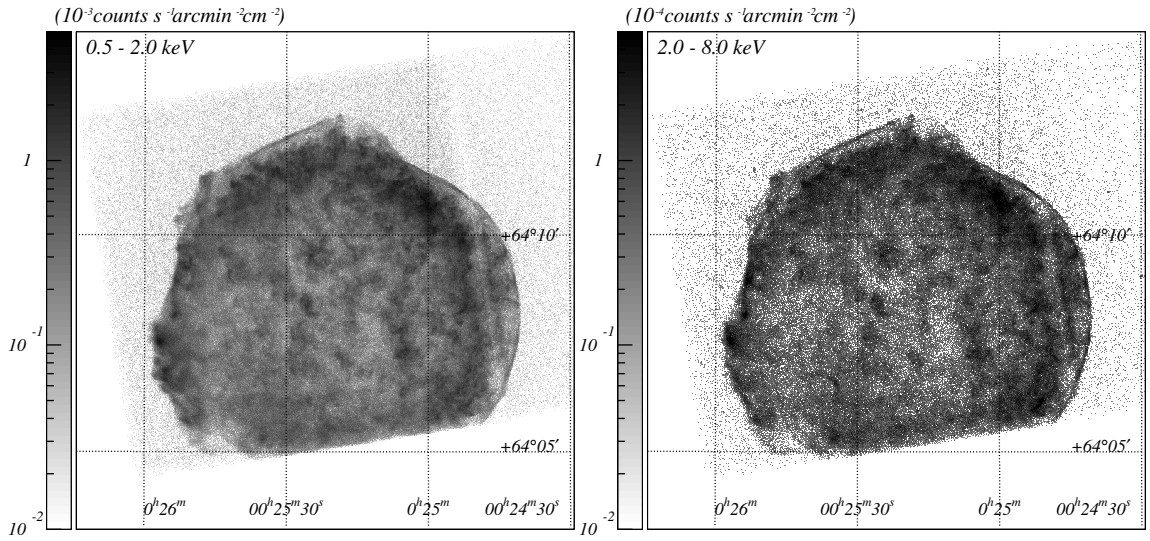

Fig. 7.21.— *Chandra* images of Tycho remnant in the 0.5–2.0 keV band (left) and 2.0–8.0 keV band (right), with J2000 coordinates. The scales in both images are in logarithmic. South edge of the remnant is out of the FOV and a line running vertically on the eastern side of the remnant is gap of the CCD.

7.3.4 Analyses of the Filaments

Spatial Analyses

We selected five regions for the spatial and spectral analyses of filaments as shown in Figure 7.22. The analyses are concentrated on the western part of the remnant, since shock fronts in eastern side have no clear edge. The spectra from the shock front region is very harder and have lines with lower equivalent widths than those just behind the shock, which have strong Si and S emission lines (Hwang et al., 2001). We found the contamination of thermal emission is negligible for photons in the 2.0–10.0 keV band (only $\sim 6\%$), and selected this band as non-thermal band. The profiles of these filaments in the 2.0–10.0 keV band are shown in Figure 7.23. Very sharp edges can be seen in both upstream and downstream in all regions.

The analyses have been done in the same way to the SN 1006 case with the model of eq.(6.2). This simple model well represents the profiles of all filaments statistically with best-fit models and parameters shown in Figure 7.23 and Table 7.5.

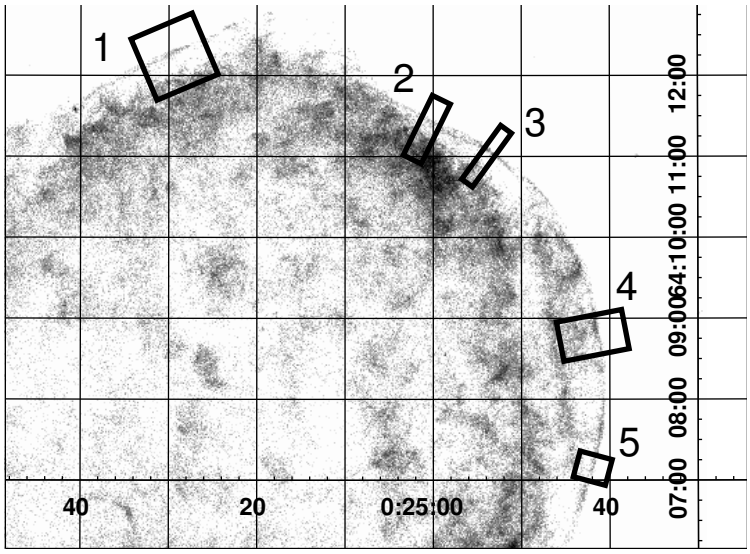

Fig. 7.22.— Closed-up image around the eastern region in the 2.0–10.0 keV band, binned with 1 arcsec. The gray scale is given logarithmically. The filament regions for spatial analyses (No.1–5) are also shown in solid rectangles.

Table 7.5: Best-fit parameters of the profiles of the filaments.[a]

No.	A [cnts arcsec^{-1}]	w_u [arcsec]	w_d [arcsec]	Reduced χ^{2b} [χ^2/d.o.f.]
1	129 (119–139)	1.18 (1.01–1.32)	5.36 (4.77–6.12)	82.7/55
2	62.3 (48.0–70.3)	0.54 (0.41–0.67)	1.70 (1.32–3.15)	42.3/32
3	79.9 (74.4–83.0)	0.49 (0.42–0.57)	2.38 (2.20–2.54)	23.4/37
4	150 (146–152)	0.86 (0.80–0.93)	5.53 (5.00–6.14)	48.9/46
5	63.3 (56.5–71.2)	1.03 (0.90–1.35)	2.47 (1.93–3.15)	17.9/21

[a]: Parentheses indicate single-parameter 90% confidence regions.
[b]: Fittings were carried out only around the filaments.

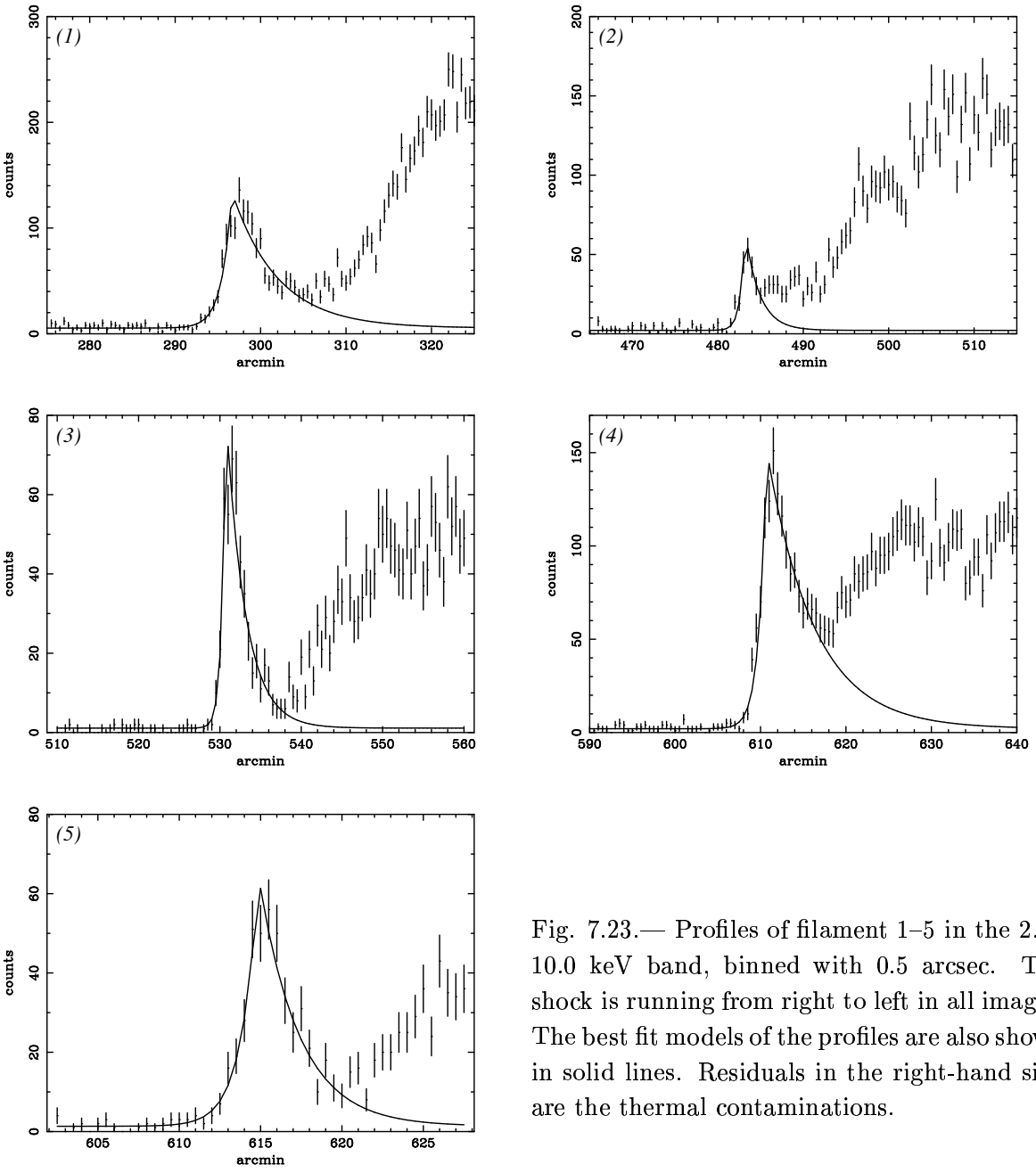

Fig. 7.23.— Profiles of filament 1–5 in the 2.0–10.0 keV band, binned with 0.5 arcsec. The shock is running from right to left in all images. The best fit models of the profiles are also shown in solid lines. Residuals in the right-hand side are the thermal contaminations.

Spectral Analyses

Spectral analyses for these filaments have been also done. Hwang et al. (2001) have done spectral analyses for them both with thermal and non-thermal models, with background spectra from outside of the remnant. Here, we selected background regions from just behind of the shock, in order to eliminate the contaminations of thermal emission. The spectra were relatively hard, then power-law and *nei* models were selected for the fitting. The best-fit parameters for each model are shown in Table 7.6. We also analysed integrated spectra of these filaments. Since filaments No. 1–3 and No. 4–5 are located in different chips from each other, we made two integrated spectra and fitted with models simultaneously except for the normalization. The both models were well fitted with the data, with the best-fit models and parameters shown in Figure 7.24 and Table 7.6, respectively.

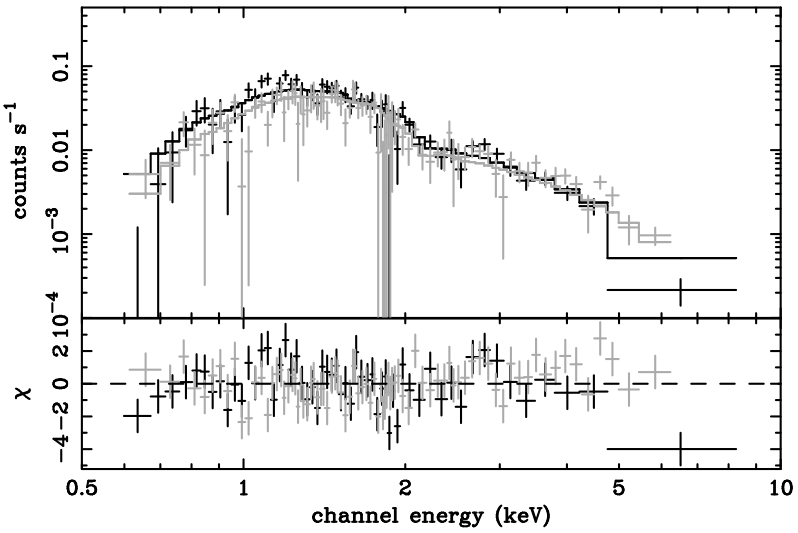

Fig. 7.24.— Integrated spectrum of the filaments. The black and gray data and models are for filament No.1–3 and No.4–5, respectively, due to they are located on the different chips each other.

7.3.5 Discussion for Tycho

The spectra of five filaments are relatively hard and have no line-like structure. Si and S lines, which existed some of spectra of filaments in previous analyses (Hwang et al., 2002), can not be seen in the spectrum (Figure 7.24). It may be because of the successful subtraction of background thermal emission. The thermal fitting is allowed only with a very low abundance (<0.2) with high temperature (see Table 7.6), implying that the emission from the filaments is not thermal but non-

Table 7.6: Best-fit parameters of the spectra of the filaments.[a]

Parameters	1	2	3	4	5	Total[b]
Power-law						
Γ	3.0 (2.8–3.3)	3.9 (2.5–5.6)	2.5 (2.2–2.9)	2.1 (2.0–2.4)	2.9 (2.5–3.3)	2.7 (2.6–2.9)
$N_{\rm H}$[c]	9.0 (7.9–10.6)	15.8 (8.6–26.6)	7.6 (6.0–9.8)	6.8 (4.6–9.6)	9.4 (6.9–13.0)	8.1 (7.3–9.0)
Flux[d]	3.4×10^{-13}	4.9×10^{-14}	1.1×10^{-13}	4.4×10^{-13}	1.1×10^{-13}	1.1×10^{-12}
χ^2/d.o.f.	104.8/70	9.05/13	43.5/43	40.9/34	55.5/49	187.7/136
srcut[e]						
$\nu_{rolloff}$[f] ...	4.0 (2.5–7.0)	1.1 (0.20–12.9)	13.0 (5.2–45)	65.0 (18.4–455)	6.4 (2.6–16.5)	8.3 (5.9–11.7)
$N_{\rm H}$[c]	8.1 (7.4–8.8)	13.2 (10.8–18.6)	6.9 (5.9–8.2)	6.2 (5.0–7.7)	8.2 (6.7–10.0)	7.2 (6.7–7.7)
$\Sigma_{\rm 1GHz}$[g]	7.0 (6.4–7.7)	14.2 (10.2–20.2)	0.51 (0.45–0.59)	0.52 (0.46–0.59)	1.2 (1.0–1.4)	7.8 (7.3–8.3)
χ^2/d.o.f.	105.9/70	9.16/13	43.2/43	40.6/34	54.4/49	185.2/136
nei						
kT (keV) ...	2.0 (1.6–2.4)	1.0 (0.58–6.9)	2.1 (1.6–2.9)	4.3 (3.0–7.0)	1.8 (1.4–2.6)	2.3 (2.0–2.6)
abundance[h] .	0.22 (0.06–0.50)	(<1.6)	0.12 (<0.37)	(<0.38)	0.05 (<0.20)	0.07 (<0.17)
$n_e t$[i]	3.4 ($> 6.9 \times 10^{-2}$)	(ND[j])	(ND[j])	(ND[j])	(ND[j])	(ND[j])
EM[k]	9.0 (6.7–11.6)	4.8 (0.53–17.9)	3.2 (1.6–4.6)	5.6 (4.4–7.5)	3.9 (2.1–6.2)	23.8 (20.8–27.5)
$N_{\rm H}$[c]	6.5 (5.4–7.5)	11.7 (6.6–19.8)	11.3 (5.7–14.6)	5.1 (3.4–10.0)	9.8 (5.1–14.3)	5.8 (5.2–6.4)
χ^2/d.o.f.	102.3/68	9.40/11	40.2/41	39.5/32	51.9/47	182.0/134

[a]: Parentheses indicate single-parameter 90% confidence regions.
[b]: Combined results of filament No.1–5. The integrated spectra were made one spectrum for one CCD chip, and fitted with models simultaneously.
[c]: Absorption column in the unit of $10^{21}\,{\rm cm}^{-2}$.
[d]: Absorbed flux in the 0.5–10.0 keV band in the unit of ergs ${\rm cm}^{-2}{\rm s}^{-1}$.
[e]: The radio spectral index is frozen to be 0.7 (DeLaney et al., 2002).
[f]: Roll-off frequency in the unit of 10^{16} Hz.
[g]: Flux density at 1 GHz in the unit of 10^{-2} Jy.
[h]: Abundance ratio relative to the solar value (Anders & Grevesse, 1989).
[i]: Ionization time-scale in the unit of 10^{13} s ${\rm cm}^{-3}$, where $n_{\rm e}$ and $t_{\rm p}$ are the electron density and age of the plasma.
[j]: ND means "not determined".
[k]: Emission measure $EM = \int n_{\rm e} n_{\rm p} dV \simeq n_{\rm e}^2 V$ in the unit of $10^{55}{\rm cm}^{-3}$, where $n_{\rm p}$ and V are the proton density and the plasma volume, respectively. The distance to Tycho is assumed to be 2.3 kpc.

thermal from high-energy electrons, together with the fact that the very sharp profiles are similar to those in SN 1006 and other SNRs.

In order to estimate $\nu_{rolloff}$, we fitted the spectra with the *srcut* model. The spectral index at 1 GHz was frozen to 0.52 following the previous radio observations by Katz-Stone et al. (2000), which is also cited by Hwang et al. (2002). The model successfully fitted with all spectra of these filaments and the combined one, with similar values of reduced χ^2 to those in power-law fittings. The best-fit parameters are also listed in Table 7.6.

We have estimated the maximum energy of accelerated electrons in Tycho in a similar way to the SN 1006 case. The values we used are as follows;

$$w_u = 0.87\ (0.76 - 1.00)\ [\mathrm{arcsec}] = 9.7\ (8.5 - 11.2)\ [\times 10^{-3}\ \mathrm{pc}]\ , \tag{7.19}$$

$$w_d = 4.07\ (3.60 - 4.77)\ [\mathrm{arcsec}] = 4.5\ (4.0 - 5.3)\ [\times 10^{-2}\ \mathrm{pc}]\ , \tag{7.20}$$

$$\nu_{rolloff} = 8.3\ (5.9 - 11.7)\ [\times 10^{16}\ \mathrm{Hz}]\ , \tag{7.21}$$

$$t_{age} = 428\ [\mathrm{yrs}]\ \text{on the observation time}\ , \tag{7.22}$$

$$u_s = 2000\ [\mathrm{km\ s^{-1}}]\ , \tag{7.23}$$

where we assumed that the distance to the remnant is 2.3 kpc (Kamper & van den Bergh, 1978).

Under the age limited assumption, the acceleration time scale is derived with eq.(3.46) as

$$t_{acc} = \frac{4}{u_s}(w_u + w_d) = 3.38 \times 10^9\ [\mathrm{sec}] = 113\ [\mathrm{years}]\ , \tag{7.24}$$

which is comparable to the value of $t_{age} = 428$ yrs. Therefore the age limited assumption is valid. Figure 7.25 shows the allowed regions in ξ_u-ξ_d planes with various θ, derived with the same method of SN 1006. We can see very narrow regions are allowed in each θ. The allowed θ is in fact $\leq 5^\circ$ under the natural assumption $\xi_u > \xi_d$. The magnetic field and maximum energy of electrons are estimated in the case of $\theta = 0^\circ$ to be

$$B_u = B_d = 70 - 110\ [\mu\mathrm{G}]\ , \tag{7.25}$$

$$E_{max} = 10 - 18\ [\mathrm{TeV}]\ . \tag{7.26}$$

When the value of θ becomes larger than 86°, the allowed region emerges again around $\xi_d = 1$ (see Figure 7.25). In this case, the B_u, B_d, and E_{max} becomes

$$B_u = \frac{1}{4}B_d = 8 - 13\ [\mu\mathrm{G}]\ , \tag{7.27}$$

$$E_{max} = 4.8 - 10\ [\mathrm{TeV}]\ . \tag{7.28}$$

The all acceptable regions in Figure 7.25 satisfy near the Bohm limit, $\xi_u \sim \xi_d \sim 1$. The estimated magnetic field is significantly smaller than the calculated value by Völk, et al. (2002) ($\sim 240\ \mu$G) regardless the value of θ.

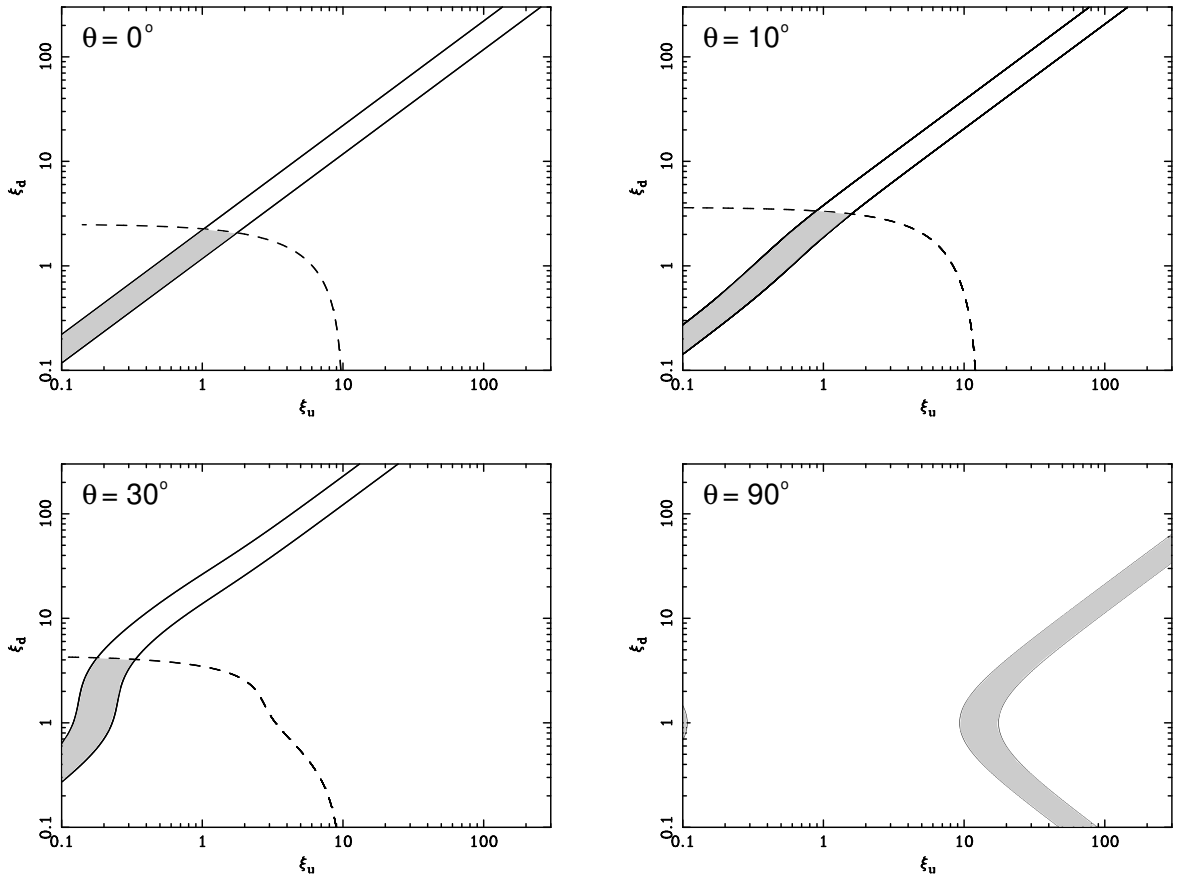

Fig. 7.25.— Allowed regions in ξ_u-ξ_d planes with various θ (shaded regions) in the age limited cases. Solid and dashed lines represents the condition written in eqs.(6.13) and (6.17) respectively, with parameters of Tycho.

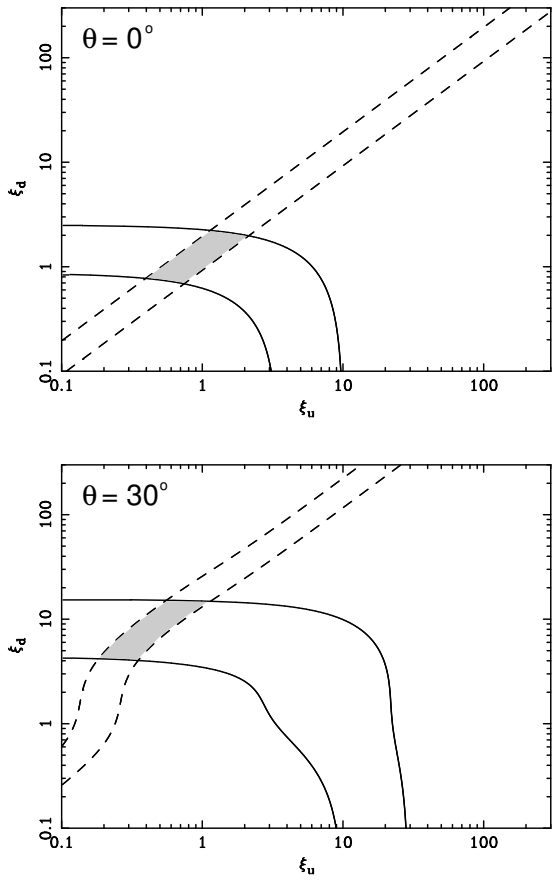

Fig. 7.26.— Allowed regions in ξ_u-ξ_d planes with various θ (shaded regions) in the loss limited cases. Solid and dashed lines represents the condition written in eqs.(6.30) and (6.31) respectively, with parameters of Tycho.

Next, let us consider the loss limited case. Figure 7.26 show the allowed regions for Tycho under the loss limit assumption, which has been already dealt in the section about SN 1006. Note that eqs.(6.23) and (6.24) always become

$$w_u = \frac{K_u}{u_s} \ , \tag{7.29}$$

$$w_d = u_d t_{cool} \ . \tag{7.30}$$

For the condition with $\theta > 10^\circ$, there is no allowed region which satisfy $\xi_u > \xi_d$, then we concluded that the expected condition in the loss limited case is nearly parallel magnetic field. In the case with $\xi_u = \xi_d = 1$ and $\theta = 0^\circ$, we estimated the $B_u = B_d$ and E_{max} as

$$B_u = B_d = 82 - 99 \ [\mu\mathrm{G}] \ , \tag{7.31}$$

$$E_{max} = 15.5 - 17.0 \ [\mathrm{TeV}] \ . \tag{7.32}$$

The estimated magnetic field is also lower than the estimation by Völk, et al. (2002) even in the loss limited case.

7.4 RCW 86

7.4.1 Previous Observations

RCW 86 was identified as a remnant of the historical supernova by Clark & Stephenson (1977), they suggested that the progenitor of the explosion on 7 December AD 185 was reported in the Later Han dynasty records (Fan You, 432). This is the oldest supernova recorded historically if the record is truly the guest star. However, Chin & Huang (1994) suggested that the event that the ancient Chinese astronomer observed was not a supernova but an unknown comet and derived the age of RCW 86 to be $\sim$ 8000 yr with a Sedov solution. Schaefer (1995) reported the possibility that the observed event might be a combined event of a supernova and one of the most famous comet, Swift-Tuttle, the parent of the Perseid meteor shower that will have a near approach to Earth on 2126 August 5. Throughout the thesis, we assume the age of the remnant to be 1816 yrs.

The radio shell of RCW 86 was identified in the MSH survey (Mills, Slee, & Hill, 1961) and soon after found to be a non-thermal and polarized source (Hill, 1964, 1967), Caswell, Clark, & Crawford (1975) measured the radio index at 1 GHz to be 0.6. identifying that it was in fact a SNR. Later higher resolution radio works (e.g., Kesteven & Caswell, 1987) showed that the SNR has a complete shell brightened on the south-western part. Dickel, Strom, & Milne (2001) analysed imaging and polarimetry data of this SNR at a frequency of 1.34 GHz and found that the SW shell is now colliding with dense gas. The bright nebula RCW 86 (Rodgers, Campbell, & Whiteoak, 1960) lies in the south-western corner of the remnant and shows strong [S II] emission, characteristic of shock-excited radiative filaments (Westerlund & Mathewson, 1966). Since RCW 86 is located in an OB star association, Rosado, et al. (1996) studied the kinematics of RCW 86 and found that there

is a physical association between this SNR and a neighboring OB stellar association, confirming that this SNR, which is now in the Sedov phase, is probably the result of an explosion of a Type II supernova; this suggestion also identifies RCW 86 with the historical supernova in AD 185.

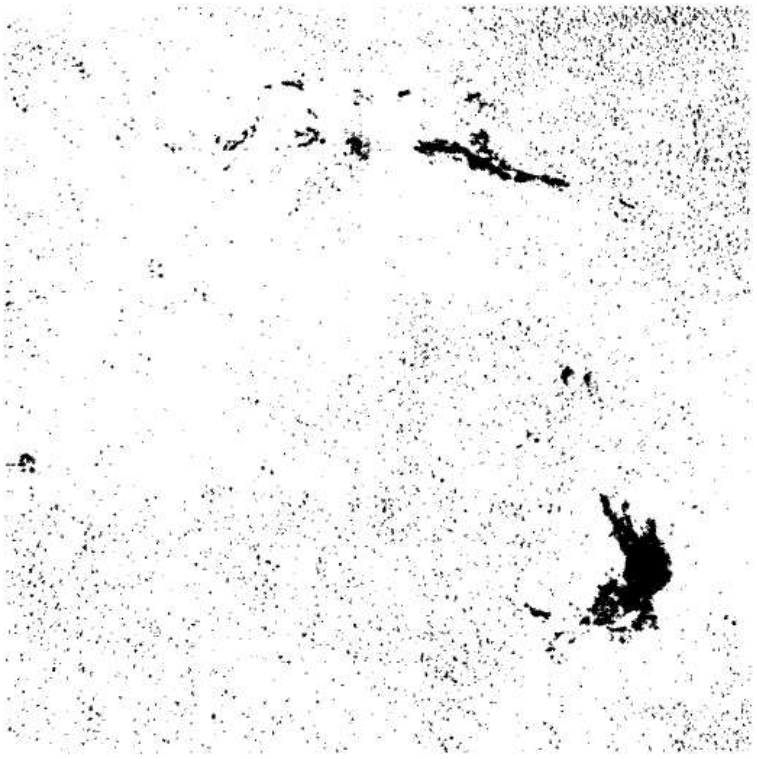

Fig. 7.27.— Hα image of RCW 86 (Smith, 1997).

Smith (1997) reported thin filaments surrounding the SNR in the Hα band image (see Figure 7.27). The velocity of blast wave is determined from observations of Balmer-dominated shocks that almost completely encircle the remnant (Long & Blair, 1990; Smith, 1997; Ghavamian et al., 2001). In this thesis, we adopt 562 ± 18 km s^{-1} as the shock velocity in RCW 86, which was estimated in a south-western region by Ghavamian et al. (2001).

X-rays from RCW 86 were discovered by Naranan et al. (1977). The X-ray spectrum obtained with the *Einstein* satellite was represented by a two-temperature plasma model (Winkler, 1978). The higher energy spectrum (2.0–20 keV) with the *Ginga* satellite was explained by a single temperature plasma of $kT \geq 4$ keV (Kaastra et al., 1992). Using the *ASCA* satellite, Vink, Kaastra, & Bleeker (1997) reported that the plasma temperature varies from region to region of the shell, from 0.8 keV to > 3 keV. They also suggested the existence of 6.4 keV Fe Kα line, which was confirmed by Bocchino et al. (2000) with *BeppoSAX*. Petre et al. (1999) found a hard X-ray tail extending to several 10 keV in the *RXTE* spectrum. They thus argued that the shell of RCW 86 has non-thermal emission and is one of the candidates for the origin of high-energy cosmic rays.

However, non-imaging instrument of *RXTE* could not clarify which region of the SNR is the hard X-ray emitter. Bamba, Tomida, & Koyama (2000) and Borkowski et al. (2001b) analysed *ASCA* data of RCW 86 independently and found that the hard X-ray spectra emitted from southern and north-eastern shells, which were suggested by (Vink et al., 1997), can be well reproduced by a power-law model, suggesting that the hard X-rays have non-thermal origin. Thermal spectra show strong O, Ne, Mg, and Si lines, suggesting that the origin of this SNR is type II (Bamba et al., 2000; Borkowski et al., 2001b). Using the *Chandra* data, Rho et al. (2002) found that the morphologies of soft (thermal) and hard (non-thermal) X-ray band images are very different from each other.

7.4.2 *Chandra* Observation

We used the *Chandra* archival data with the ACIS-I and S of RCW 86 (Observation ID = 01993) observed on February 1–2, 2001 with the targeted position at (R.A., Decl.) = ($14^{\rm h}40^{\rm m}46\overset{\rm s}{.}6$, $-62^{\rm d}39^{\rm m}43\overset{\rm s}{.}9$). The remnant is located on the aimpoint in CCD chip S3. Data acquisition from the ACIS was made in the Timed-Exposure Faint mode. The data reductions and analyses were made using the *Chandra* Interactive Analysis of Observations (CIAO) software version 2.3. The effective exposure was ~ 92 ks for the observation.

7.4.3 Images of South-Western Shell

Figure 7.28 show the south-western shell of RCW 86 taken by *Chandra* (see also Figure C.5) in the 0.5–2.0 keV (left) and 2.0–8.0 keV (right) bands. In both images, we can see many filamentary structures although the details are different from each energy bands. In the soft band image, L-shape structure constructed by many filamental structures can be seen and the direction of these filaments is roughly parallel to the shock front. Hard emission, on the other hand, concentrates on the southern part of the shell with bar-like structure and is rather clumpy. There is sparse coincidence between soft and hard band images on the small-scale structures. It is consistent with the previous results with *ASCA* that the concentration of hard component on the southern region of this shell (Bamba et al., 2000; Borkowski et al., 2001b). The hard emission traces the bright region in the radio maps (Dickel et al., 2001), whereas the soft X-rays well coincide with Hα image (Smith, 1997).

7.4.4 Analyses of the Filaments

Spatial Analyses

The photons above 2.0 keV in RCW 86 is almost pure non-thermal following the previous analysis reports on the X-ray band (Bamba et al., 2000; Borkowski et al., 2001b; Rho et al., 2002), then we selected 2.0–10.0 keV band for our analyses of non-thermal filaments. Figure 7.29 shows the closed

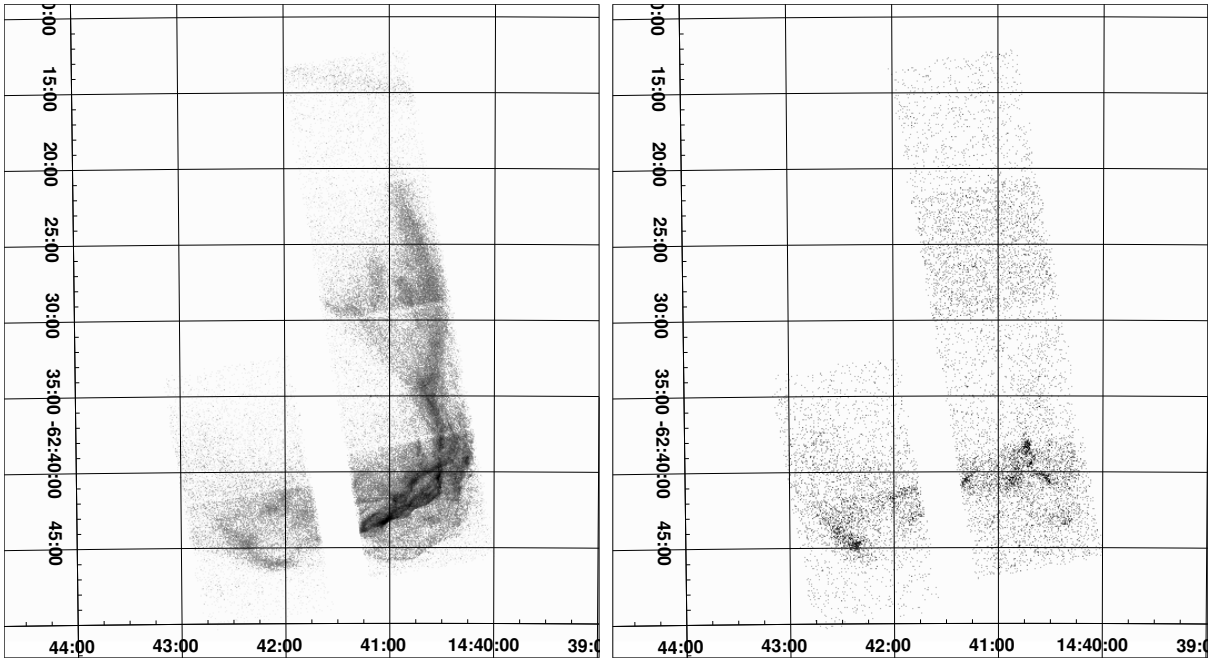

Fig. 7.28.— South-western shell image of RCW 86 binned with 1 arcsec in the 0.5–2.0 keV (left) and 2.0–8.0 keV band (right), with J2000 coordinates. The scales are in logarithmic in both images.

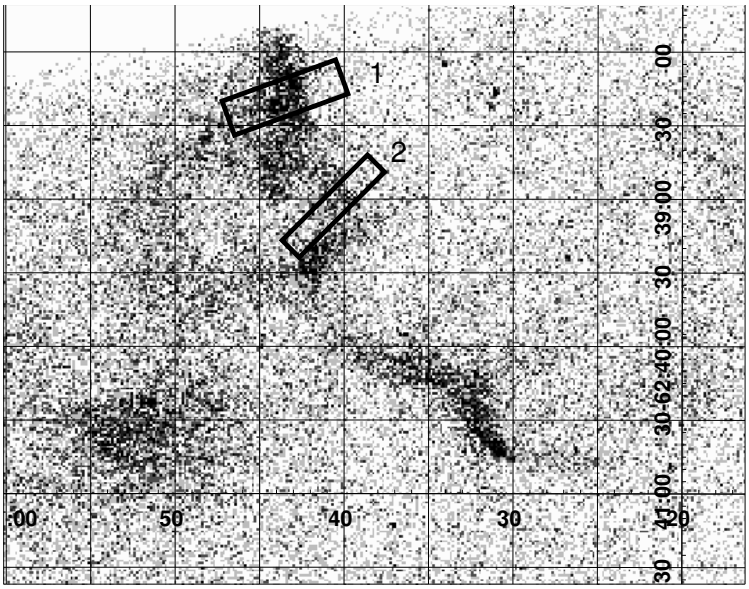

Fig. 7.29.— Close-up view of RCW 86 south-western region in the 2.0–10.0 keV band, binned with 2bin (= 1 arcmin). The regions for analyses of filaments are shown with solid lines.

up view of south-western corner of RCW 86 in this band. We see rather clumpy filaments on the corner of the shell. Borkowski et al. (2001b) have already suggested that there is little correlation between thermal and non-thermal clumps.

We selected two regions for analyses of filaments as shown in Figure 7.29 and made profiles of these filaments as shown in Figure 7.30. These filaments have very thin edges in upstream like other SNRs, while those in downstream are rather broad. The fittings in the same way to the SN 1006 case have been done for the two filaments. The model eq.(6.2) was well fitted with both filaments as the best-fit models and values shown in Figure 7.30 and Table 7.7, respectively.

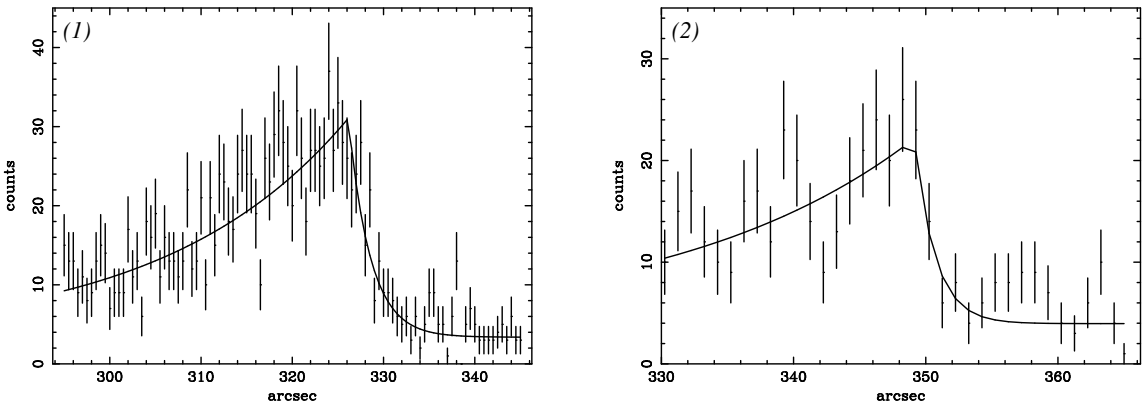

Fig. 7.30.— Profiles of the filament 1 and 2 in RCW 86. The best-fit models are shown in solid lines. The shock is running from left to right in both images.

Table 7.7: Best-fit parameters of fittings of the filaments.[a]

No.	A [counts arcsec^{-1}]	w_u [arcsec]	w_d [arcsec]	Reduced χ^2 [χ^2/d.o.f.]
1	27.7 (25.1–30.4)	2.39 (1.48–3.34)	20.1 (17.3–23.8)	113.4/95
2	18.2 (14.2–22.9)	1.56 (0.49–4.79)	18.2 (11.8–35.6)	46.8/31

[a]: Parentheses indicate single-parameter 90% confidence regions.

Spectral Analyses

The spectral analyses for these filaments have been done in the same way to the SN 1006 case. The background were selected in the downstream regions, which were free from both thermal and non-thermal emissions. The combined spectrum of these filaments is shown in Figure 7.31. They are hard and have little line-like features, and were well fitted with both a power-law model and

nei model with an absorption. The best-fit models and parameters are shown in Figure 7.31 and Table 7.8, respectively.

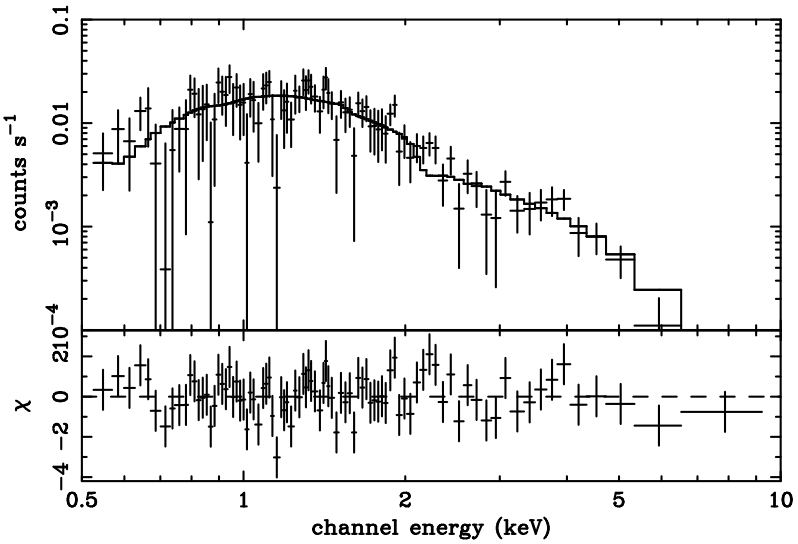

Fig. 7.31.— The combined spectrum of the filaments 1 and 2 in RCW 86 south-western shell. Best-fit model for power-law fittings are shown in solid lines.

7.4.5 Discussion for RCW 86

Under the assumption that the emission from these filaments is thermal, the temperature is much higher than those of ordinary SNRs and previous reports on RCW 86 (Bamba et al., 2000; Borkowski et al., 2001b; Rho et al., 2002). The low abundance is also unnatural for the thermal plasma in SNRs. Then, we treat the spectra of the filaments as non-thermal, same as other young SNRs. Their shapes and locations, however, are a little different from those in other SNRs; they are clumpy and are located in the inner region of thermal emission. This part of the shell is colliding with dense gas just now (Rodgers et al., 1960), then there may be a reverse shock which accelerates cosmic rays. Molecular cloud observations with better spatial resolution are necessary to confirm the hypothesis.

The fitting with *srcut* model has been done with a fixed radio index at 1 GHz of 0.6 (Caswell et al., 1975). The model was also statically accepted for all filaments with best-fit values in Table 7.8. The photon index and roll-off frequency of these filaments are a little harder than the previous results for the entire region of RCW 86 south-western shell (Bamba et al., 2000; Borkowski et al., 2001b) and other filaments (Rho et al., 2002). We can consider two reasons; the background region

Table 7.8: Best-fit parameters for the filaments.[a]

Parameters	1	2	Total[b]
Power-law			
Γ	2.5 (2.2–2.8)	2.5 (2.1–3.2)	2.4 (2.2–2.7)
$N_{\rm H}$[c]	5.4 (4.3–6.9)	2.7 (1.1–4.1)	4.7 (4.2–6.0)
Flux[d]	1.4×10^{-13}	3.2×10^{-14}	1.8×10^{-13}
χ^2/d.o.f.	68.9/60	25.7/27	82.2/87
srcut[e]			
$\nu_{rolloff}$[f]	2.0 (0.77–5.9)	1.3 (0.29–12)	2.1 (1.0–5.9)
$N_{\rm H}$[c]	4.8 (4.2–5.7)	2.3 (1.4–3.5)	4.3 (3.7–5.0)
$\Sigma_{\rm 1GHz}$[g]	1.9 (1.7–2.2)	0.51 (0.39–0.64)	2.2 (2.0–2.5)
χ^2/d.o.f.	68.8/60	25.0/27	80.8/87
nei			
kT (keV)	2.5 (1.8–3.4)	1.4 (1.0–2.2)	2.1 (1.6–2.6)
abundance[h] ...	0.03 (<0.12)	0.27 (0.02–1.0)	0.11 (<0.25)
$n_e t$[i]	(not determined)	3.5 (2.0–5.2)	4.3 (<8.0)
EM[j]	2.1 (1.6–2.8)	0.82 (0.49–1.4)	3.3 (2.1–4.3)
$N_{\rm H}$[c]	5.7 (3.3–8.3)	7.0 (3.2–9.4)	7.0 (3.1–9.2)
χ^2/d.o.f.	67.2/58	18.7/25	7.0 (3.1–9.1)

[a]: Parentheses indicate single-parameter 90% confidence regions.

[b]: Combined results of filament No.1–2.

[c]: Absorption column in the unit of $10^{21}{\rm cm}^{-2}$.

[d]: Absorbed flux in the 0.5–10.0 keV band in the unit of ergs ${\rm cm}^{-2}{\rm s}^{-1}$.

[e]: The radio spectral index is frozen to be 0.6 (Caswell et al., 1975).

[f]: Roll-off frequency in the unit of 10^{17} Hz.

[g]: Flux density at 1 GHz in the unit of 10^{-2} Jy.

[i]: Ionization time-scale in the unit of 10^9 s ${\rm cm}^{-3}$, where $n_{\rm e}$ and $t_{\rm p}$ are the electron density and age of the plasma.

[j]: Emission measure $EM = \int n_{\rm e} n_{\rm p} dV \simeq n_{\rm e}^2 V$ in the unit of $10^{55}{\rm cm}^{-3}$, where $n_{\rm p}$ and V are the proton density and the plasma volume, respectively. The distance to RCW 86 is assumed to be 2.8 kpc.

inside of the SNR may make the spectra harder by inappropriate subtraction of thermal emission. Or, this may caused by the same reason in the SN 1006 case, implying that the acceleration sites are concentrated on the shock front.

Here, we estimated the magnetic fields and the maximum energy of electrons in the same way to the SN 1006 case. We used the values of

$$w_u = 2.06\ (1.09 - 3.92)\ [\mathrm{arcsec}] = 2.8\ (1.5 - 5.3) \times 10^{-2}\ [\mathrm{pc}]\ , \tag{7.33}$$

$$w_d = 19.3\ (15.1 - 28.5)\ [\mathrm{arcsec}] = 0.26\ (0.21 - 0.39)\ [\mathrm{pc}]\ , \tag{7.34}$$

$$\nu_{rolloff} = 2.1\ (1.0 - 5.9)\ [\times 10^{17}\ \mathrm{Hz}]\ , \tag{7.35}$$

$$t_{age} = 1816\ [\mathrm{yrs}]\ \text{at the observation time}\ , \tag{7.36}$$

$$u_s = 562\ [\mathrm{km\ s^{-1}}]\ , \tag{7.37}$$

where we assumed that the distance to RCW 86 is 2.8 kpc (Rosado, et al., 1996). Consider the age limited case for the first. The acceleration time scale t_{acc} becomes

$$t_{acc} = \frac{4}{u_s}(w_u + w_d) = 6.3 \times 10^{10}\ [\mathrm{sec}] = 2.1 \times 10^3\ [\mathrm{years}]\ , \tag{7.38}$$

which is roughly the same with the value of $t_{age} = 1816$ yrs, implying that the age limited case is valid for RCW 86 case. We searched for allowed regions in ξ_u–ξ_d map with various θ ($\theta = 0°$, $30°$, $60°$, and $90°$) and found that they are found only with $\theta = 90°$, which is shown as shaded regions in Figure 7.32. The allowed ξs are rather large, $\xi_u > 50$ and $\xi_d > 10$. The magnetic field and the maximum energy of electrons can be calculated as

$$B_u = \frac{B_d}{4} = 1 - 3\ [\mu\mathrm{G}]\ , \tag{7.39}$$

$$E_{max} = 41 - 172\ [\mathrm{TeV}]\ . \tag{7.40}$$

We consider the loss limited case for the next step. Curiously, the allowed θ is in the small range around nearly $90°$, similar to those in the age limited case. The allowed ξ_u and ξ_d pairs are shown as shaded regions in Figure 7.33, which is very similar to the Figure 7.32. Therefore, the predicted magnetic field and maximum energy are also similar to those in the age limited case;

$$B_u = \frac{B_d}{4} = 1 - 3\ [\mu\mathrm{G}]\ , \tag{7.41}$$

$$E_{max} = 41 - 172\ [\mathrm{TeV}]\ . \tag{7.42}$$

The estimated magnetic field is rather small for the interstellar magnetic field.

7.5 30 Dor C

7.5.1 Previous Observations

30 Doradus (30 Dor) is the brightest H II complex associated with very active star forming regions. A radio source was discovered by Le Marne (1968) to the south-west of 30 Dor and was named

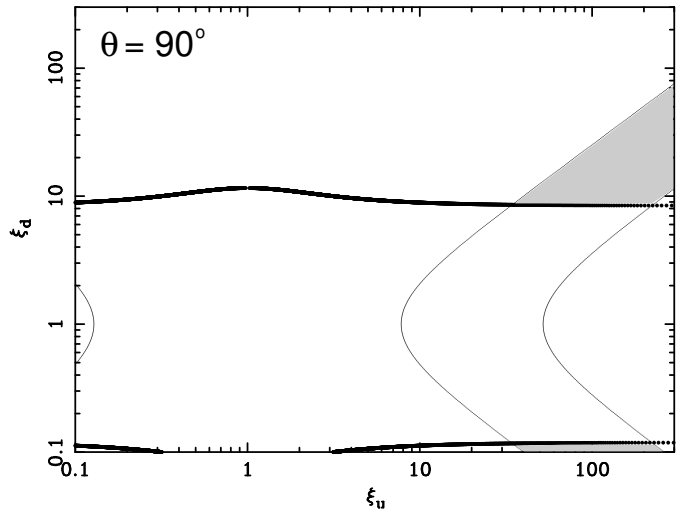

Fig. 7.32.— Allowed regions in ξ_u–ξ_d planes with various θ (shaded regions) in the age limited cases. Thin and bold lines represents the condition written in eqs.(6.13) and (6.17) respectively, with parameters of RCW 86.

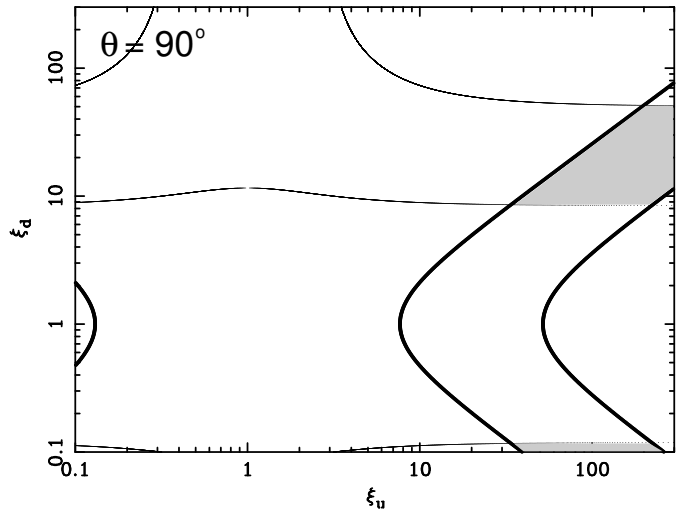

Fig. 7.33.— Allowed regions in ξ_u–ξ_d planes with various θ (shaded regions) in the loss limited cases. Bold and thin lines represents the condition written in eqs.(6.30) and (6.31), respectively, with parameters of RCW 86.

30 Dor C, which is now categorized as a super-bubble (SB). Mills et al. (1984) found a shell-like structure in the 843 MHz band observation with a radius of about 3 arcmin, corresponding to ∼40 pc at a 50 kpc distance (Feast, 1999). Along the radio shell, complex Hα, Hβ, and [SII] emissions were found, which are bright in the south-east, but dim in the other part (Mathewson et al., 1985). In the X-ray band, *Einstein* detected the eastern shell of 30 Dor region for the first time (Long, Helfand, & Grabelsky, 1981; Chu & Mac Low, 1990). Dunne, Points, & Chu (2001) reported that the *ROSAT* spectrum required a thermal model with a rather high temperature (∼1 keV). Itoh et al. (2001) found non-thermal X-rays in the *ASCA* data, but could not resolve spatially the thermal and non-thermal components in the SB. Recently, Dennerl et al. (2000) found a complete ring in soft and hard X-rays with a diameter of ∼6 arcmin with *XMM-Newton*. Bamba et al. (2004) unveiled the hard emission of 30 Dor C using both *Chandra* and *XMM-Newton* data; this SB emits non-thermal X-rays from the shell. This is the first discovery of non-thermal X-ray emitting shell out of our Galaxy.

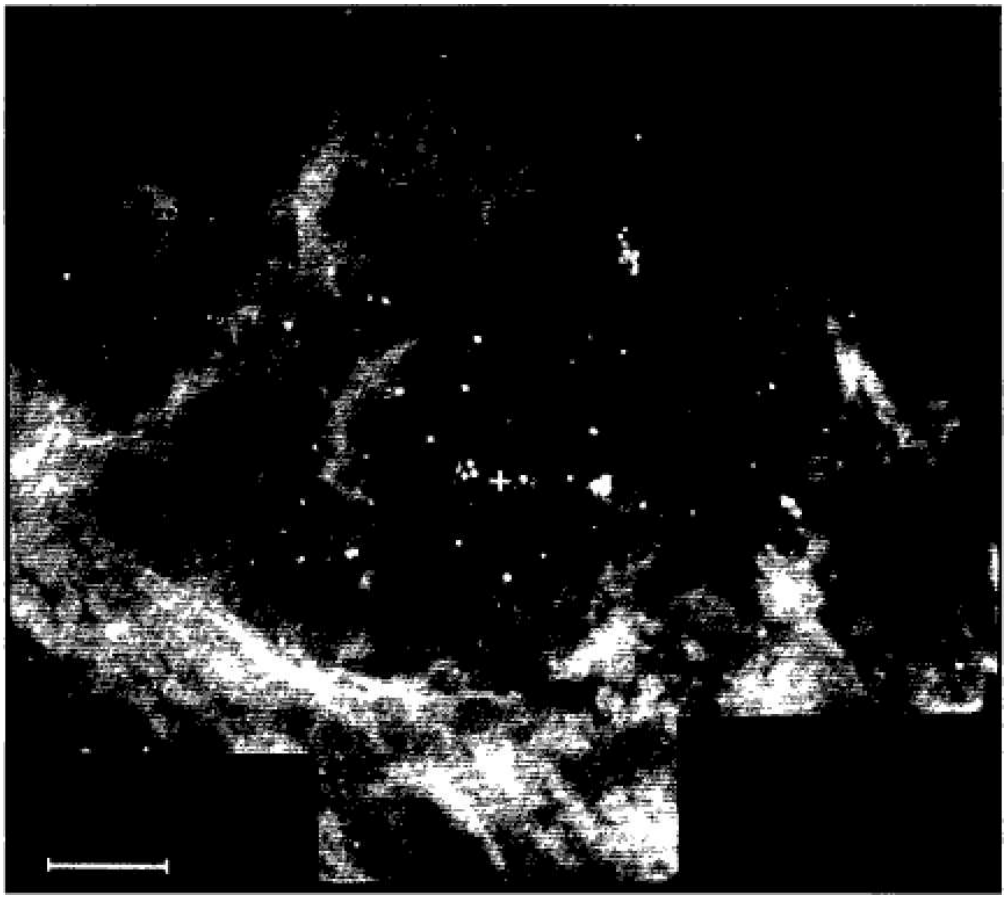

Fig. 7.34.— Hα image of 30 Dor C (Mathewson et al., 1985).

7.5.2 Observations and Data Reduction

Chandra observed SN 1987A for several times with the Advanced CCD Imaging Spectrometer (ACIS) S array. Some of the SN 1987A observations covered the 30 Dor C region by chance, which is located at about 5 arcmin northeast from SN 1987A. In order to study the diffuse structure of 30 Dor C, we selected two observations in which grating instrument is removed from the X-ray mirror axis (Observation ID = 1044 and 1967; hereafter Obs.1 and 2). The observed dates and targeted positions are given in Table 7.9. Data acquisition from the ACIS was made in the Timed-Exposure Faint mode with the readout time of 3.24 s in both observations. The data reductions and analyses were made using the *Chandra* Interactive Analysis of Observations (CIAO) software version 2.3. For the Level 1 processed events provided by the pipeline processing at the *Chandra* X-ray Center, we applied the Charge Transfer Inefficiency (CTI) correction, and selected *ASCA* grades 0, 2, 3, 4, and 6, as X-ray events. High energy events due to charged particles and hot and flickering pixels were removed. There are some "streaks" in the CCD chip S4, which are caused by a random deposition of significant amount of charges in pixels along the row during the serial read-out process. These "streak" events were removed by using the program *destreak*[1] in CIAO. The total available times for each observation, after the screening, are listed in Table 7.9.

XMM-Newton (Jansen et al., 2001) also observed SN 1987 A and the 30 Dor region several times; the satellite has the spatial resolution of $\sim$14 arcsec and a relatively wide FOV with a radius of 15 arcmin. For the spectral analyses, we selected two observations (Observation ID = 0104660301 and 0113020201; hereafter Obs.3 and 4) which cover 30 Dor C and are relatively free from high background flares due to low energy protons. The observed dates and targeted positions are shown in Table 7.9. In both the observations, only the metal oxide semiconductors (MOS) CCDs, which have the energy range of 0.1–10.0 keV and the similar energy resolution to ACIS (Turner et al., 2001), were operated in full frame mode, with the medium filter (Stephan et al., 1996; Villa et al., 1998) for blocking ultra-violet photons. The data reductions and analyses were made using the *XMM-Newton* Standard Analysis System (SAS; Watson et al 2001) version 5.4.1; we performed the basic pipeline process following the SAS guide. The background level is largely changed, particularly in Obs. 4, hence we removed the data at high background (>0.6 cnts s^{-1} in the 10.0–15.0 keV band). The exposure time in each observation after the screenings are listed in Table 7.9.

7.5.3 Analyses and Results

Diffuse Emission and Point-like Sources

Figure 7.35 shows the soft (0.7–2.0 keV) and hard (2.0–7.0 keV) band *Chandra* images around 30 Dor C, in which the two observations (Obs.1 and 2) are combined with a correction of exposure

[1]See http://asc.harvard.edu/ciao2.3/ahelp/destreak.html.

Table 7.9: Observation log around 30 Dor C.

	Satellite	Obs ID (J2000)	Position (RA, DEC)	Date (yyyy/mm/dd)	Exposure (ks)
Obs.1	*Chandra*	1044	($05^h32^m22^s.0$, $-69^d16^m33^s.0$)	2001/04/25	18
Obs.2	*Chandra*	1967	($05^h32^m22^s.0$, $-69^d16^m33^s.0$)	2000/12/07	99
Obs.3	*XMM-Newton*	0104660301	($05^h35^m28^s.0$, $-69^d16^m11^s.0$)	2000/11/25	21
Obs.4	*XMM-Newton*	0113020201	($05^h37^m47^s.6$, $-69^d10^m20^s.0$)	2001/11/19	16

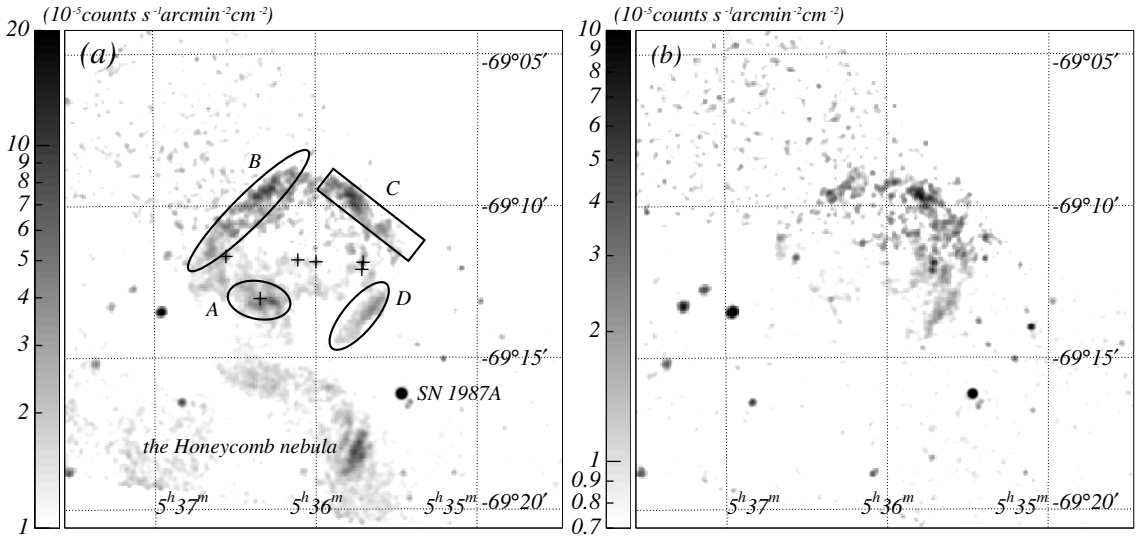

Fig. 7.35.— *Chandra* ACIS images around 30 Dor C in the 0.7–2.0 keV band (a) and in the 2.0–7.0 keV band (b), with J2000 coordinates. The scales are logarithmic with the unit of $\times 10^{-5}$ counts $s^{-1}arcmin^{-2}cm^{-2}$ as shown in the left bar for each image. The source regions used for the spectral analyses are shown by the solid lines in the left panel (Figure 7.36, Table 7.11 and 7.12). The crosses represent the position of the detected point sources shown in Table 7.10. The position of SN 1987A (Burrows et al., 2000; Park et al., 2002; Michael et al., 2002) and the Honeycomb nebula (Dennerl et al., 2000) are also shown.

times (see also Figure C.6). A clear shell-like structure with a radius of $\sim$ 170 arcsec ($R \sim 40$ pc-radius at the 50 kpc distance) is seen in both the bands. In detail, however, the morphologies are different from each other; the entire shell is seen in the soft band, whereas the hard X-rays are visible only at the western part. Catalogued SNRs, the Honeycomb nebula (SNR 0536−69.3) and SN 1987A are also seen mainly in the soft band (see Figure 7.35 and Figure C.6). The X-ray features of these objects have been reported with *XMM-Newton* (Dennerl et al., 2000) and *Chandra* (Burrows et al., 2000; Park et al., 2002; Michael et al., 2002) monitoring observations.

In addition to the diffuse structure, some point-like sources are found inside 30 Dor C. The exposure time of the *XMM-Newton* observation is short, most of the data suffer from a high background, and the spatial resolution is not sufficient. Hence, we concentrated on the *Chandra* data for the point source search and analysis. At first, point sources are searched with the *wavdetect* software[2] in CIAO in the 0.5–8.0 keV band images, then manually inspected for any spurious point-like structure due mainly to a part of the diffuse emission. We thus found six point sources with the significance level of $>7.0\sigma$, as shown in Figure 7.35 and Table 7.10. For these six point sources, we searched for optical, infrared, and radio counterparts and found that three (No.1, 3, and 4) coincide at the positions of the brightest star clusters: α, β, and γ (Lortet & Testor, 1984). We therefore checked further any X-ray emission from the other clusters, (δ, ϵ, and ζ), which are also the members of the OB association LH 90 (Lucke & Hodge, 1970) encompassed by the 30 Dor C shell. However, we found no excess X-rays from these clusters above the 3σ limit. We also searched for X-ray counterparts from *ROSAT* PSPC and HRI catalogues (Haberl & Pietsch, 1999; Sasaki, Haberl, & Pietsch, 2000), but found no candidate.

Table 7.10: Point source data around 30 Dor C.[a]

No.	Name CXO J05...	PSF[b] $''\times''$	SM[c]	Γ/kT $\cdots$ /[keV]	$N_{\rm H}^{\rm LMC}$[d] [$\times 10^{22}$ Hcm^{-2}]	Flux[e] [ergs cm^{-2}s^{-1}]	L_X [f] [ergs s^{-1}]	χ^2/d.o.f.
1 ..	3542.4−691152	7.0×3.6	MK	2.1 (1.4–3.6)	3.5 (2.5–5.1)	1.8×10^{-14}	1.2×10^{34}	9.53/12
2 ..	3542.9−691206	7.3×3.8	PL	2.1 (1.4–3.2)	7.7 (4.4–13)	2.0×10^{-14}	1.5×10^{34}	8.25/13
3 ..	3559.9−691150	7.1×4.5	PL	1.7 (1.3–2.6)	0.13 (< 1.3)	6.5×10^{-15}	2.2×10^{33}	4.03/7
4 ..	3606.6−691147	8.3×6.6	MK	1.0 (0.19–1.3)	0 (< 1.9)	2.8×10^{-15}	1.1×10^{33}	8.64/9
5 ..	3620.7−691303	8.5×4.4	PL	1.9 (1.5–2.4)	0 (< 0.22)	8.9×10^{-15}	3.1×10^{33}	19.8/20
6 ..	3633.3−691140	10.7×8.5	PL	1.8 (1.5–2.3)	0.5 (0.08–1.1)	2.0×10^{-14}	7.8×10^{33}	21.4/18

[a]: Parentheses indicate single-parameter 90% confidence regions.
[b]: The elliptic PSF size.
[c]: Spectral model; PL: power-law, MK: thin thermal plasma in collisional equilibrium (Mewe et al., 1985; Kaastra et al., 1992) with the abundance of 0.3 solar.
[d]: Absorption column in the LMC. The abundance is assumed to the average LMC values (Russel & Dopita, 1992; Hughes et al., 1998).
[e]: Flux in the 0.5–9.0 keV band.
[f]: Intrinsic luminosity (absorptions are removed) in the 0.5–9.0 keV band, at the LMC distance of 50 kpc (Feast, 1999).
Note — No.1, 3 and 4 have the optical counterparts, the stellar clusters α, β, and γ respectively (Lortet & Testor, 1984).

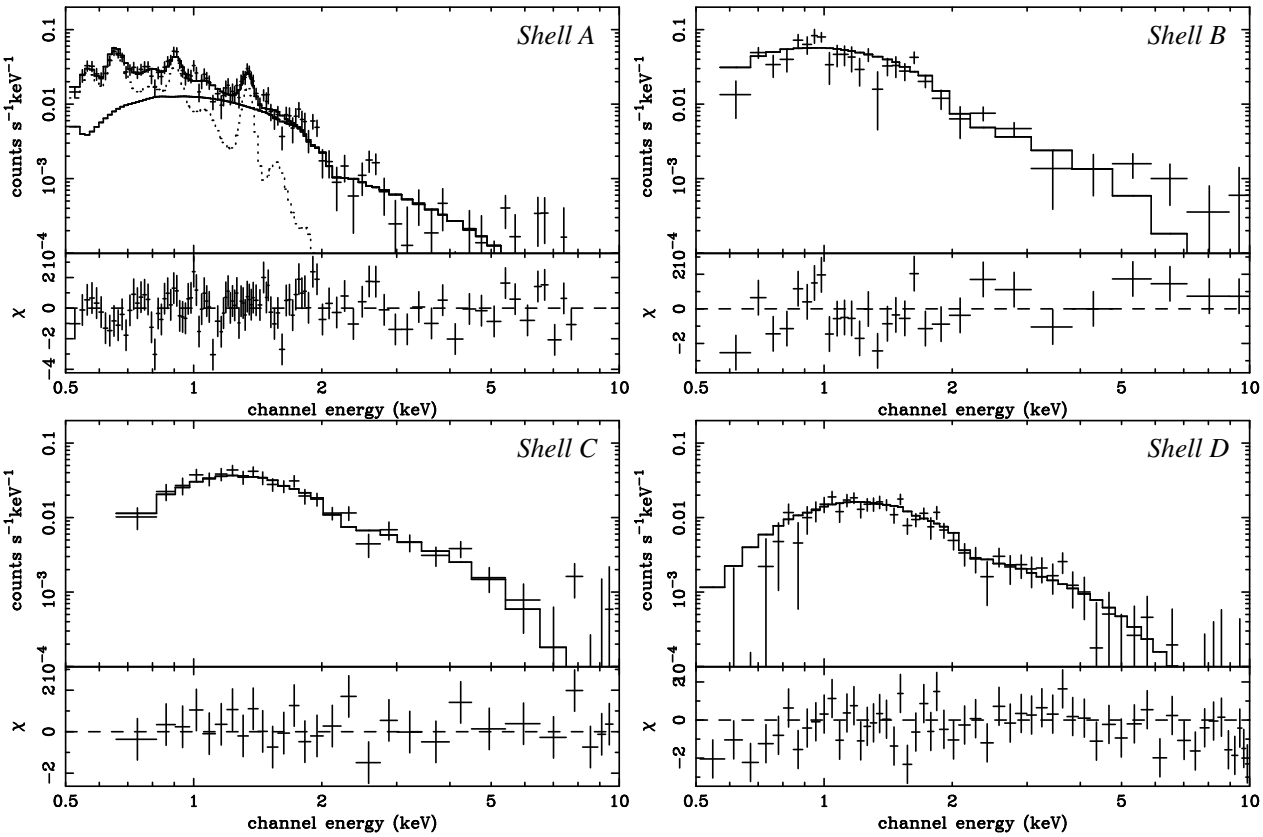

Fig. 7.36.— Upper panels: The background-subtracted spectra for the shells A–D (crosses). Although the spectral fittings were made with both the *Chandra* and XMM-Newton data simultaneously, only *Chandra* data and results are shown for brevity. The best-fit models are shown with solid (power-law) and dotted (NEI) lines. Lower panels: The data residuals from the best-fit models. These figures are credited by Bamba et al. (2004).

Spectra

In the *Chandra* observations, we can see that the diffuse structure consists of several shell fragments (see Figure 7.35 and Figure C.6), and the whole structure is widely spread over the two observed regions with the different configuration of the CCD types (back-illuminated and front-illuminated). Therefore, a spectral analysis on all the diffuse structures are technically and scientifically complicated. For this reason, we divided the diffuse structure into four regions (hereafter shells A–D) as shown in Figure 7.35, and performed the spectral analysis separately for each region. We excluded all the detected point sources from each shell. The background regions were also selected separately for each shell from the source-free regions in the same CCD and observations as those of the shells.

The *XMM-Newton* fields covered the whole diffuse structure. However, for consistency with the *Chandra* analysis, we divided the diffuse structure into shells A–D, the same as in the *Chandra* case. The background regions were selected from the source-free regions in the same observation. The spectra of each shell taken from all the available observations with *Chandra* and *XMM-Newton* were fitted simultaneously. However, for simplicity, we show only the *Chandra* spectra (background-subtracted) and the fitting results in Figure 7.36.

The spectrum of shell A shows many line-like structures with the center energies at 0.58, 0.68, 0.92, and 1.35 keV, which correspond to the emission lines of He-like O Kα and Kβ, He-like Ne, and He-like Mg, respectively. We therefore fit the spectrum with a thin-thermal plasma model in non-equilibrium ionization (NEI) (*nei*; Borkowski et al. 2001a) with the mean LMC abundances (Russel & Dopita, 1992; Hughes et al., 1998). The interstellar absorption in our Galaxy and LMC are treated separately. The Galactic absorption column is estimated using the HI data by Dickey & Lockman (1990) as $N_{\rm H,HI} = 6.35 \times 10^{20}$ cm^{-2}. Arabadjis & Bregman (1999) reported that the value of $N_{\rm H}$ measured in the X-ray band is twice that of $N_{\rm H,HI}$ in the case of $|b| > 25^{\circ}$ and $N_{\rm H,HI} > 5 \times 10^{20}$ cm^{-2}. Therefore, we fixed the galactic absorption column to be $N_{\rm H} = 1.27 \times 10^{21}$ cm^{-2}; we used the cross sections by Morrison & McCammon (1983) and the solar abundances (Anders & Grevesse, 1989). The absorption column in the LMC was, on the other hand, treated as a free parameter with the mean LMC abundance (Russel & Dopita, 1992; Hughes et al., 1998).

This thin-thermal plasma model was rejected with χ^2/degree of freedom (d.o.f.) = 331.8/211 even we allow the abundances to be free, leaving a systematic data residual at high energy band. We hence added a power-law component on the thin-thermal model. Since the two-component model still leaves large residuals at about 0.8 keV and 1.3 keV, we allow the abundance of Fe and Mg in the thermal plasma ("NEI" component) to be independent from other elements. The fitting is then greatly improved with a χ^2/d.o.f = 264.6/209. Although this two-component model is still rejected in a statistical point of view, further fine tuning on the model is beyond the scope of this paper. Figure 7.36 and Table 7.11 show the best-fit models and parameters, respectively.

Unlike shell A, the X-ray spectra of shells B–D are hard and featureless, suggesting non-thermal

[2]See http://asc.harvard.edu/udocs/docs/swdocs/detect/html/.

Table 7.11: Best-fit parameters of the shell A.[a]

Parameters	nei	Power-law
kT/Γ [keV/—]	0.21 (0.19–0.23)	2.9 (2.7–3.1)
$n_{\rm e}t_{\rm p}$[b] [10^{12}cm^{-3}s]	9.9 (>1 .4)	···
EM[c] [10^{58} cm^{-3}]	2.6 (2.1–2.8)	···
[Mg/H][d]	3.3 (2.5–4.0)	···
[Fe/H][d]	0.10 (0.06–0.14)	···
Flux[e] [ergs cm^{-2}s^{-1}]	6.8×10^{-14}	8.4×10^{-14}
$N_{\rm H}^{\rm LMC}$[f] [$\times 10^{22}$ cm^{-2}] ...	0.24 (0.21–0.28)	··· [g]

[a]: Parentheses indicate single-parameter 90% confidence regions.

[b]: Ionization time-scale, where $n_{\rm e}$ and $t_{\rm p}$ are the electron density and age of the plasma.

[c]: Emission measure $EM = \int n_{\rm e} n_{\rm p} dV \simeq n_{\rm e}^2 V$, where $n_{\rm p}$ and V are the proton density and the plasma volume, respectively. The distance to LMC is assumed to be 50 kpc (Feast, 1999).

[d]: abundance ratio relative to the solar value (Anders & Grevesse, 1989).

[e]: Flux in the 0.5–9.0 keV band.

[f]: Absorption column in the LMC. The abundances are assumed to be the average LMC values (Russel & Dopita, 1992; Hughes et al., 1998).

[g]: Fixed to the same value as that for the NEI component.

origin. In fact, a thin thermal model fitting requires an unrealistically high temperature (> 2 keV) and low abundances ($Z < 0.3$). We therefore fitted the spectra with a power-law model with absorption, which is calculated in the same way as that for shell A, and found acceptable fits for all of the spectra. The best-fit models and parameters are shown in Figure 7.36 and Table 7.12, respectively.

Table 7.12: Best-fit parameters of the shells B–D.[a]

	B	C	D
Power-law			
Photon Index.....	2.7 (2.5–2.9)	2.3 (2.1–2.4)	2.5 (2.3–2.7)
Flux[b] [ergs $s^{-1}cm^{-2}$]	4.7×10^{-13}	4.5×10^{-13}	1.5×10^{-13}
$N_{\rm H}^{\rm LMC}$ [10^{22} cm^{-2}][c]	0.10 (0.06–0.19)	1.1 (0.94–1.4)	1.0 (0.85–1.3)
χ^2/d.o.f.....	193.0/138	68.3/84	121.5/110
srcut ($\alpha = 0.5$)			
$\nu_{\rm rolloff}$ [10^{16} Hz].....	6.2 (4.1–7.9)	24 (15–47)	12 (6.4–23)
Flux density at 1 GHz [10^{-2}Jy]....	1.9 (1.5–3.0)	0.71 (0.67–0.75)	0.42 (0.25–0.83)
$N_{\rm H}^{\rm LMC}$ [10^{22} cm^{-2}][c].....	(<0.04)	1.0 (0.90–1.1)	0.89 (0.75–1.0)
χ^2/d.o.f.....	195.5/138	67.0/84	120.2/110
srcut ($\alpha = 0.6$)			
$\nu_{\rm rolloff}$ [10^{16} Hz].....	8.0 (5.3–11)	36 (20–75)	16 (8.3–35)
Flux density at 1 GHz [10^{-2}Jy]....	11 (8.2–16)	4.1 (3.9–4.3)	2.5 (1.6–4.6)
$N_{\rm H}^{\rm LMC}$ [10^{22} cm^{-2}][c].....	(<0.01)	1.0 (0.91–1.2)	1.1 (1.0–1.3)
χ^2/d.o.f.....	195.2/138	67.1/84	121.8/110

[a]: Parentheses indicate single-parameter 90% confidence regions.

[b]: Flux in the 0.5–9.0 keV band.

[c]: Absorption column in the LMC. The abundance is assumed to be the average LMC values (Russel & Dopita, 1992; Hughes et al., 1998).

It is conceivable that the spectra of shells B–D may include a small fraction of the thin-thermal component found in shell A. We therefore added the same thin-thermal spectrum as that for shell A, and fitted with this composite model (thin-thermal plus power-law). The free parameters are normalizations of the two components: power-law index and $N_{\rm H}$ value. However, no significant fraction of the thin thermal component is found from shells B–D.

For all of the point sources, the X-ray photons are collected from an ellipse with the radii of the point spread function (PSF) as listed in Table 7.10. We note that all of the sources are located far from the on-axis position of the X-ray mirror, and hence the PSFs are larger than the best value of *Chandra* PSF (~ 0.5 arcsec on the aim point). The background regions were selected from source free regions in the same way as the diffuse emissions. We first fitted the spectra with a thin-thermal plasma model in collisional equilibrium (*MEKAL*; Mewe, Gronenschild, & van den

Oord 1985; Kaastra 1992) with an absorption calculated in the same way as diffuse emission. The abundances are fixed to be 0.3 solar, the average value of interstellar medium in the LMC. The fittings are acceptable for two sources (No. 1 and 4) with reasonable temperature (2.1 and 1.0 keV), but for the spectra of the other 4 sources the models are either rejected or require unreasonably high temperature. We therefore fitted the spectra of these sources with a power-law model. The best-fit parameters and the reduced χ^2s are listed in Table 7.10.

7.5.4 Discussion for 30 Dor C

The Absorption

The absorption columns of the north-eastern shells (shells A and B) are similar to those of the most sources in the LMC ($\sim 10^{21}$ cm^{-2}), whereas those of the other shells (C and D) are significantly larger ($\sim 10^{22}$ cm^{-2}) than the typical LMC absorption. A similar trend was found for the point sources; those in the western half, No.1 and 2, have a larger $N_{\rm H}$ ($\sim 10^{22}$ cm^{-2}) than those in the eastern sources, No.3–6 ($\leq 10^{21}$ cm^{-2}). Since Dunne et al. (2001) has already reported this tendency, we have thus confirmed the results with better spatial and spectral capability of *Chandra*. This systematic increase of absorption toward the western region of 30 Dor C may be due to the extra absorption of a molecular cloud located in front of the western half of 30 Dor C. To verify our conjecture, we searched for the molecular cloud in the CO map (Figure 2(a) in Yamaguchi et al. 2001) and found the candidate with the intensity of $I({\rm CO}) \sim 3.6$ K km s^{-1}. With the conversion factor of $N({\rm H_2})/I({\rm CO}) \sim 9 \times 10^{20}{\rm cm^{-2}(K\ km\ s^{-1})^{-1}}$ (Fukui et al., 1999), the estimated absorption column due to the molecular cloud is $N_{\rm H}^{MC} \sim 6.5 \times 10^{21}$ cm^{-2}, which is consistent with our result.

The Thermal Emission

30 Dor C is a SB made by strong stellar wind and/or successive supernova explosions of massive stars located in the OB star association LH 90. The age of this star association, or that of 30 Dor C is in the order of a few to 10 Myr (Lucke & Hodge, 1970). The thermal emissions are enhanced in the south-eastern side of 30 Dor C (around shell A). The position of this component coincides with that of the Hα emission (Dunne et al., 2001). The plasma temperature of 30 Dor C is rather high compared to those of other LMC SBs (Dunne et al., 2001), although it becomes significantly lower than previous results (Dunne et al., 2001). Perhaps due to the poor spectral resolution of *ROSAT*, previous observations could not resolve the power-law component (hard spectrum) from the thermal emission.

The X-ray luminosity of 30 Dor C is significantly lower than that of the other SBs. With the assumption that the plasma in shell A distributes uniformly in the ellipsoid with the radii of $58'' \times 34'' \times 34''$ (total volume $V = 1.2 \times 10^{59}$ cm^3), the mean density $n_{\rm e}$, thermal energy E and the age of the plasma $t_{\rm p}$ are calculated as follows using the emission measure $E.M. = n_{\rm e}^2 V$ and

ionization time scale (see Table 7.11):

$$n_{\rm e} = 4.7\ (4.2-4.8)\times 10^{-1}\ [{\rm cm}^{-3}], \quad (7.43)$$

$$E \simeq 3n_{\rm e}kTV = 5.7\ (4.6-6.4)\times 10^{49}\ [{\rm ergs}], \quad (7.44)$$

$$t_{\rm p} = 6.7\ (>0.9)\times 10^{5}\ [{\rm yrs}]. \quad (7.45)$$

Together with the Hα emission around shell A (Dunne et al., 2001), we infer that the shell of 30 Dor C collides with dense matter and temporally emits thermal X-rays with a relatively high temperature. The overabundance of light element (Mg) relative to heavier element (Fe) may indicate that a type II SN occurred (Tsujimoto et al., 1995). Thus, the progenitor is a massive star which is a member of cluster LH 90 (Lucke & Hodge, 1970) near the center of 30 Dor C.

The Non-Thermal Emission

In the 843 MHz band, Mills et al. (1984) found a clear radio shell, which is brightest on the south-western side (around shells C and D) and dim on the eastern side. The non-thermal X-ray emissions are enhanced at the radio bright shell. This fact implies that the non-thermal X-rays are emitted by the same mechanism as the radio band. Therefore the non-thermal X-rays are likely synchrotron radiation from the accelerated electrons like SN 1006 (Koyama et al., 1995) and other SNRs which accelerate particles up to TeV. The X-ray photon index of 2.1–2.9 (see Table 7.12) is, in fact, typical to synchrotron emissions.

To verify the synchrotron origin, we fitted the X-ray spectra with a *srcut* model (Reynolds, 1998; Reynolds & Keohane, 1999). Since the radio index data is not accurate due to large background and contamination of thermal emission (Mathewson et al., 1985), we fixed the spectral index (α) at 1 GHz to be 0.5, which is expected from the first-order Fermi acceleration and similar to that of SN 1006 ($\alpha = 0.57$; Allen, Petre, Gotthelf 2001).

The fittings were statistically acceptable and the best-fit parameters are listed in Table 7.12. The best-fit cutoff frequency is also similar to that of SN 1006, although the age of 30 Dor C may be in the same order of LH 90 (10 Myr; Lucke & Hodge 1970), which is far larger than SN 1006. This implies that, depending on the environment, acceleration of high energy electron up to the knee energy can continue for a far longer time than the previous consensus ($\sim 10^3$ yrs; Reynolds and Keohane 1999). The electron acceleration time may have been extended, because successive supernova explosions in 30 Dor C, possibly over the course of a few Myr, may more or less continuously produce high-energy electrons. The total luminosity of the non-thermal component ($\sim 5.3\times 10^{35}$ ergs s^{-1}) is about 10 times larger than that of SN 1006 (Koyama et al., 1995). This larger non-thermal flux in 30 Dor C would be due to the large energy supply by multiple successive supernova explosions.

The expected flux density at 1 GHz is 3.0 (2.4–4.6)$\times 10^{-2}$ Jy with $\alpha = 0.5$, which is significantly smaller than the observed value (1.0 Jy; Mills et al. 1984). This "inconsistency" is not relaxed even

if we assume larger radio index of $\alpha = 0.6$ (1.8 (1.4–2.5)$\times 10^{-1}$ Jy as shown in Table 7.12). We infer that the larger observed radio flux than that expected from X-rays would be due to either the contamination of thermal radio flux or large uncertainty of the background level (see Mills et al. 1984).

The Hα emission (Dunne et al., 2001) is anti-correlated with the non-thermal components. Similar features have been observed in some of other SNRs with synchrotron X-rays, SN 1006 (Winkler et al., 2003) and RCW 86 (Smith, 1997). Because the Hα region has higher density, it may have higher magnetic field. Therefore the maximum electron energy is limited by the quick synchrotron energy loss, leading to reduced non-thermal X-rays. The discovery of synchrotron X-ray shells from 30 Dor C is the first case in the SBs.

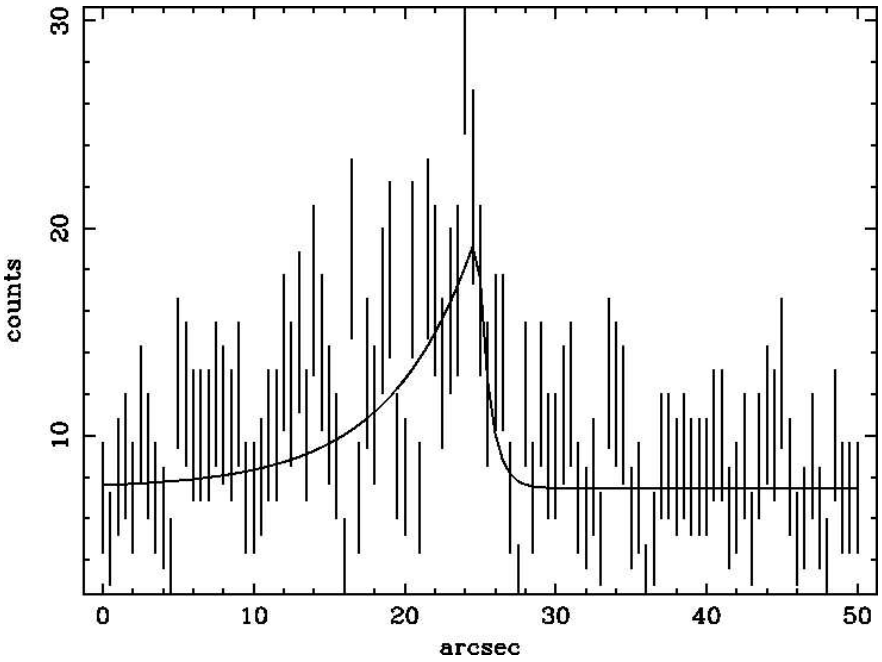

Fig. 7.37.— The profiles of shell D in the 2.0–10.0 keV band, binned with 0.5 arcsec. The best-fit models are also shown with solid lines. Upstream (south) is to the right and downstream (north) is to the left, respectively.

We made the profile of shell D, which has been observed with sufficient exposure time, in the 2.0–10.0 keV band as synchrotron X-ray band. Figure 7.37 shows the profile of shell D. In the same way of SN 1006 case, we fitted it with our empirical model shown in eq.(6.2) and got the best-fit values of

$$w_u = 0.72(0.23 - 1.2) \text{ arcsec} = 0.18(0.06 - 0.29) \text{ pc} \ , \quad (7.46)$$

$$w_d = 4.2(2.0 - 9.0) \text{ arcsec} = 1.0(0.49 - 2.2) \text{ pc} \ , \quad (7.47)$$

$$\chi^2/\text{d.o.f.} = 81.8/56 \ , \quad (7.48)$$

at 50 kpc distance (Feast, 1999), respectively. Since the shock velocity, the spectral index at 1 GHz, and age of 30 Dor C are unknown, we gave up the scale length analyses similar to those for other SNR cases.

Point Sources

We have identified three point-like X-ray sources (No. 1, 3, and 4) to the tight clusters of massive stars α, β, and γ. The spectrum of No.1 (α) is fitted with a thin thermal plasma model of $\sim$2.1 keV, which is consistent with stellar X-rays from massive stars. The cluster α is brightest of the three, with the X-ray luminosity of $\sim 10^{34}$ ergs s^{-1}. Optical spectroscopy of this cluster revealed that it includes one red giant and one Wolf-Rayet (WR) star (MG 41 and Brey 58; Lortet & Testor 1984). Hence, the latter is a possible counterpart of the 2 keV source. Then the X-ray luminosity is near the upper end of a massive star or its binary (Maeda et al., 1999). The star cluster γ also includes one OB star (Sk $-69^{\circ}212$; Sanduleak 1970) and the X-ray luminosity is consistent with that of a young massive star. Although the X-ray luminosity of No.3, a counterpart of the star cluster β, is also consistent with a massive young star, the best-fit photon index, $\sim$2 (see Table 7.10), is rather typical to a rotation powered neutron star, probably a stellar remnant of SN explosion in the active star cluster. The spectrum of No.3 (γ) is soft and well-fitted with a $kT = 1.0$ keV thermal plasma model, similar to a cluster α. The star cluster γ also includes one OB star (Sk $-69^{\circ}212$; Sanduleak 1970), and the X-ray luminosity is consistent with that of a young massive star.

The other three sources (No,2, 5, and 6) have no counterpart in optical, in infrared band (Breysacher, 1981; Lortet & Testor, 1984) nor in the SIMBAD data base. Their spectra are relatively hard, and are consistent with being background active galactic nuclei (AGNs), or stellar remnants (black hole or neutron star) by successive SN explosions.

In order to constrain the nature of the point-like X-ray sources with a power-law spectrum, we further examined the time variability with the Kolmogorov-Smirnov test (Press et al., 1992). However no significant time variability was found even between the two observations. For high resolution timing, we examined the *Chandra* High Resolution Camera (HRC) data (ObsID = 738), but no pulsation is found from any of these point sources.

Chapter 8

Discussion

The spatial and spectral analyses have been done for the filaments in five SNRs (SN 1006, Cas A, Kepler, Tycho, and RCW 86) and one super bubble (30 Dor C) in the previous chapters. In this chapter, we bring together our separate results summarized for these targets in § 8.1 and search for correlation in the observational parameters in § 8.2, discuss on what makes the evolution of the filaments in § 8.3, § 8.4, and § 8.5, and construct a scenario of cosmic ray acceleration in SNRs in § 8.6.

8.1 Summary of the results

We summarize our results of SNRs and a SB we analysed in Table 8.1. The curious fact is that the estimated t_{acc} is as same as t_{age}, except for Cas A. In the age limited cases, configurations in all SNRs require the nearly perpendicular magnetic field to the shock normal. On the other hand, the allowed θ are disunited for each SNR in the loss-limited case. The magnetic field strength is rather higher than interstellar magnetic field, except for the RCW 86 case.

8.2 Correlation between X-Ray and Other Physical Parameters

8.2.1 w_u and w_d vs. Other Physical Parameters

Figure 8.1 shows the relation between scale lengths and the apparent radius r. In all SNR cases, the scale lengths are much smaller than $1/12\,r$, which is the expected value in Sedov self-similar solution (dashed lines in Figure 8.1). The upstream scale lengths (open squares) seem to be smaller than those in the downstream (filled squares). As already shown in the previous section, the former is as small as the spatial resolution of *Chandra*, about 0.5 arcsec in each filament statistically (dotted

Table 8.1: Summary of the results of SNRs and a SB.

	Cas A	Kepler	Tycho	SN 1006	RCW 86	30 Dor C
t_{age} [yrs]	320	396	428	994	1816	6.7×10^5
t_{acc} [yrs]	28	168	113	340	2.1×10^3	···
t_{acc}/t_{age}	0.088	0.42	0.26	0.34	1.16	···
E_{max} [TeV][a]	···	16–31	4.8–18	22–69	41–172	···
E_{max} [TeV][b]	10–36	50–54	16–17	26–54	41–172	···
B_d [μG][a]	···	10–150	32–52, 70–110	14–20	4-12	···
B_d [μG][b]	139–305	72–85	82–99	23–85	4–12	···
θ [deg.][a]	···	90	< 10, 90	0–90	90	···
θ [deg.][b]	< 60	90	< 10	< 35	90	···

[a]: Under the assumption that the system is in age limited.

[b]: Under the assumption that the system is in energy loss limited.

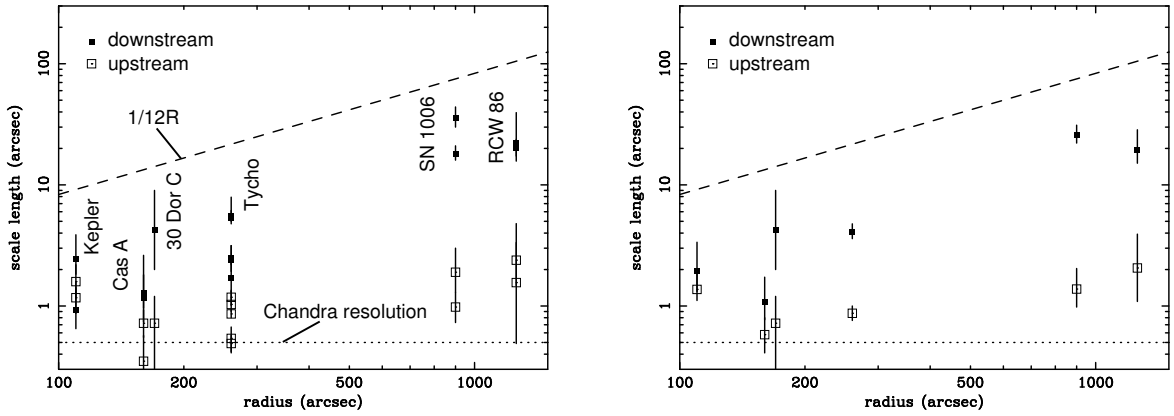

Fig. 8.1.— Correlations between apparent radius of the SNRs (r) vs. w_u (open squares) and w_d (filled squares) in logarithmic scales. The dashed and dotted lines represent the expected width from Sedov self-similar solution and the spatial resolution of *Chandra* (= 0.″5), respectively. All data points derived in previous sections are shown in the left panel, while the averaged values are in the right panel.

lines in Figure 8.1), then we can not conclude that each w_u is significantly wider than the spatial resolution. On the other hand, there is some excess from the spatial resolution in the averaged data in each SNR shown in the right panel of Figure 8.1.

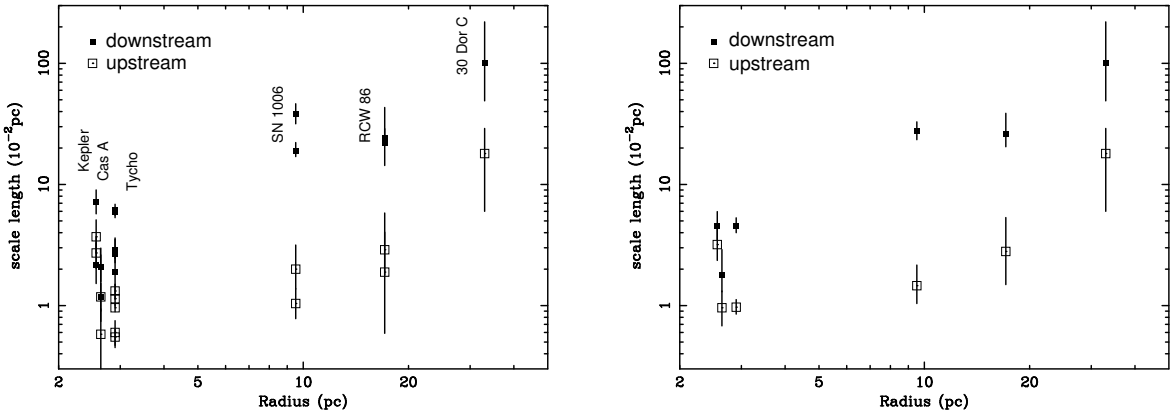

Fig. 8.2.— Correlations between radius of the SNRs (R) vs. w_u (open squares) and w_d (filled squares). Both horizontal and vertical axes are in logarithmic scales. All data points are shown in the left panel, while the averaged values are in the right panel.

Converting the apparent length to physical scales with distances adopted in previous chapters, we get the left panel of Figure 8.2, which shows the correlation between scale lengths and the radius R of the remnants. Both w_u and w_d seem to grow larger when R becomes larger. We must note that the parameters for 30 Dor C may be over-estimated because the distance is very large ant w_u may be smaller, considering the spatial resolution of *Chandra*. The averaged data in the right panel of Figure 8.2 shows a clear positive correlation even without the data of 30 Dor C. We fitted the data with a linear function $w_{u,d} = A_{u,d}R$, and got the best-fit parameters as follows;

$$A_u = 3.0\ (2.4 - 3.6)\ \times 10^{-3}\ , \tag{8.1}$$

$$(\text{reduced } \chi^2)_u = 14.8/5\ , \tag{8.2}$$

$$A_d = 1.8\ (1.5 - 2.1)\ \times 10^{-2}\ , \tag{8.3}$$

$$(\text{reduced } \chi^2)_d = 12.5/5\ . \tag{8.4}$$

This is the first quantitative result about the evolution of scale lengths of the non-thermal filaments in SNRs.

We plotted this data set again concerning age of SNRs (t_{age}). The data set of 30 Dor C were ignored, since it is not a historical SNR, Figure 8.3 shows a clear positive correlation between these two parameters both for upstream and downstream, except for the upstream parameters of Kepler. We fitted the data with a power-law model as an empirical model to represent the correlation as

$$w_{u,d} = A_{u,d} {t_{age}}^{\Gamma_{u,d}}\ . \tag{8.5}$$

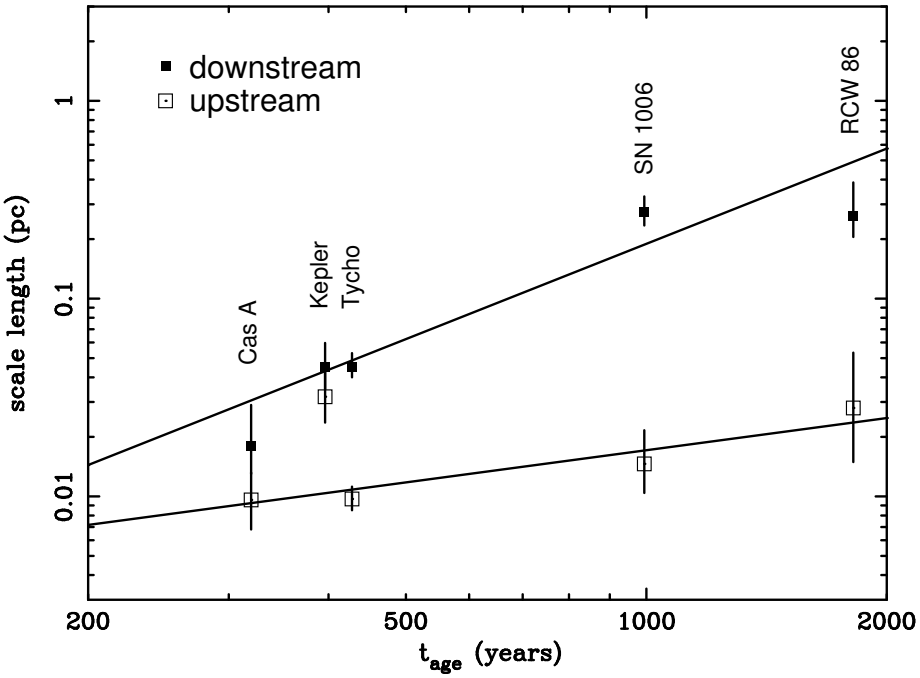

Fig. 8.3.— Correlations between t_{age} vs. w_u (open squares) and w_d (filled squares). The best-fit power-law models are shown with dotted and dashed lines for upstream and downstream, respectively.

The best-fitted relations between t_{age} and w_u, w_d are derived as

$$\Gamma_u = 0.54\ (0.51 - 0.57)\ , \tag{8.6}$$
$$A_u = 4.1\ (3.3 - 4.9) \times 10^{-4}\ , \tag{8.7}$$
$$(\chi^2/\mathrm{d.o.f})_u = 7.48/3\ , \tag{8.8}$$
$$\Gamma_d = 1.60\ (1.30 - 1.61)\ , \tag{8.9}$$
$$A_d = 3.0\ (2.4 - 3.7) \times 10^{-6}\ , \tag{8.10}$$
$$(\chi^2/\mathrm{d.o.f})_d = 9.68/3\ . \tag{8.11}$$

Figure 8.3 also shows the best-fit models both in upstream (dotted lines) and downstream (dashed line). The best-fit model well represents the time-evolution of the scale length in upstream. Note that when we fit the data without Kepler's, the reduced χ^2 becomes greatly smaller, $\chi^2/\mathrm{d.o.f.} = 0.74/3$. On the other hand, there remains huge residuals for downstream.

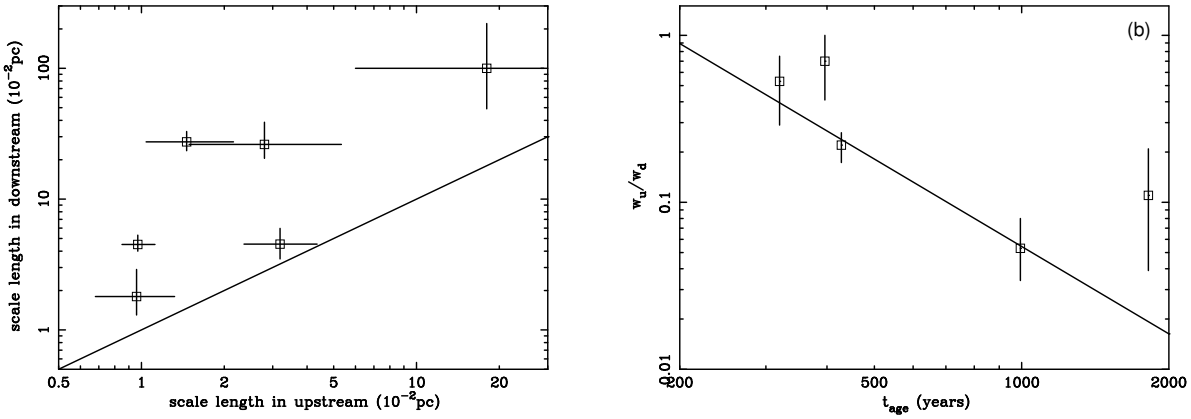

Fig. 8.4.— Left: Correlation between scale length in upstream (w_u) and downstream (w_d). The solid line represents the relation $w_u = w_d$. Right: The relation between t_{age} and ratio of w_u and w_d. The value becomes 1 when $w_u = w_d$. The solid line shows the best-fit model of a power-law fitting (see text).

With Figure 8.4, we compared the scale lengths in upstream and downstream. In the left panel of the figure, in which we plotted the data in the plane w_u vs. w_d, the all data is located upper of the solid line ($w_u = w_d$), guaranteeing the result in Figure 8.1 that filament has larger scale length in downstream than in upstream. We can see the time evolution of the ratio of w_u and w_d in the right panel of Figure 8.4. The scale length in downstream grows faster than that in upstream and the ratio becomes smaller. We fitted them with an power-law function of

$$\frac{w_u}{w_d} = A \cdot {t_{age}}^{-\Gamma}\ . \tag{8.12}$$

The fitting was statistically accepted with the best-fit parameters as follows;

$$A = 19.0\ (16.7 - 21.3) \times 10^3\ , \quad (8.13)$$

$$\Gamma = 1.74\ (1.70 - 1.79)\ , \quad (8.14)$$

$$\text{reduced } \chi^2 = 4.32/3\ . \quad (8.15)$$

The model of eq.(8.12) with the best-fit parameters is shown with the solid line in the right panel of Figure 8.4.

8.2.2 Photon Index, $\nu_{rolloff}$ vs. Other Physical Parameters

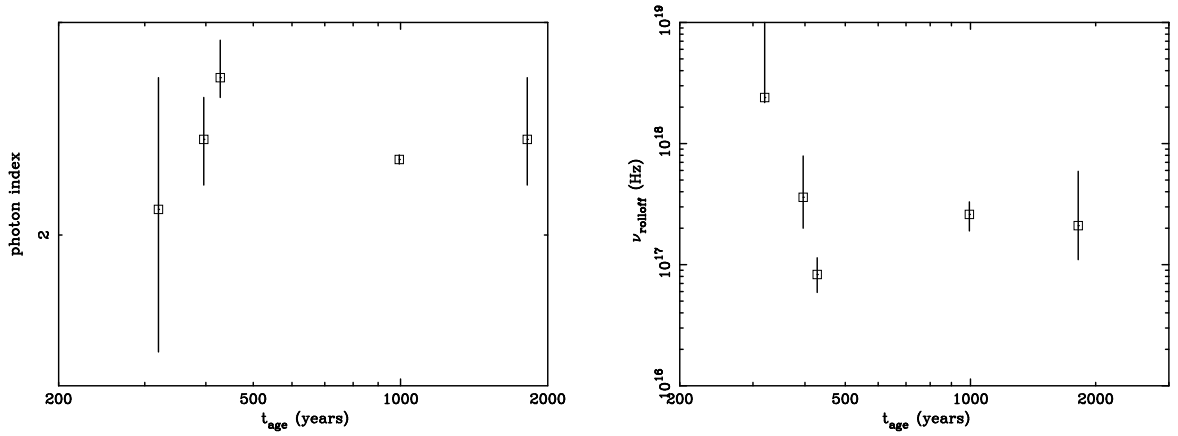

Fig. 8.5.— Left: Correlation between t_{age} and photon index. Right: same but photon indices are changed to $\nu_{rolloff}$ with *srcut* model. We adopted averaged data for all of the target. The data of 30 Dor C has been omitted in the right panel since derived $\nu_{rolloff}$ strongly depends on the assumed spectral index at 1 GHz (see Table 7.12).

The left panel of Figure 8.5 shows the relation between the photon indices of the spectra and t_{age}. In the very young stage ($\leq$300 yrs), SNRs shows harder synchrotron spectra. The growth of the spectrum stops, on the other hand, when they age further. The photon indices are converted into rolloff frequency in *srcut* model, $\nu_{rolloff}$, as shown in the right panel of Figure 8.5. We ignored the data of 30 Dor C, because the spectral index at 1 GHz is unknown for this target (Mathewson et al., 1985). The similar tendency of the left panel can bee seen in this figure; the higher $\nu_{rolloff}$ in the younger phase and being a constant in the the older phase. However, we must notice that the parameter $\nu_{rolloff}$ is determined by rather indirect and complicated parameters, E_{max} and B_d in eq.(6.1). The condition of acceleration sites in Cas A may have much stronger magnetic field than those in other SNRs, for example. It must be also considered the selection effect that we can detect synchrotron emission only in the case that the $\nu_{rolloff}$ is in the X-ray band; in fact, the all

SNRs we analysed have $\nu_{rolloff}$ of $\sim 10^{17}$ Hz, while most of the SNRs catalogued in Green (2001) must have smaller $\nu_{rolloff}$. Therefore, it is rather difficult to show how the tendency is determined clearly and concisely.

8.3 Age limited or Loss Limited?

Except for the Cas A case, acceleration time scale we estimated is roughly consistent with the age of the SNR as shown in Table 8.1. It indicates that electrons accelerated in almost all SNRs we analysed are now reaching the maximum energy in the SNR life time. In our analyses, we divided the acceleration history into the two cases, age limited and loss limited. The reality, however, must not be so simple. The acceleration time scale grows larger as electrons are accelerated (see eq.(3.46)), whereas the energy loss occurs more frequently (see eq.(3.48)). The efficient acceleration of particles may also brake the shock and change these time scales. As a result, the three time scales (t_{age}, t_{acc}, and t_{loss}) become a similar value in the history of acceleration. In order to follow the precise history of acceleration in the SNR shocks, we must carry out some numerical calculations. The age limited case is adopted in the following discussion for the reasonable assumption from Table 8.1.

8.4 What Determine the Scale Lengths?

The index of t_{age}–w_u relation, $\Gamma_u \sim 0.4$ (see eq.(8.6)), is consistent with that in Sedov self-similar solutions (see eq.(4.7)), although the normalization is very different from each other. Comparing eq.(8.7) with eq.(4.7), we find that the derived scale length in upstream is about 0.3% of the radius derived by Sedov solutions;

$$\frac{w_u}{R_s} = \frac{9.8 \times 10^{-2}}{5.0 \times \left(\frac{E_{51}}{n_0}\right)^{1/5} \cdot \left(\frac{t_3}{t_{age}}\right)^{2/5}} \sim 3.1 \times 10^{-3} \quad . \tag{8.16}$$

This fact suggests that the acceleration region in the shock evolves following the Sedov self-similar solutions. The inclination is also consistent with our observational result shown in Figure 8.2 and eq.(8.1).

Assuming the age limited case (see Table 8.1), then we can derive the relation between $t_{acc} = t_{age}$ and w_u as follows;

$$\begin{aligned} t_{acc} = t_{age} &= \frac{4}{u_s}\left(\frac{K_u}{u_s} + \frac{\frac{1}{R(\theta)\chi}K_u}{\frac{1}{r}u_s}\right) \quad , \\ &= \frac{3}{u_s}\left(\frac{r}{r-1}\right)\left(1 + \frac{r}{R\chi}\right) \cdot w_u \quad , \end{aligned} \tag{8.17}$$

$$\chi \equiv \frac{\xi_u}{\xi_d} \ , \tag{8.18}$$

where r and $R = R(\theta)$ is the compression ratio of the shock and the magnetic field derived in eq.(3.11), respectively. Using the conversion from u_s to t_{age} of Sedov self-similar solutions (see eq.(4.9)), w_u can be rewritten with R_s, the radius of the SNR derived from eq.(4.7) as

$$w_u = \frac{2}{15}\left(\frac{r-1}{r}\right)\left(\frac{1}{1+\frac{r}{R\chi}}\right)\cdot R_s \ . \tag{8.19}$$

With the reasonable assumptions that $r = 4$, $R(\theta) = 4$ ($\theta = 90^\circ$ in other words), and $\chi = 1$, the relation becomes

$$w_u = 5 \times 10^{-2} R_s \ . \tag{8.20}$$

This inclination is roughly the same as that of eq.(8.16), although there is a difference in about one order. The value changes depending on r, R, and χ. The compression r changes when the acceleration occurs efficiently, may be up to 10 or more (Berezhko et al., 2003), which also brings about the increase of $R(\theta)$, and as a result, the inclination is insensitive to the change of r. When θ becomes smaller (the magnetic field becomes parallel to the shock normal) and $R(\theta)$ becomes near to 1, the inclination can be smaller to 2×10^{-2}, although the parallel magnetic field is unrealistic for some middle-aged SNRs (see Table 8.1). The χ also changes the inclination; it must be larger than 1, and larger χ causes larger inclination. These uncertainty may make the difference between the observational and estimated inclinations.

The ratio of the scale length w_u/w_d is determined from eq.(6.13) in the age limited case as

$$\frac{w_u}{w_d} = r^{-1}\frac{f}{g} \ , \tag{8.21}$$

where r is the compression ratio and f and g are determined with θ, ξ_u, and ξ_d in eqs.(3.39) and (3.40). Table 8.1 suggests that the condition in relatively old SNRs require the perpendicular magnetic field ($\theta \sim 90^\circ$). with Bohm limit in downstream ($\xi_d \sim 1$). In such a condition, w_u/w_d takes the value of

$$\frac{w_u}{w_d} = \frac{1}{r}\cdot\frac{\xi_u r}{1+\xi_u^2}\cdot 2r = \frac{2\xi_u r}{1+\xi_u^2} \ , \tag{8.22}$$

which coincides with the observational value 0.06 (see the right panel of Figure 8.4) when $\xi_u \sim 10^2$ and $r = 4$, which is the upper limit of the range which ξ_u must satisfy $1 \le \xi_u \le c/u_s \sim 10^2$, where c and u_s is the light speed and shock velocity, respectively (Jokipii, 1987). When the magnetic field is parallel to the shock normal ($\theta = 0^\circ$), the ratio between w_u and w_d becomes

$$\frac{w_u}{w_d} = \frac{1}{r}\frac{\xi_u}{\xi_d} \sim \frac{\xi_u}{r} \quad \text{in Bohm limit} \ , \tag{8.23}$$

which is larger than that in the perpendicular magnetic field derived in eq.(8.22) in the natural case that $\xi_u \gg 1$ and the more oblique magnetic field (larger θ) makes smaller w_u/w_d. Therefore, the result in Figure 8.4 may be caused by the rotation of the magnetic field. This is the first suggestion

for the condition of the magnetic field around the acceleration sites from the observational point of view. The perpendicular magnetic field is suggested theoretically by Ratkiewicz et al. (1994), who insists that the perpendicular component of the magnetic field grows preferentially in the evolution of the shock. In the efficient acceleration case, there occurs two-stream instability of cosmic ray and upstream plasma and amplifies the perpendicular component of magnetic field Lucek & Bell (2000). Our result is consistent with these suggestion. The time scale τ_r in eq.(8.14) may imply the time scale of two-stream instability, although Lucek & Bell (2000) insists that the instability emerge in much smaller time scale, about gyro-period of cosmic rays.

8.5 Evolution of B_d, E_{max}, and Energy Densities

In this section, we infer the time evolution of B_d and E_{max} under the age-limited assumption. These parameters twine each other, then we should untangle them carefully.

As the first step, we eliminate the parameter E_{max} in order to examine the pure evolution of B_d using eqs.(6.1) and (6.9) as follows;

$$\nu_{rolloff} \propto E_{max}^2 B_d \ , \tag{8.24}$$

$$w_d \propto \frac{E_{max}\xi_d}{B_d u_d} \ , \tag{8.25}$$

$$\longrightarrow \quad \frac{\nu_{rolloff}}{w_d^2} \propto {B_d}^3 {u_s}^2 \equiv B(\nu_{rolloff}, w_d, t_{age}) \ . \tag{8.26}$$

Of course, eq.(8.26) depends on other time-dependent parameters, such as ξ_d and θ, we can ignore these influence because only u_s and B_d have very strong dependence for $B(\nu_{rolloff}, w_d, t_{age})$ with the index of 2 and 3.

Figure 8.6 shows the time evolution of $B(\nu_{rolloff}, w_d, t_{age})$. The B decays as the SNRs age. This is the consistent result with our analyses of magnetic field estimation for each SNR separately (see Table 8.1). From this figure, we have a conjecture that the magnetic field in downstream becomes weaker as SNRs age. The data was well reproduced by a power-low model with the best-fit parameters of

$$B(\nu_{rolloff}, w_d, t_{age}) \equiv A\, {t_{age}}^{-\Gamma_B} \ , \tag{8.27}$$

$$A = 2.6\ (1.3 - 3.9)\ \ [\times 10^{27}\ \mathrm{Hz\ pc^{-2}}] \ , \tag{8.28}$$

$$\Gamma_B = 2.96\ (2.90 - 3.07) \ , \tag{8.29}$$

$$\chi^2/\mathrm{d.o.f.} = 2.03/3 \ . \tag{8.30}$$

The result tells us the time dependence of the magnetic field. In the free expansion phase, the shock velocity is a constant ant the B_d and the energy density of the magnetic field u_B evolve as

$$B_d^{f\,3} {u_s}^2 \propto {t_{age}}^{-3} \ , \tag{8.31}$$

$$B_d^f \propto {t_{age}}^{-1} \ , \tag{8.32}$$

$$u_B^f = \frac{{B_d^f}^2}{8\pi} \propto {t_{age}}^{-2} \ , \tag{8.33}$$

whereas they evolve in the Sedov phase ($u_s \propto {t_{age}}^{-\frac{3}{5}}$; see eq.(4.9)) as,

$$B_d^s \propto {t_{age}}^{-\frac{3}{5}} \ , \tag{8.34}$$

$$u_B^s = \frac{{B_d^s}^2}{8\pi} \propto {t_{age}}^{-\frac{6}{5}} \ . \tag{8.35}$$

Remember that the thermal energy density ($\equiv u_{th}$) evolves with the time dependence of ${t_{age}}^{-\frac{6}{5}}$ in the Sedov phase (see eq.(4.8)), which is the same dependency of u_B.

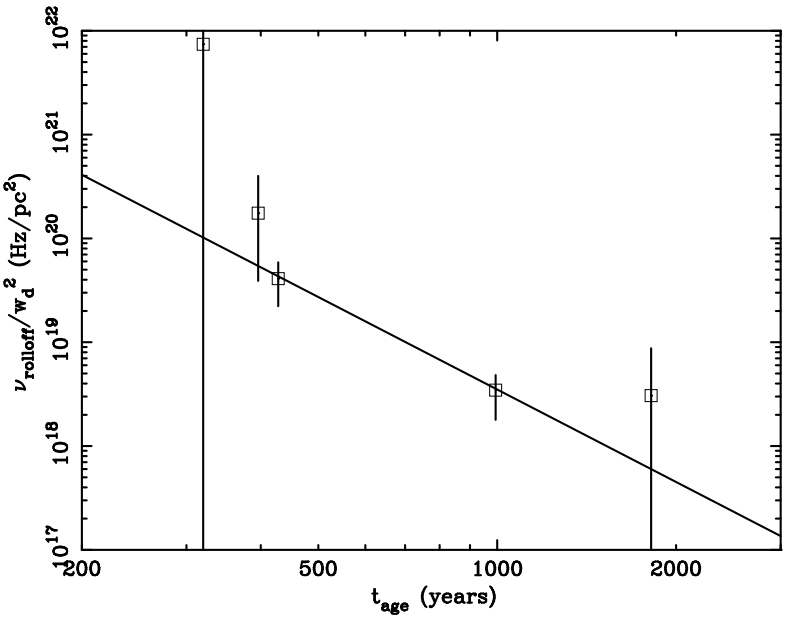

Fig. 8.6.— Time evolution of $\nu_{rolloff}/w_d^2$. The both axes are written in logarithmic. The solid line represents the best-fit model of a power-law fitting.

We also investigate the time evolution of E_{max} in the similar way to B_d. With eqs.(8.24) and (8.25) again, the parameter B_d can be eliminated as

$$\begin{aligned} \nu_{rolloff} \cdot w_d &\propto E_{max}^2 B_d \cdot \frac{E_{max}\xi_d}{B_d u_s} \\ &\propto E_{max}^3 \xi_d {u_s}^{-1} \equiv E(\nu_{rolloff}, w_d, t_{age}) \ . \end{aligned} \tag{8.36}$$

The function E is insensitive to the change of ξ_d, then E_{max} is estimated independently from the magnetic field. We can see the time evolution of $E(\nu_{rolloff}, w_d, t_{age})$ in Figure 8.7.

We fitted the data with a power-law model and got the best-fit parameters as bellow, although the reduced χ^2 was not so good as the case of the function $B(\nu_{rolloff}, w_d, t_{age})$.

$$E(\nu, w_d, t_{age}) \equiv A {t_{age}}^{\Gamma_E} \ , \tag{8.37}$$

$$A = 2 \times 10^{-6} \ (1 \times 10^{-6} - 3 \times 10^{-6}) \ [10^{15}\mathrm{pcHz}] \ , \tag{8.38}$$

$$\Gamma_E = 2.43 \ (2.35 - 2.49) \ , \tag{8.39}$$

$$\text{reduced } \chi^2/\text{d.o.f.} = 6.2/2 \ . \tag{8.40}$$

This relation indicates that $E(\nu, w_d, t_{age})$ increases with the ratio of $\sim {t_{age}}^{\frac{12}{5}}$. Then the time evolution of E_{max} can be derived as

$$E_{max} \propto {t_{age}}^{\frac{4}{5}} u_s^{\frac{1}{3}} \tag{8.41}$$

$$\propto \begin{cases} {t_{age}}^{\frac{4}{5}} \cdot const. = {t_{age}}^{\frac{4}{5}} & \text{in the free expansion phase} \\ {t_{age}}^{\frac{4}{5}} \cdot {t_{age}}^{\frac{1}{5}} = {t_{age}}^{\frac{3}{5}} & \text{in Sedov phase} \end{cases} \ . \tag{8.42}$$

As a result, the maximum energy of electrons increases as the SNR ages.

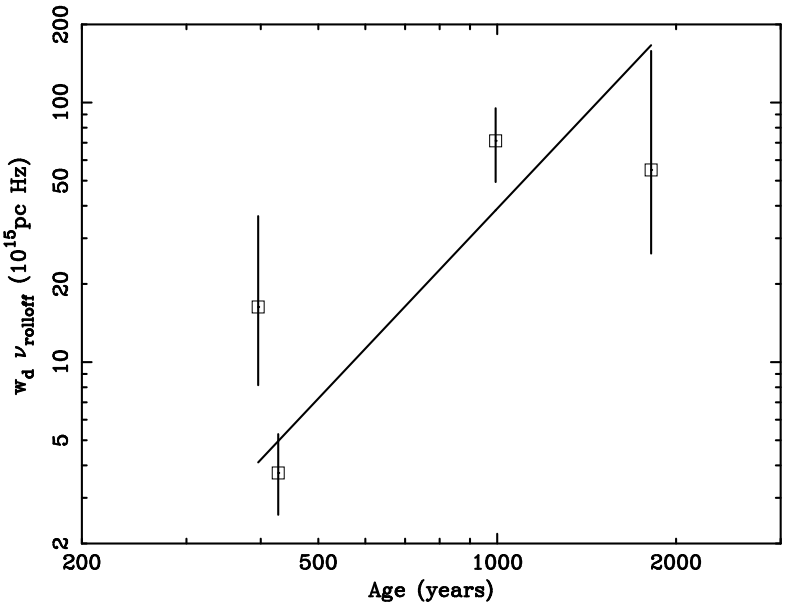

Fig. 8.7.— Time evolution of $\nu_{rolloff} w_d$ plotted in the logarithmic scale. The best-fit model of eq.(8.36) is shown with the solid line. The data for Cas A is ignored because it is far from in the age limited case.

The energy density of accelerated cosmic rays ($\equiv u_{CR}$) can be estimated from the relation between u_{CR} and u_B derived by Lucek & Bell (2000) in the case that cosmic rays and magnetic

field have strong interaction with each other, as

$$u_B = \frac{u_A}{u_s} u_{CR} \ , \tag{8.43}$$

$$u_A = \frac{B}{\sqrt{4\pi\rho}} \ , \tag{8.44}$$

where u_A is the Alfvén velocity. Using the time dependence of B and u_B, u_{CR} is found to evolve as

$$u_{CR} \propto B \times u_s \propto \begin{cases} {t_{age}}^{-1} \cdot const. = {t_{age}}^{-1} & \text{in the free expansion phase} \\ {t_{age}}^{-\frac{3}{5}} \cdot {t_{age}}^{-\frac{3}{5}} = {t_{age}}^{-\frac{6}{5}} & \text{in Sedov phase} \ . \end{cases} \tag{8.45}$$

Note that the energy density of cosmic rays has the same time-dependence as other energy densities in the Sedov phase, Although it seems to have a discrepancy in the result of increasing maximum energy of electrons, the main energy keeper of cosmic rays have the energy of $\sim mc^2$ (see eq.(3.27)) and the particles with the energy of E_{max} have no influence to the energy deposit.

Table 8.2: Time dependency of the energy density of the shock, thermal plasma, magnetic field, and cosmic rays.

	u_{kin}	u_{th}	u_B	u_{CR}
Free expansion phase	${t_{age}}^{0}$	$\cdots$	${t_{age}}^{-2}$	${t_{age}}^{-1}$
Sedov phase	${t_{age}}^{-\frac{6}{5}}$	${t_{age}}^{-\frac{6}{5}}$	${t_{age}}^{-\frac{6}{5}}$	${t_{age}}^{-\frac{6}{5}}$

Table 8.2 summarizes the time dependency of each energy density in each phase. The curious result is that the time dependence of energy densities is same each other in the Sedov phase. In the SN 1006 case, the energy densities of thermal plasma, magnetic field, and the accelerated electrons are nearly equipartition as suggested in § 6.6.3). Therefore, Table 8.2 says that the all kinds of energy density evolve conserving the equipartition.

There are some theoretical works about the interaction between the evolution of SNRs and cosmic rays (non-linear effect; e.g., Dorfi & Völk, 1996; Decourchelle et al., 2000; Berezhko et al., 2002). However, most of previous works considered only the evolution of kinetic, thermal, and cosmic ray energies (left two items in Figure 8.8). The self similar solutions of the shock evolution with magnetic field (the right two items in Figure 8.8) have been studied by some authors (e.g., Fulbright & Reynolds, 1990; Ratkiewicz et al., 1994; Balsara et al., 2001). Lucek & Bell (2000) estimated the third interaction, between magnetic field and cosmic rays (lower two items in Figure 8.8). However, there is still no work including all of three interactions in Figure 8.8, although the importance of the interaction with the magnetic field energy has been suggested by MacKenzie & Völk (1982), since it is so complicated to include the effect and have been ignored. Our result suggests that there must be strong interaction among these energy densities and we must consider the acceleration of cosmic rays in the evolving shock.

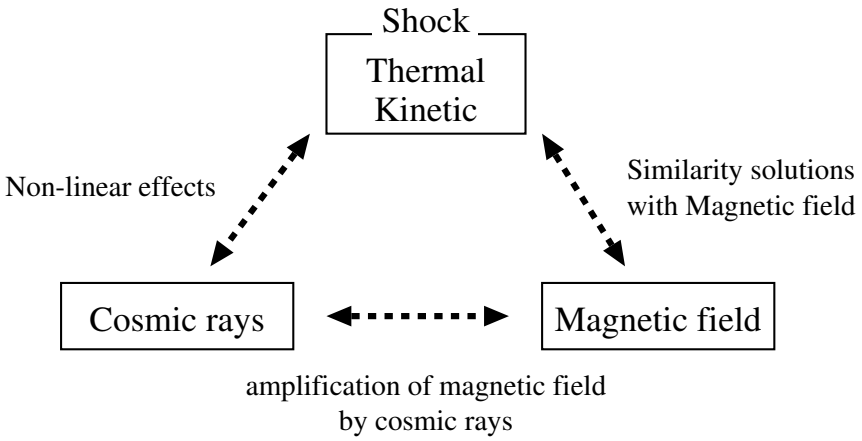

Fig. 8.8.— Schematic view of interaction of energy densities, u_{kin}, u_{th}, u_B, and u_{CR}.

8.6 Acceleration and Evolution History of the Shock and Cosmic Rays

Together with time scales, the evolution of the scale lengths, magnetic field, and the maximum energy of electrons, we can draw two types of acceleration and evolution history of cosmic rays and the shock of SNRs as follows;

1. The electrons accelerated rapidly on the SNR shocks amplify the magnetic field, which becomes perpendicular to the shock normal in relatively short time scale. The acceleration continue with strong interaction of four energy densities (kinetic, thermal, cosmic rays, and magnetic field), keeping the energy equipartition for each other. The acceleration time scale becomes longer the system becomes older, keeping $t_{acc} \sim t_{age} \sim t_{loss}$.

2. The acceleration time scale and the maximum energy of the electron highly depends on the explosion energy and environment of the SNRs. In the low magnetic field environment, acceleration occur slowly and electrons are accelerated up to higher energy. On the other hand, SNRs in strong magnetic field accelerates and decelerates electrons rapidly. Anyway, magnetic field tends toward perpendicular to the shock normal.

It is still unclear whether these tendencies are the real evolution in each SNR, or they are the "apparent" evolution of conditions in which synchrotron emission from accelerated electrons is visible in the hard X-ray band. The reason why we can not justify one of these scenario is our limited band of the synchrotron emission survey; it needs that searching for synchrotron emission in other many samples, having the peak frequency out of the X-ray band, which must be done in the future.

Chapter 9

Conclusion and Future Works

We summarize the main results of our spatial and spectral analyses of non-thermal X-rays from SN 1006 and other five samples (Cas A, Kepler, Tycho, RCW 86, and 30 Dor C) with *Chandra* data as follows;

1. We found very hard and thin "filaments" on the outer edge of north eastern shell of SN 1006. The spectra of the filaments is well reproduced by a power-law model with the photon index of ~ 2.3.

2. The scale length of the non-thermal filaments are incredibly small, ~ 0.05 pc in upstream and ~ 0.2 pc in downstream. This is the first result of spatial analyses of non-thermal X-rays.

3. Thermal emission has rather wider scale length than non-thermal X-rays, which is consistent with the density profile derived by the Sedov self-similar solutions.

4. We made models to understand the small scale length of non-thermal filaments, under the assumptions of age limited and loss limited cases. In the former case, the magnetic field requires quasi-perpendicular field to the shock normal, whereas it should be quasi-parallel in the loss limited case. In both cases, the magnetic field in downstream is fully turbulent. We also determined the maximum energy of electrons and strength of the magnetic field in each case.

5. The injection efficiency has been also calculated. The electrons are accelerated very efficiently in a localized region on the contrary to previous estimations. The energy density of accelerated electrons is roughly same as those of thermal plasma and magnetic field.

6. We discovered that four other SNRs and one super-bubble also have very thin non-thermal filaments. The scale length is much smaller than the width expected from Sedov solutions. All of the filaments have been analysed in the similar way to the SN 1006 case.

7. The scale length of filaments evolves wider as SNRs get older, at a rate of $t_{age}{}^{0.5}$ in upstream and faster in downstream.

8. The magnetic field configuration in the upstream of perpendicular to the shock normal is always accepted in all SNR cases.

9. The magnetic field energy density decays with same time dependence of those of thermal and kinetic of the shock. That of cosmic rays also decays with the same dependence of them. This implies that the energy densities of these components have strong interaction each other.

There are still many unsolved problems. We propose some ideas in order to untangle them as follows.

1. The study of the plasma around the shock with high spectral resolution will reveal us the injection efficiency directly. *ASTRO-E II* has the best detector, X-Ray Spectrometer (XRS).

2. The sample SNRs with synchrotron X-rays are still sparse to study them statistically. The search for more samples is inevitable and it is now being carried out with *ASCA* Galactic plane survey and so on. The detail of our search is written in § B.

3. We must search for synchrotron emission out of the X-ray band (in UV, optical, and so on) to make uniform sample of $\nu_{rolloff}$, which enable us to judge whether the time evolution we discovered is real or not.

4. The numerical simulations for cosmic ray acceleration in the shock must be done in consideration of the energetic interaction between not only kinetic, thermal, cosmic rays, but also magnetic field.

References

Aharonian, F.A., & Atoyan, A.M. 1999, A&A, 351, 330

Aharonian, F. et al. 2001a, A&A, 370, 112

Aharonian, F. A. et al. 2001b, A&A, 373, 292

Allen, C. W. 1973, London: University of London, Athlone Press, —c1973, 3rd ed.

Allen, G. E. et al. 1997, ApJ, 487, L97

Allen, G.E., Petre, R., & Gotthelf, E.V. 2001, ApJ, 558, 739

Anders, E., & Grevesse, N. 1989, Geochim. Cosmochim. Acta, 53, 197

Arabadjis, J. S. & Bregman, J. N. 1999, ApJ, 510, 806

Aschenbach, B. 1985, Rep. Prog. Phys, 48, 579

Ashworth, W. B. 1980 J. Hist. Astron., 11, 1

Atoyan, A. M., Tuffs, R. J., Aharonian, F. A., & Völk, H. J. 2000, A&A, 354, 915

Baade, W. 1943, ApJ, 97, 119

Baade, W. 1945, ApJ, 102, 309

Baldwin, J. E. & Edge, D. O. 1957, The Observatory, 77, 139

Balsara, D., Benjamin, R. A., & Cox, D. P. 2001, ApJ, 563, 800

Bamba, A., Tomida, H., & Koyama, K. 2000, PASJ, 52, 1157

Bamba, A., Ueno, M., Nakajima, H., & Koyama, K. 2004, ApJ, 602, 257

Bamba, A., Ueno, M., Koyama, K., & Yamauchi, S. 2001, PASJ, 53, L21

Bamba, A., Ueno, M., Koyama, K., & Yamauchi, S. 2003, ApJ, 589, 253

Bamba, A., Yamazaki, R., Ueno, M., & Koyama, K. 2003, ApJ, 589, 827

Bandiera, R. 1987, ApJ, 319, 885

Barbon, R., Ciatti, F., & Rosino, L. 1973, A&A, 29. 57

Becker, R. H., Szymkowiak, A. E., Boldt, E. A., Holt, S. S., & Serlemitsos, P. J. 1980, ApJ, 240, L33

Bell, A. R. 1978, MNRAS, 182, 443

Berezhko, E. G., Ksenofontov, L. T., & Völk, H. J. 2002, A&A, 395, 943

Berezhko, E. G., Ksenofontov, L. T., & Völk, H. J. 2003, A&Aletter, accepted (astroph/0310862)

Blair, W. P., Long, K. S., & Vancura, O. 1991, ApJ, 366, 484

Blandford, R. D., & Eichler, D. 1987, Phys. Rep., 154,1

Blandford, R. D., & Ostriker, J. P. 1978, ApJ, 221, L29

Bleeker, J. A. M., Willingale, R., van der Heyden1, K., Dennerl, K., Kaastra, J. S., Aschenbach, B., & Vink, J. 2001, A&A, 365, L225

Bocchino, F., Vink, J., Favata, F., Maggio, A., & Sciortino, S. 2000, A&A, 360, 671

Bolton, J. G., Gardner, F. F., & Mackey, M. B. 1964, Australian Journal of Physics, 17, 340

Borkowski, K.J., Lyerly, W.J., & Reynolds, S.P. 2001a, ApJ, 548, 820

Borkowski, K.J., Rho, J., Reynolds, S.P. & Dyer, K.K. 2001b, ApJ, 550, 334

Borkowski, K. J., Sarazin, C. L., & Blondin, J. M. 1994, ApJ, 429, 710

Boyd, T. J. M., & Sanderson, J. J. 1969, Plasma dynamics, Nelson

Braun, R. 1987, A&A, 171, 233

Bressaard, P. J. & van de Hulst. H. C. 1962, Rev. Mod. Phys., 34, 507

Breysacher, J. 1981, A&AS, 43, 203

Burrows, D. N. et al. 2000, ApJ, 543, L149

Cargill, P. J. & Papadopoulos, K. 1988, ApJ, 329, L29

Case, G. L. & Bhattacharya, D. 1998, ApJ, 504, 761

Cassam-Chenaï, G., Decourchelle, A., Ballet, J., Hwang, U., Hughes, J. P., & Petre, R. 2004, A&A, 414, 545

Caswell, J. L., Clark, D. H., & Crawford, D. F. 1975, Australian Journal of Physics Astrophysical Supplement, 39

Cioffi, D. F., McKee, C. F., & Bertschinger, E. 1988, ApJ, 334, 252

Chakrabarty, D., Pivovaroff, M. J., Hernquist, L. E., Heyl, J. S., & Narayan, R. 2001, ApJ, 548, 800

Chevalier, R. A. 1974, ApJ, 188, 501

Chevalier, R. A. 1982, ApJ, 258, 790

Chevalier, R. A. & Raymond, J. C. 1978, ApJ, 225, L27

Chin, Y. N. & Huang, Y. L. 1994, Nature, 371, 398

Chu, Y. & Mac Low, M. 1990, ApJ, 365, 510

Clark, D. H. & Stephenson, F. R. 1977, Oxford; (New York: Pergamon Press, 1977. 1st ed.)

Decourchelle, A., & Petre, R. 1999, Astronomische Nachrichten, 320, 203

Decourchelle, A., Ellison, D. C., & Ballet, J. 2000, ApJ, 543, L57

Decourchelle, A. et al. 2001, A&A, 365, L218

DeLaney, T., Koralesky, B., Rudnick, L., & Dickel, J. R. 2002, ApJ, 580, 914

Dennerl, K., Haberl, F., Aschenbach, B., Briel, U.G., Balasini, M., Bruninger, H., Burkert, W., Hartmann, R., et al. 2001, A&A, 365, L202

Dickel, J. R., Strom, R. G., & Milne, D. K. 2001, ApJ, 546, 447

Dickey, J. M. & Lockman, F. J. 1990, ARA&A, 28, 215

Doggett, J. B. & Branch, D. 1985, AJ, 90, 2303

Dorfi, E. A. & Vólk, H. J. 1996, A&A, 307, 715

Douvion, T., Lagage, P. O., Cesarsky, C. J., & Dwek, E. 2001, A&A, 373, 281

Drury, L. O'C. 1983, Rep. Prog. Phys., 46, 973

Dunne, B.C., Points, S.D., & Chu, Y-H. 2001, ApJS, 136, 119

Dyer, K.K., Reynolds, S.P., Borkowski, K.J., Allen, G.E., & Petre, R. 2001, ApJ, 551, 439

Dyer, K. K., Reynolds, S. P., & Borkowski, K. J. 2003, ApJ, accepted

Ellison, D. C., Berezhko, E. G., & Baring, M. G. 2000, ApJ, 540, 292

Enomoto, R. et al. 2002, Nature, 416, 823

Esposito, J. A., Hunter, S. D., Kanbach, G., & Sreekumar, P. 1996, ApJ, 461, 820

Fan You 432, "Houhanshu", 6, 3260

Favata, F. et al. 1997, A&A, 324, L49

Feast, M. 1999, PASP, 111, 775

Fesen, R. A., Becker, R. H., Blair, W. P., & Long, K. S. 1989, ApJ, 338, L13

Fink, H. H., Asaoka, I., Brinkmann, W., Kawai, N., & Koyama, K. 1994, A&A, 283, 635

Fisk, L. A. 2003, Nature, 426, 21

Flemsteed, J. 1725, "Historia Coelestia star catalog"

Friedman, H., Byram, E. T., & Chubb, T. A. 1967, Science, 156, 374

Fujiwara, T. 1242, "Mei-Getsu-Ki"

Fukui, Y. et al. 1999, PASJ, 51, 745

Fulbright, M. S. & Reynolds, S. P. 1990, ApJ, 357, 591

Gaetz, T. J. & Salpeter, E. E. 1983, ApJS, 52, 155

Garcia-Munoz, M., Mason, G. M., & Simpson, J. A. 1977, ApJ, 217, 859

Gardner, F. F. & Milne, D. K. 1965, AJ, 70, 754

Gehrels, N. & Williams, E. D. 1993, ApJ, 418, L25

Ghavamian, P., Raymond, J., Smith, R. C., & Hartigan, P. 2001, ApJ. 548, 995

Ghavamian, P., Winkler, P. F., Raymond, J. C., & Long, K. S. 2002, ApJ, 572, 888

Goldstein, B. R. & Peng Yoke, H. 1965, AJ, 70, 748

Gordon, W. 1929, Ann. Phys., 2, 1031

Gotthelf, E. V., Koralesky, B., Rudnick, L., Jones, T. W., Hwang, U., & Petre, R. 2001, ApJ, 552, L39

Green, D.A. 2001, A Catalogue of Galactic Supernova Remnants (2001 December version), (Cambridge, UK, Mullard Radio Astronomy Observatory) available on the WWW at http://www.mrao.cam.ac.uk/surveys/snrs/

Greisen,K. 1956, Prog. Cosmic. Ray Physics, 3, 1

Harkness, R. P., & Wheeler, J. C. 1990, in Supernovae, ed. A. G. Petschek (New York: Springer-Verlag), 2

Haberl, F. & Pietsch, W. 1999, A&AS, 139, 277

Hamilton, A. J. S., Chevalier, R. A., & Sarazin, C. L. 1983, ApJS, 51, 115

Hamilton, A. J. S. & Sarazin, C. L. 1984a, ApJ, 281, 682

Hamilton, A. J. S. & Sarazin, C. L. 1984b, ApJ, 284, 601

Hamilton, A. J. S., Sarazin, C. L., & Szymkowiak, A. E. 1986, ApJ, 300, 698

Hanbury, B. R., Hazard, C. 1952, Nature, 170, 364

Hess, V. F. 1911, Phys. Zeits., 12, 998

Hess, V. F. 1912, Phys. Zeits., 13, 1084

Hester, J.J. 1987, ApJ, 314, 187

Hill, E. R. 1964, IAU Symp. 20: The Galaxy and the Magellanic Clouds, 20, 107

Hill, E. R. 1967, Australian Journal of Physics, 20, 297

Hillas, A. M. 1984, ARA&A, 22, 425

Holt, S. S., Gotthelf, E. V., Tsunemi, H., & Negoro, H. 1994, PASJ, 46, L151

Hoshino, M., & Shimada, N. 2002, ApJ, 572, 880

Hughes, J. P. 1999, ApJ, 527, 298

Hughes, J.P., Hayashi, I., & Koyama, K. 1998, ApJ, 505, 732

Hughes, J. P. & Helfand, D. J. 1985, ApJ, 291, 544

Hughes, J. P., Rakowski, C. E., Burrows, D. N., & Slane, P. O. 2000, ApJ, 538, L109

Hwang, U. & Gotthelf, E. V. 1997, ApJ, 475, 665

Hwang, U., Holt, S. S., & Petre, R. 2000, ApJ, 537, L119

Hwang, U., Szymkowiak, A. E., Petre, R., & Holt, S. S. 2001, ApJ, 560, L175

Hwang, U., Decourchelle, A., Holt, S. S., & Petre, R. 2002, ApJ, 581, 1101

Itoh, M., Tanaka, R., & Komatsu, H. 2001, PASPConf. Seri., 251, 250

Jansen, F., et al. 2001, A&A, 365, L1

Jokipii, J.R, 1987, ApJ, 313, 842

Jones, F. C. 1968, Physical Review, 167, 1159

Jones, F.C., & Ellison, D.C. 1991, Space Science Rev., 58, 259

Kaastra, J. S., Asaoka, I., Koyama, K., & Yamauchi, S. 1992, A&A, 264, 654

Kamper, K. & van den Bergh, S. 1976, ApJS, 32, 351

Kamper, K. W. & van den Bergh, S. 1978, ApJ, 224, 851

Karzas, W. J. & Latter, R. 1961, ApJS, 6, 167

Katz-Stone, D. M., Kassim, N. E., Lazio, T. J. W., & O'Donnell, R. 2000, ApJ, 529, 453

Kepler, J. 1606. "De stella nova"

Kesteven, M. J. & Caswell, J. L. 1987, A&A, 183, 118

Kinugasa, K. & Tsunemi, H. 1999, PASJ, 51, 239

Kirshner, R., Winkler, P. F., & Chevalier, R. A. 1987, ApJ, 315, L135

Koyama, K., Kinugasa, K., Matsuzaki, K., Nishiuchi, M., Sugizaki, M., Torii, K., Yamauchi, S., & Aschenbach, B. 1997, PASJ, 49, L7

Koyama, K., Petre, R., Gotthelf, E.V., Hwang, U., Matsura, M., Ozaki, M., & Holt S. S. 1995, Nature, 378, 255

Krimigis, S. M., Decker, R. B., Hill, T. P., Armstrong, G., Gloeckler, D. C., Hamilton, D. C., Lanzerotti, L. J., & Roelof, E. C. 2003, Nature,426, 45

Lamb, R. C. & Weekes, T. C. 1987, Science, 238, 1528

Landau, L. D. & Lifshits, E. M. 1959, Fluid Mechanics, London, Pergamon

Leroy, M., Winske, D., Goodrih, C. C., Wu, C. S., & Papadopoulos, K. 1982, Geophys. Res. Lett., 87, 5081

Le Marne, A. E. 1968, MNRAS, 139, 461

Liedahl, D. A., Osterheld, A. L., & Goldstein, W. H. 1995, ApJ, 438, L115

Lipkin, H. J. & Peshkin, M. 1972, Physical Review Letters, 28, 862

Long, K. S., Helfand, D. J., & Grabelsky, D. A. 1981, ApJ, 248, 925

Long, K. S., & Blair, W. P. 1990, ApJ, 358, L13

Long, K. S., Reynolds, S. P., Raymond, J. C., Winkler, P. F., Dyer, K. K., & Petre, R. 2003, ApJ, 586, 1162

Longair, M. S. 1994, Cambridge: Cambridge University Press, —c1994, 2nd ed.,

Lortet, M. C., & Testor, G. 1984, A&A, 139, 330

Lucek, S. G. & Bell, A. R. 2000, MNRAS, 314, 65

Lucke, P. B., & Hodge, P. W. 1970, AJ, 75, 171

MacKenzie, J. F. & Vólk, H. J. 1982, A&A, 116, 191

Maeda, Y., Koyama, K., Yokogawa, J., & Skinner, S. 1999, ApJ, 510, 967

Malkov, E., & Drury, L.O'C. 2001, Rep. Prog. Phys., 64, 429

Mantsch, P. M. 2003, Proc. SPIE, 4858, 115

Masai, K. 1989, ApJ, 437, 770

Mathewson, D. S., Ford, V. L., Tuohy, I. R., Mills, B. Y., Turtle, A. J., & Helfand, D. J. 1985, ApJS, 58, 197

Matsui, Y., Long, K. S., Dickel, J. R., & Greisen, E. W. 1984, ApJ, 287, 295

Maza, J., & van den Bergh, S. 1976, ApJ, 204, 519

McDonald, F. B., Edward, C. S., Cummings. A. C., Cummings,B. H., Heikkila, B., LAL, N., & Webber, R. W. 2003, Nature, 426, 48

McLaughlin, M. A., Cordes, J. M., Deshpande, A. A., Gaensler, B. M., Hankins, T. H., Kaspi, V. M., & Kern, J. S. 2001, ApJ, 547, L41

Mewe, R., Gronenschild, E.H.B.M., & van den Oord, G.H.J. 1985, A&AS, 62, 197

Mewe, R., Lemen, J. R., & van den Oord, G. H. J. 1986, A&AS, 65, 511

Michael, E. et al. 2002, ApJ, 574, 166

Mills, B. Y., Slee, O. B., & Hill, E. R. 1961, Australian Journal of Physics, 14, 497

Mills, B.Y., Turtle, A.J., Little, A.G., & Durdin, J.M. 1984,

Minkowski, R. 1941, PASP, 53, 224

Minkowski, R. 1966, AJ, 71, 371

Miyata, E. & Tsunemi, H. 1999, ApJ, 525, 305

Morgan, H. L., Dunne, L., Eales, S., Ivison, R., & Edmunds, M. G. 2003, ApJ, 597, L33

Morrison, R., & McCammon, D. 1983, ApJ, 270, 119

Muraishi, H. et al. 2000, A&A, 354, L57

Murray, S. S., Ransom, S. M., Juda, M., Hwang, U., & Holt, S. S. 2002, ApJ, 566, 1039

Naito, T. & Takahara, F. 1994, Journal of Physics G Nuclear Physics, 20, 477

Naranan, S., Shulman, S., Yentis, D., Fritz, G., & Friedman, H. 1977, ApJ, 213, L53

Nomoto, K., Thieleman, F., & Yokoi, K. 1984, ApJ, 266, 644

Ohashi, T. et al. 1996, PASJ, 48, 157

Papadopoulos, K. 1988, Ap&SS, 144, 535

Park, S., Burrows, D. N., Garmire, G. P., Nousek, J. A., McCray, R., Michael, E., & Zhekov, S. 2002, ApJ, 567, 314

Petre, R., Allen, G. E., & Hwang, U. 1999, Astronomische Nachrichten, 320, 199

Pravdo, S. H., & Smith, B. W. 1979, ApJ, 234, L195

Press, W.H., Teukolsky, S.A., Vetterling, W.T., & Flannery, B. P. 1992, Numerical Recipes in C (2d ed.; Cambridge: Cambridge Univ. Press)

Ratkiewicz, R., Axford, W.I., & McKenzie, J.F. 1994, A&A, 291, 935

Rankine, W. J. M. 1870, Phol. Trans. Roy. Soc. 160, 277

Reed, J. E., Hester, J. J., Fabian, A. C., & Winkler, P. F. 1995, ApJ, 440, 706

Reynolds, S. P. 1996, ApJ, 459, L13

Reynolds, S.P. 1998, ApJ, 493, 375

Reynolds, S. P. & Chevalier, R. A. 1981, ApJ, 245, 912

Reynolds, S.P., & Gilmore, D.M. 1993, 106, 272

Reynoso, E. M. & Goss, W. M. 1999a, AJ, 118, 926

Reynoso, E. M., Velázquez, P. F., Dubner, G. M., & Goss, W. M. 1999, AJ, 117, 1827

Reynolds, S.P., & Keohane, J.W. 1999, ApJ, 525, 368

Rho, J., Dyer, K. K., Borkowski, K. J., & Reynolds, S. P. 2002, ApJ, 581, 1116

Rho, J., Reynolds, S. P., Reach, W. T., Jarrett, T. H., Allen, G. E., & Wilson, J. C. 2003, ApJ, 592, 299

Rodgers, A. W., Campbell, C. T., & Whiteoak, J. B. 1960, MNRAS, 121, 103

Rosado, M., Ambrocio-Cruz, P., Le Coarer, E., & Marcelin, M. 1996, A&A, 315, 243

Russel, S.C., & Dopita, M.A. 1992, ApJ, 384, 508

Rybicki, G.B., & Lightman, A.P. 1979, "Radiative Processes in Astrophysics", Wiley-Interscience, New York

Sagdeev, R. Z., & Shapiro, V. D. 1973, JETP Lett. Engl. Transil., 17, 279

Sanduleak, N. 1970, Contributions from the Cerro Tololo Inter-American Observatory, 89

Sasaki, M., Haberl, F., & Pietsch, W. 2000, A&AS, 143, 391

Sedov, L. I. 1959, Similarity and Dimensional Methods in Mechanics, 10th ed. (New York: Academic Press)

Schaefer, B. E. 1995, AJ, 110, 1793

Shimada, N. & Hoshino, M. 2000, ApJ, 543, L67

Skilling, J. 1975, MNRAS, 172, 557

Slane, P., Gaensler, B. M., Dame, T. M., Hughes, J. P., Plucinsky, P. P., & Green, A. 1999, ApJ, 525, 357

Slane, P., Hughes, J. P., Edgar, R. J., Plucinsky, P. P., Miyata, E., Tsunemi, H., & Aschenbach, B. 2001, ApJ, 548, 814

Smith, R. C., Kirshner, R. P., Blair, W. P., & Winkler, P. F. 1991, ApJ, 375, 652

Smith R.C. 1997, AJ, 114, 2664

Sokolsky, P. 1989, Introduction to Ultrahigh Energy Cosmic Ray Physics (Addison-Wesley Publisiong Company Inc.)

Sollerman, J., Ghavamian, P., Lundqvist, P, & Smith, R. C. 2003, A&A, 407, 249

Spitzer, L. Jr. 1967, Physics of Fully Ionized Gas (New York: Wiley-Interscience)

Stecker, F. W. 1979, ApJ, 228, 919

Stephan, K., Reppin, C., Hirschinger, M., Maier, H.J., Frischke, D. Fuchs, D., Mueller, P., Guertler, P. 1996, Proc. SPIE, 2808, 421

Stephens, S. A. & Badhwar, G. D. 1981, Ap&SS, 76, 213

Strom, R. G. 1994, A&A, 288, L1

Strom, R. G., Goss, W. M., & Shaver, P. A. 1982, MNRAS, 200, 473

Sugizaki, M., 1999, Ph.D. Thesis, University of Tokyo

Sugizaki, M., Mitsuda, K., Kaneda, H., Matsuzaki, K., Yamauchi, S., & Koyama, K. 2001, ApJS, 134, 77

Tanimori, T., Hayami, Y., Kamei, S., Dazeley, S.A., Edwards, P.G., Gunji, S., Hara, S., Hara, T. et al. 1998, ApJ, 497, L25

Tanimori, T., Naito, T., Yoshida, T., & CANGAROO collaboration 2001, to appear in proceedings of 27th ICRC, astro-ph/0108031

Tatischeff, V., Ramaty, R., & Kozlovsky, B. 1998, ApJ, 504, 874

Terasawa, T. et al. 2000, Geophys. Res. Lett., 27, 3781

The, L.-S., Leising, M. D., Kurfess, J. D., Johnson, W. N., Hartmann, D. H., Gehrels, N., Grove, J. E., & Purcell, W. R. 1996, A&AS, 120, 357

Tonello, N. for the HEGRA Collaboration 2003, Proc. of the 28th International Cosmic Ray Conference, 2389

Trulove, J. K., McKee, C. F. 1999, ApJS, 120, 299

Tsujimoto, T., Nomoto, K., Yoshii, Y., Hashimoto, M., Yanagida, S., & Thielemann, F.-K. 1995, MNRAS, 277, 945

Turner, M.J.L. et al. 2001, A&A, 365, L27

Tycho, B. 1573, "De Stella Nova" (Copenhagen: Laurenentius)

van den Bergh, S. & Kamper, K. W. 1983, ApJ, 268, 129

Ueno, M., Bamba, A., Koyama, K., & Ebisawa, K. 2003, ApJ, 588, 338

Villa, G.E. et al. 1998, IEEE Trans. Nucl. Sci., 45, 921

Vink, J., Kaastra, J. S., & Bleeker, J. A. M. 1997, A&A, 328, 628

Vink, J., Kaastra, J.S., Bleeker, J.A.M., & Preite-Martinez, A. 2000, A&A Rev., 354, 931

Vink, J. & Laming, J. M. 2003, ApJ, 584, 758

Völk, H. J., Berezhko, E. G., & Ksenofontov, L. T. 2003, A&A, 409, 563

Völk, H. J., Berezhko, E. G., Ksenofontov, L. T., & Rowell, G. P. 2002, A&A, 396, 649

Watson, M.G. et al. 2001, A&A, 365, L27

Weekes, T.C. 1988, Pysics Reports, 160, 1

Weisskopf, M. C., Brinkman, B., Canizares, C., Garmire, G., Murray, S., & Van Speybroeck, L. P. 2002, PASP, 114, 1

Westerlund, B. E. & Mathewson, D. S. 1966, MNRAS, 131, 371

Wheeler, J. C., Harkness, R. P. 1986, in Galaxy Distances and Deviations from Universal Expansion, eds. B. F. MaDore & R. B. Tully (Dordrechet: Reidel), 45

White, R. L., & Long, K. S. 1983, ApJ, 264, 196

Willingale, R., Bleeker, J. A. M., van der Heyden, K. J., Kaastra, J. S., & Vink, J. 2002, A&A, 381, 1039

Winkler, P. F. 1978, ApJ, 221, 220

Winkler, P. F., & Long, K. S. 1997, ApJ, 491, 829

Winkler, P. F., Gupta, G., & Long, K. S. 2003, ApJ, 585, 324

Wright, M., Dickel, J., Koralesky, B., & Rudnick, L. 1999, ApJ, 518, 284

Wu, C. S. et al. 1984, Space Science Reviews, 37, 63

Yamaguchi, R., Mizuno, N., Onishi, T., Mizuno, A., & Fukui, Y. 2001, PASJ, 53, 959

Yamazaki, R., Yoshida, T., Terasawa, T., Bamba, A., & Koyama, K. 2003, A&A, accepted

Zank, G. P., Pauls, H. L., Cairns, I. H., & Webb, G. M. 1996, J. Geophys. Res., 101, 457

Appendix A

Comments on the Results of SN 1006

We analysed the scale lengths of non-thermal filaments in the north eastern shell of SN 1006 in §6, under the assumption that the shock and magnetic field get no influence from accelerated particles, in other words, test particle approximation. In this chapter, we briefly comments on our analyses and discuss how our results may change if the approximation is dropped.

A.1 Conditions of Time Scales

We can show that the condition $t_{loss} < t_{acc}$ is always satisfied. Substituting eqs.(6.27) and (6.28) into eq.(6.16), we obtain

$$t_{loss} = 2.7 \times 10^2 \text{ yrs} \left(\frac{r}{4}\right) \left(\frac{w_d}{0.2 \text{ pc}}\right) \left(\frac{u_s}{2.89 \times 10^8 \text{ cm s}^{-1}}\right)^{-1} \frac{f + rg}{R^{-2} f + rg} \quad . \tag{A.1}$$

Then, $t_{loss} < t_{age}$ reduces

$$\frac{1 + rg/f}{R^{-2} + rg/f} < 3.7 \left(\frac{r}{4}\right)^{-2} \left(\frac{w_d}{0.2 \text{ pc}}\right)^{-1} \left(\frac{u_s}{2.89 \times 10^8 \text{ cm s}^{-1}}\right) \left(\frac{t_{age}}{1000 \text{ yrs}}\right) \quad . \tag{A.2}$$

Using eq.(6.31), we rewrite the left hand side of this equation as

$$\frac{1 + rg/f}{R^{-2} + rg/f} = 1 + \left(1 - R^{-2}\right) \phi \left(\frac{r}{4}\right)^{-1} \frac{w_u}{w_d} \tag{A.3}$$

and derive

$$w_d + \left(1 - R^{-2}\right) \phi \left(\frac{r}{4}\right)^{-1} w_u < 0.74 \text{ pc} \left(\frac{r}{4}\right)^{-1} \left(\frac{u_s}{2.89 \times 10^8 \text{ cm s}^{-1}}\right) \left(\frac{t_{age}}{1000 \text{ yrs}}\right) \quad . \tag{A.4}$$

This equation is always satisfied since w_u and w_d range 0.01–0.1 pc and 0.06–0.4 pc, respectively.

A.2 Conditions of Scale Length in the Loss Limited Case

In this section, we validate eqs.(6.25) and (6.26), by confirming the conditions

$$\frac{K_u}{u_s} < (K_u t_{cool})^{\frac{1}{2}} \quad , \tag{A.5}$$

$$u_d t_{cool} > (K_d t_{cool})^{\frac{1}{2}} \quad , \tag{A.6}$$

are always satisfied for the parameters of our interest. Using eqs.(6.1), (3.37), and (3.48), eq.(A.5) can be rewritten as

$$f < 19.0 \left(\frac{u_s}{2.89 \times 10^8 \text{ cm s}^{-1}} \right)^2 \left(\frac{\nu_{rolloff}}{2.6 \times 10^{17} \text{ Hz}} \right)^{-1} \quad . \tag{A.7}$$

This equation, together with eq.(6.29), reduces

$$\frac{w_u}{w_d} < r \quad , \tag{A.8}$$

which is always satisfied since $w_u = 0.01$–0.1 pc and $w_d = 0.06$–0.4 pc. On the other hand, from eqs.(6.1), (3.38), (3.48), and (A.6), we derive

$$g < 1.2 \left(\frac{r}{4} \right)^{-2} \left(\frac{u_s}{2.89 \times 10^8 \text{ cm s}^{-1}} \right)^2 \left(\frac{\nu_{rolloff}}{2.6 \times 10^{17} \text{ Hz}} \right)^{-1} \quad . \tag{A.9}$$

Combing this equation and eq.(6.30), we eliminate $\nu_{rolloff}$ and u_s as

$$\left[1 - \left(\frac{r}{4} \right)^{-1} \phi \right] g < \frac{1}{4} \left(\frac{r}{4} \right)^{-2} \phi R^{-2} f \quad . \tag{A.10}$$

As long as $r \leq 4$, this equation is always satisfied since $1 - (r/4)^{-1}\phi - (r-4)/(r-1) \leq 0$.

A.3 Non-Linear Effects on Our Analyses

Although we should consider the spatial structure is modified, for example, in the upstream precursor region, we simply argue the case of $r > 4$ that are thought to be caused by non-linear effects. Indeed, Berezhko et al. (2002) showed that the present value of total compression ratio is about 6. In the age limited case, when r becomes large (up to $\sim$7), the allowed region are slightly changed in any case of θ with inferred magnetic fields slightly smaller than that of the $r = 4$ case. On the other hand, in the loss limited case, the allowed region in theξ_u–ξ_d plane becomes narrow and only the cases of $\theta = 0^\circ - 10^\circ$ can exist for $4 < r \leq 6$ while no allowed region for $r \sim 7$ case. This comes from the fact that another restriction, eq.(A.10) emerges. For the larger r, the stronger the constraint because of the less efficient advection for fixed shock velocity u_s. Furthermore, it can be shown that there exists no case in which w_d is given by $(K_d t_{cool})^{\frac{1}{2}}$, since the condition $t_{acc} = t_{cool}$ is incompatible with the condition $u_d t_{cool} < (K_d t_{cool})^{\frac{1}{2}}$ in the parameter range of our interest.

It is important to determine the magnetic field configuration in order to discuss the acceleration and/or injection efficiency. In this paper, using the spatial distribution of non-thermal X-rays, we have shown that roughly two cases can exist in the case of SN 1006; high and parallel, and low and perpendicular magnetic field. In the latter case, the back reaction of accelerated particles is small and thus a test-particle treatment is a good approximation. The magnetic field amplification process pointed by Lucek & Bell (2000) does not work well. While in the former case, non-linear effects are so efficient that the magnetic field can be large. The difference between these cases probably comes from the fact that the (proton) injection rate depends strongly on the shock obliquity and diminishes as θ increases (Völk, Berezhko, & Ksenofontov, 2003). In addition to our result, radio polarization data with high spatial resolution may become further information about the magnetic field configurations.

Appendix B

Estimation of Total Number of Non-Thermal SNRs

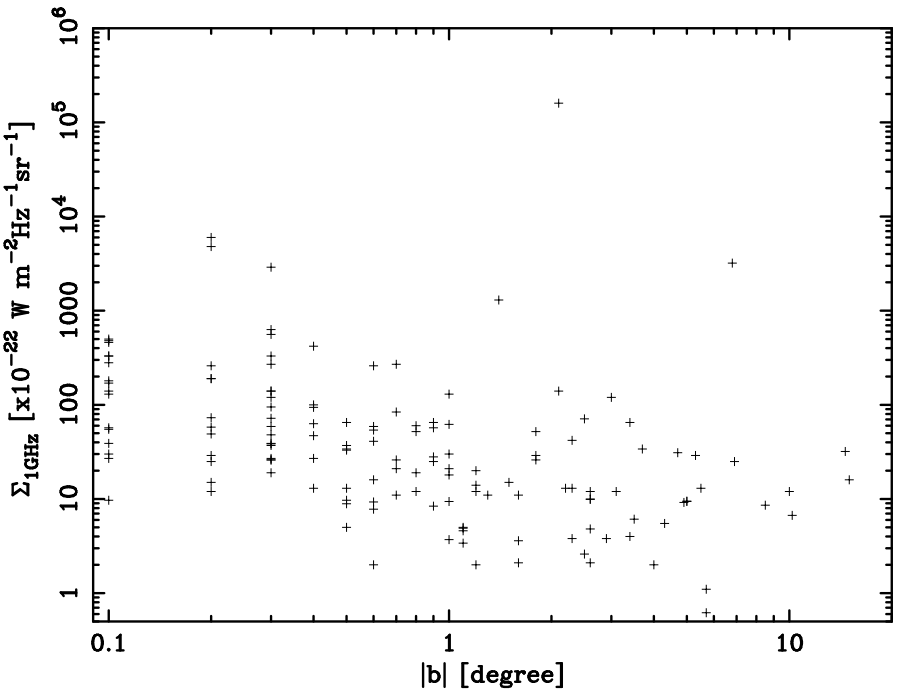

Fig. B.1.— Relation between the longitude of the SNR $|b|$ and flux density at 1 GHz (Case & Bhattacharya, 1998).

The SNRs with synchrotron X-rays are now listed up to ~ 10, but we need more samples to

study them systematically and quantitatively. The survey of SNRs have been done mainly in the radio band and the catalogued number is up to more than 200 (e.g., Green, 2001). However, nobody believes that all SNRs in our Galaxy have been found; Case & Bhattacharya (1998) claimed that only about half of the Galactic SNRs have been discovered by previous surveys. Figure B.1 shows the relation between the distance to the Galactic plane of the SNR and flux density at 1 GHz. There is no SNR with small flux density found near the Galactic plane, implying that radio surveys are not good at searching for SNRs near the Galactic plane, maybe due to contamination of other bright sources and galactic plane emission, and SNRs near the Galactic plane are often far from us. Hard X-ray surveys have many advantages to search such dim SNRs in the radio band as follows;

1. Hard X-rays do not affected by absorptions, then we can search for SNRs beyond the deep absorption.
2. SNRs which accelerate cosmic rays up to high energy, like SN 1006, is ordinary dim in the radio band. Therefore, the hard X-ray surveys can find them efficiently.

In fact, G347.3−0.5, which is the second sample of SNRs with synchrotron X-rays, have been discovered by *ROSAT* all sky survey and later identified in the radio band (e.g., Koyama et al., 1997; Slane et al., 1999).

Keeping these facts in our mind, we searched for the SNR candidates with synchrotron X-rays from *ASCA* Galactic plane survey data, which covers Galactic plane with $|l| < 45^\circ$ and $|b| < 0.4^\circ$ but about 10% of the region suffered from heavy contamination of stray lights from very bright sources (e.g., Sugizaki , 1999; Sugizaki et al., 2001). As a result, we found seven candidates and follow-up observations for three of them with *ASCA* (Bamba et al., 2003a), one with *ASCA* and *Chandra* (Bamba et al., 2001; Ueno et al., 2003), two with *XMM-Newton* (Ueno et al., in preparing). Their origin is still unknown, may be unresolved point sources, pulsar wind nebulae, or SNRs with synchrotron X-rays we search for.

In the survey region, we found eight SNRs and candidates; seven by our survey and G347.3−0.5 by Koyama et al. (1997). Therefore the number of expected SNRs in the surveyed field is

$$8 \times \frac{1}{1 - 0.1} \sim 8.9 \quad . \tag{B.1}$$

If we assume that the spatial density of SNR is uniform in the inner Galactic disk of $|l| \leq 60.^\circ 0$ and $|b| \leq 1.^\circ 0$ field, then the expected number is

$$8.9 \times \frac{120}{90} \times \frac{2}{0.8} = 30 \quad . \tag{B.2}$$

Since the X-ray surface brightness of the new SNR is only 2–3 times of the background Galactic ridge emission, we may miss detections of more samples with lower surface brightness (Bamba et al., 2003a). Thus the number of SNRs with non-thermal X-rays in our Galaxy would far exceed 30.

Appendix C

Two-Color Images of the SNRs

This chapter shows the two-color figures of SNRs we analysed, taken by *Chandra*. Taking a walk in this gallery, you will be able to enjoy the beautiful images of one of the biggest explosions in the universe.

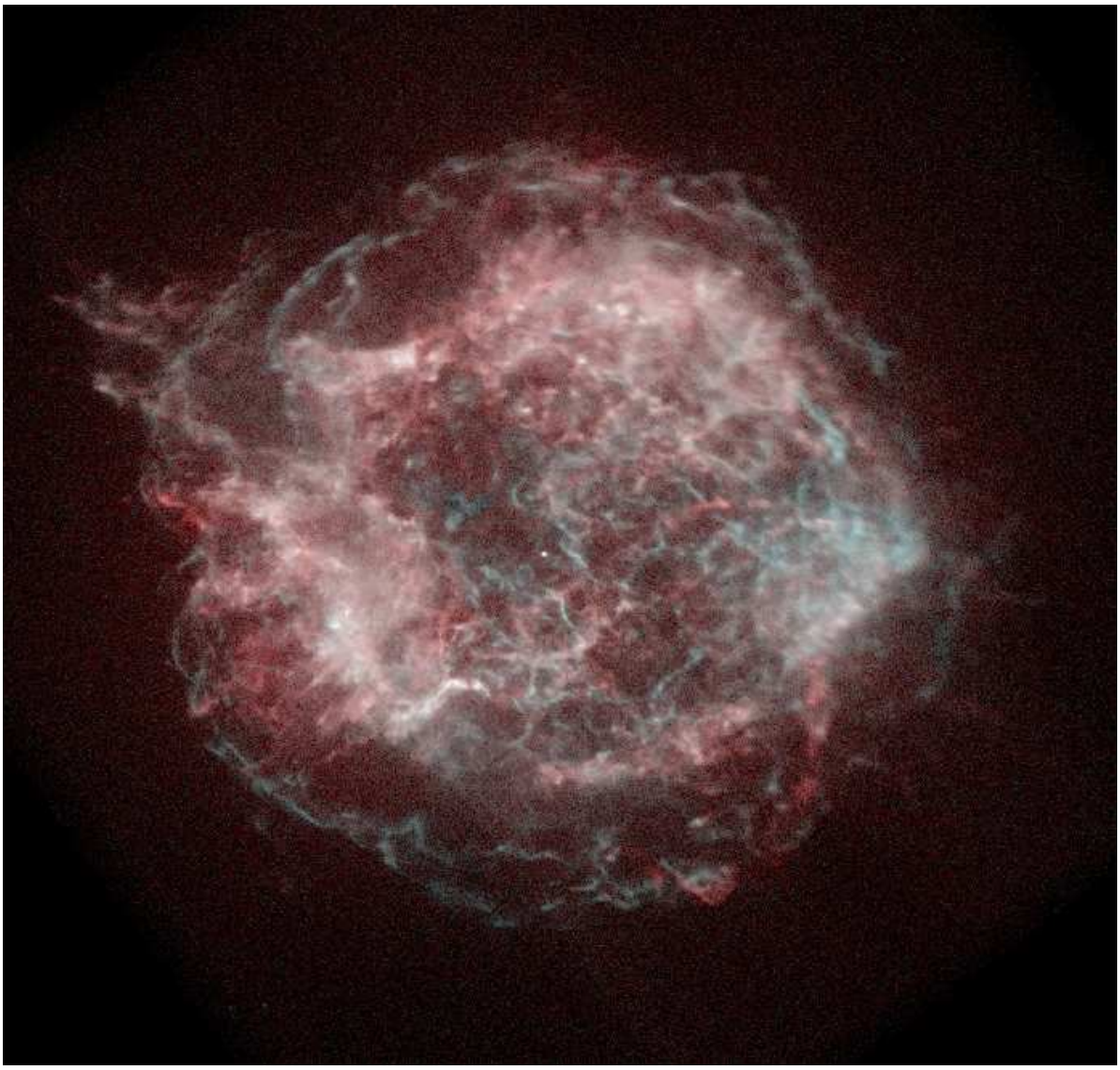

Fig. C.1.— Two color image of Cas A (red; 0.5–2.0 keV, blue; 2.0–8.0 keV).

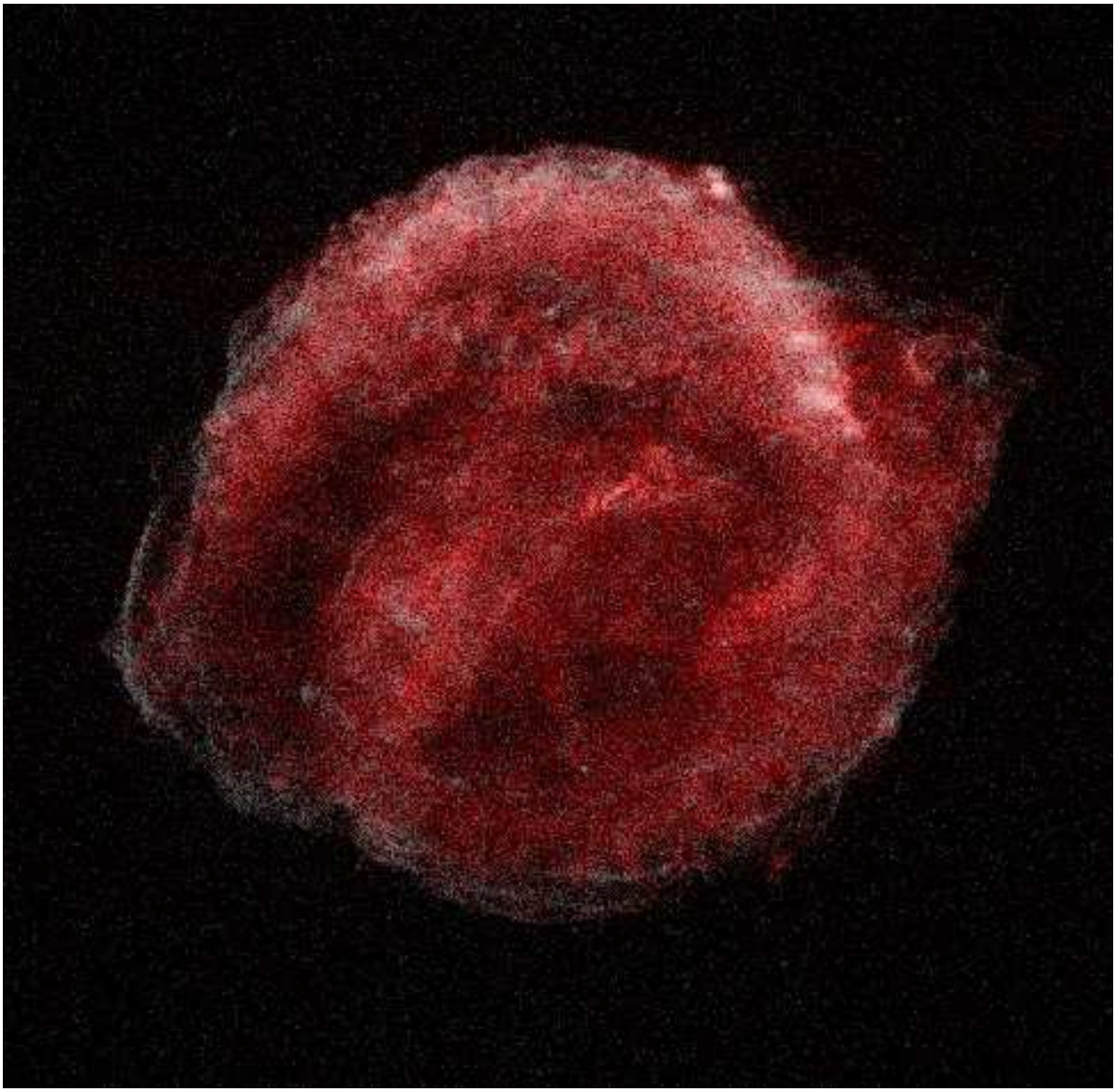

Fig. C.2.— Two color image of Kepler (red; 0.5–2.0 keV, blue; 2.0–8.0 keV).

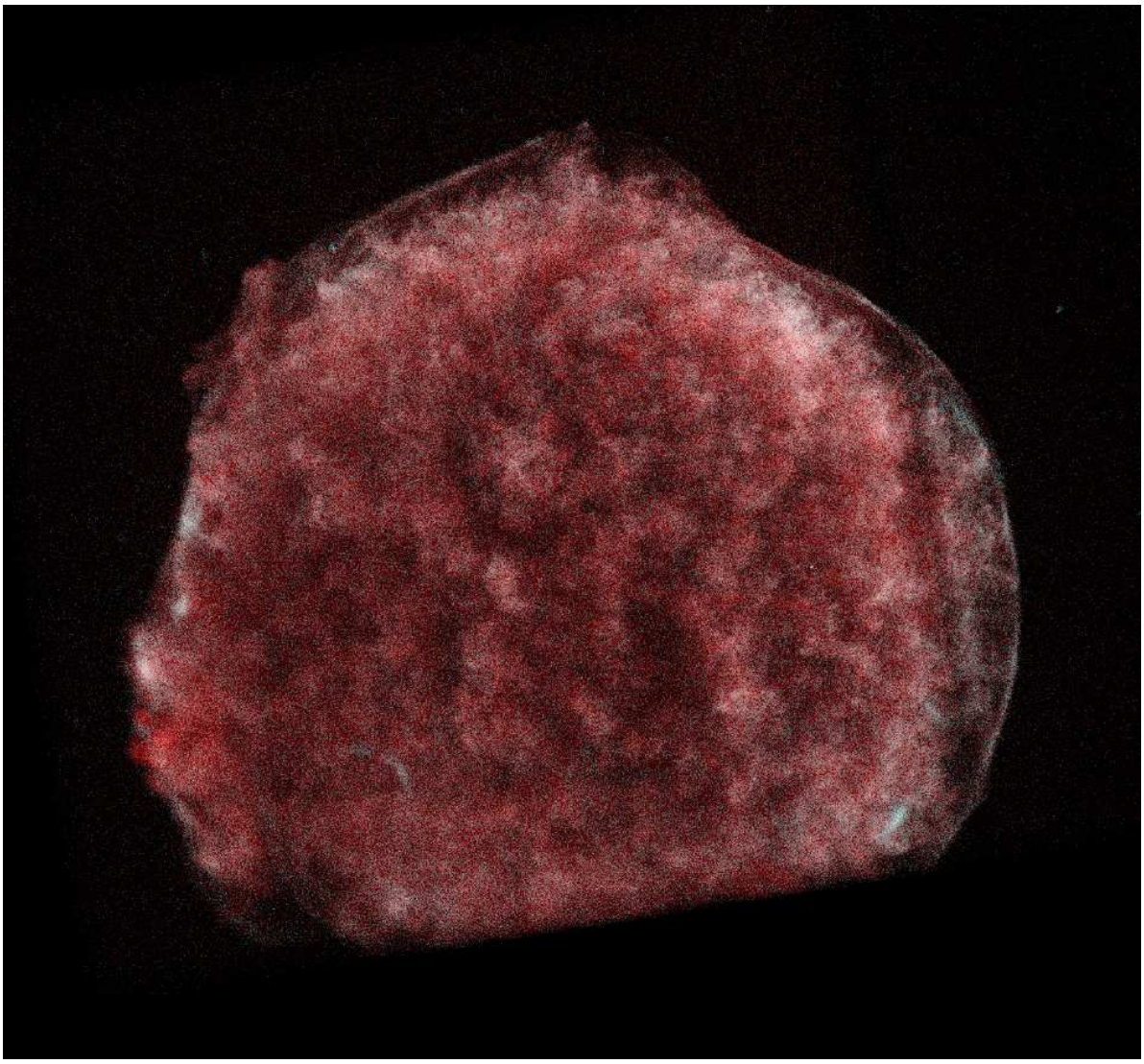

Fig. C.3.— Two color image of Tycho (red; 0.5–2.0 keV, blue; 2.0–8.0 keV).

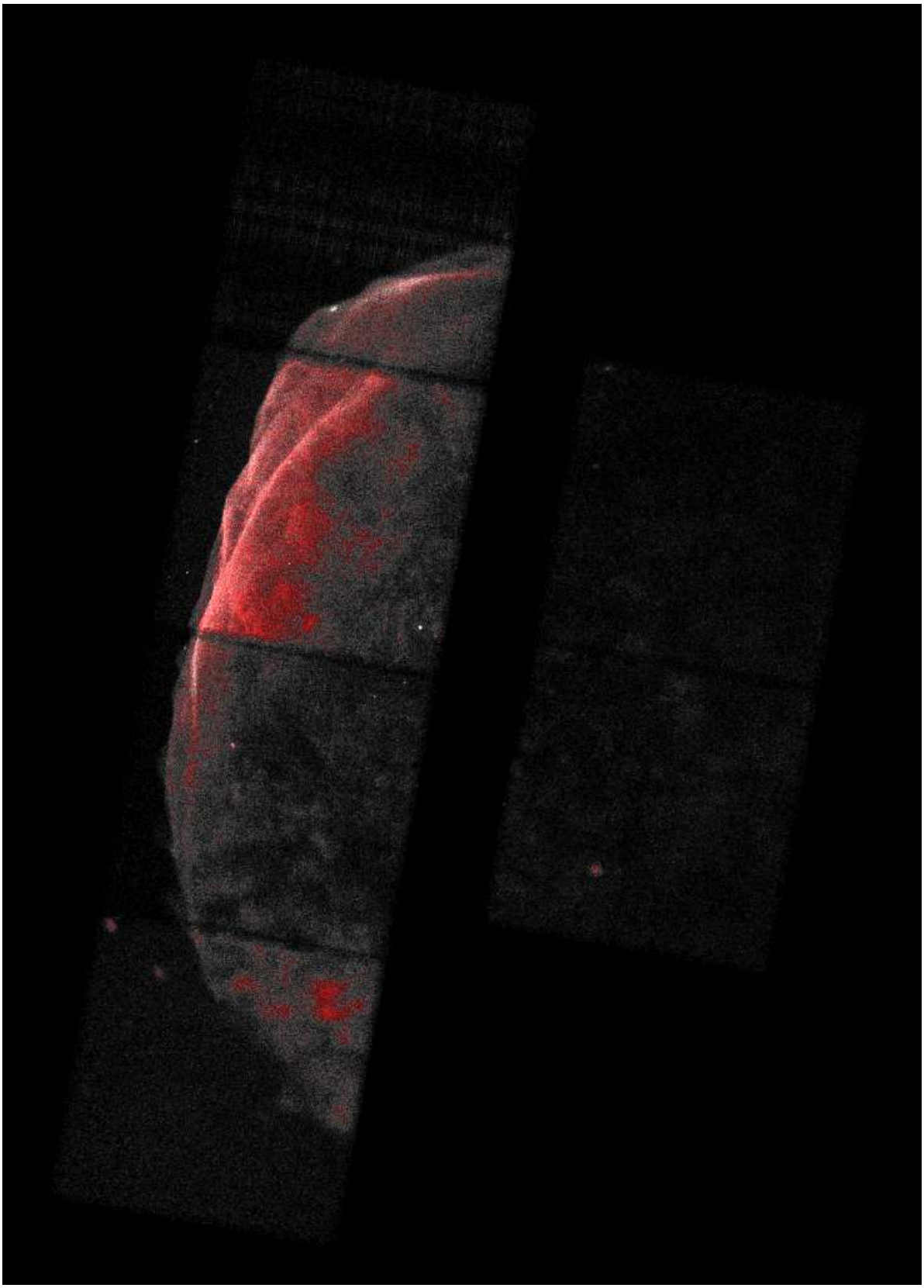

Fig. C.4.— Two color image of SN 1006 (red; 0.5–1.5 keV, blue; 1.5–8.0 keV).

Fig. C.5.— Two color image of RCW 86 south western shell (red; 0.5–1.5 keV, blue; 1.5–8.0 keV).

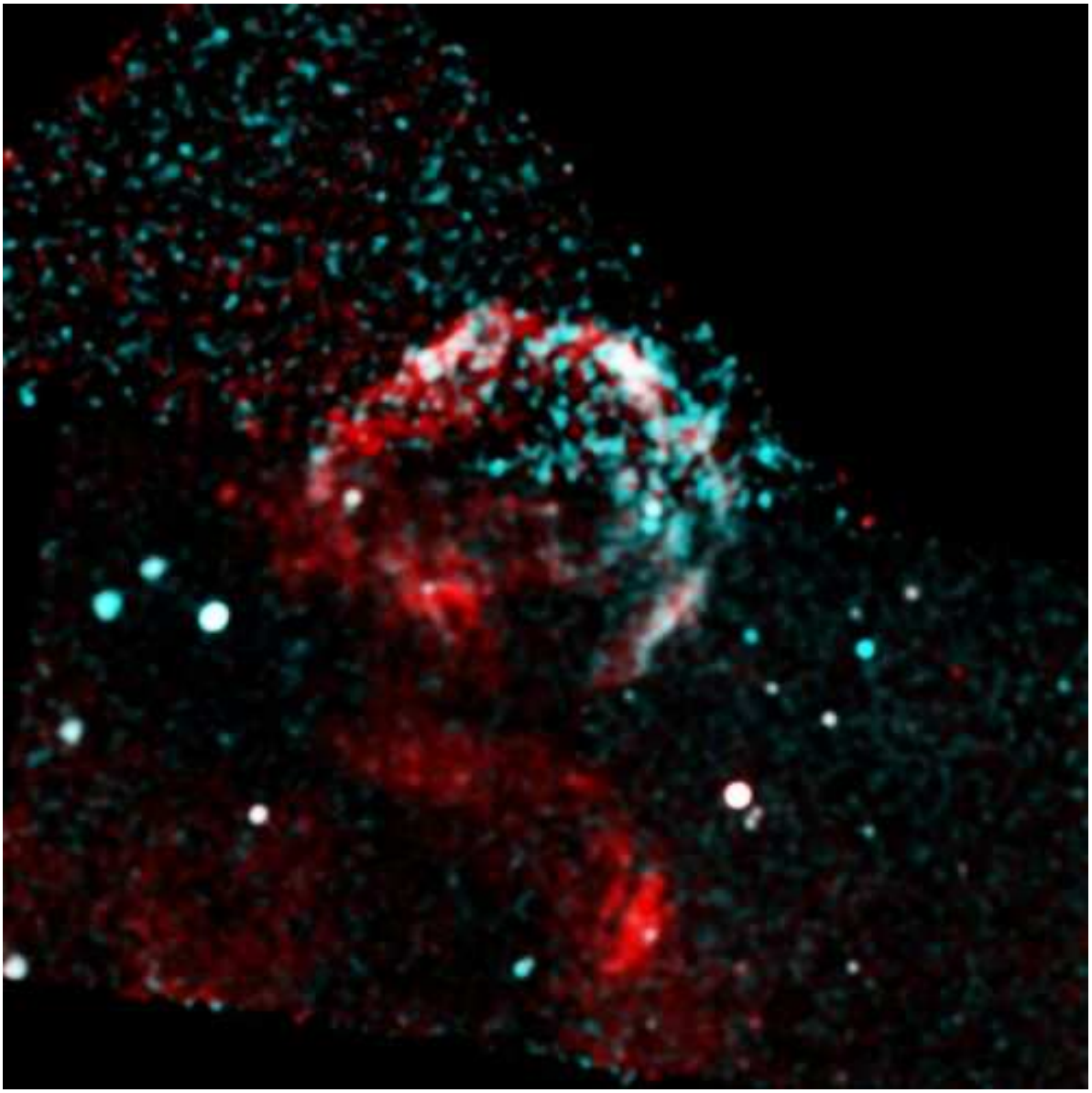

Fig. C.6.— Two color image of 30 Dor C (red; 0.5–2.0 keV, blue; 2.0–8.0 keV). The data we used was combined and exposure was corrected.

Acknowledgments

I deeply appreciate to Professor Katsuji Koyama for his guidance and encouragements in my graduate school life. This thesis would not have been completed without his support. I would like to thank my collaborators; Toshio Terasawa (Univ. of Tokyo), Tatsuo Yoshida (Ibaraki Univ,) Ryo Yamazaki, Masaru Ueno, and Hiroshi Nakajima (Kyoto Univ.).

My gratitude is also for Heinrich Völk (Max-Plank Institut), Stephen Reynolds (North-Carolina State Univ.), Alex Lazarian (Univ. of Wisconsin), Tohru Tanimori (Kyoto Univ.), Fumio Takahara (Osaka Univ.), Masahiro Hoshino (Univ. of Tokyo), Shuichiro Inutuka (Kyoto Univ.), and Leonid Ksenofontov (ICRR), who discussed with me about SN 1006 and the filaments in the remnant. The works on RCW 86 was accelerated by Hiroshi Tomida (JAXA), Masayuki Itoh (Kobe Univ.) gave me a plenty of information about 30 Dor C. Many helpful comments and discussions were given by Shigeo Yamauchi (Iwate Univ.) and Ken Ebisawa (ISDC). about the search for SNRs with *ASCA* Galactic plane survey. Masahiro Tsujimoto (Penn State Univ.) helped me to improve the manuscript. I am grateful to all the members of the cosmic ray laboratory in Kyoto University for their continuous discussions, encouragements, and technical advice.

The *Chandra* data were obtained through the Chandra X-ray Observatory Science Center (CXC) operated for NASA by the Smithsonian Astrophysical Observatory. This work is financially supported by the Japan Society for Promotion of Science for Young Scientists, the Hayakawa Satio Foundation, and a Grant-in-Aid for the 21st Century COE "Center for Diversity and Universality in Physics".

Finally, I express supreme thanks to all of my family and friends. They gave me an attractive dream of becoming an astrophysical scientist, and supported me to realize the dream financially and morally.